



UNIVERSITAT^{DE}
BARCELONA

Effects of substrate-derived cues in driving the self-organization of organoid-derived intestinal epithelia

Enara Larrañaga Carricajo



Aquesta tesi doctoral està subjecta a la llicència **Reconeixement 4.0. Espanya de Creative Commons.**

Esta tesis doctoral está sujeta a la licencia **Reconocimiento 4.0. España de Creative Commons.**

This doctoral thesis is licensed under the **Creative Commons Attribution 4.0. Spain License.**

Tesis doctoral

Effects of substrate-derived cues in driving the self-organization of organoid-derived intestinal epithelia

Autora: Enara Larrañaga Carricajo

Directora: Elena Martínez Fraiz



**UNIVERSITAT DE
BARCELONA**

Effects of substrate-derived cues in driving the self-organization of organoid-derived intestinal epithelia

Programa de doctorado en Nanociencias

Autora: Enara Larrañaga Carricajo

Directora: Elena Martínez Fraiz

Tutor: Josep Samitier Martí

Instituto de Bioingeniería de Cataluña



**UNIVERSITAT DE
BARCELONA**

Para mis amigas

Acknowledgements

Frente al cambio y el actual huracán de bofetadas y caricias, no es ningún secreto que añoro la rutina.

Esta tesis ha sido una de las etapas mejores y más complicadas de mi vida. Es el resultado del apoyo, la colaboración y la confianza de personas maravillosas que me han acompañado durante todo este tiempo. Hay muchas formas hermosas de dar las gracias, por ejemplo dando un abrazo o cruzando una mirada de complicidad. En este contexto, voy a tratar a buscar palabras que evoquen mi absoluta gratitud.

He aprendido que todo es temporal. Momentos. Sentimientos. Personas. Flores.

Empiezo expresando mi más sincero agradecimiento a la directora de esta tesis, Elena. Tu paciencia y ayuda me han guiado a lo largo de las aventuras y desventuras que han conformado este proceso. Agradeceré siempre tu apoyo y tus sabios consejos. Gracias por tu trato sincero y cuidado. Gracias por ofrecerme la oportunidad de formar parte de tu equipo. Por ayudarme a entender y aprender. Te admiro <3

Jordi, te agradezco enormemente tu ayuda incondicional así como tu total disponibilidad. Mi más sincera gratitud por todo tu tiempo dedicado tanto a este proyecto como a mi formación como investigadora. Eres para mi un referente en todos los aspectos. Tienes paciencia y aguante. No has dejado de mostrar valentía e ilusión frente a lo que haces. Gracias por los interminables consejos. Por enseñarme a abordar y confrontar la ciencia.

He aprendido que no siempre somos fuertes, que también dudamos.

Evocándome al inicio de la tesis, la primera científica con la que compartí un tiempo realmente enriquecedor fue Vero. Gracias por enseñarme a desenvolverme en un laboratorio, por el cariño, el cuidado y la delicadeza con que guiaste mis primeros avances. Gracias a Albert, Maria y Gizem por inundar de música el laboratorio amenizando el trabajo, por promover las discusiones científicas. Agradecer también la acogida del laboratorio de *Nanobioengineering*, a Anna L. y David I. por vuestra buena disposición a ayudarme y enseñarme.

He aprendido que la vulnerabilidad es siempre la elección correcta, porque es fácil ser frío en un mundo que hace que sea difícil ser tierno.

Un agradecimiento especial a Vane por transmitirme tu pasión por la biología y fundar el *organoids team*. Por enseñarme a crecer tanto a nivel profesional como personal. Ha sido un verdadero placer poder trabajar con una investigadora como tú.

Aina, amiga y cómplice. La magia existe y son aquellas personas que se sonrojan cuando alguien les dice todo lo que ellas dicen de las otras. Me fascina que compartamos conocimientos y discusiones científicas, imaginemos viajes juntas, susurremos secretos y hablemos de alegrías, daños y heridas. Cuando me di cuenta ya estaba contándote mi color favorito, y eso, es bello. Me maravillan las ganas de aprender que mostraste desde el primer día, eres brillante. Soy muy feliz de poder crecer a tu lado.

Vero, Giulia, María y Núria, vuestras aportaciones a este proceso tienen para mí un valor incalculable. Que hayáis formado parte lo ha hecho aún más enriquecedor. Muchas gracias por vuestro cariño y aprecio sincero. La reciprocidad en vuestras sonrisas ha sido siempre una motivación para mí. Gracias por fomentar las discusiones científicas y empaparne en conocimientos. Habéis sido y sois imprescindibles e irremplazables para mí tanto a nivel científico como personal.

Anna V., muchas gracias por estos 5 años, significas mucho para mí. Celebro vuestras miradas de complicidad y brindo por la delicadeza y la intensidad de todos los momentos compartidos. Y si me pides que esté, allí estaré.

A Angela, Livia, Renata, Marina y Daniel, la diversidad de nuestros proyectos enriquece y fomenta la interdisciplinalidad. Gracias por vuestra contribución.

Me gustaría dar las gracias a Mireia, que fue la primera estudiante con la que tuve el placer de compartir proyecto. Gracias por tu preciosa capacidad de ilusionarte y por tu colaboración a este proyecto. Quiero agradecerte todas las discusiones científicas y esa actitud tan enriquecedora de querer aprender y entender de cada paso que das. Me ayudaste a progresar como científica.

Me gustaría también dar las gracias a otros estudiantes que pasaron por el laboratorio, de los que tengo un valioso recuerdo. Gracias a Jon, Raquel, Augusto, Edu y Tere.

He aprendido que el tiempo todo lo cura.

Gracias a Silvia, Manu y Janfra, por hermosas discusiones que prenden la ciencia con feminismo.

Samuel, gracias por tu constante motivación, por tu paciencia, tu perseverancia, esfuerzo e ilusión. Por todas las emociones compartidas. Agradecer el interés en mis progresos. He aprendido mucho de tí. Agradezco profundamente la confianza depositada en mí.

Gracias Anna S., tienes esa melodía en la risa que me trae calma.

Quiero agradecer también el apoyo del laboratorio *Biosensors for bioengineering*. Gracias a Javi, Mariale, Ferran, Xiomara, Laura y Juanma por vuestro apoyo y cuidado.

He aprendido que el helado de menta con trocitos de chocolate lo soluciona todo y para lo que no pueda arreglar siempre están los abrazos de las personas a las que quiero.

Gracias a mis amigas y compañeras, las de Madrid y las de Barcelona, por enriquecer mi vida con vuestra manera de pensar, (de)construir y vivir. Por vuestro apoyo constante y sentir que somos familia. Porque cuidándonos somos más fuertes y más libres ya que el afecto sigue siendo un acto revolucionario.

Muy especialmente a mi amiga Júlia. Imagina la vida como si fuera un pilla-pilla contra los rivales del otro equipo del colegio, pues ella, es casa. Gracias por estar ahí, por acompañarme y regalarme un poco de tu magia. Por cuidarme y darme un aire más liviano. Por brindarme tu amistad. Llegar para abrazarme. Llegar para quedarte. Solo puedo estar agradecida de que nuestros caminos se hayan cruzado.

Gracias a mi familia. Os quiero.

Finalmente agradecer a mi abuela Julia por ser un referente como mujer y transmitirme el amor por las matemáticas, me gustaría pensar que estás orgullosa de mi.

Table of contents

Acknowledgements	4
Table of contents	7
Abstract	11
Abbreviations	13
1 Introduction	16
1.1 Epithelial tissues	16
1.2 Epithelial cell polarization	17
1.2.1 <i>Cell-cell interactions in epithelial tissues</i>	18
1.2.2 <i>Cell-extracellular matrix interactions in epithelial tissues</i>	20
1.2.3 <i>Wetting/de-wetting analogies to explain epithelial tissue behavior</i>	22
1.3 3D organoid cultures	25
1.3.1 <i>Intestinal organoids</i>	26
1.3.2 <i>Signals guiding intestinal self-organization and compartmentalization in vivo</i>	27
1.3.3 <i>Cell-extracellular matrix interactions in intestinal organoids</i>	29
1.3.4 <i>Cell-cell interactions in intestinal organoids</i>	31
1.4 Organoid-derived intestinal epithelial monolayers	32
2 Objectives	37
3 Materials and Methods	38
3.1 Cell line cultures	38
3.2 Culture of primary mouse small intestinal epithelial cells	39
3.2.1 <i>Mouse model</i>	39
3.2.2 <i>Intestinal crypt isolation and organoid culture</i>	39
3.2.3 <i>Obtention and culture of organoid-derived single cells</i>	41
3.3 Fabrication of Polyacrylamide (PA) hydrogel substrates with tunable stiffness	41
3.3.1 <i>Fabrication of PA hydrogel substrates</i>	41
3.3.2 <i>Activation and functionalization of PA hydrogel substrates</i>	43

3.4	Substrate coating with extracellular matrix (ECM) proteins	44
3.4.1	<i>Preparation of ECM-coated substrates</i>	44
3.4.2	<i>Characterization of the protein distribution and thickness of Matrigel thin films.....</i>	45
3.4.3	<i>Characterization of the mechanical properties of Matrigel thin films.....</i>	47
3.5	Cell culture on ECM-coated substrates	47
3.5.1	<i>Cell seeding and culture on the ECM-coated substrates.....</i>	47
3.5.2	<i>Quantification of cell markers on ECM-coated substrates</i>	49
3.5.3	<i>Quantification of cell surface coverage on ECM-coated substrates.....</i>	50
3.5.4	<i>Morphological characterization of single cells or cellular aggregates on ECM-coated substrates</i>	51
3.5.5	<i>Morphological characterization of cellular networks on ECM-coated substrates</i>	52
3.5.6	<i>Time-lapse microscopy experiments and quantification of cell migration on ECM-coated substrates.....</i>	54
3.6	Substrate biochemical micropatterning.....	56
3.6.1	<i>Micro-contact printing procedure.....</i>	56
3.6.2	<i>Preparation and characterization of hydrogels for micro-contact printing.....</i>	58
3.6.3	<i>Generation and characterization of biochemical patterns.....</i>	59
3.7	Cell culture on biochemically micropatterned substrates	60
3.7.1	<i>Cell seeding and culture on the micropatterned substrates</i>	60
3.7.2	<i>Cell nucleus orientation and position with respect to the biochemical patterns.....</i>	62
3.7.3	<i>Analysis of crypt- and villus-like domains on the micropatterned substrates.....</i>	63
3.8	Statistical Analysis	65
4	Results.....	66
4.1	Effects of cell-extracellular matrix interactions on the self-organization of organoid-derived intestinal monolayers.....	66
4.1.1	<i>Intestinal organoid-derived single cells self-organize in 3D-tubular networks that transit to 2D-monolayers on Matrigel thin films</i>	66

4.1.2	<i>Intestinal organoid-derived single cells organization presents a wetting phase transition depending on Matrigel concentration</i>	68
4.1.3	<i>Epithelial cell polarity depends on Matrigel concentration</i>	71
4.1.4	<i>Epithelial tubular networks have well-defined geometrical properties</i>	73
4.1.5	<i>Cell migration depends on Matrigel concentration and drives the formation of tubular networks</i>	76
4.1.6	<i>Epithelial cell lines form transient 3D cell aggregates but not tubular networks on Matrigel thin films</i>	78
4.1.7	<i>Wetting phase transition in epithelial cell lines also depends on Matrigel concentration</i>	80
4.1.8	<i>Epithelial monolayers formed at low Matrigel concentrations present an apico-basal polarity regardless of the cell type</i>	82
4.1.9	<i>3D epithelial transient structures formed at high Matrigel concentrations present cell-dependent apico-basal polarization</i>	84
4.1.10	<i>Epithelial cells redistribute the ECM of the coated substrates to form 3D transient structures</i>	85
4.1.11	<i>Intestinal organoid-derived single cells redistribute the ECM as a function of the stem cell distribution</i>	87
4.1.12	<i>3D-tubular networks can form onto Matrigel-coated substrates but not onto collagen I-coated substrates</i>	88
4.1.13	<i>Intestinal epithelial monolayers present a wetting phase transition depending on the substrate stiffness</i>	92
4.1.14	<i>Intrinsic self-organization properties of the intestinal organoid-derived epithelial cells depend on the stem cell ratio</i>	94
4.2	Effects of cell-cell and cell-secreted biomolecular signals on the self-organization of organoid-derived intestinal monolayers	100
4.2.1	<i>Micropatterns of ephrinB1 retain the biological activity of the ligand</i>	101
4.2.2	<i>EphrinB1 signaling strength can be effectively controlled through micropatterns</i>	105
4.2.3	<i>Biochemical micropatterns can be successfully transferred on Matrigel-coated surfaces</i>	106
4.2.4	<i>Matrigel-coated substrates support the growth of intestinal organoid-derived single cells after being freeze-dried and reconstituted</i>	108

4.2.5	<i>Epithelial monolayers maintain in vivo-like cell type composition and spatial organization on freeze-dried and reconstituted Matrigel.....</i>	110
4.2.6	<i>Design and fabrication of micropatterns with regular geometry and crypt-like domains morphology and dimensions</i>	114
4.2.7	<i>Micropatterns of ephrinB1 and Wnt3a ligands are able to guide the distribution of crypt-like domains in organoid-derived epithelial monolayers</i>	116
4.2.8	<i>The characteristic dimensions of ephrinB1 and Wnt3a micropatterns might be counterbalanced by the intrinsic self-organization properties of the organoid-derived intestinal epithelial monolayers.</i>	120
4.2.9	<i>Micropatterns of different biomolecules modulate the crypt-like domain morphology and distribution in epithelial monolayers according to their biological role.....</i>	123
4.2.10	<i>Crypt-like domain areas depend on the size of the micropatterned features.....</i>	125
5	Discussion	126
6	Conclusions.....	135
7	References.....	137
8	Resumen en castellano	148

Abstract

Intestinal cells self-organize into 3-dimensional (3D) organoids that recapitulate the *in vivo* structural and functional characteristics when embedded in a 3D cell-derived protein mixture (Matrigel). However, these very same cells self-organize into 2-dimensional (2D) intestinal epithelial monolayers that recapitulate the *in vivo*-like cell organization when seeded on thin layers of the same cell-derived protein mixture. Moreover, *in vivo*, the intestine integrates regulation from paracrine and juxtacrine signals to establish its characteristic crypt-villus axis self-organization. However, direct experimental manipulation of these paracrine and juxtacrine signals, as well as their functional concentrations and effects at the cellular level, has been hampered by limitations of the *in vivo* and *in vitro* currently available systems. In general, changes in epithelial cell organization are characterized by a cross-talk between cell-substrate and cell-cell interactions, but the role of the ECM dimensionality, protein composition and spatial distribution in the intestinal epithelial cells' organization is not fully understood.

In this thesis, we show that intestinal epithelial cells self-organize in 2D-monolayers or 3D-tubular networks depending on the Matrigel protein concentration when the dimensionality is fixed. These self-assembles tubular networks have inner apical polarization and are similar to soap foams or de-wetted collagen networks. They have well defined topological and metrical properties and become spontaneously ordered at large length scales. Interestingly, stem cells have particular dynamics during the formation of each self-organized patterns. On low Matrigel concentration, stem cells present a confined random movement to form a 2D-monolayer. In contrast, on higher Matrigel concentration, stem cells perform a direct motion towards a specific target to form the 3D-tubular networks. By reducing the proportion of stem cells in the culture, the formation of 3D-tubular networks is impaired. Instead, primary cells form aggregates when seeded above the transition protein concentration, similar to two other epithelial cell types (Caco-2 and MDCK cells). On the other hand, the 2D-monolayers formed on low Matrigel concentration contain crypt- and villus-like domains resembling those found *in vivo*. These compartments are randomly distributed and their shape is not uniform. However, by producing localized micropatterns of immobilized Wnt and ephrin factors on freeze-dried Matrigel-coated substrates by micro-contact printing, we can drive the compartmentalization of the intestinal epithelial monolayers by spatially positioning the crypt- and villus-like domains. Finally, by changing the shape and dimension of the patterns we can control the distance between the crypt-like domains as well as their dimensions and shape.

Overall, our experiments illustrate how Matrigel concentration regulates intestinal epithelial cell organization as a function of cell-substrate adhesion, and show that

primary intestinal epithelial cells self-organize in structures with well-defined sizes and shapes independently of dimensionality or external signaling gradients. Also, we show that the amount of stem cells in the culture regulates the geometry of those self-organized structures. On the other hand, micropatterns of immobilized proteins to the ECM provides accurate control of the crypt-villus domain positioning in our epithelial monolayers. Thus, our work could yield insights about the roles of stem cells and protein concentration in tissue morphogenesis and their influence in the *in vivo* tissue morphological features such as the dimension of the crypts. In addition, we believe our platform will allow an easy and reliable manner to analyze the effect of relevant proteins on the epithelial cell compartmentalization, as well as the study of important intestinal epithelial processes such as stem cells proliferation, cell migration and differentiation both in homeostasis and pathological processes.

Abbreviations

2D	Two Dimensional
3D	Three Dimensional
AFM	Atomic Force Microscope
AJ	Adherens Junction
Apc	<i>Adenomatous polyposis coli</i>
AU	Airy Unit
BME	basement membrane extract
BMP	Bone Morphogenetic Protein
BSA	Bovine Serum Albumin
Caco-2	Colon Carcinoma cell line
CFTR	Cystic Fibrosis Transmembrane Conductance Regulator
Ck20	Cytokeratin 20
DAPI	4',6-diamidino-2-phenylindole
DLS	Dynamic light scattering
DMEM	Dulbecco's Modified Eagle Medium
dpi	day post-irradiation
E-cadherin	Epithelial cadherin
ECM	Extracellular Matrix
Edu	5-ethynyl-2'-deoxyuridine
EGF	Epidermal Growth Factor
EMT	Epithelial-Mesenchymal Transition
F-Actin	Filamentous Actin
FBS	Fetal Bovine Serum
Fc	Fragment crystallizable
FNT	Fibronectin
FWHM	Full width at half maximum

GFP	Green Fluorescence Protein
IgA	Immunoglobulin A
ISC	Intestinal Stem Cell
Lgr5	Leu-rich repeat-containing G protein-coupled receptor 5
Ln	Laminin
LSM	Laser Scanning Microscope
Lyz	Lysozyme
MDCK	Madin-Darby Canine Kidney cell line
MEM-NEAA	Minimum Essential Medium Non-Essential Amino Acids solution
MSD	Mean-square displacement
NMuMG	Normal Murine Mammary Gland
NA	Numerical Aperture
PA	Polyacrylamide
PBS	Phosphate Buffered Saline
PDMS	Polydimethylsiloxane
PEG	Poly (ethylene glycol)
PEN	polyethylene naphthalate
PLL	Poly-L-lysine
ROCK	Rho kinase
ROI	Region of interest
RT	Room Temperature
S-180	Murine Sarcoma cell line
SD	Standard deviation
SEM	Standard error of the mean
StrTx	Streptavidin Texas
TA	Transit-amplifying
TCF	Temporal correlation function
TEAD	Transcriptional Enhanced Associate Domain
TEER	Transepithelial Electrical Resistance

TEMED	Tetramethylethylenediamine
TJ	Tight Junctions
UV	Ultraviolet light
Vil1	Villin
WD	Working Distance
Wnt	Wingless/Int
YAP	Yes-associated protein 1
ZO-1	Zonula Occludens 1

1 Introduction

1.1 Epithelial tissues

Epithelial tissues cover body surfaces and line major organs. One of their main functions is to act as selective barriers that protect the body against external physical, chemical, and microbial insults. Besides protection, these tissues have other functions such as secretion, selective absorption, transcellular transport, and detection of sensation. To perform their barrier functions, cells in epithelial tissues join together into highly cohesive sheets (Figure 1.1 (a))¹. Epithelial tissues such as skin, lung alveoli, kidney, uterus, trachea, cornea or intestine are arranged in three dimensional (3D) complex structures such as invaginations, evaginations, spherical cysts or tubular structures (Figure 1.1 (b)). This 3D organization is of fundamental importance for physiological processes such as tissue homeostasis, development and regeneration. Actually, epithelial tissues are in a continuous and relatively rapid state of self-renewal. This active renewal is enabled by the presence of pools of stem cells such as those residing in the limbal niches of the cornea or the crypts of the intestinal tissue². This high cell turnover, makes epithelial tissues a major site for carcinogenesis³⁻⁵.

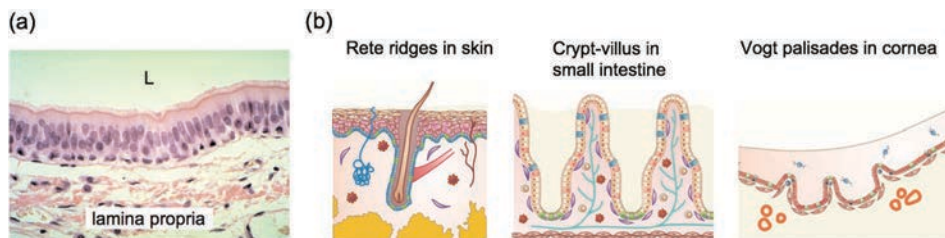


Figure 1.1. (a) Simple epithelia formed by a monolayer of epithelial cells that separates the lumen (L) from the underlying lamina propria of the tissue. Adapted from circulatorysystemmvb.weebly.com. (b) Schematic representation of native 3D structures formed by epithelial tissues in vivo. Adapted with permission from Torras et al., 2018.

3D structures of simple epithelia, such as the intestine, enclose a central lumen lined with epithelial cells, which sit on top of a specific matrix called basement membrane. The basement membrane is a thin layer of extracellular matrix (ECM) that contains mainly laminin and collagen⁶⁻⁸. The basement membrane separates the epithelium from the underlying connective tissue or lamina propria. This specific ECM also influences cell behavior and dictates its shape, gene expression, adhesion, migration, proliferation, and apoptosis^{9,10}.

To properly perform their functions, epithelial cells need to be polarized, which means that they have different structure, composition and function between their

apical and basolateral domains. The apical domain typically faces the lumen of the tissue and regulates the interaction with luminal contents. The basolateral domain establishes the cell-to-cell contacts, anchors the cells to the ECM, and communicates with stromal cells residing in the lamina propria. Both cell-cell and cell-substrate interactions are necessary for cell polarization and epithelial organization.

1.2 Epithelial cell polarization

As stated above, a fundamental aspect in the organization of the epithelial tissues is cell polarity^{11,12}. Polarity refers to the formation of structurally and functionally distinct apical and basolateral cellular domains, limited by cell-cell adhesion structures called tight junctions. The two domains have, for instance, different distribution of phospholipids, protein complexes, and cytoskeletal components¹³. Such cytoskeletal components include the actomyosin cytoskeleton, the microtubules and the intermediate filaments. All of them are in constant communication, which is of fundamental importance to maintain apico-basal cell polarity.

In particular, actin, one of the proteins forming the actomyosin cytoskeleton, has a predominant role in defining epithelial cell polarity. Filamentous actin (F-actin) protein accumulates at different cell locations along the apico-basal cell axis (Figure 1.2 (a)). At the apical cell side, F-actin bundles provide mechanical support to cell structures called microvilli that form the so-called brush-like borders (Figure 1.2 (b), upper panel)¹⁴. Microvilli are cellular membrane protrusions of approximate $\sim 1.5 \mu\text{m}$ long and 100 nm in diameter¹³. They possess several functions such as absorption, secretion and assisting the cell in response to its environment¹⁵. On the other hand, at the cell lateral domains epithelial cells show a belt of F-actin at their contact sites (Figure 1.2 (b), middle panel). This adhesion belt links the cytoskeleton of adjacent cells and controls the intercellular surface tension and the cell shape¹⁶. Additionally, F-actin is also found underneath the cell membrane in the form of cell cortex (Figure 1.2 (b), lower panel). Cell-cell junctions couple the actomyosin cortex of neighboring epithelial cells together and direct tissue organization¹⁷. Specifically, the actomyosin cortex regulates the hexagonal cell shape^{18,19} in epithelial monolayers. Finally, at the cell basal domain contacting the ECM, F-actin can be assembled into fiber bundles named stress fibers. These structures typically contain myosin and actin proteins and are also able to generate contractile forces. Many epithelial cell types such as kidney cells show basal actin stress fibers *in vivo* (Figure 1.2 (c))²⁰⁻²². Their physiological role is to regulate the intraluminal pressure through their contractility and to reinforce the attachment of cells to the ECM²⁰. Moreover, collectively migrating cells generate protrusive forces through lamellipodia or filopodia at their basal level^{23,24}. Recently, it has been reported that migrating

enterocytes, which are absorptive cells of the intestine, display actin-rich basal aggregate protrusions *in vivo* that are oriented in their migration direction²⁵ (Figure 1.2 (d)).

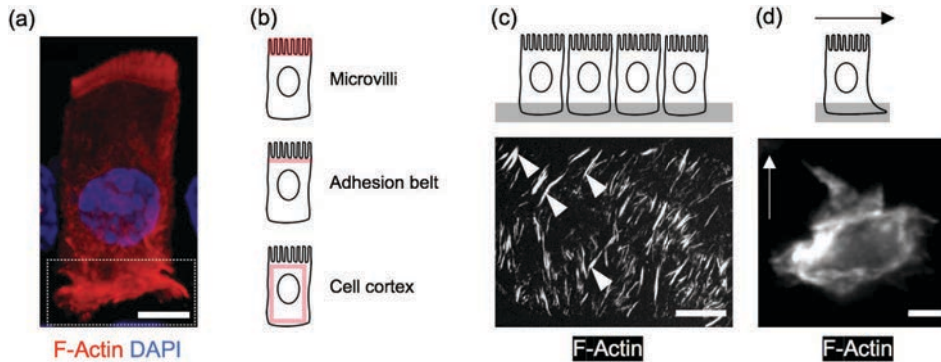


Figure 1.2. (a) Fluorescence image of an enterocyte obtained with super-resolution microscope, showing F-Actin and cell nucleus (DAPI). Scale bar: 4 μm . Adapted with permission from Krndija et al., 2019. (b) Schematic representation of different accumulations of F-Actin in epithelial cells: microvilli, adhesion belt and cell cortex (red). (c) Representative image obtained with a confocal microscope of F-Actin located at the cellular basal zones of isolated renal tubes of rabbit kidneys. White arrowheads indicate stress fibers. Scale bar: 10 μm . Adapted with permission from Goto et al., 1998. (d) Representative image of maximum intensity Z projections for F-Actin at the basal level. Intestinal epithelial cells displayed actin-rich basal protrusions oriented in the direction of migration. The arrows indicate the direction of migration. Scale bar: 3 μm . Adapted with permission from Krndija et al., 2019.

1.2.1 Cell-cell interactions in epithelial tissues

To be polarized, epithelial cells form specialized cell junctions with neighbouring cells that are essential for the epithelial tissue organization and barrier function. These junctions are positioned along the lateral sides of the epithelial cells and consist primarily in tight junctions (TJs), adherens junctions (AJs) and desmosomes. All of them form physical connections between cells, organize and regulate the cell cytoskeleton and modulate cell signaling pathways.

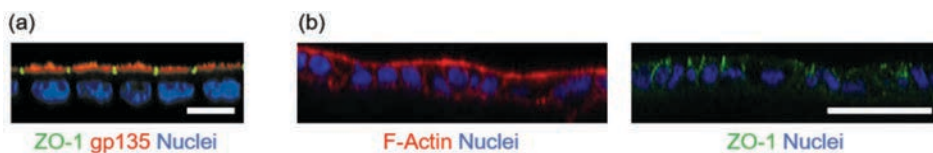


Figure 1.3. (a) Zonula occludens 1 (ZO-1) protein (tight junction protein), gp135 (apical plasma membrane protein) and cell nuclei for a MDCK monolayer. Scale bar: 10 μm . Adapted with permission from O'Brian et al., 2001. (b) Representative image obtained with a confocal microscope of F-Actin, ZO-1 and cell nuclei for Caco-2 monolayers. Scale bar: 10 μm . Adapted with permission from Vila et al., 2020.

In particular, the TJ intercellular structures are established at the apical cellular domains and have two main functions: fencing membrane proteins into segregated

apical and basolateral domains; and gating the paracellular passage of ions and solutes in-between cells²⁶. TJ structures contain two types of transmembrane proteins, occludins and claudins, which confer these functions, and associated cytoplasmic proteins that may link TJs to the actin-cytoskeleton and the AJs. For example, zonula occludens 1 (ZO-1)²⁷ bridges the transmembrane protein occludin to the actin cytoskeletal elements²⁸. This bridge forms a link between TJs structures and actomyosin contractile ring structures and is essential for the formation and stabilization of functional epithelial TJs structures (Figure 1.3).

The first intercellular junctions that develop when epithelial cells make direct physical contact with one another are the AJs¹⁴. AJs are mainly formed by cadherins, which are a family of transmembrane proteins that form cell-cell adhesions in a calcium-dependent manner. Differential cadherin expression allows cells to recognize and bind to similar cells, which facilitates tissue organization²⁹. In particular, epithelial cadherin (E-cadherin) has a pivotal role in tissue organization^{29,30}. E-cadherin is a well characterized molecule and its role has been determined in both normal and pathological tissue conditions. Typically, this research has been carried out *in vitro* employing cultures of Madin-Darby Canine Kidney (MDCK) cell monolayers^{31,32}. These are epithelial cells from the kidney tubule of an adult dog. By blocking E-cadherin using anti- E-cadherin antibodies, it has been shown that these molecules are necessary for the formation of AJs³¹. Moreover, inhibition of E-cadherin expression revealed that it also affects the localization of basolateral proteins, thus disrupting the epithelial apico-basal polarity³². On the other hand, downregulation of E-cadherin has been associated with epithelial-mesenchymal transition (EMT)³³. The EMT is correlated with the loss of epithelial morphology and the acquisition of mesenchymal characteristics. EMT is involved in physiological processes such as embryonic development and pathological processes such as cancer, and indicates the transition from collective migration to single-cell invasion, where cells lose their cell-cell junctions via a variety of mechanisms³³.

Finally, the intercellular structures named desmosomes provide strong adhesion between cells because they link to the intermediate filament cytoskeleton and form the adhesive bonds in a network that give mechanical strength to epithelial tissues³⁴. The adhesion of desmosomes is mediated by members of the cadherin family, specifically the desmosomal cadherins. These cadherins tail through a series of protein interactions, which serve to recruit intermediate filaments to sites of desmosome assembly³⁵.

1.2.2 Cell-extracellular matrix interactions in epithelial tissues

Epithelial cells are supported by a special ECM, the basement membrane, mainly composed of laminin and collagen type IV. Cell-ECM interactions regulate cell polarity, differentiation, growth, apoptosis and gene expression³⁶. A pioneer model for the study of cell-ECM interactions involved the culture of a monolayer of epithelial cells grown onto a protein matrix and covered by more protein matrix³⁷. MDCK and Normal Murine Mammary Gland (NMuMG) cell lines and collagen type I matrix have been extensively used in this approach. The establishment of 3D structures generates a better understanding of epithelial cell organization. Both cell types respond to the overlaying matrix by undergoing a reorganization process, resulting in the formation of spherical structures with basal-out polarity, meaning that the apical cell domain is facing a lumen enclosed within the sphere and the basal cell domain sits on the surrounding matrix³⁷.

Similar results have also been found when single cells, instead of monolayers, are embedded within 3D matrices. These cells proliferate and self-organize into well-polarized aggregates containing a single hollow lumen and recreating the spherical structure of some epithelial organs. MDCK aggregates in a collagen type I matrix exhibited the basal-out polarity described for the matrix-covered monolayers (Figure 1.4 (a)). Interestingly, these very same aggregates when cultured in suspension, without the surrounding matrix of ECM proteins, reversed their polarity and exhibited apical-out polarity (Figure 1.4 (b))³⁸. Caco-2 single cells, which are from a human colorectal adenocarcinoma, were also embedded in Matrigel (a cell-secreted protein mixture rich in laminin and collagen IV) or in collagen-Matrigel mixtures, proliferated and formed aggregates with basal-out polarity that enclosed a central lumen³⁹⁻⁴¹. However, this polarity is inverted when Caco-2 cells are mutated to be anoikis resistant, so cell death is prevented when they are detached from the surrounding ECM, and are embedded in a collagen-Matrigel mixture (Figure 1.4 (c))⁴¹.

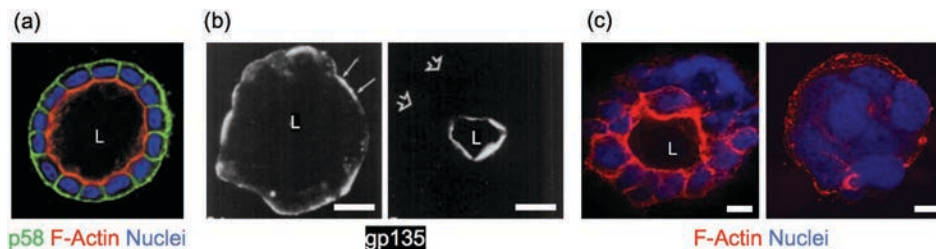


Figure 1.4. (a) Confocal image of p58 (basal and lateral domains), F-Actin and cell nuclei for MDCK cells embedded in collagen type I matrix. The aggregate consists in basal-out polarized cells that enclose a central lumen (L) and is surrounded by the ECM. Adapted with permission from O'Brian et al., 2002. (b) Image of gp135 (apical membrane protein) for a MDCK cell aggregate cultured in suspension for ~ 5 days and showing apical-out polarization (left panel). When transferred to collagen gels, after 16-24 hours the aggregate polarity is reverted to basal-out (right panel). Scale bars: 16 μ m. Adapted with permission from

Wang et al., 1998. (c) Confocal image of F-Actin and cell nuclei for Caco-2 cells embedded within a collagen-Matrigel mixture for ~ 10 days. The native Caco-2 cells presented basal-out polarization (left panel). In contrast, Caco-2 aggregates formed from mutated cells being anoikis resistant exhibited apical-out polarization (right panel). Scale bars: 20 μm . Adapted with permission from Patankar et al., 2019.

Further examples include growing mammary epithelial cells, both primary cells and cell lines, within 3D Matrigel matrices. The structures formed by normal and cancer cells were immediately and reproducibly distinguishable (Figure 1.5 (a))^{42,43}. Normal cells entered in growth arrest and organized in basal-out polarized aggregates. In contrast, tumor cells formed disorganized masses⁴³. Interestingly, when tumoral cells were cultured within a healthy ECM, they successfully reverted their malignant phenotype (Figure 1.5 (b))⁴⁴. Taken together, these experiments demonstrated that epithelial tissue organization, and in particular cell polarization, not only depends on cell-cell interactions but is also strongly determined by the interactions between the cells and the basement membrane matrix.

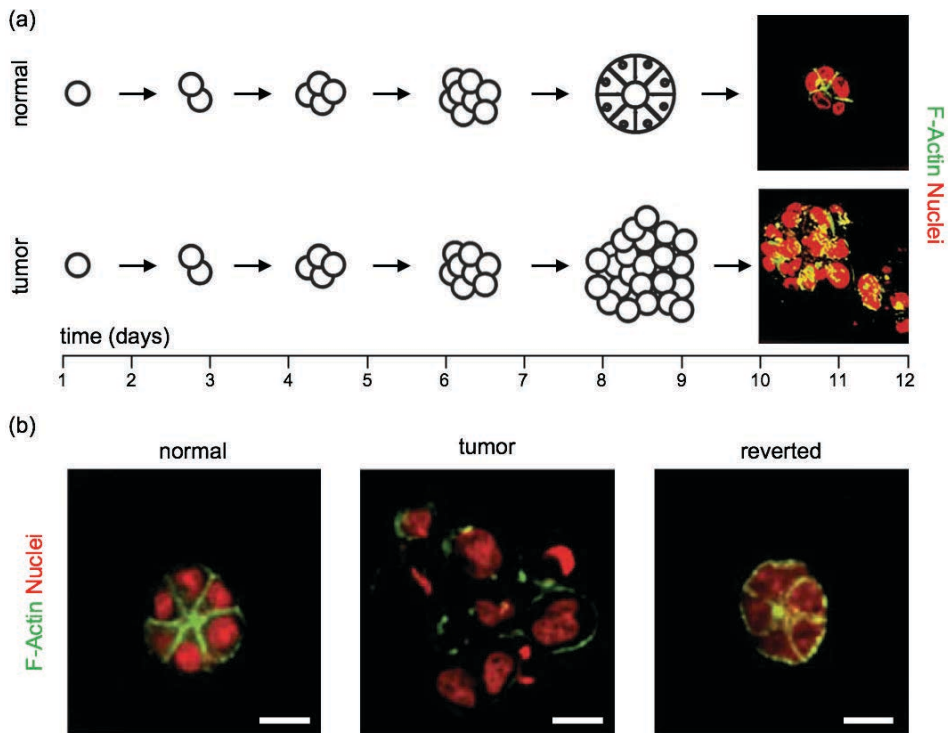


Figure 1.5. (a) Scheme depicting the growth of normal and tumoral mammary cells over time and confocal fluorescence images of F-Actin and nuclei. Normal mammary epithelial cells cultured embedded in Matrigel exhibited growth arrest and organized into basal-out aggregates (acini-like structures) (upper row). In contrast, mammary tumoral cells continue to proliferate into disorganized masses (lower row). Adapted with permission from Weaver et al., 1995. (b) Confocal representative images of F-Actin and nuclei of normal and tumoral mammary cells aggregates. Normal cells organize into basal-out aggregates (left panel) while tumoral cells grow into disorganized masses (middle panel). Mammary tumor cells reverted their status and organized the cortical actin (right panel). Scale bars: 15 μm . Adapted with permission from Wang et al., 1998.

In addition, the *in vitro* models described above have also contributed to determine the relevance of the matrix composition for the epithelial polarization. For example, it has been reported that MDCK cells, when embedded in collagen type I matrices, are able to produce their own laminin and assemble it along their basal surface. This creates a basement membrane to which integrins, the main cellular receptors mediating cell-substrate adhesions, can attach⁴⁵. When the ability of MDCK cells to assemble endogenous laminin is impaired by using genetic models, the polarity of the MDCK aggregates is reverted⁴⁵. However, when the culture is supplemented with exogenous laminin, the basal-out polarity of the aggregates is restored⁴⁵. In addition, MDCK cells grown within Matrigel, which has a high content of laminin, grow faster than when cultured in collagen⁴⁶. Altogether, these results point out the relevance of laminin for the epithelial organization and support the preference of using Matrigel as 3D matrix for *in vitro* studies rather than collagen type I.

Although these 3D culture models have been able to recapitulate the epithelial morphogenesis, they do not offer the possibility of studying individual contributions of cell-cell and cell-ECM interactions. Moreover, the 3D aggregates embedded in ECM are randomly distributed and heterogeneous in size, which complicates standardization, the use of conventional microscopy for experimental data collection and data analysis. For this reason, another way to study the cell-ECM interactions consists in culturing cells on a two dimensional (2D) substrate with a concentration range several orders of magnitude below the typical concentration of the 3D-matrices previously introduced^{47,48}. For example, MDCK cells are cultured on substrates of variable fibronectin concentrations (0 - 80 $\mu\text{g mL}^{-1}$)⁴⁸. Cells on high fibronectin concentration grew into large and flat monolayers, whereas on low fibronectin concentration cells form aggregates. Another example used primary hepatocytes and Matrigel as substrate⁴⁷. The authors observed how reducing the Matrigel concentration (1 - 0.01 $\mu\text{g cm}^{-2}$) changed the cell organization from monolayers to aggregates. It is worth noticing that these approaches, however, involve the use of ECM protein concentrations which are several orders of magnitude below the ones found in the 3D and tissue matrices.

1.2.3 *Wetting/de-wetting analogies to explain epithelial tissue behavior*

Classically, wetting models have been used to study the dynamics of liquid-solid interfaces by considering soft matter models. When a liquid drop contacts a solid surface, its spreading dynamics depend on the balance of the liquid cohesive forces and the liquid-surface adhesive forces. This leads to different wetting regimes: the drop can spread creating a film (complete wetting), or it can stay as a drop in a partial wetting situation and forming a certain contact angle with the surface at the equilibrium. On the other hand, a liquid thin film forced to contact a surface using, for instance, spin-coating or painting might remain wetting the surface or might

retract in a de-wetting process. De-wetting processes might form holes in the liquid film, which can later coalesce to form a network of filaments and break into liquid droplets (Figure 1.6 (a)). De-wetting phenomena have been described in systems such as polymeric films, protein films or soap foams on substrates. In particular, polygon networks of connected strings of material, like Voronoi patterns, have been described (Figure 1.6 (b-d))⁴⁹⁻⁵⁴. Their morphology has been extensively studied by applying mathematical methods of stochastic geometry. These networks have strong similarities in their structure. They form hexagonal holes, i.e. the average number of edges of the polygon is six, and the average angle between edges is 120° . Moreover, these networks are relatively well ordered. This ordered status can be reached by coalescence, i.e. rupture of the thinnest rims between polygons of different sizes, or diffusion of gas through the edges of polygons with different pressures. These morphologies of de-wetted polymer networks are spontaneously established in nature and have been extensively described, for instance, in vascular networks formed by endothelial cells⁵⁵.

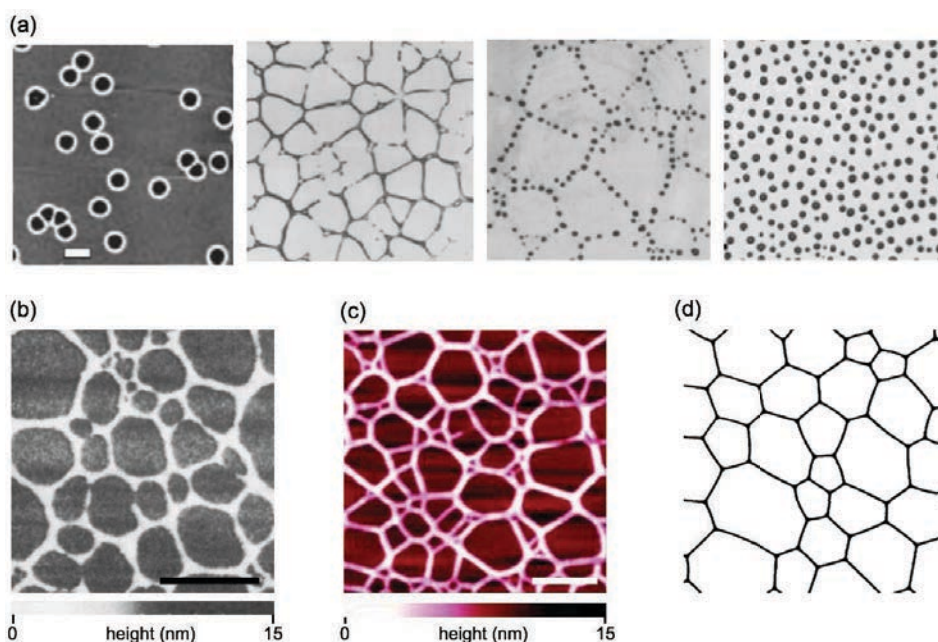


Figure 1.6. (a) Typical morphologies associated with de-wetting of thin polymer films: nucleated holes, polygonal patterns, final polygonal patterns after of rims into spherical droplets, and random droplets resulting from de-wetting. Adapted with permission from Mukherjee et al. 2015. (b) Scanning Tunneling Microscopy images of polystyrene networks on a silicon surface. Scale bar: $1\mu\text{m}$. Adapted with permission from Stange et al. 1992. (c) Scanning force microscopy micrographs of collagen network on mica surface. Scale bar: $1\mu\text{m}$. Adapted with permission from Mertig et al. 1997. (d) Representative detail photograph of 2D soap foams. Adapted with permission from Glazier et al. 1987.

In epithelial biological systems, the wetting analogy has been applied to explain epithelial cell organization. In these systems, the cell spreading dynamics are governed by a competition between cell-cell and cell-substrate interactions⁵⁶. With this analogy, the tissue spreading parameter S could be determined taking into account the balance between the adhesion energies attributed to cell-cell (W_{cc}) adhesion and those attributed to cell-substrate (W_{cs}) adhesion, in such a way that $S = W_{cs} - W_{cc}$. The sign of this parameter changes at the wetting transition that separates tissue spreading ($S > 0$, wetting) from retraction ($S < 0$, de-wetting).

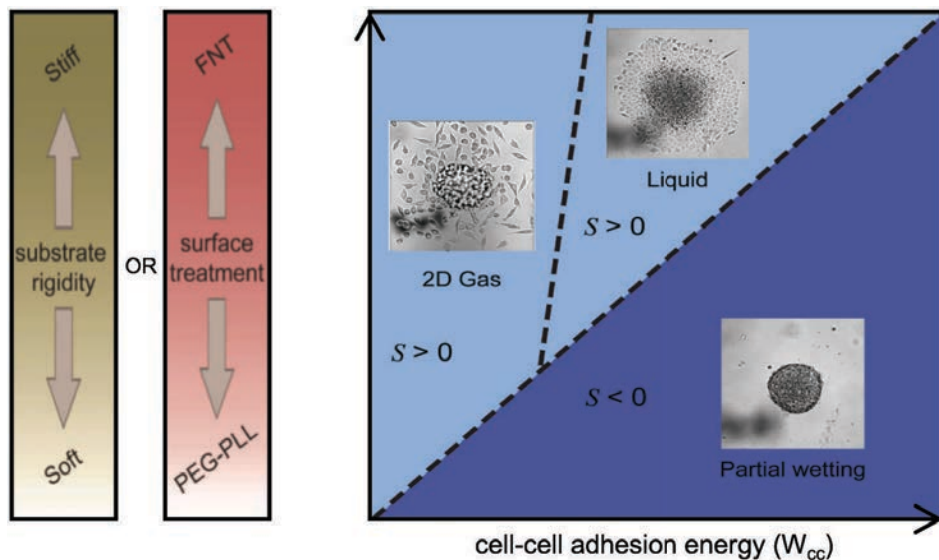


Figure 1.7. Phase diagram of tissue wetting. The aggregate spreading is governed by a competition between cell-cell adhesion energy W_{cc} and cell-substrate adhesion energy W_{cs} , and the difference sets the sign of the spreading parameter $S = W_{cs} - W_{cc}$. The images show the long-term fate of cell aggregates in each of the regions. The cell-substrate energy W_{cs} can be controlled either by modifying the substrate's surface chemistry [non-adhesive PEG-poly-L-lysine (PEG-PLL) versus adhesive fibronectin (FNT)] or its rigidity (soft versus stiff). Adapted with permission from Gonzalez-Rodriguez et al. 2012.

For epithelial systems, cell-cell adhesion depends on the expression of molecules such as E-cadherins while cell-substrate adhesion depends on the surface chemistry and the surface stiffness (Figure 1.7). To study biological systems using the wetting analogy, the experiments performed consisted in 3D cell aggregates spreading on substrates with varying cell-cell and cell-substrate adhesivities⁵⁷⁻⁶¹. In particular, spheroidal aggregates of a mouse sarcoma cell line (S-180) were employed in a set of experiments^{58,59}. Cell-cell adhesion was controlled by the cell E-cadherin expression, while cell-substrate adhesion could be chemically tuned using a mixture of poly (ethylene glycol) (PEG) and fibronectin to coat the substrates, thus modifying cell-ECM interactions. When cell aggregates were placed on PEG-coated substrates (non-adhesive), they remained spherical ($S < 0$, partial wetting). In contrast, when

cell aggregates were placed on fibronectin-coated substrates (adhesive), a precursor film of cells spread around the aggregates ($S > 0$, wetting). In cohesive aggregates that have strong cell-cell contacts (high expression of E-cadherin), this cell film was a continuous monolayer. In contrast, in weakly cohesive aggregates (lower E-cadherin expression) individual cells detached from the aggregates and spread⁵⁸. This could be interpreted as a wetting transition from a liquid to a 2D gas state, and the cells leaving the aggregate can be interpreted as a hallmark of epithelial-mesenchymal transition (EMT) in tissues.

On the other hand, cell-substrate adhesion could also be physically tuned by varying the substrate rigidity. This can also induce a wetting transition, so the cell aggregates remained spherical below a threshold of substrate rigidity ($S < 0$, partial wetting), while cells spread around the aggregates above this threshold ($S > 0$, wetting). For example, cells of S-180 spheroidal aggregates deposited on fibronectin-coated polydimethylsiloxane (PDMS) substrates with high stiffness (~ 1.8 MPa) spread and formed cellular monolayers expanding around the aggregates. Conversely, these aggregates remained spherical on fibronectin-coated polyacrylamide (PA) hydrogels with lower stiffness (< 8 kPa)⁵⁹.

On the other hand, de-wetting of epithelial monolayers has also been tested. By culturing mouse sarcoma cells on top of PEG-coated substrates (non-adhesive) or soft substrates, cells spontaneously withdraw from the surface to form aggregates ($S < 0$, de-wetting)⁶². De-wetting has also been reported in human breast adenocarcinoma cells from the MDA-MB-231 line, where increasing the expression level of E-cadherin triggered a sudden morphological transition from monolayers into 3D aggregates⁶³.

Despite the extensive literature studying wetting phenomena in epithelial systems, experiments accounting for the multicellular population present at epithelia *in vivo* are scarce. Experiments comprise homogeneous epithelial cell populations and do not consider cell differentiation or even polarization. Attempts to overcome these drawbacks involve the use of primary epithelial cells, which possess a short life and limited expansion capacity, or animal models, which are difficult to control, standardize, analyze and are subjected to ethical concerns.

1.3 3D organoid cultures

As described before, *in vitro* research on cell epithelial organization has been mainly enabled through the culture of immortalized cell lines seeded on or within protein matrices. However, traditionally these culture models have had several shortcomings based on their limited resemblance to normal epithelia. In the latest years, new opportunities have been available in the field through the culture of primary tissues in 3D structures called organoids. Organoids are 3D cellular

structures that resemble in their multicellular cell composition, function and architecture to specific epithelial tissues and organs^{64,65}. They are formed upon the proliferation, differentiation, and self-organization of either adult tissue-specific stem cells or pluripotent stem cells. These are grown in suitable 3D matrices in the presence of specific biochemical factors that mimic the *in vivo* stem cell niches.

Organoids derived from intestine⁶⁶, cornea⁶⁷, lung⁶⁸, skin⁶⁹, liver⁷⁰ and pancreas⁷¹ among other tissues, have been successfully obtained. Organoids resemble the cell composition, structure, and function of the organ *in vivo* and allow long-term expansion. Thus, they have become the gold standard *in vitro* culture model of these epithelia. They have a wide range of applications in basic and translational research^{64,72}. Organoids serve as models of disease, drug testing and personalized medicine, since they have the ability to mimic pathologies at the organ level^{64,72}. For example, intestinal organoids derived from patients with cystic fibrosis (disorder caused by mutations on the CFTR gene encoding the CFTR channel) serve as simple and robust assays for experimental treatments, since the CFTR channel functionality is easy to assess *in vitro*⁷³. Organoids are also used as models to perform toxicological studies⁷⁴. For example, liver and cardiac organoids derived from humans indicated toxicity to mercury and glyphosate but at higher doses than observed with cultured cell lines or animal models⁷⁵.

1.3.1 Intestinal organoids

Intestinal organoids, also called mini-guts, were the first long-term organoids established and have become a preferred system to model the small intestine⁶⁶. *In vivo*, the small intestinal epithelium is organized in a 3D architecture composed of finger-like protrusions called villi and invaginations called crypts⁷⁶. These are lined by an epithelial monolayer containing several cell types, including differentiated and proliferative cells (Figure 1.8 (a)). Such cell types are distributed and highly-organized along the distinct tissue areas. The small intestinal epithelium is the fastest tissue of adult mammals in getting regenerated, as it basically renews every 4-5 days in mice⁷⁷. Such a fast cell turnover is driven by the presence of an adult intestinal stem cell (ISC) population characterized by being Lgr5⁺ (Leu-rich repeat-containing G protein-coupled receptor 5). These ISCs, together with the so-called Paneth cells reside at the bottom of crypts. ISCs undergo self-renewal and generate transit-amplifying (TA) cells, which migrate upwards the top of the crypt compartments⁷⁸. Absorptive enterocytes, mucus-secreting goblet cells, and hormone-secreting enteroendocrine cells arise from TA cells and continue their migration up along the crypt-villus axis. After reaching the villus tips, cells undergo apoptosis, are extruded into the lumen, and are replaced by a new generation of cells, ensuring intestinal homeostasis⁷⁸.

Intestinal organoids originate from the culture of crypt pieces or single *Lgr5*⁺ ISCs embedded in 3D matrices of Matrigel^{66,79}. When supplemented with the proper cell culture medium, ISCs proliferate, differentiate and form closed structures consisting in a central lumen lined by a cell monolayer (Figure 1.8 (b)). Proliferative cells develop budding forms that protrude from the spherical structures. Mice genetic models and tracing experiments have demonstrated that these buds are composed by ISCs, Paneth and TA cells⁶⁶. Thus, these buds recapitulate the multicellular population and arrangement found in crypts *in vivo* and are called crypt-like domains (Figure 1.8 (c-d)). On the other hand, organoids also contain differentiated cells able to perform absorptive, and secretory functions⁶⁶. They also maintain the organoid homeostasis by dying, being exfoliated, and getting accumulated within the lumen. Thus, they mimic the villi found *in vivo* and are called villus-like domains. As such, intestinal organoids recapitulate the cell compartmentalization and the main functions of the *in vivo* tissue. In addition, intestinal organoids can grow for several months within Matrigel drops and can be passaged in a similar manner as cells grown in monolayers⁶⁶. Therefore, organoids constitute an affordable and highly reliable primary cell source for the study of the small intestinal epithelial tissue.

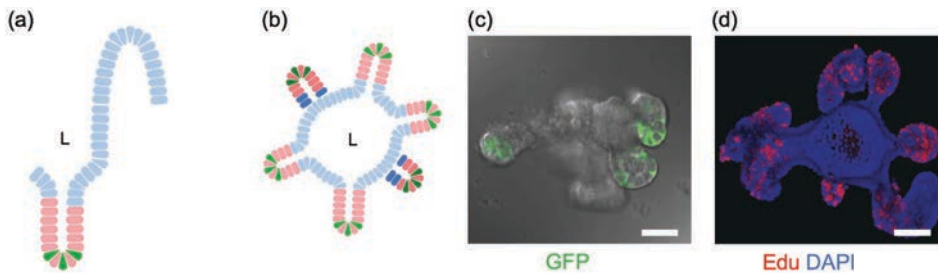


Figure 1.8. (a) Schematic representation of the small intestine morphology. The intestine is lined with a single layer of epithelial cells organized into villus (light blue) and crypt (pink) domains. *Lgr5*⁺ stem cells (in green) are localized at the bottom of the crypts. (b) Schematic representation of an intestinal organoid, consisting of a central lumen (L) lined by villus-like domains (light blue) and crypt-like domains (pink). *Lgr5*⁺ stem cells (in green) are localized at the bottom of the crypt-like domains. (c) Representative image of an intestinal organoid (14 days after single cell culture) overlapping bright field and GFP fluorescence signals. *Lgr5*-GFP⁺ cells are localized at the bottom of the crypt-like domains. (d) Organoids cultured with the thymidine analogue EdU for 1 hour. Note that only crypt-like domains incorporate EdU. (c-d) Scale bar: 50 μ m. Adapted with permission from Sato et al., 2009.

1.3.2 Signals guiding intestinal self-organization and compartmentalization *in vivo*

In vivo, intestinal epithelial compartmentalization is supported by a set of differential cell-cell and cell-ECM interactions along the crypt-villus axis. Several signaling pathways such as Wnt, Notch, bone morphogenetic protein (BMP) or Eph/ephrin receptor/ligand among others, are involved in this process (Figure 1.9 (a))⁸⁰. Some of these pathways involve diffusible signaling molecules displayed as

concentration gradients which induce differential patterns of cell types along the vertical axis of the tissue. For instance, it is known that Paneth cells secrete Wnt signals that maintain the ISC niche. Wnt signaling is present at the crypt bottom and its expression decreases in a gradient fashion toward the crypt top (Figure 1.9 (b))⁸¹. Notch is also essential to maintain the undifferentiated state of the ISC niche and forms a spatial gradient from the bottom to the top of the crypts⁸². Finally, BMP signals are active in the villus compartment, ensuring cell differentiation, while the BMP antagonist Noggin is mainly expressed in the crypt⁸³. On the other hand, signaling molecules such as Eph receptors and ephrin ligands are membrane-bound, so they only interact through direct cell-cell contacts and their signaling is bi-directional. Eph/ephrin repulsive interactions control cell positioning along the crypt-villus axis⁸⁴. Proliferative cells within crypts express EphB receptors in a decreasing gradient from the bottom to the top of the crypts, whereas ephrinB ligands are expressed in an increasing gradient from the bottom of the crypts until the tips of the villi (Figure 1.9 (c))^{84,85}.

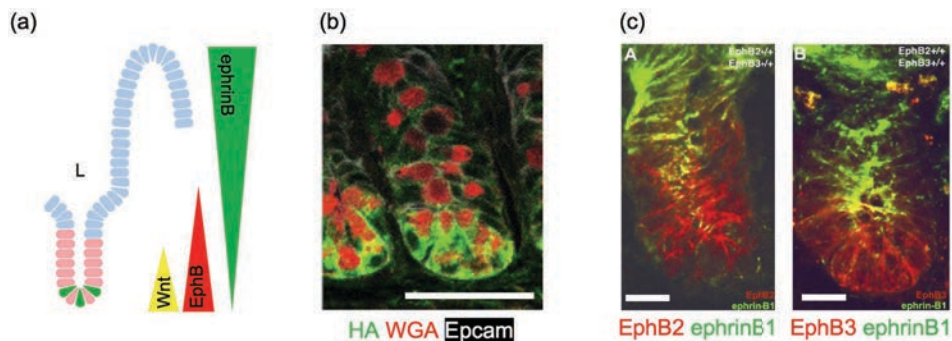


Figure 1.9. (a) Schematic representation of the main gradient signals governing the intestinal morphology: villus (light blue) and crypt (pink) domains. $Lgr5^+$ stem cells (in green) are localized at the bottom of the crypts. (b) Confocal imaging in *Wnt3^{HA/HA}* mice intestinal tissues of HA (Wnt3), Epam (membranes) and WGA (secretory granules). Scale bars: 50 μm . Adapted with permission from Farin et al., 2016. (c) Eph/ephrin receptor/ligand pairs form opposite gradients and overlap in the middle of the mouse intestinal crypts. EphB3 is predominantly expressed by Paneth cells and EphB2 by progenitor cells. EphrinB1 is more expressed by differentiated cells than by crypt cells. Scale bars: 40 μm . Adapted with permission from Holmberg et al., 2006.

Additionally, cell-ECM interactions directly attributed to the laminin isoforms present along the crypt-villus axis have also been described as relevant in guiding cell position and differentiation⁸⁶. In particular, the presence of rich laminin $\alpha 5$ isoform has been detected in the basement membrane of the villus regions. In addition to their molecular content, other ECM properties such as their rigidity have shown to be fundamental in regulating intestinal tissue. Recent papers attribute a relevant role in this process to Yes-associated protein 1 (YAP). YAP is recognized as a mechanosensor protein which regulates its activation by mechanical cues such as the ECM stiffness. *In vivo*, YAP activation induces its translocation from cell cytosol

to cell nucleus, where it activates the transcription of a sets of genes. This process has been demonstrated as essential in cellular reprogramming during tissue repair, promoting the regenerative capacity of intestinal stem cells^{87,88}. For example, upon exposure to whole-body irradiation (12 Gy), YAP was predominantly cytoplasmic with certain cells displaying weak nuclear accumulation at 1 day post-irradiation (dpi), which was mainly nuclear at 2 dpi, and by 4 dpi returned to a prominent cytoplasmic localization⁸⁹. However, the function of YAP in the intestinal development or homeostasis is not clear. Although a recent paper using *in vivo* delivery of interfering RNAs against YAP suggested that YAP may regulate intestinal epithelial proliferation and goblet cell differentiation⁹⁰, other papers showed that the genetic removal of YAP had no apparent phenotype in intestinal epithelium during homeostasis⁸⁹.

Besides the signals originated at the epithelium, non-epithelial (stromal) cells residing in the intestinal lamina propria such as fibroblasts, myofibroblasts, endothelial and immune cells, also secrete biomolecules impacting the intestinal epithelial organization through Wnt, Notch and BMP signaling pathways⁹¹. For example, Wnt signals, which play a crucial role in regulating the proliferation and organization of epithelial cells, arise from multiple cell sources in the tissue⁹²⁻⁹⁴. In addition to being secreted by Paneth cells located at the epithelial monolayer, stromal cells such as myofibroblasts also secrete Wnt molecules⁹⁴⁻⁹⁶. Indeed, it has been reported that *in vivo* the absence of Paneth cells does not disrupt the normal intestinal homeostasis, while intestinal organoids development is dependent on Paneth cells as a source of Wnt signaling, thus evidencing the multiple sources of this signal *in vivo*⁹⁷⁻⁹⁹. Given these redundant sources of signaling, it is unclear which role is performed by each signal in regulating the epithelium. However, what is known is that the disruption of tissue homeostasis is a critical event linked to intestinal diseases, such as inflammatory bowel disease⁸ or colorectal cancer⁴. Within this context, the use of intestinal organoids as accessible, well controlled *in vitro* models with only the epithelial components of the tissue is seen as an unique opportunity to shed light on the complex biology of the tissue by trying to capture *in vivo* cell-ECM and cell-cell interactions in the *in vitro* systems.

1.3.3 Cell-extracellular matrix interactions in intestinal organoids

Intestinal organoids are cultured embedded within a 3D ECM, as single intestinal cells undergo anoikis outside their tissue context. As exemplified in section 1.3.1, Matrigel is usually employed to support intestinal epithelial growth. Matrigel has been successfully used for the culture of intestinal organoids because of its molecular composition, rich in laminin and collagen IV, which is similar to the basement membrane of the intestinal epithelial tissue^{66,100,101}. This ECM has been proven to be appropriate to provide the structural support and the biochemical cues

required for the adhesion, growth and differentiation of the Lgr5⁺ intestinal stem cells. Collagen type I has been investigated as an alternative scaffold. However, collagen type I 3D matrices are only able to sustain the growth of intestinal organoid-derived cells when these are co-cultured with intestinal subepithelial myofibroblasts or with the addition of Matrigel^{87,102}. Although through comparative analysis gene expression in organoids co-cultured with intestinal subepithelial myofibroblasts embedded in collagen was shown to be relatively similar to Matrigel controls, cell monolayers were also found in collagen¹⁰². This result suggests that the organoid growth properties are different when matrices are altered. On the other hand, when organoids were embedded in collagen type I mixed with Matrigel, they formed a smoother epithelium and displayed decreased budding¹⁰³. Recently, another study also showed an intriguing relationship between the *in vitro* behavior of intestinal organoids and the ECM¹⁰⁴. In particular, it stated the soft matrices and full-length recombinant laminins are essential for ISC differentiation and organoid formation¹⁰⁴. The matrices should be mechanically dynamic for ISC expansion and, subsequently, permissive to their differentiation and intestinal organoid formation. Overall, these studies indicate that intestinal epithelial organoids growth is achieved only when the mechanical factors and the composition of the ECM are appropriately provided.

On the other hand, recent works link the maintenance of primary intestinal epithelial cells *in vitro* to culture environments able to induce the activation of the Yes-associated protein 1 (YAP)^{104,105}. As explained in *in vivo* systems, YAP proteins are found in both the cytoplasm and the nucleus of cells. When it is activated, YAP translocates from the cytoplasm to the nucleus, where it binds and activates TEAD transcriptional factors thereby regulating downstream gene transcription. Among other pathways, it has been reported that YAP activation can be regulated by mechanical cues¹⁰⁶. Specifically, it has been shown that YAP activates *in vitro* in response to sustained increased ECM rigidity, strain or adhesive area¹⁰⁷. When referring to mouse intestinal organoids, YAP transient activation has been found to be essential to induce ISC symmetry breaking and thus lead to organoid development (Figure 1.10)⁸⁸.

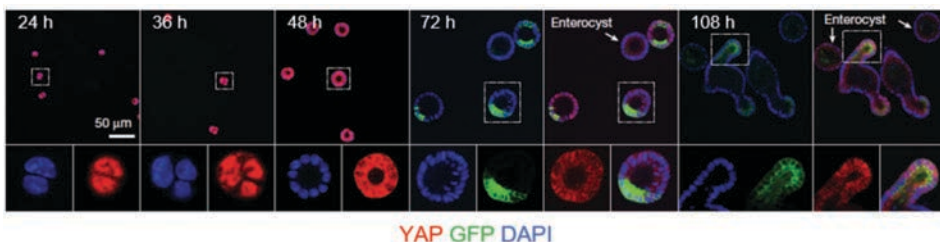


Figure 1.10. (a) Time course images of YAP, GFP (GFP⁺ cells corresponding to Lgr5⁺ intestinal stem cells) and cell nuclei (DAPI) for the symmetry breaking during the formation of organoids. The corresponding time lapse for each image is shown in each panel. Scale bar: 50 μm . Adapted with permission from Serra et al., 2019.

1.3.4 Cell-cell interactions in intestinal organoids

As previously explained, *in vivo*, cell-cell interactions and cell-secreted biomolecules of epithelial and non-epithelial origin impact on the organization of the intestinal epithelium. *In vitro*, such complex interactions are mimicked by culturing the intestinal organoids using a medium supplemented with intestinal biomolecules. The culture medium components closely replicate the main signaling pathways identified as being able to sustain the *in vivo* stem cell niche, Wnt, Notch and BMP⁶⁶. These factors create biochemical gradients along the crypt-villus axis of the intestine and control the growth, migration and differentiation of the ISCs⁸². The essential ingredients of the intestinal organoids culture medium include pre-defined amounts of epidermal growth factor (EGF), Noggin and R-spondin 1 biomolecules. Some authors have also reported the use of additional components to boost the stemness of the cultures. These are two small molecules, CHIR99021 and valproic acid, which modulate Wnt, Notch and BMP signaling pathways¹⁰⁸.

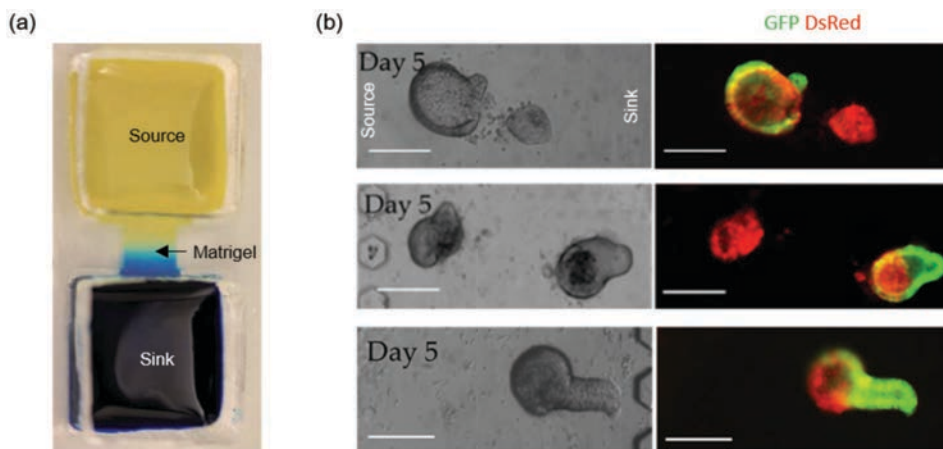


Figure 1.11. (a) Gradient generating microdevice. (b) Brightfield (left panels) and fluorescence (right panels) images of GFP (GFP+ cells corresponding to Lgr5+ intestinal stem cells), and DsRed (actin) for organoids in the absence of gradients (upper panels), for organoids growth in the presence of Wnt3a/R-spondin 1 gradient (middle panels) and organoid from a single cell growing in the presence of Wnt3a/R-spondin 1 gradient (lower panels). Scale bars: 50 μm . (a-b) Reproduced with modifications by permission of Attayek et al., 2015.

By employing intestinal organoids and different engineering approaches, the role of these molecules in controlling the signaling pathways has been investigated. For example, a microfluidic device was used to expose colon organoids to a linear gradient of Wnt3a and R-spondin 1 biomolecules (Figure 1.11)¹⁰⁹. In this setup, it was observed that organoid morphologies were polarized, with the crypt-like domains localized within the region of the highest concentration of Wnt3a/R-spondin 1 biomolecules, resembling the organization of the colonic crypts *in vivo*. Interestingly, organoids obtained from the culture of single stem cells under the

gradients were more responsive to the biochemical signals and more polarized than fully grown organoids. This result suggests that single stem cells, only in contact with a matrix but not with other cells are able to tune their self-organization in response to exogenous biomolecular patterns.

However, despite the great benefits found in the use of intestinal organoids to study epithelial organization, in practice they have several drawbacks when using them as *in vitro* models of the intestinal tissue. From the functional point of view, they have a closed lumen, which prevents the access to the cell apical side to perform absorbance tests or study epithelial-pathogen interactions. On the other hand, they usually have large differences in size and shape, which hinders the standardization of the measurements performed, while the 3D matrix by which they are surrounded complicates microscopy data collection and the associated analysis. In addition, the 3D structure adds yet another layer of complexity, as tissue curvature has the potential to reshape morphogen gradients¹¹⁰. For all these reasons, in recent years organoid-derived intestinal monolayers have been proposed as alternative *in vitro* models for intestinal studies.

1.4 Organoid-derived intestinal epithelial monolayers

Recently, there is an increased interest in intestinal epithelial monolayers that recapitulate the physiology of the *in vivo* tissue while overcoming the limitations imposed by the closed geometry of 3D organoids. Several attempts to “open-up” the spherical 3D organoids into 2D monolayers have been explored¹¹¹⁻¹¹⁵. These intestinal monolayers have been obtained from organoid-derived crypts and single cells from a variety of species including murine, porcine and humans. Crypt pieces or single cells were seeded onto porous membranes in Transwell inserts coated with gelatin¹¹¹, collagen type IV¹¹² or Matrigel¹¹³⁻¹¹⁵. The culture medium was supplemented with Noggin, R-spondin 1 and Wnt3a. Cells in these cultures displayed a characteristic polarized morphology and markers of mature intestinal epithelium such as tight junctions. In addition, these monolayers typically formed a continuous barrier with a transepithelial electrical resistance (TEER) that is sufficiently high to support physiological assays such as immunoglobulin A transcytosis and pathogen-epithelium interactions^{111,113}. However, these monolayers were grown for short times and it is unclear whether they were able to compartmentalize in crypt-and villus-like domains, maintain stem cell niches, and recapitulate *in vivo* tissue self-renewing capabilities.

In a recent study, self-renewing epithelial monolayers grown from organoid-derived colonic crypts were reported by culturing these cells onto collagen type I hydrogels (thickness ≥ 1 mm and concentration of 1 mg mL^{-1}) (Figure 1.12 (a))¹¹⁶. The culture medium was supplemented with epidermal growth factor (EGF), Noggin, R-spondin

1 and Wnt3a. These set-ups support the formation of monolayers with stem cells and all differentiated cell types. The differentiated cells were compartmentalized at the center of the monolayers while the proliferative cells were mainly found along the edges of the expanding monolayers. No physiological spatial compartmentalization of proliferative and differentiated cells similar to the tissue *in vivo* was found in these systems.

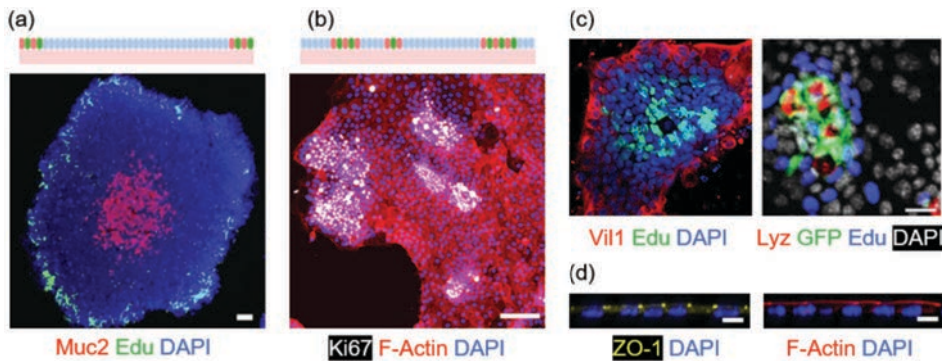


Figure 1.12. (a) Representative fluorescence image of Muc2 (Goblet cells), Edu (proliferative TA cells) and cell nuclei (DAPI) for epithelial monolayers grown on collagen type I for 8 days. Scale bars: 100 μm . Adapted with permission from Wang et al., 2017. (b) Representative fluorescence image of Ki67 (proliferative cells), F-Actin and cell nuclei (DAPI) for organoid-derived single-cells cultured on Matrigel. Scale bars: 100 μm . Adapted with permission from Altay et al., 2019. (c) Confocal representative images of Villin (Vil1, enterocyte), Lysozyme (Lyz, Paneth cells), GFP (GFP⁺ cells corresponding to Lgr5⁺ intestinal stem cells), Edu (proliferative TA cells) and cell nuclei (DAPI) for epithelial monolayers grown on Matrigel-coated substrates. Scale bar: 25 μm . Adapted with permission from Thorne et al., 2018. (d) Immunostaining of ZO-1, F-Actin and cell nuclei (DAPI) for epithelial monolayers cultured on Matrigel-coated substrates for 7 days. Orthogonal cross-sections of the monolayers. Scale bars: 10 μm . Adapted with permission from Altay et al., 2019.

Other studies also support the self-renewal of stem cells through the culture of organoid-derived crypts onto thin coatings of collagen type I. However, in this case the culture medium is supplemented with intestinal subepithelial myofibroblasts conditioned medium, epidermal growth factor (EGF), Noggin and R-spondin 1¹¹⁷. In combination, these observations suggest that the maintenance of the proliferative cell population is attributed to the proper combination of substrate mechanical properties and biochemical factors.

The compartmentalization in crypt-and villus-like domains is a key property of *in vivo* intestinal epithelium that has also been pursued to mimic *in vitro* on organoid-derived intestinal epithelial monolayers. For example, a collagen coated membrane was patterned with micropores to enable the spatially localized application of biochemical factors that control the compartmentalization of the organoid-derived monolayers¹¹⁸. More recently, protocols to obtain intestinal organoid-derived epithelial monolayers that spontaneously self-organize into proliferative crypt-like domains and differentiated villus-like regions have been proposed (Figure 1.12

(b))¹¹⁹⁻¹²¹. These intestinal monolayers are obtained from organoid-derived crypts and single cells from mice. These are seeded on top of Matrigel-coated substrates¹²⁰ or polyacrylamide (PA) hydrogels functionalized with a solution of collagen type I and laminin¹²¹, and cultured with medium supplemented with epidermal growth factor (EGF), Noggin, R-spondin 1 and sometimes CHIR99021 and valproic acid. These intestinal monolayers produce all major intestinal cell types and cells are properly polarized (Figure 1.12 (c-d)). To mimic the luminal and stromal compartments of the tissue *in vivo*, monolayers are often grown on Transwell inserts, which allow the addition of different cell culture media at the apical and at the basal chambers. When cultured with the proper biochemical factors, these monolayers can be maintained for up to 20 days preserving their self-renewal properties and maintaining the spatial cell compartmentalization in crypt- and villus-like domains for up to 2 months¹¹⁹. These results revealed the synergistic influence of ECM stiffness, porosity and composition on the compartmentalization of the organoid-derived intestinal epithelial monolayers.

Because of their 2D format, these monolayers allow the systematic study of the perturbation of signals such as Wnt and BMP¹²⁰. These signals are factors that regulate cell proliferation in the intestinal epithelium in the opposite way. While Wnt promotes stem cell renewal and thus, proliferation, BMP promotes cell differentiation. In a set of enlightening experiments, these endogenous signals were perturbed through inhibition via IWP-2 for Wnt and inhibition via LDN for BMP. Also, the signals were exogenously modified by varying the composition of the cell culture medium employed. Although the monolayers did not have tissue architecture nor non-epithelial components, this study revealed that a feedback-loop between intrinsic Wnt and BMP signals is established (Figure 1.13 (a)) and it is responsible for the monolayer organization and the maintenance of the homeostasis¹²⁰. In addition, while proliferation of the cultures can be recovered in the absence of intrinsic Wnt signals by exogenous stimuli, exogenous Wnt or BMP signals are not able to rescue tissue compartmentalization in the absence of the intrinsic signaling.

Additionally, not only the biochemical signals generated by cell-cell and cell-secreted factors can be evaluated using intestinal monolayers, but these models are also suitable for mechanical studies (Figure 1.13 (c)) involving cell-cell and cell-ECM interactions¹²¹. For this purpose, the monolayers were grown onto polyacrylamide hydrogels and traction force microscopy measurements were performed. The experiments revealed some insights on the formation process of the crypt-like and villus-like domains *in vitro*. It was observed that the stem cell domain pushes the underneath ECM and folds, generating a negative tensile gradient. Then, TA cells pull the ECM and elongate, reaching a minimum of tension. On the other hand, at the

villus-like domains, a second tension gradient builds up. Finally, proliferative cells are pulled out of the TA domain along a gradient of increasing tension.

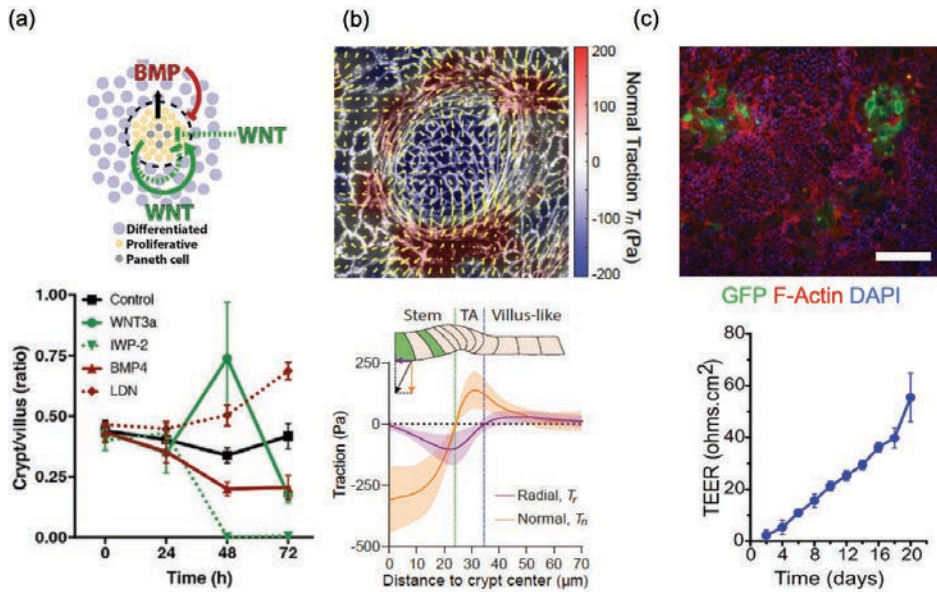


Figure 1.13. (a) Organoid-derived epithelial monolayers are compartmentalized in crypt- and villus like domains. Schematic representation of monolayers self-organization via Wnt/BMP signaling (upper panel); and graph plotting the ratio of crypt to villus cell number (lower panel) Adapted with permission from Thorne et al., 2018. (b) Mechanical compartmentalization of organoid-derived monolayers. Traction map overlap with a brightfield image of a crypt-like domain where yellow vectors represent components tangential to the substrate and the color map represents the component normal to the substrate (upper panel); and circumferentially averaged normal tractions T (orange) and radial tractions T (purple) as a function of the distance to the crypt-like domain center (lower panel). Adapted with permission from Pérez-González et al., 2020. (c) Organoid-derived epithelial monolayers show effective barrier function. Representative fluorescence images of GFP (GFP⁺ cells corresponding to Lgr5⁺ intestinal stem cells), F-Actin and cell nuclei (DAPI) for epithelial monolayers cultured on Matrigel-coated Transwell inserts (upper panel); and graph plotting the transepithelial electrical resistance (TEER) values for the epithelial monolayer as a function of cell culture time (lower panel). Scale bar: 100 μm . Adapted with permission from Altay et al., 2019.

Finally, organoid-derived intestinal monolayers also allowed the introduction of non-epithelial signals in an easy manner. In our laboratory, we cultured organoid-derived monolayers onto porous membranes in Transwell inserts¹¹⁹ (Figure 1.13 (b)). To obtain monolayers fully covering the substrate and thus, being functional in tissue barrier assays such as permeability tests, the proliferation of the stem cells was boosted by including stromal biochemical signals. This was performed by supplementing the culture medium added to the basolateral compartment with medium recovered from the culture of intestinal subepithelial myofibroblasts isolated from the tissue. Although these experiments represent relevant advances in the field, the complexity of the biochemical signal added hinders the unravelling of the effects attributed to individual biochemical components of non-epithelial

origin in the epithelial organization and the maintenance of the homeostatic behavior.

Within this context, the central challenge of this thesis has been to propose well controlled systems through which we could explore the effects of substrate-derived cues in driving the self-organization of organoid-derived intestinal epithelia. For this purpose, we have made use of our knowledge to generate 2D intestinal epithelial monolayers and the expertise of the lab in tuning and characterizing the substrate functionalization using micropatterning techniques.

2 Objectives

The gold standard advanced *in vitro* culture models of the intestinal epithelium are intestinal organoids since they recapitulate key parameters of the *in vivo* tissue. These models allow the study of epithelial tissue organization and have confirmed the crucial role of the crosstalk between substrate-derived cues and cell-dependent signaling molecules for tissue development, homeostasis, and regeneration. However, as organoids are cultured embedded in 3D cell-derived protein mixtures, the spatial distribution of extracellular matrix proteins and the signaling molecules derived from cells that coordinate the tissue organization *in vivo* cannot be readily retrieved. The recent development of organoid-derived intestinal epithelial monolayers that also recapitulate the physiology of the tissue *in vivo* provided new avenues in overcoming the limitations imposed by the closed geometry of 3D organoids. The aim of this thesis is to make use of this biological *in vitro* model and bioengineering tools to investigate the impact of substrate-derived cues in the self-organization process of organoid-derived intestinal epithelial cells. To achieve this ambitious goal, the two following specific objectives are defined:

- To assess the role of ECM cues in driving the self-organization of organoid-derived intestinal epithelia. Specifically, to assess the impact of ECM density and composition in cell self-assembly process that guides the transition between scattered organoid-derived single cells to fully grown intestinal monolayers compartmentalized in crypt- and villus-like domains.
- To optimize and characterize a platform to allow for the precise localization of epithelial or stromal cell-derived signals in a surface-bound manner through micro-patterning technology. To evaluate the effects of these cell-derived signals on the self-organization of organoid-derived intestinal epithelial monolayers and their impact in the compartmentalization of crypt-like domains.

3 Materials and Methods

3.1 Cell line cultures

Caco-2 cells, which correspond to a human colon adenocarcinoma cell line, have been extensively employed to model the intestinal epithelium *in vitro* since they display many physiological and morphological features of mature enterocytes¹²². Madin-Darby Canine Kidney (MDCK) cells have been widely used as *in vitro* epithelial cell models because they retain many of the structural and functional properties of epithelia *in vivo*¹²³. We used both Caco-2 and MDCK cell lines as *in vitro* models to study epithelial cell organization as a function of substrate extracellular matrix (ECM) density. These cell models represent two distinct types of epithelia since they originate from different organs and differ in their three-dimensional (3D) architecture *in vivo*.

On the other hand, the impact of biomolecular signaling patterns in epithelial cell organization was also studied in this thesis. Specifically, the role of ephrinB1 ligands and their EphB2 receptors on intestinal epithelial organization was assessed *in vitro*. Preliminary tests were carried on employing NIH/3T3 mouse embryonic fibroblasts. These cells were selected because they endogenously express the EphB2 receptor¹²⁴ and they rapidly attach and spread on the chosen substrates^{125,126}.

Caco-2 cells (ATCC® HTB-37™), MDCK cells (ATCC® CC-34™) and NIH/3T3 fibroblasts (ATCC® CRL-1658™) were cultured at 37°C in a humidified incubator under a 5% CO₂ atmosphere. Culture medium was DMEM (Gibco) medium supplemented with 10% Fetal Bovine Serum (FBS) (Life Technologies), 1% L-glutamine (Gibco), 1% sodium pyruvate (Invitrogen), and 1% Penicillin-Streptomycin (Sigma-Aldrich). Additionally, Caco-2 cells culture medium included 1% Minimum Essential Medium Non-Essential Amino Acids solution (MEM-NEAA, Gibco, ThermoFisher). For the experiments, cells were rinsed with Phosphate Buffered Saline solution (PBS) (Life Technologies) at 37°C before adding Trypsin-EDTA (Life Technologies) at 37°C. Caco-2 cells were incubated for 5 minutes, MDCK cells for 8 minutes and NIH/3T3 fibroblasts for 3 minutes at 37°C in 5% CO₂ atmosphere. Following the incubation period, Trypsin-EDTA was neutralized adding an equal volume of culture medium and centrifuged at 1000 rpm for 5 minutes. For the maintenance of the cultures, Caco-2 cells were passaged in 75 cm² culture flasks every 7 days with a seeding concentration of 2 × 10⁵ cells/flask, and the medium was changed every 3 to 4 days. MDCK cells and NIH/3T3 fibroblasts were passaged every 3-4 days, with a split ratio of 1:10 when cells were 70-80% confluent, using 25 cm² culture flasks.

3.2 Culture of primary mouse small intestinal epithelial cells

Primary cells represent advanced culture models and should potentially recapitulate *in vitro* the physiology of their original tissue *in vivo*. Therefore, we employed primary mouse small intestinal epithelial cells to investigate their epithelial organization in our experiments.

3.2.1 Mouse model

All experimental protocols involving mice were approved by the Animal care and Use Committee of Barcelona Science Park (CEEA-PCB) and the Catalan government and performed according to their relevant guidelines and regulations. *Lgr5-EGFP-IRES-creERT2* mice were used. These mice have been previously described⁷⁸. Briefly, *Lgr5-EGFP-IRES-creERT2* mice were generated by homologous recombination in embryonic stem cells targeting the *EGFP-IRES-creERT2* cassette to the ATG codon of the stem cell marker *Lgr5* locus, allowing the visualization of *Lgr5*⁺ stem cells located in the crypts of the mouse intestines through the expression of green fluorescent proteins (GFP). The *Lgr5-EGFP-IRES-creERT2* mice were kindly provided by the Laboratory of Prof. Eduard Batlle at Institute for Research in Biomedicine (IRB, Barcelona, Spain).

3.2.2 Intestinal crypt isolation and organoid culture

Intestinal crypts from *Lgr5-EGFP-IRES-creERT2* mice were isolated as previously described (Figure 3.1 (a))^{127,128}. Briefly, small intestines were flushed with PBS and cut longitudinally. Intestinal villi were removed mechanically, and the intestinal crypts were isolated by incubating the tissue with PBS containing 2 mM EDTA (Sigma-Aldrich) for 30 minutes at 4°C. The digested material was filtered through a 70 µm pore cell strainer (Biologix Research Co.), and the so-called crypt fraction was obtained. Then, crypts were plated within drops of the commercial protein mixture Matrigel (BD Bioscience) and supplemented with medium: advanced DMEM/F12 (Invitrogen) plus 1% Glutamax (Gibco), 1% HEPES (Sigma-Aldrich), Normocin (1:500, Invitrogen), 2% B27 (Gibco), 1% N2 (Gibco), and 1.25 mM N-acetylcysteine (Sigma-Aldrich). The medium was supplemented with recombinant murine epidermal growth factor, EGF (100 ng mL⁻¹, Gibco), recombinant murine Noggin (100 ng mL⁻¹, Peprotech), and recombinant human R-spondin 1 (200 ng mL⁻¹, R&D Biosystems) to obtain what we called ENR-medium. This medium was changed every 2 to 3 days. For the first 4 days of culture, Rho kinase (ROCK) inhibitor Y-27632 (10 µM, Sigma-Aldrich) was added to the medium. ROCK inhibitor was used to block anoikis¹²⁹, which is a cell death mechanism that might occur in anchorage-dependent cells that have just been detached from their ECM. When cultured in Matrigel drops, the intestinal crypts grow and develop 3D closed structures called

intestinal organoids. These consist of a central lumen lined by an epithelium with crypt- and villus-like domains, with crypts budding from spherical structures (Figure 3.1 (b)). For some experiments, organoid cultures were enriched in their stem cell amount by supplementing the ENR-medium with two small molecules, CHIR99021 (3 μM) and valproic acid (1 mM), leading to ENR_CV-medium¹⁰⁸. In an alternative strategy, we also enriched the stem cell content by doubling the concentration of recombinant human R-spondin 1 molecule, leading to EN2R-medium.

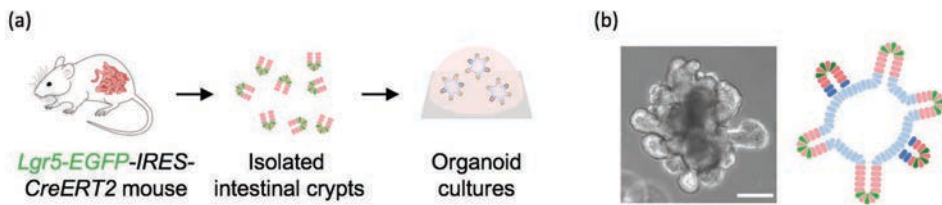


Figure 3.1. (a) Scheme depicting the intestinal crypt isolation and organoid culture. Intestinal crypts from *Lgr5-EGFP-IRES-creERT2* mice were isolated and plated in Matrigel drops to obtain organoid cultures. (b) Right panel: brightfield microscopy image of a representative intestinal organoid. Scale bar: 100 μm . Left panel: schematic representation of an intestinal organoid, consisting of a central lumen lined by crypt- and villus-like domains. *Lgr5*⁺ stem cells (in green) are localized at the crypt-like domains.

For the maintenance of the organoid culture, outgrowing crypts were passaged twice a week. Independently of their culture media, all the organoid cultures were passaged simultaneously to allow comparisons. To obtain crypt pieces homogeneous in size, full-grown organoids were subjected to a mild digestion protocol as previously described¹¹⁹. Briefly, Matrigel drops containing organoids were disrupted by pipetting with TrypLE Express1X (Gibco) and transferred to a Falcon tube at 4°C. In there, they were mechanically disrupted using a syringe with a 23 G 1" needle (BD Microlance 3). The resulting solution was centrifuged at 700 rpm for 3 minutes. Crypt pieces were then plated again in Matrigel drops. Organoid stocks were maintained for up to 4 months at 37°C in a humidified incubator under a 5% CO₂ atmosphere.

To characterize the organoids embedded in Matrigel drops, regular immunofluorescence staining was used, but including some adjustments to preserve the 3D organization of the structures. Specifically, glutaraldehyde was added to the fixation solution, low temperatures were avoided, and detergents (such as Triton X-100) were removed from all solutions. Briefly, cells were fixed with 2% paraformaldehyde (PFA) (Electron Microscopy Sciences) and 0.1% glutaraldehyde (GA) (Sigma-Aldrich) in PBS for 30 minutes at room temperature (RT), and blocked for at least 2 hours at RT with a blocking buffer containing 1% BSA (Sigma-Aldrich) and 3% donkey serum (Millipore) in PBS. Antibodies were diluted in 0.1% BSA and 0.3% donkey serum in PBS. Primary antibody anti-Ki67 (1:100, Abcam) was

incubated on Matrigel drops with organoids overnight at 4°C. Secondary antibody was Alexa Fluor® 647 donkey anti-rabbit (Jackson ImmunoResearch) diluted at 1:500 and it was incubated on Matrigel drops for 2 hours at RT. Alexa Fluor® 568 phalloidin was used to stain filamentous actin (F-actin). Nuclei were stained with 4',6-diamidino-2-phenylindole (DAPI) (1:1000) diluted in 0.1% BSA and 0.3% donkey serum in PBS and incubated on cells 40 minutes at RT. All the incubation steps included orbital agitation to ensure adequate diffusion of the reagents into the hydrogel. Finally, samples were mounted with Fluoromount® (Thermo Fisher) for microscope imaging.

Brightfield images were acquired using an epifluorescence inverted microscope (Eclipse Ts2, Nikon) with 4x air and 10x air objectives. Fluorescence images were acquired with a confocal laser scanning microscope (LSM 800, Zeiss) with a 10x air objective (NA = 0.3, WD = 2.0) or 20x air objective (NA = 0.8, WD = 0.55). The pinhole diameter was set to 1 Airy Unit (AU). For all images acquired, the optimal z-step was used as indicated by the equipment software.

3.2.3 *Obtention and culture of organoid-derived single cells*

To obtain organoid-derived single cells, full-grown organoids were now subjected to a harsh digestion protocol similar to the one previously described by our research group¹¹⁹ but introducing slight changes. In short, Matrigel drops containing organoids were enzymatically disrupted by pipetting them with TrypLE Express1X (Gibco). The TrypLE Express1X activity was previously reduced by heating it at 37°C for 1 hour in a water bath. The solution containing the disrupted organoids was transferred to a Falcon tube at 4°C, where enzymatical disruption was followed by mechanical disruption using a syringe with a 23 G 1" needle (BD Microlance 3). Single cells or small cell clusters were obtained by incubating such solution for approximately 5 minutes at 37°C under agitation every minute and centrifuged at 1000 rpm for 5 minutes. When seeded in culture for our experiments, these organoid-derived single cells were cultured with ENR_CV-medium plus ROCK inhibitor Y-27632 (10 µM, Sigma-Aldrich) to prevent anoikis¹²⁹.

3.3 **Fabrication of Polyacrylamide (PA) hydrogel substrates with tunable stiffness**

3.3.1 *Fabrication of PA hydrogel substrates*

Polyacrylamide (PA) hydrogels were fabricated on 35 mm glass-bottom Petri dishes (Mattek) following the experimental set-up depicted in Figure 3.2, which was previously described by our research group and others^{126,130,131}. First, the glass bottom was silanized to ensure a stable attachment of PA hydrogels. For that, the

glass was incubated for 5 minutes with a 50% (v/v) solution of (3-aminopropyl) trimethoxysilane (Sigma-Aldrich) in Milli-Q water, followed by another incubation with Milli-Q water for 30 minutes on an orbital shaker. Then, the glass was rinsed with Milli-Q water several times and incubated for another 30 minutes with a 0.5% (v/v) solution of glutaraldehyde (Sigma-Aldrich) in Milli-Q water again on an orbital shaker. Finally, the glass was rinsed with Milli-Q water, dried using nitrogen and stored in a vacuum desiccator until use. In parallel, pools to polymerize and shape PA hydrogels were created by employing polydimethylsiloxane (PDMS) membranes cut into ring-shaped pieces (external and internal diameters of 10 mm and 5 mm, respectively). The PDMS was prepared by using a mixture of Sylgard 184 Silicon Elastomer and curing agent (DowCorning) at a ratio of 10:1 w/w, and cured for 3 hours at 65°C. PDMS rings were then bound to the silanized glass to form a pool.

	%Acrylamide	%Bis-acrylamide	Young's modulus (kPa)
PA1	7.5	0.050	3 ± 1
PA2	12	0.150	37 ± 6
PA3	12	0.600	145 ± 7

Table 3.1. List of polyacrylamide (PA) hydrogel compositions and resulting Young's moduli. Values were measured by atomic force microscopy (AFM) and are reported as mean ± SEM (N = 3). Adapted from Comelles et al¹²⁶.

PA hydrogels were prepared through chemical polymerization in a range of varying stiffnesses (Figure 3.2 (a)). To control the stiffness, the concentrations of acrylamide and bis-acrylamide (bioRad) were varied (see Table 3.1). These prepolymer solutions were mixed with 0.05% (w/v) ammonium persulfate (Serva) and 1% (v/v) tetramethylethylenediamine (TEMED) (Sigma-Aldrich). Immediately after their preparation, 100 $\mu\text{L cm}^{-2}$ of the prepolymer solutions were poured into the pools formed by the PDMS rings and the silanized glasses (Figure 3.2 (b), left panel). The pools were reversibly closed on their tops by a sheet of a flexible, low oxygen permeability polymer, polyethylene naphthalate (PEN). A weight was placed above the PEN cover to keep it sealed while the polymerization took place. The polymerization process was carried out for 2 hours at room temperature (RT). The polymerized hydrogels were demolded by carefully removing the flexible mold and then stored in PBS at 4°C until further use.

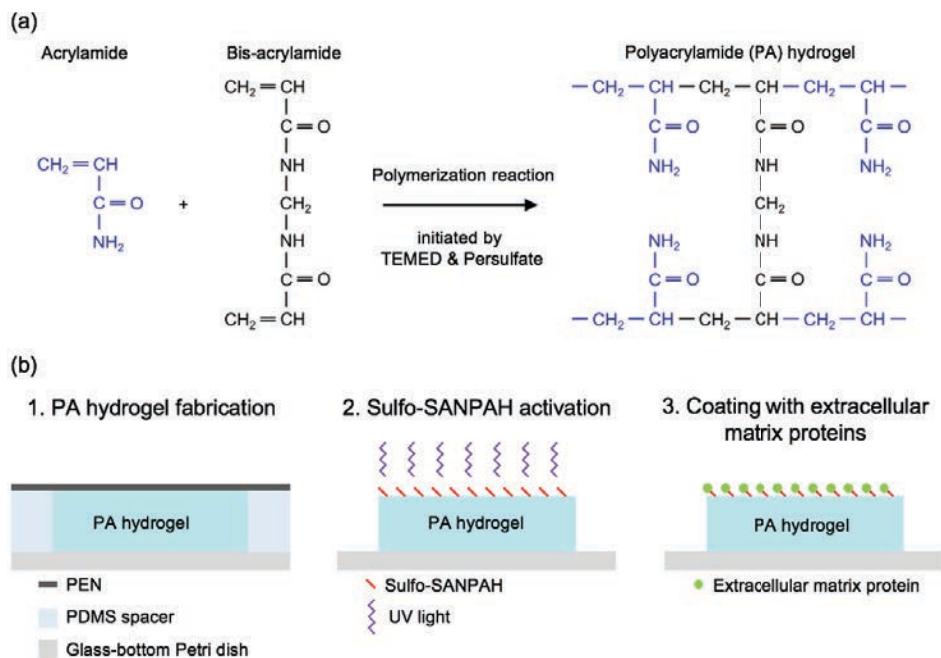


Figure 3.2. Scheme of the fabrication steps to obtain functionalized Polyacrylamide (PA) hydrogels. (a) Scheme of the chemical polymerization to form PA networks. TEMED accelerates the formation of persulfate free radicals, that convert acrylamide monomers into radicals. These acrylamide radicals react with inactivated monomers and bis-acrylamide forming the polyacrylamide (PA) hydrogel. (b) Fabrication set-up, consisting in a reversibly bonded PDMS pool containing the PA prepolymer solution and a PEN cover. The structure was disassembled after polymerization and PA hydrogels were obtained (1). Hydrogels were then activated using Sulfo-SANPAH crosslinker and UV light (2), then coated with ECM proteins (3).

3.3.2 Activation and functionalization of PA hydrogel substrates

PA does not sustain cell adhesion, so for cell culture it was functionalized with extracellular matrix (ECM) components (Figure 3.2 (b)). To covalently bind ECM proteins to the PA hydrogels, Sulfo-SANPAH reagent (Sigma-Aldrich) was used^{126,131}. The PA hydrogels were first rinsed with sterile PBS, and the PBS excess was carefully eliminated with vacuum. Then, a Sulfo-SANPAH solution was freshly prepared at a concentration of $2 \mu\text{g } \mu\text{L}^{-1}$ in Milli-Q water and $150 \mu\text{L cm}^{-2}$ were added on top of each PA hydrogel. The PA hydrogels with the Sulfo-SANPAH solution were UV-irradiated (Light Source LQ-HXP 120 UV, LEJ) for 30 seconds and then rinsed several times with PBS before carefully drying them with vacuum to remove any excess of buffer. As a bifunctional crosslinker, Sulfo-SANPAH contains a phenylazide group at one end that immobilizes to PA hydrogels upon photoactivation, and an ester group at the other end to covalently link with primary amines of proteins¹³¹. The activated PA hydrogels were then incubated with Matrigel to get them stably bonded to their surface (see section 3.4.1).

3.4 Substrate coating with extracellular matrix (ECM) proteins

3.4.1 Preparation of ECM-coated substrates

A variety of substrates were coated with ECM components by employing the method described in this section. These substrates were: glass-bottom Petri dishes with a glass area of 35 mm in diameter and stiffness of ~ 5 GPa; polymer well plates (Ibidi μ -Slide 8 Well, Ibidi GmbH) with an area of $1 \text{ cm}^2/\text{well}$ and stiffness of ~ 3 GPa; and PA hydrogels with an area of 0.2 cm^2 and different stiffnesses, ranging between 3 and 145 kPa.

Matrigel, a protein mixture secreted by a mouse sarcoma cell line, was employed as an extracellular matrix (ECM) surrogate and the substrates described above were coated with it. Matrigel-based cultures have been successfully used for the growth of primary intestinal epithelial cells and intestinal stem cells (ISCs) because of its molecular composition, rich in laminin and collagen IV, which is similar to the basement membrane of the intestinal epithelial tissue^{66,100,101}. Matrigel was used at the stock concentration or as diluted Matrigel solutions. Matrigel solutions at different concentrations were prepared by diluting Matrigel in DMEM/F-12 (Invitrogen). The Matrigel concentrations used ranged between 0.25 and 10 mg mL^{-1} .

Collagen type I (high concentration, rat tail, Corning) was employed as an alternative ECM component to coat the substrates of interest in some experiments. Collagen gelation is pH- and temperature-dependent and the product must be neutralized to allow its polymerization. Collagen type I was neutralized using the alternate gelation procedure included in the lot-specific Certificate of Analysis¹³², to generate solutions at several concentrations. To that aim, a basic solution 1 N of NaOH (PanReac Applichem) was used as neutralizing method: 10X PBS was added (one-tenth of the total volume) to make 1X PBS after neutralization, and culture media was added to adjust the collagen concentration. Finally, the NaOH solution was carefully added to adjust the pH.

Both Matrigel and collagen type I solutions gel at 37°C , so they formed hydrogels when coating the substrates. To form hydrogel thin films, substrates were coated with $10 \text{ }\mu\text{L cm}^{-2}$ of the ECM solutions. To achieve good surface coverage, reproducible results, and avoid the formation of bubbles, these solutions were slowly spread throughout the substrate surfaces releasing them from the pipette without lifting the pipette tip from the substrate following a pre-defined pattern (Figure 3.3). For solutions with concentrations lower than 1 mg mL^{-1} , $200 \text{ }\mu\text{L cm}^{-2}$ instead of $10 \text{ }\mu\text{L cm}^{-2}$ were used to ensure the total surface coverage and protein homogeneous distribution. Once spread, the solutions were incubated at 37°C and 5% CO_2 for 1 hour. To prevent the hydrogel gelation during the coating process, the products and materials were placed on ice, and the substrates and the pipette tips

were kept at -20°C prior their usage. Once coated, the substrates were immediately used.

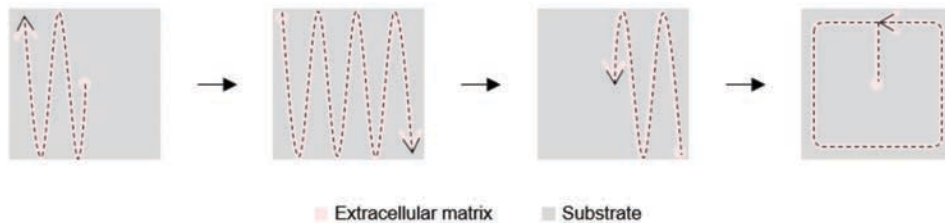


Figure 3.3. Scheme depicting the pattern followed to coat the substrates with extracellular matrix hydrogel films. After pipetting, the ECM solutions were spread slowly throughout the substrate surface while releasing it without lifting the pipette tip from the substrate: starting at the center point going up and down to the left, then going up and down to the right, returning to the center point and finishing through the four corners.

Laminin (Invitrogen), one of the main components of Matrigel¹³³, was also employed to coat some of the substrates, as it is a major component of the basement membrane of the intestinal tissue. Laminin was diluted in PBS and used at a concentration of $20\ \mu\text{g mL}^{-1}$ ¹³⁴. Laminin coatings were performed incubating the solutions on 35 mm glass-bottom Petri dishes (Mattek) for 90 minutes at RT. To avoid evaporation of the solutions during incubation, the chambers were carefully covered with parafilm. Once coated, the substrates were stored in PBS at 4°C until further use.

3.4.2 Characterization of the protein distribution and thickness of Matrigel thin films

In the case of Matrigel-coated substrates, Matrigel thin films were characterized by immunofluorescence using antibodies against laminin. To minimize losing Matrigel material during the immunostaining process, the fixation step was eliminated, low temperatures were avoided, and detergents (such as Triton X-100) were removed from all solutions. Thus, Matrigel-coated substrates were blocked with a blocking buffer containing 1% BSA (Sigma-Aldrich) and 3% donkey serum (Millipore) in PBS for 30 minutes. Antibodies were diluted in PBS containing 0.1% BSA, and 0.3% donkey serum. Hydrogels were incubated with anti-laminin (1:200, Abcam) primary antibody for 30 minutes at room temperature (RT). Alexa Fluor[®] 647 donkey anti-rabbit (Jackson ImmunoResearch) diluted at 1:500 was used as secondary antibody, and it was incubated for 45 minutes at RT. Finally, samples were mounted with Fluoromount[®] (Thermo Fisher) for imaging.

Images of the samples were acquired at randomly selected locations with a confocal laser scanning microscope (LSM 800, Zeiss) equipped with a 100x oil objective (NA = 1.40, WD = 0.17). The pinhole diameter was set to 1 Airy Unit (AU). For all images acquired, a z-step of $0.1\ \mu\text{m}$ was used.

To characterize the surface protein distribution, projection images of the confocal z-stacks were obtained by adding the intensities of each z-slice. Then, average intensities of the resulting projection images were measured as follows: 10 x 10 μm ROIs (regions of interest) were defined and their average intensity were obtained. Finally, the average intensity of each ROI was normalized by the maximum intensity of the corresponding projection image. Three different ROIs of each projection image were measured for three independent samples. Finally, the average intensity of all the ROIs was computed.

On the other hand, Matrigel thickness was estimated by a method based on confocal microscopy, following a previously described procedure¹³⁵ (Figure 3.4). Briefly, we extracted all the orthogonal views of the confocal laminin images and added them up by summing their intensities. This generated an intensity profile of the film cross-sections. To mitigate the noise effects, intensity across the z-profile was obtained by averaging the intensity values of 10 μm width regions. The obtained profiles x were fitted by a Gaussian distribution:

$$y(x) = a + (b - a)e^{-\frac{(x-c)^2}{2\sigma^2}}, \quad [1]$$

where the coefficient a sets the Gaussian baseline, $(b - a)$ is the Gaussian amplitude, c sets the peak position, and σ is the Gaussian width parameter. Then, for each profile the full width at half maximum (FWHM) of the peak was calculated as $2\sqrt{(2\ln 2)\sigma}$, and this value was attributed to the Matrigel film thickness. The measurements were conducted using a custom-made ImageJ macro (<http://rsb.info.nih.gov/ij>, NIH) (code available upon request).

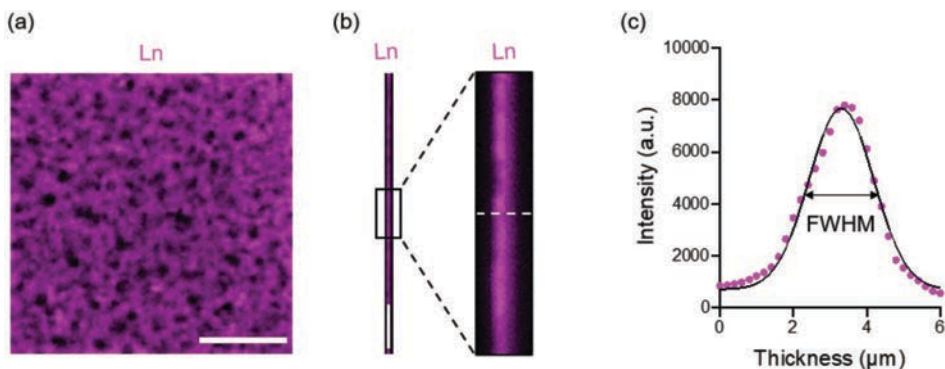


Figure 3.4. Characterization of Matrigel layer thickness. (a) Representative confocal sum intensity projection of an immunofluorescent image for laminin. Scale bar: 20 μm . (b) Representative sum of all orthogonal cross-sections of Matrigel-coated substrates stained for laminin (left panel) and the zoom collected from the black rectangle. Scale bar: 10 μm . (c) Graph representing the intensity collected along the white dashed line in (b) versus the thickness of the laminin layer. The symbols correspond to the experimental measurements, and the solid line is the fit of the data using a Gaussian function. The thickness of the Matrigel layer was estimated by calculating the FWHM of peak.

3.4.3 Characterization of the mechanical properties of Matrigel thin films

Young's moduli of the Matrigel films on PA hydrogels were measured in liquid conditions keeping the hydrogels with a PBS drop^{126,136}. We used a NanoWizard® 4 Bioscience atomic force microscope (AFM) (JPK Instruments) mounted onto an inverted microscope (Eclipse Ti Series, Nikon) to perform indentation measurements. At least three regions per hydrogel and ten indentations per region were done to obtain statistically meaningful values. Silicon nitride pyramidal tips (NanoWorld) with nominal spring constants of 0.08 N m^{-1} were employed. The deflection sensitivity was calibrated by repeated contact mode indentations on a clean glass slide. To obtain the elastic modulus of the samples, the Hertz model for a pyramidal tip was fitted to the measured force-distance curves, using the proprietary JPK data analysis software.

3.5 Cell culture on ECM-coated substrates

3.5.1 Cell seeding and culture on the ECM-coated substrates

ECM-coated substrates (section 3.4.1) were air-dried for 15 minutes at room temperature, and cells were seeded following the steps shown in Figure 3.5. In brief, a $10 \mu\text{L}$ drop of cell suspension was placed on top of the ECM-coated substrates. For the experiments employing organoid-derived single cells, 10^5 cells per drop were cultured. For the experiments employing Caco-2 cells, $2 \cdot 10^4$ cells per drop were cultured. For the experiments employing MDCK cells, $5 \cdot 10^4$ cells per drop were cultured. These cell densities were individually selected as those allowing to obtain confluent 2D monolayers cultured on the substrates according to previous experiments. After 30 minutes of incubation at 37°C in a humidified incubator under a $5\% \text{ CO}_2$ atmosphere to allow cells to attach, more medium at 37°C was added. Cells were then cultured for different periods of time depending on the experiment. In all the cases, the medium was changed at 24 hours, and then every 48 hours.

Immunofluorescence staining was used to reveal the epithelial cell organization when cultured on the ECM-coated substrates, meaning the epithelial cell types and their distribution. When the experiments were finished, both cell lines (Caco-2 and MDCK) and primary cells were fixed with 10% neutralized formalin (Sigma-Aldrich) for 40 min at 4°C , permeabilized with 0.5% Triton X-100 (Sigma-Aldrich) for 30 min at room temperature (RT) and blocked for at least 2 hours at RT with a blocking buffer containing 1% BSA (Sigma-Aldrich), 3% donkey serum (Millipore), and 0.2% Triton X-100 in PBS. All primary antibodies were diluted in 0.1% BSA, 0.3% donkey serum and 0.2% Triton X-100 in PBS, and incubated on cells overnight at 4°C . The primary antibodies used, which depended on the cell type and experimental layout, were: anti-GFP ($1:100$, Life Technologies), anti-GFP ($1:100$, Abcam), anti-Ki67

(1:100, Abcam), anti-Ki67 (1:100, BD Biosciences), anti-Lysozyme (1:100, Dako), anti-Cytokeratin 20 (1:100, Dako), anti-EphB2 (1:200, R&D Systems), anti-laminin (1:200, Abcam), anti-YAP (Santa Cruz Biotech). The secondary antibodies were diluted in 0.1% BSA and 0.3% donkey serum in PBS and incubated on cells 1 hour at RT. The secondary antibodies used were: Alexa Fluor[®] 488 donkey anti-goat, Alexa Fluor[®] 488 goat anti-mouse, Alexa Fluor[®] 488 donkey anti-rabbit, Alexa Fluor[®] 647 donkey anti-goat, Alexa Fluor[®] 647 goat anti-mouse, Alexa Fluor[®] 647 donkey anti-rabbit (all from Jackson ImmunoResearch) diluted at 1:500. Alexa Fluor[®] 568 phalloidin was used to stain filamentous actin (F-actin). Nuclei were stained with 4',6-diamidino-2-phenylindole (DAPI) (1:1000) diluted in 0.1% BSA and 0.3% donkey serum in PBS and incubated on cells 40 min at RT. Finally, samples were mounted with Fluoromount[®] (Thermo Fisher).

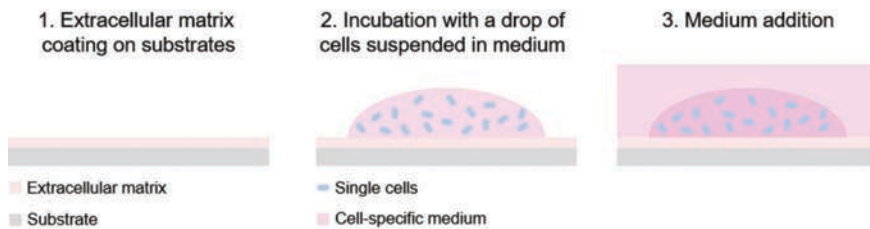


Figure 3.5. Scheme depicting the cell seeding procedure on extracellular matrix (ECM)-coated substrates. After the ECM coating, samples were air-dried for 15 minutes at room temperature (1). Then, a 10 μ l drop of medium containing the cell suspension was placed on top of the ECM coating (2). Then, samples were incubated for 30 min at 37°C to allow cells to attach, and more medium at 37°C was added (3).

Brightfield (or fluorescence), images (or tiles) were acquired using an epifluorescence inverted microscope (Axio Observer 7, Zeiss) with 5x air (NA = 0.16), 10x air (NA = 0.30) or 20x air (NA = 0.40) objectives. Images were acquired at randomly selected locations. The tiles were made up of several individual images to inspect the whole sample. The tiles used a 10% spatial overlap to stitch the single images into a map of the full screened surface by the ZEN software (Zeiss). In addition, fluorescence images were acquired with a confocal laser scanning microscope (LSM 800, Zeiss) with a 10x air objective (NA = 0.3, WD = 2.0) or 20x air objective (NA = 0.8, WD = 0.55). The laser excitation and emission light spectral collections were optimized for each fluorophore, especially for the four-color scans, where the emission bands were carefully adjusted to avoid overlapping channels. The pinhole diameter was set to 1 Airy Unit (AU). For all the images acquired, the optimal z-step was used as indicated by the equipment software. The images were used to characterize several features of the cultures such as cell markers, surface epithelial coverage and cell morphology, among others.

3.5.2 Quantification of cell markers on ECM-coated substrates

Cells cultured on the ECM-coated substrates were characterized for proliferative cells through Ki67 marker (nuclear marker). Also, the presence of Lgr5⁺ intestinal stem cells (ISCs) by positive GFP signal and epithelial markers such as cytokeratin 20 (Ck20) (cytoskeleton marker for terminally differentiated enterocytes and goblet cells) was checked. To allow quantifications, cell contour was defined through F-actin, and cell nuclei were located through DAPI identification. To quantify the different cell markers, two image processing methods were used, a custom-made ImageJ macro and a semi-automatized routine implemented in the Imaris software (version 9.1.0; Bitplane) (codes available upon request).

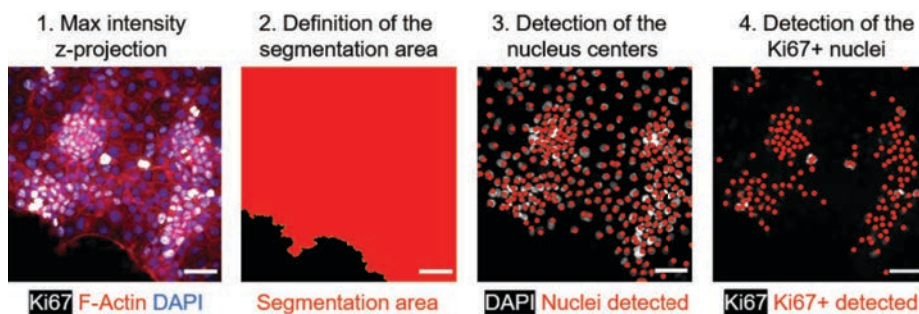


Figure 3.6. Example illustrating the quantification of cell markers through Image J customized macro. Confocal immunofluorescent stacks obtained for proliferative cells (Ki67), F-Actin and cell nuclei (DAPI) of epithelial monolayers were z-projected using maximum intensities (1). The F-Actin channel defines the segmentation area (2). A total of 322 individual nuclei were detected applying a Laplacian of Gaussian filter with 8 μm radius (3). Then, the Ki67 marker mean intensity was measured where the nuclei were detected. A mean intensity value above a threshold automatically identified 49.4% of nuclei as Ki67+. Scale bars: 50 μm .

The custom-made ImageJ macro was used to quantify the number of Ki67 and Ck20 positive cells among the total cells in each particular image (see Figure 3.6). Briefly, confocal images were z-projected using maximum intensities. The F-actin channel was employed to define the segmentation area. Then, individual cell nuclei were filtered by applying a Laplacian of Gaussian filter with a radius adapted to the characteristic size of the nuclei. This filter treats cell nuclei as blobs and detects their centers¹³⁷. Then, for each epithelial marker, its mean intensity was measured where individual cell nuclei were detected. When this mean intensity was above a user-defined threshold, the macro counted that nucleus as positive for that particular marker.

Imaris software was employed to quantify Ki67 and GFP positive cells related to the total cell number. First, cell nuclei were detected in the reconstructed 3D images as spots using the smallest values of their diameters previously measured for representative images. Spot number detection was adjusted based on the signal

quality (differences in intensity and shape) to improve nuclei detection. Then, F-actin channel was used as a filter to define the segmentation area of the nuclei. To quantify the number of cells positive for a specific marker relative to the total cell population, the mean intensity of that specific marker was filtered by the total nuclei signal found in each F-actin positive area. When the mean intensity of the marker was above a threshold, we counted the nucleus as positive for that particular marker. This process was performed for both Ki67 and GFP markers.

3.5.3 Quantification of cell surface coverage on ECM-coated substrates

To quantify the cell surface coverage from immunostaining images, the fluorescence image tiles of F-actin were used. The tiles were pre-processed and analyzed using ImageJ software as described in Figure 3.7. First, we applied a mean filter with a radius of 15 μm to smoothen the surface edges. The filtered images were then segmented using the default ImageJ threshold to obtain a binary mask where the area occupied by the cells appeared in white, and cell-free regions or holes in the cell monolayers appeared in black. To remove the background noise, the binary mask was twice eroded followed by twice dilated using ImageJ specific functions. The area was the filled region that describes the projected area (Figure 3.7 (a), left panel). Then, from the binary image, the area occupied by the cell monolayer (including holes) and cell aggregates was determined (Figure 3.7 (a), middle panel) and, by inverting the binary image, the areas of the holes (cell-free areas) were obtained (Figure 3.7 (a), right panel). Subtracting both, the projected area effectively occupied by cell structures was evaluated. This area was then normalized by the seeding area (yellow line in Figure 3.7 (b)). Also, in some experiments, cell surface coverage over culture time was alternatively quantified by analyzing brightfield images with ImageJ software. Briefly, the projected area occupied by cellular structures was measured by outlining its shape and normalizing it to the total area of the image.

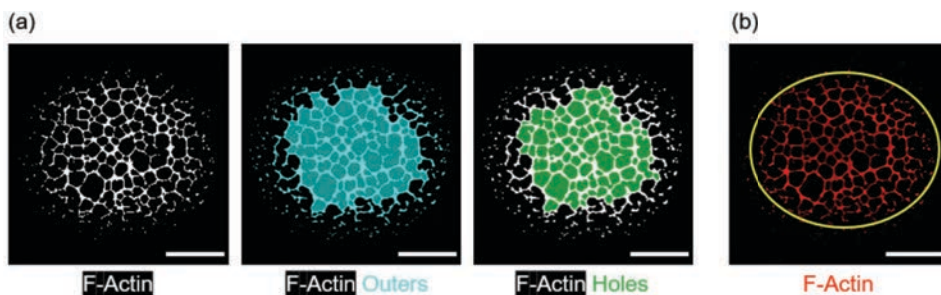


Figure 3.7. Representative quantification of the surface coverage of cellular structures grown on ECM-coated substrates from organoid-derived single cells. (a) Binary image from the thresholded F-Actin image (left panel), binary image overlaid with areas where cells are found including holes (middle panel), and holes (cell-free areas) formed on the cell seeding area (right panel). The projected area filled by cells was obtained by subtracting the holes from the outers. (b) Immunofluorescence image tile of F-Actin with the seeding area contoured in yellow. Scale bars: 2 mm.

3.5.4 Morphological characterization of single cells or cellular aggregates on ECM-coated substrates

Depending on the experiment performed, cells or cell aggregates were obtained, and their morphology was analyzed as single objects following the procedures described in what follows.

Single cells or cellular structures were segmented using fluorescence images and tiles processed by ImageJ software as described in Figure 3.8 (a-d). For instance, cell nuclei were segmented from the DAPI or Ki67 intensity channels. First, the images were subjected to a median filter with a radius of 1 μm to remove the noise, homogenize the staining, and prevent losing the edges. In the case of cell aggregates, which were segmented using the F-actin staining images, these were subjected to a mean filter with a radius of 2 μm to smoothen surface edges. Next, the filtered images were subjected to the default ImageJ threshold to obtain single object binary masks. These masks were eroded twice followed by dilating them twice using the Image J corresponding functions to remove the background noise. After applying the threshold, individual structures with overlapping contours were separated performing a watershed segmentation, while incomplete structures overlapping with the edges of the images were removed (Figure 3.8 (c)). Then, segmented structures were fitted by ellipses (Figure 3.8 (d)).

For each individual cell or cell aggregate, we measured its surface projected area, centroid position (x, y), elongation index, orientation index and solidity to define its morphology (Figure 3.8 (e)). The elongation index was assessed from the fitted ellipses as $(\text{major axis} - \text{minor axis}) / (\text{major axis} + \text{minor axis})$. With this definition, the elongation index equals 0 for a circle, and has a maximum value of 1 corresponding to a line. The orientation index was calculated as $\cos(2\theta)$, where θ is the angle between the major axis of the fitted ellipses and the axis of interest (the horizontal one) (Figure 3.8 (e)). Thus, the orientation index has a value between -1 and 1. It has a value of 1 for a structure with the elongation perfectly aligned with the selected axis (here horizontal), and a value of -1 if the structure is aligned perpendicularly to such axis. When assessing orientation from a collection of structures, a randomly oriented distribution has an orientation index close to 0. Last, the solidity measures the convexity of the structures, and is defined as the ratio between their area and the area of their convex hull: $\text{area}/\text{convex_area}$. Whereas a perfectly convex ellipsoid (undeformed) has a solidity of ~ 1 , objects with irregular boundaries or containing holes have solidity values < 1 . When the elongation index was ~ 0 , and the solidity was ~ 1 , the objects were considered as perfect circles, and their diameters were calculated as $2\sqrt{(\text{area}/\pi)}$.

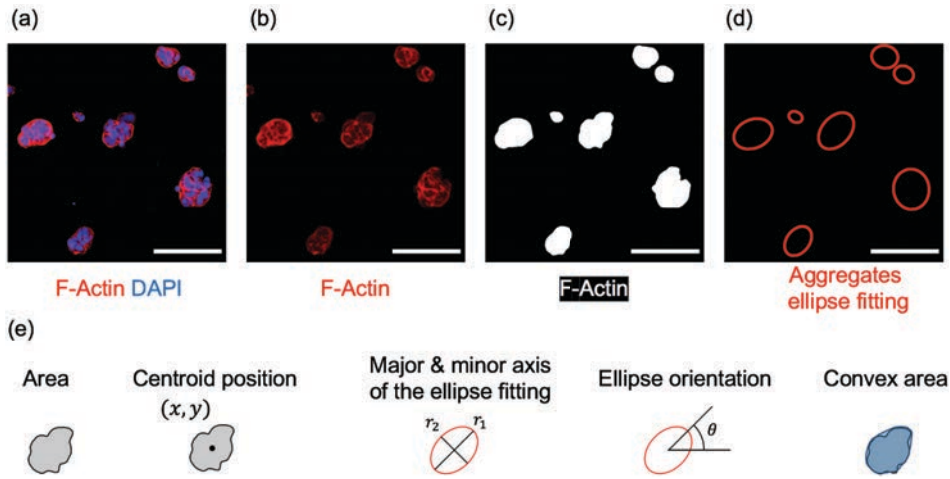


Figure 3.8. Representative images of the segmentation steps of single cells or cell aggregates. (a) Immunofluorescence image of F-Actin and cell nuclei (DAPI). Scale bar: 100 μm . (b) F-Actin image subjected to a mean filter with a radius of 5 pixels to smoothen surface edges. Scale bar: 100 μm . (c) Binary image from the thresholded fluorescence image of F-Actin. The aggregates touching the edges of the image were removed. Scale bar: 100 μm . (d) Aggregate fitting by ellipses. Scale bar: 100 μm . (e) Schematic drawings showing the aggregate projected area, centroid position, major and minor axes of the ellipse fitting, ellipse orientation and the convex area (used to compute solidity).

3.5.5 Morphological characterization of cellular networks on ECM-coated substrates

For some experiments, cellular structures corresponding to cell monolayers with holes, overall resembling cellular networks, were obtained. Therefore, we defined a methodology to characterize such networks through quantitative parameters based on Voronoi tessellation of the F-actin images. A Voronoi diagram is a subdivision of a plane into polygons for a point distribution in such a way that the collection of all Voronoi polygons fills the plane without any gaps. Each polygon is associated with a point of the point distribution and defines the region of space that is closer to that point than to any others.

First, F-actin fluorescence tiles were pre-processed with ImageJ software. They were subjected to a mean filter with a radius of 10 μm to smoothen surface edges. Next, the filtered tiles were processed using the default ImageJ threshold to obtain a binary image. To remove the background noise, the binary tiles were twice eroded, followed by twice dilated. Then, we extracted the (x, y) position of the center of each hole found in the cellular monolayers using the *find maxima* function of Image J. Finally, the binary tiles were segmented using the *Voronoi* function (Figure 3.9 (a)), and the areas of the polygonal structures were obtained.

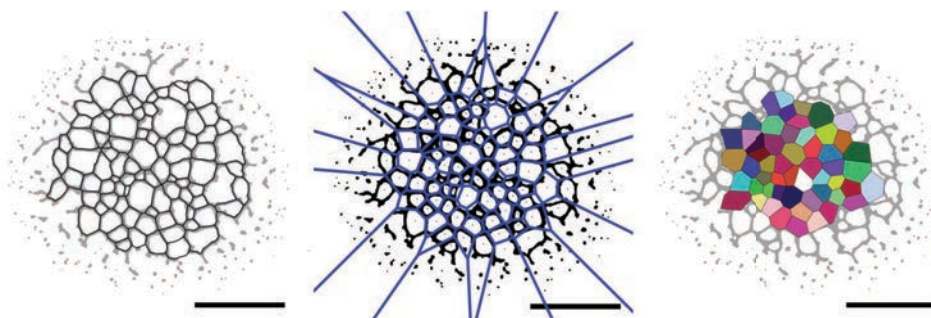


Figure 3.9. Representative images of the morphological characterization of cellular networks. (a) Binary image of F-Actin overlay with its segmentation using the Voronoi function from ImageJ. Scale bar: 2 mm. (b) Binary images of F-Actin overlay with its segmentation using the Voronoi function from Matlab. Scale bar: 2 mm. (c) Binary image of F-Actin overlay with the remaining Voronoi polygons after filtering the Voronoi network. Scale bar: 2 mm.

To complete the characterization provided by the codes available for ImageJ, a customized code was also designed and implemented in Matlab (The MathWorks) (code available upon request). Voronoi networks were retrieved with the *Voronoi* function using the (x, y) position of the center of each hole in the network extracted previously with ImageJ (Figure 3.9 (b)). Then, the areas of the polygons, the number of their edges, their edge sizes and their edge angles were determined with the function *voronoiDiagram*. With this code, the images were thresholded, and polygons with infinite coordinates (touching the edges of the image) and their neighbors were removed. Also, the polygons with edge angles below a threshold defined as $mean_{edge\ angle} - 2SD_{edge\ angle}$ (SD is the standard deviation) were removed. The thresholded polygons were represented using the *patch* function (Figure 3.9 (c)). We then compared the areas of the polygons obtained using network segmentation in ImageJ and the Voronoi code in Matlab and we found non-significant differences between both them (Figure 3.10). Therefore, assumed that our cellular networks could indeed be described as Voronoi tessellations to quantify their geometry, arrangement and degree of order.

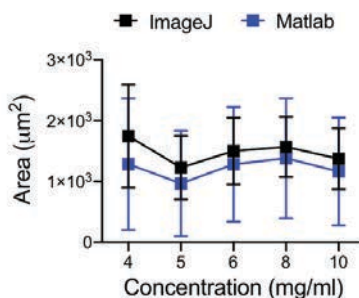


Figure 3.10. Comparison of areas using network segmentation (ImageJ analysis) and Voronoi polygons (Matlab analysis). Mean \pm SD. N = 3 experiments.

Thus, statistical distributions of the network variables both metric and topological, such as number of edges, edge size, area and edge angle were computed. For each variable, its statistical distribution was characterized by its mean value, and its second moment, defined as:

$$\mu_2^f = \frac{1}{\langle f \rangle^2} \frac{1}{N} \sum_{i=1}^N (f_i - \langle f \rangle)^2, \quad [2]$$

Where f is the variable (n edge number, a area, β angle, s edge size), $\langle \dots \rangle$ its mean value, f_i is the value of f for polygon i , and N the total number of polygons. We used the second moment of the distribution of number of edges μ_2^n as a measure of the disorder of the network. This value is zero in the absence of disorder (corresponding to a purely deterministic motion), and it becomes non-zero in the presence of perturbations. The second moment was employed to compare networks resulting from different experimental systems^{52,138}.

3.5.6 Time-lapse microscopy experiments and quantification of cell migration on ECM-coated substrates

Organoid-derived single cells migration on ECM-coated substrates was monitored by time-lapse microscopy experiments. *Lgr5-EGFP-ires-CreERT2* mouse intestinal organoids allowed the visualization of *Lgr5*⁺ stem cells thanks to a green fluorescent protein (GFP) reporter. An epifluorescence inverted microscope (Axio Observer 7, Zeiss) with a 10x dry objective (NA = 0.4) was used to collect phase-contrast and GFP images of cells every 5-10 minutes for up to 24 hours. The microscope was equipped with thermal, CO₂ and humidity controls. Sequential couples of phase contrast and GFP images were acquired at a rate of 1 frame every 5-10 minutes during the duration of the experiment (~ 16 hours). Three zones per condition, two replicas per condition and two conditions were imaged in parallel using a motorized stage.

The time-lapse fluorescence images of GFP⁺ signals were pre-processed using ImageJ software. Their background noise was reduced with the *subtract background* function by using a rolling ball radius of 10 μm . The resulting images were then subjected to a mean filter with a radius of 1 μm to homogenize the staining. The pre-processed images were then loaded to the *TrackMate* plugin¹³⁹, which tracked the trajectories of GFP⁺ cells by treating the GFP signal as blobs and detecting their centers. The GFP signal was detected using the following settings: DownSample Log Detector and blob diameter 15 μm . Finally, we obtained data containing the time and position for each GFP⁺ cell.

Data analysis was performed using two different custom-made codes in Matlab (code available upon request). The function *importTrackMateTracks* was used in both codes to import the data extracted from the TrackMate analysis. Each cell i 's

trajectory ($i = 1, 2, \dots, M$), where M is the total number of cells, was obtained by connecting the position of the cell in all the images (Figure 3.11 (a)). One code allowed us to represent the cell trajectories. Using the other code, cell mean-square displacement (MSD), which is a measure of the average distance that each cell travelled, was computed as:

$$MSD(t) = \langle |\mathbf{r}_i(t + \Delta t) - \mathbf{r}_i(t)|^2 \rangle, \quad [3]$$

where $\mathbf{r}_i(t)$ (bold letters refers to a vector) denote cell i 's position in space at time t , Δt is the time lag and the average $\langle \dots \rangle$ is taken over all GFP⁺ cells. In order to describe the migratory characteristics of the GFP⁺ cells, the MSD of cell trajectories were fitted using a single exponential time-dependent diffusion model described by:

$$MSD \propto t^\alpha, \quad [4]$$

where α is a time-dependence coefficient that describes the type of migration exhibited by the cells. For $\alpha \sim 1$, which represents MSD trajectories that increase linearly with time, the cells undergo random movement (Brownian motion). A cell with Brownian motion diffuses freely and explores all the available space with equal probability (Figure 3.11 (b), right panel). In contrast, $\alpha < 1$ represents a partially confined random movement. In a partially confined random movement, a cell remains confined inside a sub-volume from which it cannot escape (Figure 3.11 (b), middle panel). Finally, $\alpha > 1$ indicates that the particle is moving in a directed manner. A cell with directed motion moves to a specific target (Figure 3.11 (b), left panel).

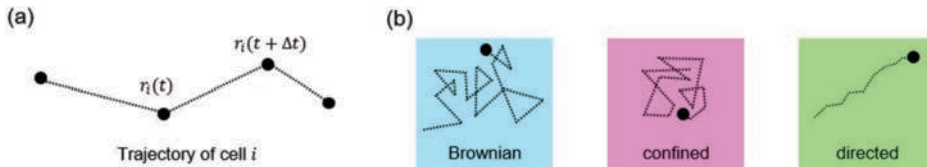


Figure 3.11. (a) Schematic trajectory of cell i (black point) connecting its position in space and time $\mathbf{r}_i(t)$ through different images. (b) Schematic trajectories representing the different modes of diffusion. Brownian motion (light blue), partially confined random movement (pink), and directed motion (green).

We also computed the temporal correlation function (TCF), which is a measure of the cell velocities and was defined as:

$$TCF(\tau) = \left\langle \frac{|\mathbf{r}_i(t + \Delta t) - \mathbf{r}_i(t)|^2}{\tau} \right\rangle, \quad [5]$$

where $\tau = \Delta t, 2\Delta t, \dots$ is the time evolution, and the average $\langle \dots \rangle$ is taken over all cells.

3.6 Substrate biochemical micropatterning

3.6.1 Micro-contact printing procedure

Micro-contact printing is a widely employed technique to transfer biomolecular patterns to surfaces of usually hard materials^{140,141}. In here, we applied this technique to transfer biomolecular patterns on top of the extracellular matrix (ECM) (Matrigel mainly)-hydrogel films coating the substrates described in section 3.4.1. Micro-contact printing was performed following the experimental set-up depicted in Figure 3.12 (a). First, a silicon master, which contained the microfeatures of interest (Figure 3.12 (b)), was fabricated. For this, high-quality acetate photomasks (CAD/Art Services Inc.) were designed using CleWin Layout Editor software (PhoeniX Technologies, Netherlands). Arrays of the different motifs were printed over square areas of 12 x 12 mm. Design (1) consisted of lines of equal width and pitch spacing (L). We chose to use linear patterns because they allow easy read-outs of quantitative parameters characterizing cell phenotype such as cell alignment and orientation^{125,126}. The dimensions of the lines (L = 10 or 20 μm) were selected according to the mean area of the NIH/3T3 fibroblast nuclei, which was measured experimentally. Design (2) consisted of circles of 100 or 200 μm in diameter (\varnothing) with a spacing (center-to-center) (a) increasing from 150 μm to 400 μm . We chose these designs because of their similarity with the 2-dimensional (2D) organization of the small intestine in crypt- and villus-like domains when cultured in monolayers (see section 3.5)^{119,120}. The dimensions were selected according to the mean diameter of crypt-like domains and their mean interdomain distances, which were experimentally determined. Design (2) was prepared as a positive and as a negative mold, meaning ready to fabricate either holes or pillars to match the requirements of the different biological experiments performed. The microfeatures obtained were characterized using an optical microscope (Eclipse L150, Nikon) with 10x (NA = 0.3, WD = 6.5), 20x (NA = 0.45, WD = 3.0) or 50x (NA = 0.5, WD = 10.6) air objectives (Figure 3.12 (b)).

Silicon masters were fabricated onto silicon wafers by standard microfabrication processes involving UV-photolithography and reactive ion etching (D+T Microelectrónica AIE). The masters had a height of 1 μm for the design (1) and 3 μm for the design (2). This ratio between the feature dimensions and height avoids the collapse of the printed structures and facilitates the transfer of patterns over relatively large areas. Then, masters were silanized to facilitate the demolding of PDMS replicas that would be later used as stamps for the patterning process¹⁴². To that aim, the silicon masters were first cleaned with Milli-Q water, acetone (PanReac Applichem), and isopropanol (PanReac Applichem) and dried using nitrogen. Subsequently, their surface was activated via immersion in a piranha solution (H_2SO_4 : H_2O_2 ; 7: 3; v/v) (PanReac Applichem) for 30 minutes, followed by washing with Milli-Q water and drying using nitrogen. After activation, the silicon masters

were placed into a desiccator with a small vial containing 1 or 2 drops of trichloro(1H, 1H, 2H, 2H-perfluorooctyl) silane (Sigma-Aldrich) and kept under vacuum for 1 hour. Thereafter, the silanized masters were placed in the oven at 80°C for 30 minutes. Finally, they were washed with toluene (PanReac Applichem) and isopropanol, and then dried using nitrogen.

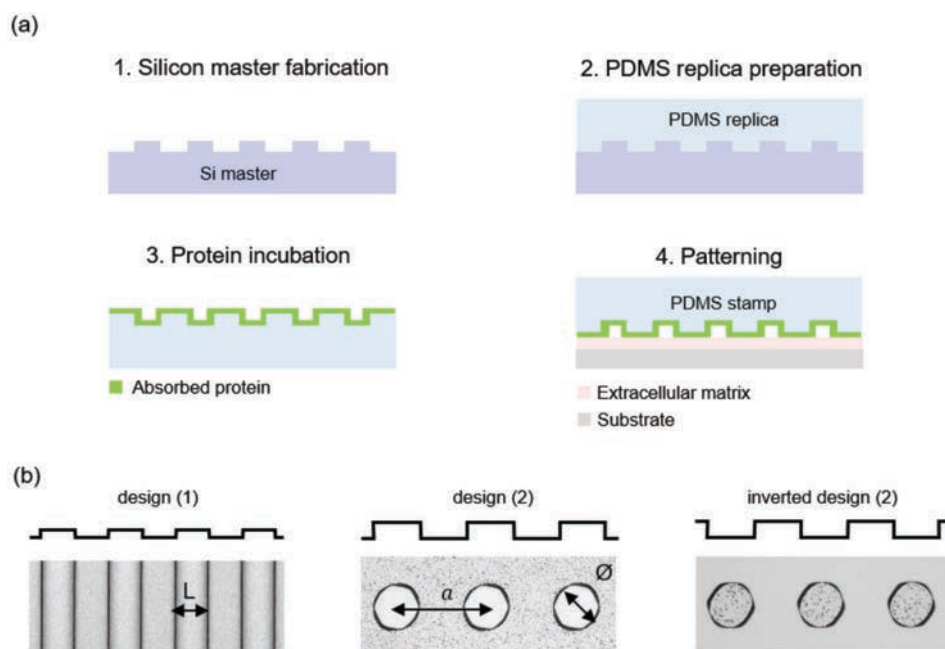


Figure 3.12. (a) Scheme depicting the micro-contact printing technique. First, silicon masters containing the microfeatures of interest were fabricated (1). Second, we freshly prepared the PDMS replicas (2). Then proteins were physically adsorbed to the surfaces (3). Finally, the PDMS replicas containing the proteins were used as stamps to transfer proteins onto the surface of the substrates (4). (b) Representative brightfield images of three silicon masters with different designs showing their characteristic dimension parameters: ridge and pitch width (L); circle diameter (\varnothing), and interdomain spacing (a).

PDMS replicas were freshly prepared to be used as stamps and transfer biomolecules to the substrates of interests. To that aim, a mixture of Sylgard 184 Silicon Elastomer and curing agent (DowCorning) at a ratio of 10:1 w/w was used. For design (1), PDMS was spun-coated onto the silicon masters forming PDMS replicas of 50 μm in thickness. For design (2), the PDMS was directly casted on the silicon master forming thick replicas (few mm). In both cases, replicas were then cured for 3 hours at 65°C. After curing, PDMS microstructures were simply manually demolded from the masters and cut into pieces of 5 mm in diameter.

Then, PDMS replicas were incubated with 20 μL of solutions containing different proteins of interest and used as stamps to pattern the substrates used for cell culture. PDMS replicas were incubated for 45 minutes at room temperature. To

avoid evaporation of the protein solutions during the incubation, this was performed under moisture. Once incubated, the PDMS stamps were washed with PBS and Milli-Q water and air-dried. Finally, the PDMS stamps with the proteins on their surfaces were put in contact with the substrates for 10 minutes to transfer these proteins. The thinnest PDMS stamps (design (1)) self-provided conformal contact with the substrate. However, in the case of the thickest PDMS stamps (design (2)), low pressure was manually applied to ensure the conformal contact between the stamps and the substrates.

3.6.2 Preparation and characterization of hydrogels for micro-contact printing

When the micro-contact printing process was applied onto hard surfaces, the PDMS stamps were used directly on those surfaces. However, when the micro-contact printing was performed onto soft hydrogels such as Matrigel, these were previously subjected to a freeze-drying process to make them mechanically resistant to sustain the PDMS stamp pressure, following a process developed by our research group (Figure 3.13)¹²⁵. In short, Ibidi plates were coated with $200 \mu\text{L cm}^{-2}$ of Matrigel solution (diluted at 0.25 mg mL^{-1}) (see section 3.4). After gelation (1 hour at 37°C), the excess of the solution was removed, and samples were carefully rinsed first with PBS and then with Milli-Q water to avoid the presence of salts. Subsequently, samples were freeze-dried by immersion in liquid nitrogen and vacuum dried for 24 hours at -50°C and 0.06 mbar of pressure (1-4 LD-2, Christ Alpha). Matrigel samples prepared following this process were characterized by the immunostaining of laminin. Their thickness and surface distribution were evaluated as described in section 3.4.2. Diluted fresh Matrigel (non-freeze-dried) samples, which were used as controls in cellular experiments, were also characterized this way.

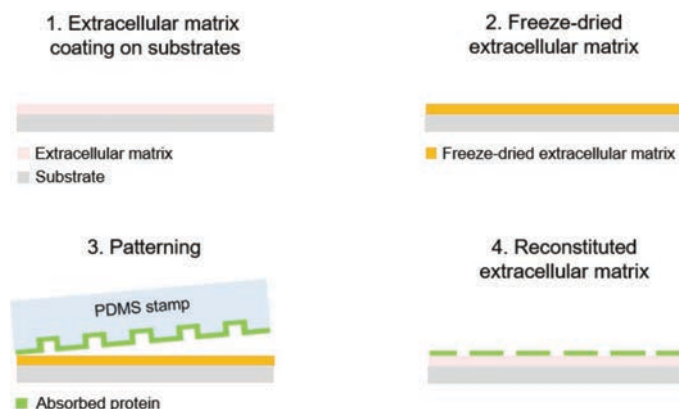


Figure 3.13. Scheme depicting the preparation of ECM-coated substrates for the micro-contact printing process. Diluted Matrigel was poured on substrate (1) and subsequently freeze-dried (2). Then, the micro-contact printing procedure was performed onto the dried surfaces (3). Afterwards, samples were reconstituted with PBS (4).

Micro-contact printing was then carried out on the freeze-dried Matrigel. As no chemical modification of the hydrogel surface was performed; the proteins were immobilized by physical adsorption. Finally, Matrigel substrates were reconstituted adding PBS at room temperature, incubating for at least 30 minutes at 37°C. Samples were then stored under moisture at 4°C until cell seeding.

3.6.3 Generation and characterization of biochemical patterns

Matrigel was biochemically patterned through micro-contact printing following the protocol described above. As proteins, we used recombinant mouse Wnt3a protein (Abcam), recombinant mouse EphB2/Fc receptor (R&D Systems), recombinant mouse ephrinB1/Fc ligand (R&D Systems) or recombinant Human IgG1 Fc (R&D Systems). The protein concentrations were individually selected for each protein and are listed in table 3.2.

	Wnt3a	EphB2/Fc	ephrinB1/Fc	Fc
$\mu\text{g mL}^{-1}$	10	100	69.0	69.0

Table 3.2. List of micro-contact printed proteins and their selected concentrations.

It is worth mentioning that Eph receptor activity requires stimulation not by a single ligand, but by clusters of ephrinB1 ligand to initiate its downstream signaling¹⁴³. Moreover, the ligand itself is actually commercialized as a dimer, where two ephrinB1 molecules are fused to immunoglobulin Fc molecules and form dimers upon binding through the disulfide groups. Fc groups are then used to produce ligand clusters through their binding using anti-Fc antibodies. Therefore, for the patterning experiments, the oligomers were prepared conjugating ligand (ephrinB1 fused to Fc, named ephrinB1/Fc) and control (only Fc) dimers with anti-Fc antibodies (Jackson ImmunoResearch) at 2:5 molar ratio for 30 min under constant shaking. If not stated otherwise, in this thesis we will refer to ephrinB1 or Fc in this clustered fashion.

The hydrodynamic diameters of the oligomers generated by antibody-conjugated ephrinB1 were determined by dynamic light scattering (DLS) as we previously published¹⁴⁴. The particle size distribution was computed from the intensity values obtained at 25°C using a Möbius instrument (Wyatt Technology Corp.) equipped with a 532 nm laser and a 163.5° scattering angle. The samples were prepared as we described above. As control, anti-Fc solution was measured. Measurements were performed immediately after clustering using the Möbius dip cell. Three independent samples were measured in triplicate. Dynamics software (Wyatt Technology Corp.) was used for data acquisition and data treatment. The anti-Fc antibody has an average size of 9 ± 1 nm in diameter (Figure 3.14 (a)), correlating

with the size reported. EphrinB1 oligomers exhibit a main peak of 72 ± 4 nm in diameter (Figure 3.14 (b)). This peak corresponds to tetramers (one anti-Fc antibody complexing two ephrinB1 fused to Fc dimers) (Figure 3.14 (c)), in agreement with measurements reported for the same crosslinking procedure¹⁴³.

The micropatterns were then visualized by immunofluorescence following the protocol described in section 3.4.2. The following antibodies were employed: as primary antibodies anti-laminin (1:200, Abcam), anti-EphB2 (1:200, R&D Systems), anti-Wnt3a (1:200, Abcam) and anti-Fc ($560 \mu\text{g mL}^{-1}$, Jackson ImmunoResearch). As secondary antibodies, Alexa Fluor[®] 488 goat anti-goat, Alexa Fluor[®] 488 goat anti-mouse, Alexa Fluor[®] 488 donkey anti-rabbit, and Alexa Fluor[®] 647 donkey anti-rabbit (all from Jackson ImmunoResearch) diluted at 1:500 were employed. Finally, samples were mounted with Fluoromount[®] (Thermo Fisher) for their observation under the microscope.

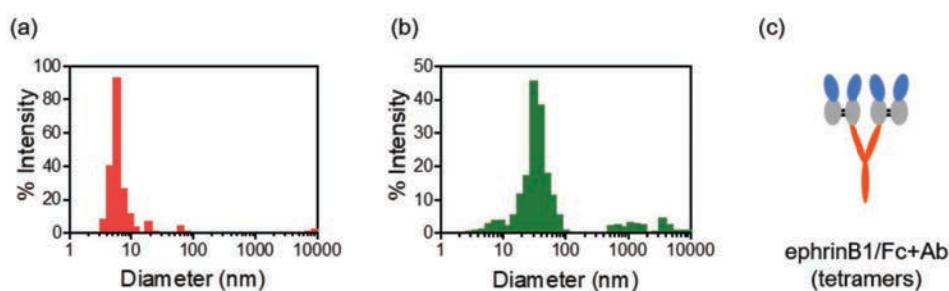


Figure 3.14. Dynamic Light Scattering (DLS) measurements. Size distribution of (a) anti-Fc antibody and (b) antibody-conjugated ephrinB1/Fc. The anti-Fc antibody has an average size of 9 ± 1 nm in diameter, correlating with the size reported. EphrinB1/Fc oligomers exhibit a main peak of 72 ± 4 nm in diameter. This peak corresponds to tetramers (one anti-Fc antibody complexing two ephrinB1/Fc dimers), in agreement with measurements reported for the same crosslinking procedure. Mean. $N = 3$. (c) Scheme depicting the tetramer.

The success of the printing procedure (uniformity, reproducibility, and stability of the biochemical micropatterns) was checked using an epifluorescence inverted microscope (Axio Observer 7, Zeiss) with a 63x oil objective ($NA = 1.4$). Images were analyzed using ImageJ software. The protein coverage was quantified by measuring the fluorescence intensity of the antibodies. For comparison of the intensity measurements, all images were acquired using the same microscope settings.

3.7 Cell culture on biochemically micropatterned substrates

3.7.1 Cell seeding and culture on the micropatterned substrates

NIH/3T3 fibroblasts were first used to check the role of micropatterned ephrinB1 ligands on cell organization and morphology, as they endogenously express the EphB2 receptor¹²⁴. For these experiments, we chose to pattern ephrinB1 molecules

in lines of two different widths ($L = 10$ and $20 \mu\text{m}$) because they allow for easy read-outs of the quantitative parameters of the cell phenotype in response to the patterns (cell alignment and orientation). Briefly, 35 mm glass-bottom Petri dishes (Mattek) were functionalized incubating $20 \mu\text{g mL}^{-1}$ laminin solution following the steps described in section 3.4.1. Then, ephrinB1 lines were micro-contact printed onto the laminin-coated surfaces of glass-bottom Petri dishes. Once printed, samples were stored in culture medium until cell seeding. NIH/3T3 fibroblasts were cultured at densities of 10^5 , $3 \cdot 10^5$ or $5 \cdot 10^5$ cell cm^{-2} . These cell densities were selected to obtain single cells or cells connecting with each other. Cells were then cultured for 24 hours at 37°C in a humidified incubator under a 5% CO_2 atmosphere. Immunofluorescence staining was used to reveal the NIH/3T3 fibroblast organization. When the experiments were finished, NIH/3T3 fibroblasts were fixed with 10% neutralized formalin (Sigma-Aldrich) for 40 min at 4°C , permeabilized with 0.5% Triton X-100 (Sigma-Aldrich) for 30 min at room temperature (RT) and blocked for at least 2 hours at RT with a blocking buffer containing 1% BSA (Sigma-Aldrich), 3% donkey serum (Millipore) and 0.2% Triton X-100 in PBS. We used anti-Fc (1:100, Jackson ImmunoResearch) as primary antibody and diluted it in 0.1% BSA, 0.3% donkey serum and 0.2% Triton X-100 in PBS and incubated on cells overnight at 4°C . Secondary antibody used was Alexa Fluor[®] 647 donkey anti-goat (1:500, Jackson ImmunoResearch) and it was diluted in 0.1% BSA and 0.3% donkey serum in PBS and incubated on cells 1 hour at RT. Alexa Fluor[®] 568 phalloidin was used to stain filamentous actin (F-actin). Nuclei were stained with 4',6-diamidino-2-phenylindole (DAPI) (1:1000) diluted in 0.1% BSA and 0.3% donkey serum in PBS and incubated on cells for 40 min at RT. Finally, samples were mounted with Fluoromount[®] (Thermo Fisher). Fluorescence images were acquired using an epifluorescence inverted microscope (Axio Observer 7, Zeiss) with 10x air (NA = 0.30) or 20x air (NA = 0.40) objectives. Images were acquired at randomly selected locations.

Organoid-derived single cells were then tested onto micropatterns of designs (2) and inverted design (2) (Figure 3.12 (b)), where recombinant mouse Wnt3a protein (Abcam) and recombinant mouse ephrinB1/Fc ligand (R&D Systems) conjugated with anti-Fc antibodies (Jackson ImmunoResearch) were stamped on top of Matrigel-coated surfaces. Cells were seeded at a density of 10^5 cells per drop (see section 3.5.1). This cell density was selected to obtain a confluent monolayer after 24 hours of culture according to previous experiments. The cells were cultured for different periods of time depending on the experiment. In all the cases, the medium was changed at 24 hours, and then every 48 hours. Immunofluorescence staining was used to reveal the epithelial cell organization following the procedure described in section 3.5.1. Finally, samples were mounted with Fluoromount[®] (Thermo Fisher). Images were acquired using an epifluorescence inverted microscope (Axio

Observer 7, Zeiss) with 10x air (NA = 0.30) or 20x air (NA = 0.40) objectives. Images were acquired at randomly selected locations.

3.7.2 Cell nucleus orientation and position with respect to the biochemical patterns

To define the orientation and position of cell nuclei with respect to the biochemical patterns performed, fluorescence images showing both the cells and the linear micropatterns were employed. On these images, the degree of colocalization between the nuclei and the printed proteins was measured using an object-based method (see Figure 3.15 (a-c)). To perform this procedure, the two fluorescence images were segmented into objects (see section 3.5.4). Briefly, the images of cell nuclei were subjected to a median filter with a radius of 1 μm to remove the noise, homogenize the staining, and prevent losing the edges. The protein patterning images were subjected to a mean filter with a radius of 2 μm to smoothen stamp edges. Next, the filtered images were segmented using the default ImageJ threshold function to obtain binary masks. To remove the background noise, the binary masks were eroded twice and dilated twice. After threshold, fused single objects were separated, performing a watershed segmentation, and single objects touching the edges of the image were removed.

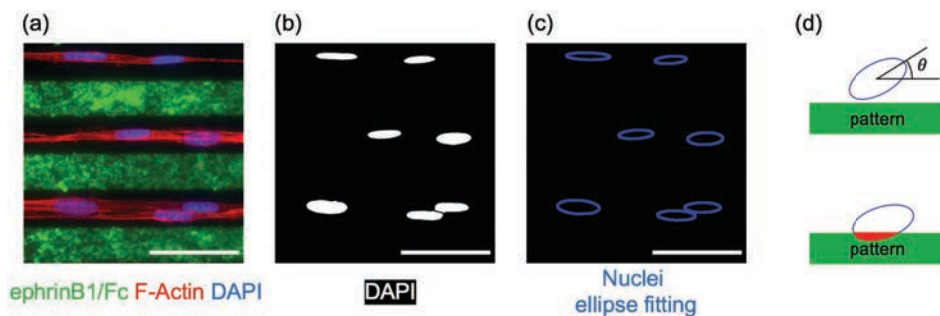


Figure 3.15. Representative images of the analysis procedure followed to determine the position of cell nuclei with respect to linear patterns. (a) Immunofluorescence image of ephrinB1/Fc and NIH/3T3 cells stained for F-Actin and cell nuclei (DAPI). Scale bar: 100 μm . (b) Binary image from the thresholded fluorescence image of F-Actin. Fused nuclei were separated performing a watershed segmentation. Scale bar: 100 μm . (c) Ellipse fitting of nuclei. Scale bar: 100 μm . (d) Schematic drawing showing the angle between the major axis of the fitted ellipse with respect of the pattern (θ), and the nucleus position with respect to the pattern, which is performed quantifying the red area showed in the scheme.

The nuclei orientation was calculated as $\cos(2\theta)$, where θ is the angle between the major axis of ellipses fitting the nuclei and the patterned lines. Thus, the nucleus orientation index has a value between -1 and 1, as we previously described (section 3.5.4) (see Figure 3.15 (d) upper panel).

The nucleus position with respect to the pattern features (lines or circles) was quantified using ImageJ. Using the *redirect* tool of this program we computed the

correlation between the nuclei intensity images and the binary images of the micropatterns. The result was the red area showed in the scheme of Figure 3.15 (d), lower panel. The red area allowed us to define the nucleus position index between 0 and 1 quantifying how much the nucleus overlapped on the line. For a nucleus on a non-patterned area, the nucleus position index is 0.

3.7.3 Analysis of crypt- and villus-like domains on the micropatterned substrates

2-dimensional (2D) monolayers of organoid-derived single cells were organized in proliferative regions (crypt-like domains) and non-proliferative areas (villus-like domains)^{119,120}. To define these domains, we developed a method to identify, segment and characterize them on non-patterned and micropatterned substrates based on the projected cell areas. Fluorescence images were employed.

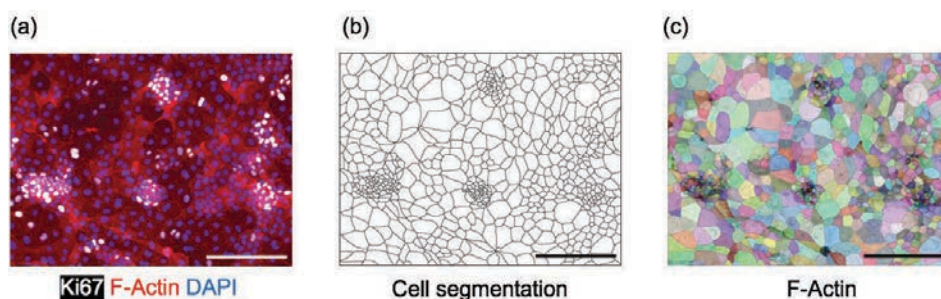


Figure 3.16. Representative images of organoid-derived single cell monolayer segmentation process. (a) Immunofluorescence image of the epithelial monolayer stained for proliferative cells (Ki67), F-Actin and cell nuclei (DAPI). Scale bar: 200 μm . (b) Representative figure of the cell segmentation process. Scale bar: 200 μm . (c) Each of the cells were labelled with a color code and overlaid with the F-Actin images. Scale bar: 200 μm .

The area of each cell was first identified by the segmentation of the cell monolayers (Figure 3.16). F-actin fluorescence images were pre-processed with ImageJ, as previously described¹⁴⁵. Briefly, the background noise of the F-actin images was reduced with the *subtract background* function by using a rolling ball radius of 10 μm . The resulting images were then subjected to a band-pass filter with upper and lower limits of 15 μm and 1 μm , respectively. The band-pass filter corrects for uneven illumination by removing the high-frequency component from the image and mitigates the effect of fibers, noise, and/or other features than cells by removing low-frequency components. The background noise from this output was reduced by using the *subtract background* command again with a rolling ball radius of 10 μm . The F-actin pre-processed images from each experiment were then loaded to Tissue analyzer¹⁴⁶ for edge detection and 2D monolayer segmentation (Figure 3.16 (b-c)). The segmented 2D monolayer images were then used to quantify various parameters such as cell area, and cell centroid positions (x, y).

2D cell area contour maps were performed using a custom-made code in Matlab (code available upon request) using the cell area, and cell centroid positions obtained from the segmented 2D monolayers (Figure 3.17 (a)). The contour map is represented in logarithmic scale to enhance visualization. To identify crypt-like domains, the cell area contour maps were correlated with the segmented epithelial cell marker Ki67 images (Ki67 stains positive for proliferative cells) (Figure 3.17 (b)). For the Ki67 segmentation, we followed the protocol described in section 3.5.4. To identify villus-like domains, the cell area contour maps were correlated with the inverted of the segmented Ki67 images. From these two correlations, the distributions of the crypt- and villus-like domains were plotted (Figure 3.17 (c)). These distributions were fitted with two independent Gaussian functions (see equation [1]) and were characterized by their mean values and standard deviations (SD): $mean_area_{Ki67+}$ and SD_area_{Ki67+} , respectively.

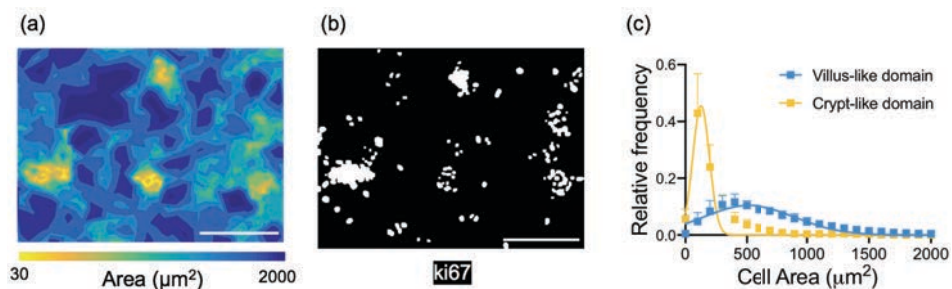


Figure 3.17. Representative images to describe the correlation between crypt- and villus-like domains with cell areas. (a) Cell area contour map. Scale bar: 200 μm . (b) Binary image from the thresholded fluorescence image of proliferative cells (Ki67). Scale bar: 200 μm . (c) Cell area distributions in the crypt- and villus-like domains. The symbols correspond to the experimental measurements, and the solid lines are the fitting of the data using a Gaussian function. Mean \pm SEM. N = 4 experiments.

Cells areas ($mean_area_{Ki67+} + SD_area_{Ki67+}$) below threshold were counted as proliferative cells. These proliferative cells generate a binary image with proliferative domains. In addition, we imposed that the area of a proliferative domain should be above $10mean_area_{Ki67+}$ threshold to be considered as a crypt-like domain (Figure 3.18 (a)). Binary crypt-like domain images were treated as single object images (Figure 3.18 (b)). So, from them, we extracted the area, (x, y) centroid position, elongation index, orientation index and solidity of the crypt-like domains to define their morphology (parameters described in section 3.5.4).

The organization of crypt-like domains with respect to the biochemical micropatterns was analyzed with 2-dimensional (2D) Bravais lattice parameters. These are defined in crystallography as lattices which fill all the space without gaps. The parameters used to characterize the lattice were the primitive lattice vectors first-neighbor (a) and second-neighbor (b), and the angle in between ($\theta = \cos^{-1}(\mathbf{a} \cdot \mathbf{b}/|\mathbf{a}| \cdot |\mathbf{b}|)$). Binary images of crypt-like domains and the patterns

were used for these analyses. These were processed using ImageJ to extract the centroid position (x, y) of each crypt-like domain and each micropattern. These coordinates were used to determine the distance between first- and second-neighbors (a and b) and the angle in between (θ) (Figure 3.18 (a-b)) by using a custom-made code in Matlab (code available upon request). The angle was represented as $\cos(2\alpha)$, where α is the angle between first- and second-neighbors minus the angle of the pattern (Figure 3.18 (c)). Thus, the orientation index has a value between -1 and 1. The orientation index has a maximum value of 1 for crypt-like domains perfectly aligned with the pattern, it has an average value of 0 if the crypt-like domains are randomly oriented, and it has a minimum value of -1 for crypt-like domains with their first- and second-neighbors forming a skinny triangle.

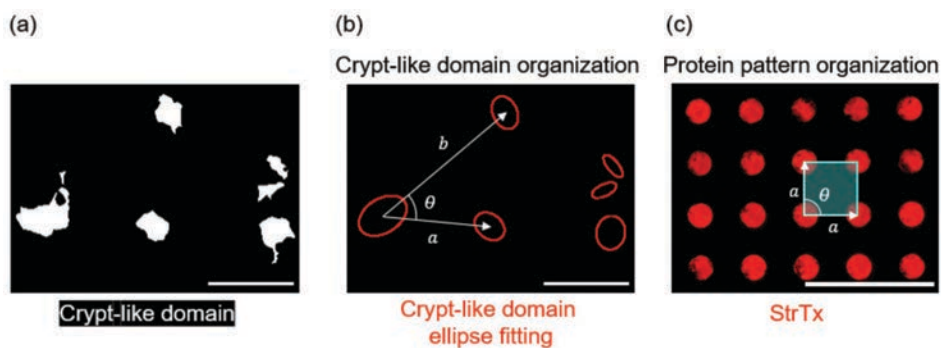


Figure 3.18. Representative images to describe the analysis of the organization of crypt-like domains. (a) Binary image from a thresholded cell area contour map. Scale bar: 200 μm . (b) Ellipse fitting of the crypt-like domains and representative parameters to define their organization: interdomain spacing (a) and angle (θ). Scale bar: 200 μm . (c) Representative protein pattern from design (2). Streptavidin Texas Red (StrTx Red) stamped on glass with their lattice (cyan). The protein pattern was organized in square Bravais lattice and the representative parameters of the lattice were: interdomain space ($a = 200, 300$ or $400 \mu\text{m}$) and angle ($\theta = 90^\circ$). Scale bar: 500 μm .

3.8 Statistical Analysis

Statistical analysis was done using GraphPad Prism software (GraphPad Software Inc.). Results are presented as mean \pm standard deviation (SD) or as mean \pm standard error of the mean (SEM). The number of experiments from which data were extracted is specified in each case. Normality of the datasets was tested by the d'Agostino-Pearson normality test. Statistical differences were analyzed by t-test or ANOVA test (Gaussian distribution) and Mann-Whitney test (non-Gaussian distribution). A p-value smaller than 0.05 was considered as statistically significant: (*) $p < 0.05$, (**) $p < 0.01$ and (***) $p < 0.001$.

4 Results

4.1 Effects of cell-extracellular matrix interactions on the self-organization of organoid-derived intestinal monolayers

Understanding epithelial cell organization is of fundamental importance for several physiological and pathological processes such as tissue homeostasis, regeneration and cancer^{1,2}. Intestinal epithelial cells self-organize into 3-dimensional (3D) organoids that recapitulate the structural and functional characteristics of the tissue *in vivo* when embedded within a 3D cell-derived protein mixture (Matrigel)³. However, these very same cells self-organize into 2-dimensional (2D) intestinal epithelial monolayers that also recapitulate the *in vivo*-like cell type composition and organization when seeded on thin layers of the same cell-derived protein mixture^{4,5}. In general, and as described in the introductory chapter of this thesis, changes in epithelial cell organization are characterized by a cross-talk between cell-extracellular matrix and cell-cell interactions⁶. However, the dynamics of this process and the role of the dimensionality imposed by the matrix, and its protein composition and concentration in the cellular complex self-organization process is not fully understood. To explore this subject constitutes one of the objectives of this thesis, and the experiments and the results obtained toward this goal are described in this section.

4.1.1 Intestinal organoid-derived single cells self-organize in 3D-tubular networks that transit to 2D-monolayers on Matrigel thin films

It has been reported that intestinal organoid-derived crypts can form two-dimensional (2D) epithelial monolayers when cultured on substrates coated with Matrigel or collagen^{102,114,116,119,120}. On the other hand, it has been reported that *Lgr5*⁺ single cells are able to form organoids with all intestinal epithelial cell types when cultured within Matrigel drops⁶⁶. Therefore, we were wondering whether organoid-derived single cells would also be able to form 2D monolayers or if crypt pieces would be needed for that purpose. To answer this question, we cultured intestinal organoid-derived single cells on Matrigel thin films. Intestinal organoids derived from *Lgr5-EGFP-IRES-creERT2* mice, which express GFP under the *Lgr5* promoter, were digested using a harsh digestion protocol to obtain single cells. These single cells were then seeded on top of Matrigel thin films at 10 mg mL⁻¹ Matrigel concentration and we followed their culture over time.

We then observed that indeed single cells were able to form 2D epithelial monolayers after 96 hours of cell culture. These results, that we have already published, revealed the intrinsic capacity of the intestinal epithelium to self-

organize and form monolayers with *in vivo*-like domains when grown on Matrigel thin films^{119,120}. However, we also observed that, before the monolayers were formed, single cells were able to self-organize in transient structures which resembled networks of 3D tubular-like structures at 24 hours of culture (Figure 4.1.1 (a and b)). At this time point, Lgr5⁺ intestinal stem cells (ISCs) (GFP⁺ cells) appeared homogeneously distributed along these tubular-like structures (Figure 4.1.1 (b), upper left panel). Later (48 hours, Figure 4.1.1 (b), upper right panel), the tubular structures appeared to flatten and Lgr5⁺ ISCs clustered and rearranged in budding formations that are reminiscent of the 3D crypt-like domains observed in organoids and that closely mimic the *in vivo* stem cell arrangement at the crypt bases (Figure 4.1.1 (b), inset). At 72 and 96 hours of culture, GFP⁻ cells spread out and migrated, generating epithelial monolayers composed of crypt- and villus-like domains (Figure 4.1.1 (b), lower panels). This process of monolayer formation and the transient structures formed could be quantitatively followed over time by evaluating the projected area effectively occupied by the cells, that we called surface coverage. Surface coverage was obtained from the binary images of F-actin staining (Figure 4.1.1 (c)). Our results show that surface coverage percentage increased significantly with time until confluent monolayers were formed (surface coverage ~ 100%) (Figure 4.1.1 (d)).

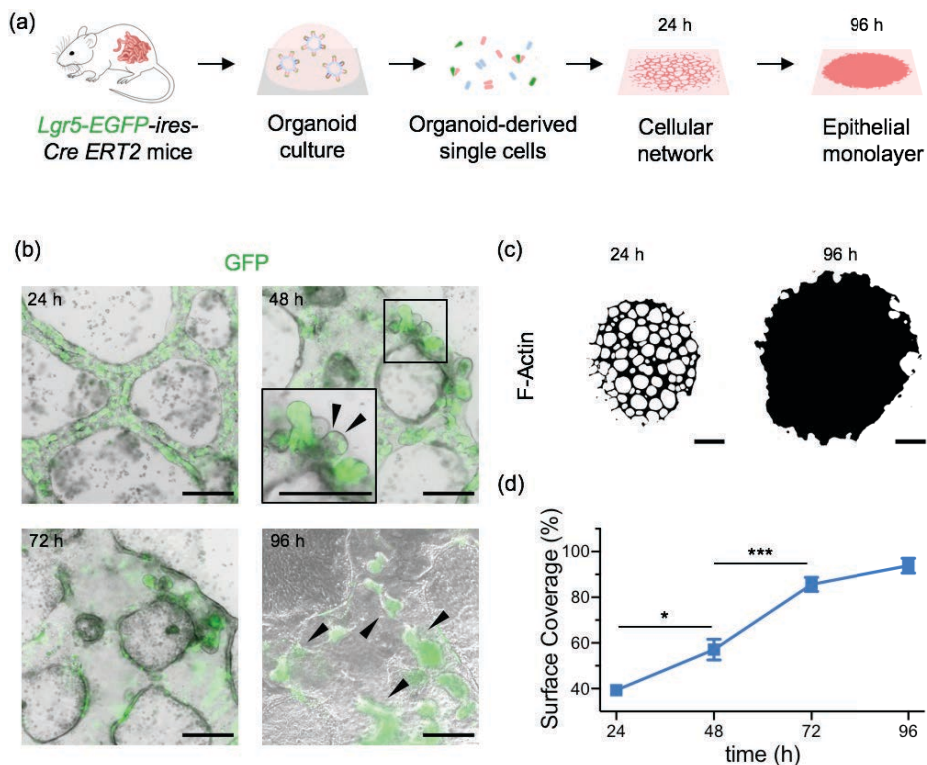


Figure 4.1.1. (a) Scheme depicting the formation of epithelial monolayers and transient cellular network structures from the culture of organoid-derived single cells on thin films of Matrigel deposited at a concentration of 10 mg mL⁻¹. (b) Representative snapshots of a 96 hours time-frame microscopy experiment overlapping bright field and GFP fluorescence signals. The corresponding time for each snapshot is shown in each panel. Black arrowheads indicate Lgr5-GFP⁺ cells. Scale bars: 200 μ m. (c) Representative binary images from thresholded fluorescence images of F-Actin for organoid-derived single cell cultures after 24 or 96 hours on Matrigel at 10 mg mL⁻¹. Scale bars: 1 mm. (d) Surface coverage percentage (with respect to the total surface area) as a function of culture time for organoid-derived single cell cultures. Values are reported as the mean \pm SEM. (*) $p < 0.05$, (***) $p < 0.001$, t-test. $N \geq 3$ experiments.

From these experiments, it was evident that, even when organoid-derived cells were cultured as single cells and constrained to planar surfaces, they were able to rearrange and generate 3D tubular network structures before transiting to 2D monolayers. Remarkably, these 3D structures were formed when employing substrates coated with thin layers of Matrigel at a high concentration (10 mg mL⁻¹), the same that is used when cultured these cells in Matrigel drops. Therefore, in our system cells have the ability to generate 3D structures irrespective of the matrix dimensionality (2D or 3D). We then took advantage of this property, which facilitates the analysis, to investigate the role of cell-matrix interactions in the cell self-organization process. As a first step, we explored how cells organized when changing the concentration of the protein matrix.

4.1.2 *Intestinal organoid-derived single cells organization presents a wetting phase transition depending on Matrigel concentration*

It is known that epithelial cells *in vivo* can form 3D complex structures such as invaginations, evaginations, spherical cysts or tubules. To decouple the role of dimensionality from other factors governing the complex process of cell self-organization such as matrix composition and/or protein concentration is not an easy task. In our system, due to the ability of organoid-derived single cells to generate 3D structures on thin layers of Matrigel, we could remove the role of dimensionality and at the same time, tune different parameters affecting the matrix. Therefore, we decided to examine whether ECM-coating concentration would affect intestinal epithelial cells organization. To investigate this, intestinal organoid-derived single cells were cultured on deposited thin films of different concentrations of Matrigel.

Fluorescence microscopy images showed that on low concentrated Matrigel thin films (3 mg mL⁻¹), single cells rapidly self-organized in 2D intestinal monolayers only after 24 hours of culture, and this organization remained constant over the culture time (Figure 4.1.2, left panels). This was a very different outcome that the one previously described for these very same cells cultured on high concentrated Matrigel thin films (10 mg mL⁻¹) or on Matrigel drops. In both cases, 3D tubular-like and 3D spherical aggregate structures, respectively, were formed after 24 hours of culture (Figure 4.1.2, upper row, middle and right panels). Later on, these 3D

structures transitioned to 2D monolayers or mature 3D organoids (Figure 4.1.2, lower row, middle and right panels).

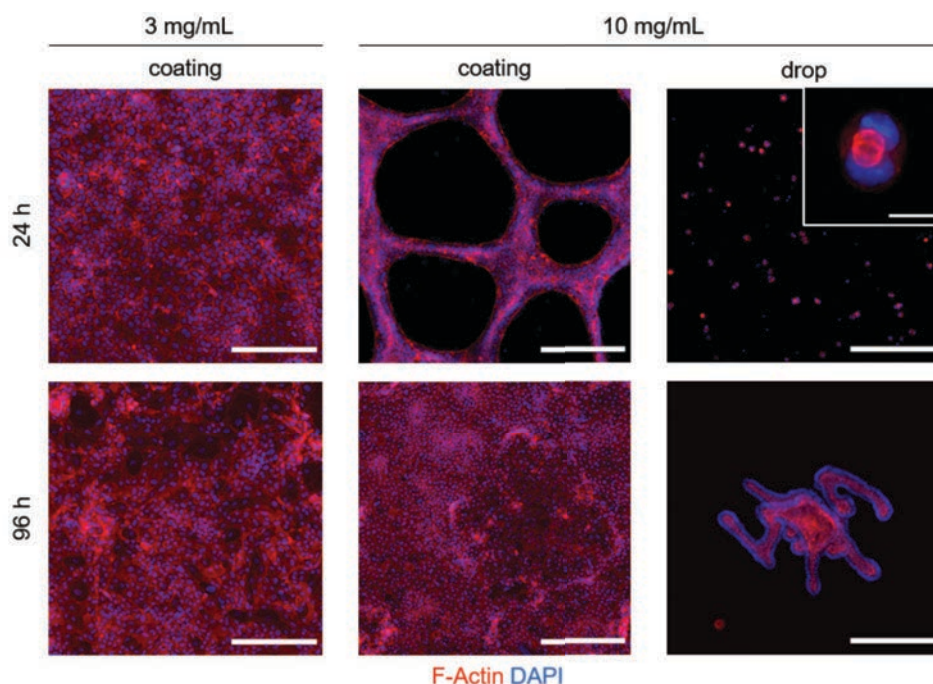


Figure 4.1.2. Confocal representative sum intensity fluorescence images of F-Actin and cell nuclei (DAPI) for organoid-derived single cells culture forming: monolayer on Matrigel thin films with 3 mg mL^{-1} (left panel), network on Matrigel thin films with 10 mg mL^{-1} (middle panel), or organoid embedded on Matrigel with 10 mg mL^{-1} (left panel). After 24 hours (upper panel) or 96 hours (lower panel). Scale bars: $200 \mu\text{m}$, zoom $10 \mu\text{m}$.

We then performed experiments screening for cell organization at 24 hours of culture within a broad range (from 1 to 10 mg mL^{-1}) of Matrigel concentrations. We consistently observed the same result: depending on the matrix concentration, fully packed monolayers or cellular networks were obtained (Figure 4.1.3 (a)). For a very narrow concentration range (from 4 to 5 mg mL^{-1}), both structures were coexisting simultaneously (Figure 4.1.3 (b)). The projected area images of F-actin were employed to evaluate the surface coverage, which is plotted as a percentage of the total cell seeding area as a function of the concentration (Figure 4.1.3 (b-c)). The experimental data, to which a sigmoidal function could be fitted, could be interpreted as a transition between two clearly distinct phases, monolayers (surface coverage $\sim 100\%$) and networks (surface coverage $\sim 45\%$). These two phases, monolayers and networks, were observed to form below threshold concentrations of 3 mg mL^{-1} and above threshold concentrations of 6 mg mL^{-1} , respectively. There was also an intermediate state where both organizations coexist at the same time (4 and 5 mg mL^{-1}). Given the behavior of cells as active soft matter, it has been proposed

that their organization on a substrate could be studied using the same formalism as in a fluid wetting problem^{56,58-61,63}. With this analogy, the so-called tissue spreading parameter S could be determined by considering the balance between the energies encoded for cell-cell (W_{cc}) and cell-substrate (W_{cs}) adhesion, in such a way that $S = W_{cs} - W_{cc}$. This parameter changes its sign at the wetting transition that separates tissue spreading ($S > 0$, wetting) from retraction ($S < 0$, de-wetting). In terms of this wetting analogy, we propose to attribute the two phases found in the tissue organization in our experiments to a complete-to-partial wetting transition from monolayers ($S > 0$, Matrigel concentration $\leq 3 \text{ mg mL}^{-1}$) to 3D structures ($S < 0$, Matrigel concentration $> 5 \text{ mg mL}^{-1}$) induced by Matrigel concentration.

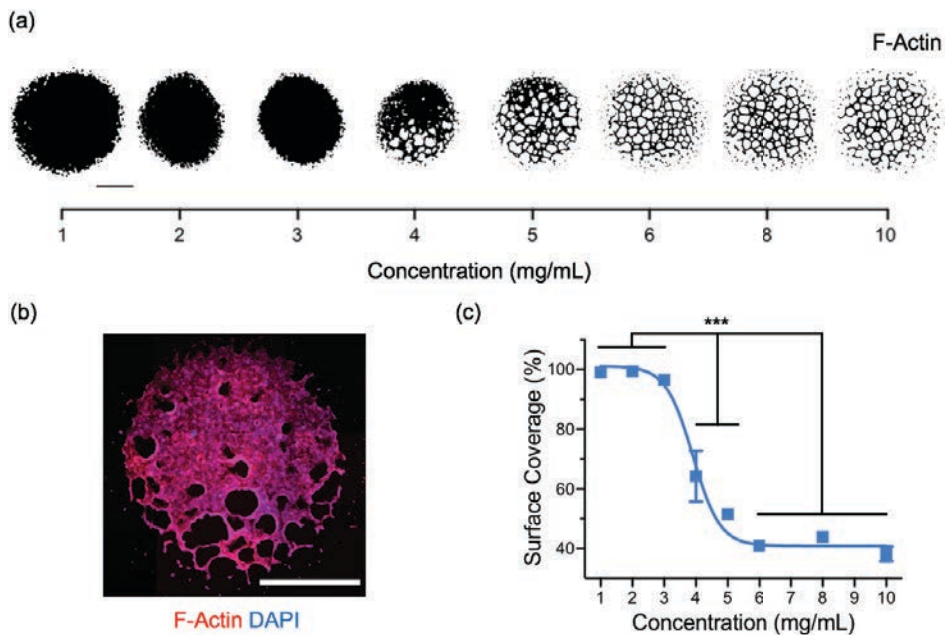


Figure 4.1.3. (a) Representative binary images from thresholded fluorescence microscopy pictures of F-Actin for organoid-derived single cells cultured on substrates coated with Matrigel at different concentrations after 24 hours of culture. Scale bar: 2 mm. (b) Representative fluorescence image of F-Actin and cell nuclei (DAPI) for organoid-derived single cells forming co-existing monolayer and network cultured on 4 mg mL^{-1} Matrigel thin films after 24 hours. Scale bar: 2 mm. (c) Surface coverage percentage of the cultures (with respect to the total seeded surface area) as a function of Matrigel concentration. The symbols correspond to the experimental measurements. The line represents the fitting performed using a sigmoidal function. Values are plotted as the mean \pm SEM. (***) $p < 0.001$, t-test. $N \geq 3$ experiments.

At this point, we were wondering if by changing the Matrigel concentration we were affecting the thickness of the thin film deposited on the substrate, therefore introducing this variable in the system. To interrogate this issue, Matrigel thin films produced at low and high concentrations were visualized by immunofluorescence using laminin antibodies. We decided to use 3 mg mL^{-1} of Matrigel concentration as representative of low concentrations, where cells organize in monolayers, and 10

mg mL⁻¹ of Matrigel concentration as representative of high concentrations, where cells organize in networks. Representative images, shown in Figure 4.1.4 (a) revealed that protein surface density and distribution depend on Matrigel concentration (Figure 4.1.4 (b)). However, image cross-sections showed that thickness of the films was maintained regardless of Matrigel concentration (Figure 4.1.4 (c)). On the basis of these results, we attributed the wetting phase transition of cells on Matrigel-coated surfaces to the differences in protein surface density.

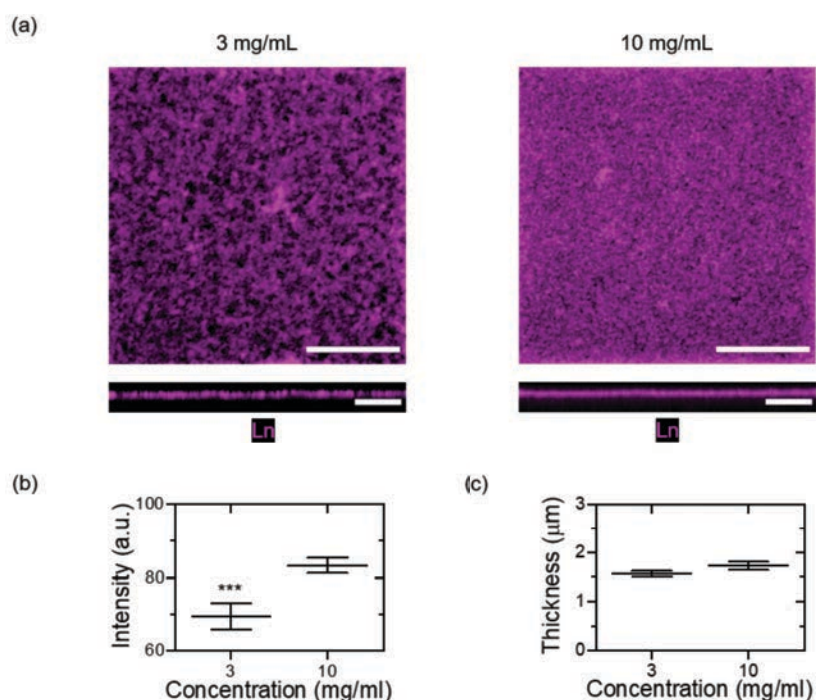


Figure 4.1.4. Characterization of Matrigel-coated substrates varying Matrigel concentration. (a) Immunofluorescence confocal microscopy maximum intensity projections for laminin at Matrigel concentrations of 3 and 10 mg mL⁻¹ (upper row) and corresponding cross-sections. Scale bars xy: 20 µm. Scalebars xz: 10 µm. (b) Average fluorescence intensity of laminin over the surfaces. Mean ± SEM. (***) $p < 0.001$, t-test. N = 3 experiments. (c) Matrigel thicknesses for the two concentrations tested. Mean ± SEM. N = 3 experiments.

4.1.3 Epithelial cell polarity depends on Matrigel concentration

A hallmark of epithelial cell organization is cell polarity⁴⁵. Apico-basal polarization of epithelial cells involves cell morphological and functional changes, hence the structural organization and orientation of the cytoskeleton¹³. Accumulation of the F-actin at the apical side can be used to define cell polarity for the cells cultured for 24 hours at low (3 mg mL⁻¹) and high (10 mg mL⁻¹) Matrigel concentrations. For cells forming monolayers onto Matrigel-coated substrates at low concentration, the actin

intensity distribution demonstrated that cells were polarized with the apical surface exposed to the medium (lumen) while the basal surface faced the Matrigel (ECM) (Figure 4.1.5, left panels). However, when employing highly concentrated Matrigel, regardless of as coatings (Figure 4.1.5, middle panels) or as drops (Figure 4.1.5, right panels), the 3D structures formed exhibited a basal-out polarity. In agreement with the literature, cell spheroids cultured within the 3D Matrigel drops developed inner luminal cavities and faced their apical sides towards them, while their basal sides were in contact with the extracellular matrix. Interestingly, cells organized in tubular structures also formed an inner lumen and were polarized with the apical side towards this lumen even though they were seeded on 2D Matrigel thin layers. Overall, from these set of experiments we concluded that on Matrigel-coated surfaces, Matrigel concentration induced a transient state in which a phase transition in the intestinal epithelial phenotype was identified. Organoid-derived single cells self-organized on monolayers or 3D-tubular networks with inner lumens. Cells in monolayers showed luminal apical polarization, while this was reverted in the tubules, with the cell apical side facing the newly created lumens similar to cells embedded in 3D matrices.

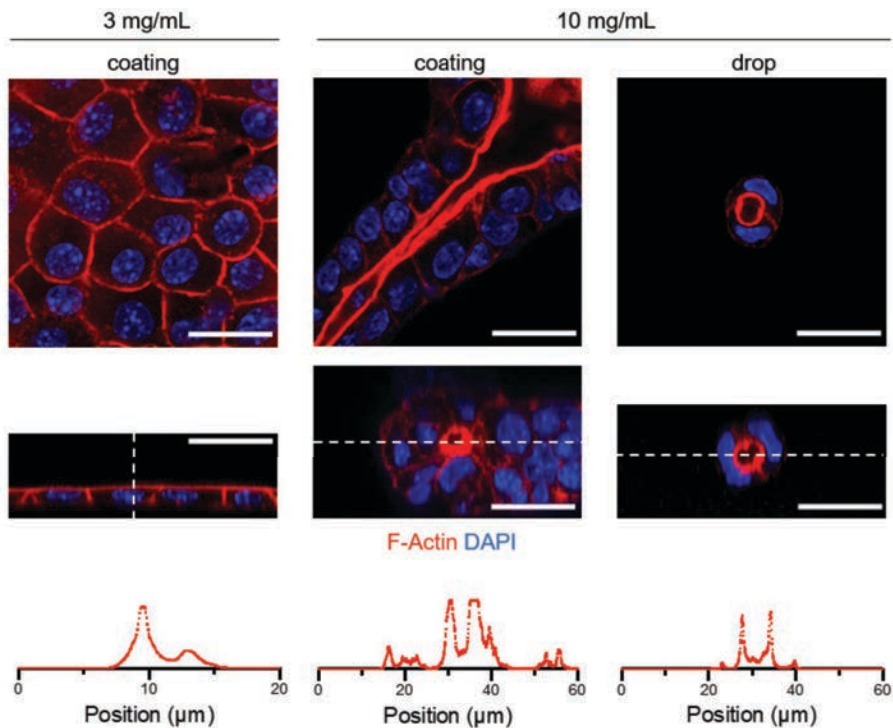


Figure 4.1.5. Confocal microscopy images of representative middle z-stacks (upper row) and orthogonal cross-sections (lower row) of cells cultured on Matrigel-coated surfaces at 3 and 10 mg mL⁻¹ and Matrigel drops at 10 mg mL⁻¹, all stained for F-Actin and cell nuclei (DAPI). The graphs plot the F-Actin intensity (arbitrary units) along the white dashed line of the orthogonal cross-sections. Scale bars: 20 μm.

4.1.4 Epithelial tubular networks have well-defined geometrical properties

We have seen that Matrigel concentration induces a phenomenon that can be described as a wetting phase transition in the intestinal epithelium organization. As a next step, we were interested in exploring the organization of the tubular networks formed on high concentrations of Matrigel, as those recapitulated some features of 3D organoid structures such as the presence of an inner lumen and apical cell polarity, but on 2D substrates. At a first glance, these structures are similar to soap foams^{49,50,138}, de-wetted collagen networks^{52,138}, or de-wetted polystyrene networks^{51,138}, whose morphology has been extensively studied by applying mathematical methods of stochastic geometry. To specifically evaluate whether such tubular networks could also be described with well-defined properties, we analyzed their geometrical properties following the wetting formalism described for other systems.

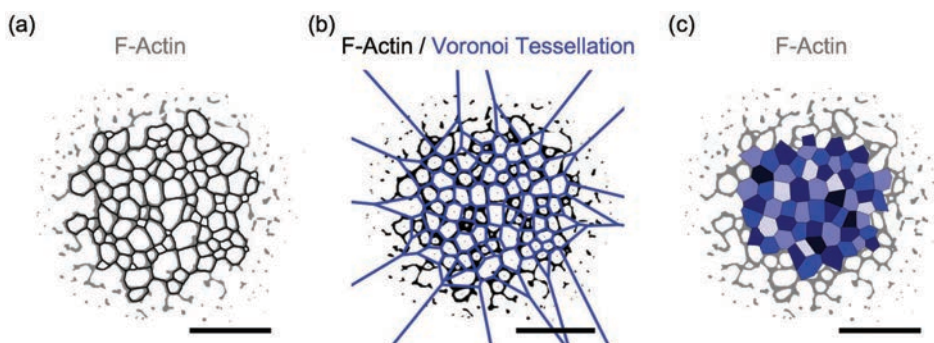


Figure 4.1.6. (a) Representative image overlaying the binary image of the projected surface intensity for F-Actin (in grey) and its segmentation (in black) obtained by using the Voronoi function from ImageJ. Scale bar: 2 mm. (b) Representative image overlaying the binary image of the projected surface intensity for F-Actin (in black) and its segmentation (in blue) obtained by using the Voronoi function from Matlab. Scale bar: 2 mm. (c) Representative image overlaying the binary image of the projected surface intensity for F-Actin (in grey) with the resulting Voronoi polygons after filtering the Voronoi network. Scale bar: 2 mm.

We decided to work with the tubular networks formed on Matrigel when deposited in concentrations ranging from 4 to 10 mg mL⁻¹. By applying segmentation processes to the projected surface images of F-actin, we could assess that the tubular networks were forming polygons distributed according to a Voronoi tessellation (Figures 4.1.6 and 3.16). Voronoi polygons were mostly composed by regular hexagons, as demonstrated by the narrow distributions computed for their number of edges (centered at 6, Figure 4.1.7 (a)) and their edge angles (centered at 120°, Figure 4.1.7 (b)). The distributions of these two parameters were not statistically significant different when varying the Matrigel concentration within the range studied. Networks co-existing with monolayers were slightly different in area and edge size of the polygons (Figure 4.1.7 (c-d)). However, in the network phase, we found no differences. Interestingly, the mean edge size of the polygons of the

network phase ($\sim 200 \mu\text{m}$) is comparable with the *in vivo* dimensions of intestinal crypts¹⁴⁷. It has been reported that in de-wetted collagen networks, rod-collagen monomers are aggregated at the rims of the polygons stabilizing their structure. The length of the collagen monomers is comparable to the characteristic diameter of the pores and it is assumed that the mechanical strength provided by the interaction of the molecules compensates the capillary forces that want to break the rims^{52,148}. In our system, we speculate that a similar phenomenon might be happening, and the stability of the structures might be provided by the cell-cell interactions happening at the 3D tubular structures forming the rims of the polygons.

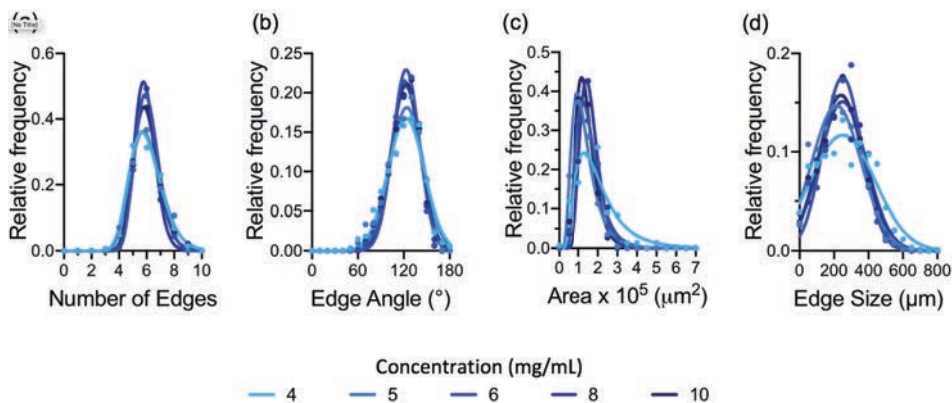


Figure 4.1.7. Frequency distributions of the parameters selected to describe the geometry of the Voronoi polymers formed upon culturing organoid-derived single cells for 24 hours onto Matrigel-coated surfaces with concentrations ranging from 4 to 10 mg mL^{-1} : (a) polymer edge number, (b) polymer edge angle, (c) polymer area and (d) polymer edge size. The dots correspond to histograms of the experimental data. The lines correspond to Gaussian fittings for (a) and (b) and Lognormal fittings for (c) and (d). $N \geq 3$ experiments with $n > 30$ polygons each.

Next, we analyzed the order in the tubular networks by computing the second moment of the distributions of the various geometrical parameters obtained for the Voronoi pattern, following a procedure previously described^{52,138}. In particular, we computed the second moment of the distribution of the number of polygon edges, μ_2^n , for the structures formed at different Matrigel concentrations (Table 4.1.1). The value of this parameter is 0 for a structure entirely formed by hexagons and increases as the system escapes of this perfect structural arrangement. We can observe that, on one side, values are higher than those expected for lattices only composed by hexagons. On the other side, we can also see that μ_2^n maximum occurs for concentrations where both monolayer and tubular organizations coexist (4 and 5 mg mL^{-1}). Then, networks present overall more geometrical disorder for these intermediate states, while the order is increased for the single-phase samples.

Concentration (mg/mL)	4	5	6	8	10
μ_2^n	4.4	4.5	2.7	3.2	3.5

Table 4.1.1. Comparison of the second moments of the distributions obtained for the number of edges of Voronoi polygons formed by organoid-derived single cells seeded on Matrigel thin films at 4, 5, 6, 8 and 10 mg mL⁻¹ Matrigel concentrations. μ_2^n values are provided as non-normalized parameters.

In addition, the second moment of the area (μ_2^a) and edge angle (μ_2^β) distributions provide information about the homogeneity in the size of the polygonal structures formed and about their regular hexagonal shape. These parameters were computed for the tubular networks formed onto Matrigel-coated surfaces taking into account all the concentrations. The obtained results were compared with the same parameters reported in literature for different experimental systems also yielding similar geometrical structures (see Table 4.1.2).

	Organoid-derived single cells	Collagen ^{52,138}	Polystyrene ¹³⁸	Soap foams ^{52,138}
μ_2^n	3.7 ± 0.3	2 – 5	~2	~1.4
μ_2^a	0.15 ± 0.02	0.4 – 1.5	~0.3	0.4 – 1.2
μ_2^β	0.028 ± 0.004	0.05 – 0.07	0.03 – 0.05	~0.015

Table 4.1.2. Comparison of the second moments of the distributions obtained for the number of edges, area and edge angles of Voronoi polygons formed by of organoid-derived single cells seeded on Matrigel thin films at a concentration of 10 mg mL⁻¹ (Mean \pm SEM), de-wetted collagen networks, de-wetted polystyrene networks and soap foams.

We can see that regarding the lattice of polygons formed, the order of our cellular networks is close to the order shown by protein collagen networks, and both systems are more disordered than synthetic polymer (polystyrene) networks or soap foams. On the other hand, both the second moments of the area and edge angle distributions are smaller for the tubular networks formed by organoid-derived single cells than for any of the other systems listed in the table. It has been reported that the formation of Voronoi tessellation-like networks is related to de-wetting processes that occur almost simultaneously across large areas. In systems such as soap foams or collagen networks, such process is driven by the evaporation rate of the solvent, which drags the molecules in a passive manner. In our system, however, we hypothesize that the formation of such tubular networks might be related to the active migration of the cells that form the structures.

4.1.5 Cell migration depends on Matrigel concentration and drives the formation of tubular networks

With the results we obtained so far, we were wondering if (i) tubular networks were only able to form on high Matrigel concentrations or if they were also formed at earlier times on low Matrigel concentrations, and if (ii) the formation of tubular networks was related to the active migration of cells resulting in these structures. To gain insight into these questions, we performed time-lapse experiments following the cell cultures from the moment of seeding ($t = 0$) until the moment when network structures were observed ($t = 840$ min). For these experiments, we used organoid-derived single cells seeded on Matrigel at 3 mg mL^{-1} , as representative low Matrigel concentration, and at 10 mg mL^{-1} , as representative of high Matrigel concentration. We then took advantage of the genetically modified mouse model to track the movement of Lgr5^+ intestinal stem cells (ISCs) marked with the green fluorescence signal (GFP^+ cells).

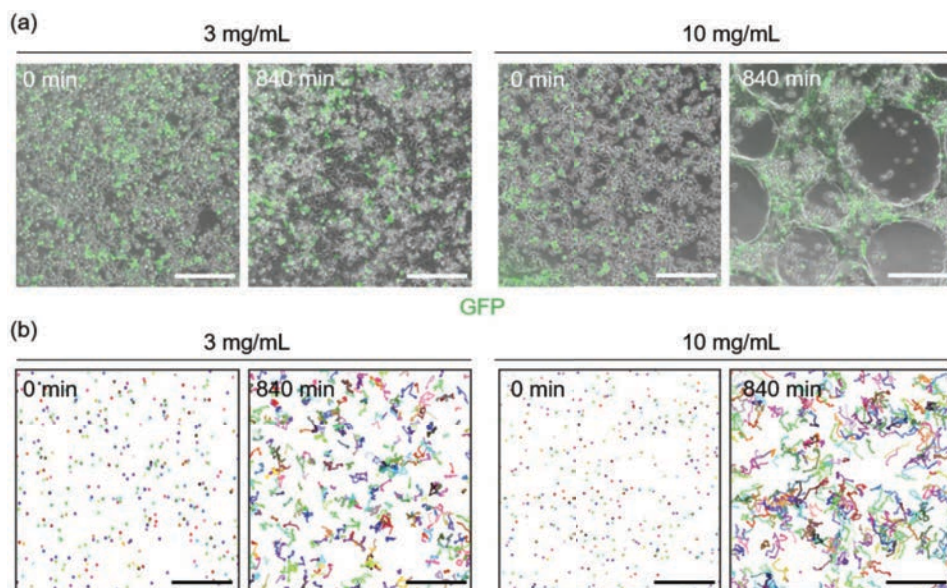


Figure 4.1.8. (a) Representative snapshots of time-lapse experiments performed with organoid-derived single cells onto substrates coated with two representative Matrigel concentrations (3 and 10 mg mL^{-1}). Images at the seeding time ($t = 0$) and after 840 min of culture are shown. Phase contrast images are overlapped with the channel of GFP signal. Scale bars: $200 \mu\text{m}$. (b) GFP^+ cell initial positions ($t = 0$) and trajectories for the time-lapse experiments depicted in (a). Scale bars: $200 \mu\text{m}$.

We could notice that, immediately after seeding, stem cells showed a random distribution on both low and high Matrigel concentration substrates (Figure 4.1.8). However, after 14 hours of culture, cells formed a fully packed monolayer on the low concentrated Matrigel coatings without going into any distinctive transient phase. Meanwhile, by the same time, cells at high Matrigel concentrations self-arranged

forming large circular holes surrounded by cells that were being accumulated at the rims of the structures. When following the single stem cells trajectories along this timeframe for the different conditions, we found remarkable differences. In particular, stem cells trajectories were visibly much shorter for samples of low Matrigel concentration than for samples of high Matrigel concentration (Figure 4.1.8 (b)).

To get quantitative data about stem cells migration, their mean-square displacements (MSDs) were computed and plotted against cell culture time (Figure 4.1.9 (a)). The values obtained for the MSDs on the high Matrigel concentration samples almost doubled those obtained for the cells seeded on low Matrigel concentrations, therefore confirming the dependence of cell mobility with surface protein density. In addition, while cells' displacement with cell culture time showed a constant slope on low concentrations of Matrigel, a biphasic behavior could be identified for the cells cultured on high ECM concentrations. Both curves were fitted by single exponential functions with time ($\text{MSD} \propto t^\alpha$) and α fitting parameters were obtained and compared. For the stem cells cultured on low Matrigel concentration substrates, a value of $\alpha \sim 0.8$ was obtained, corresponding to cells remaining confined inside a sub-volume from which they could not escape, performing a partially confined random movement (see section 3.5.6) (Figure 4.1.9 (a)). For cells cultured on high Matrigel concentrations, initially stem cells moved with a value of $\alpha \sim 1.1$, which corresponds to a directed motion towards a specific target. Later in time, these stem cells migrated with a value of $\alpha \sim 0.6$, performing a partially confined random movement. We attributed this biphasic behavior to stem cells becoming part of a cohesive cellular structure where cell-cell contacts might be becoming predominant as a consequence of the formation of cell aggregates at the rims of the holes formed. In these structures, cell movement would be restricted.

We analyzed the temporal correlation function (TCF) of stem cells velocities. For both organization processes, the TCF gradually decreased over time, but quicker on lower Matrigel concentration thin films (Figure 4.1.9 (b)). In this condition, cells lost the correlation of velocities early on, whereas for the formation of networks, the higher TCF values at the onset indicated that cell movements were persistent. Later, as cell movement became more confined, time correlation decreased to values similar to low Matrigel concentration thin films. As before, we attributed this behavior to stem cells becoming part of a structure. The different TCFs on low and high Matrigel concentration substrates suggest that cells on lower Matrigel concentration thin films arrive earlier to the equilibrium, i.e. the monolayer was formed faster than the network.

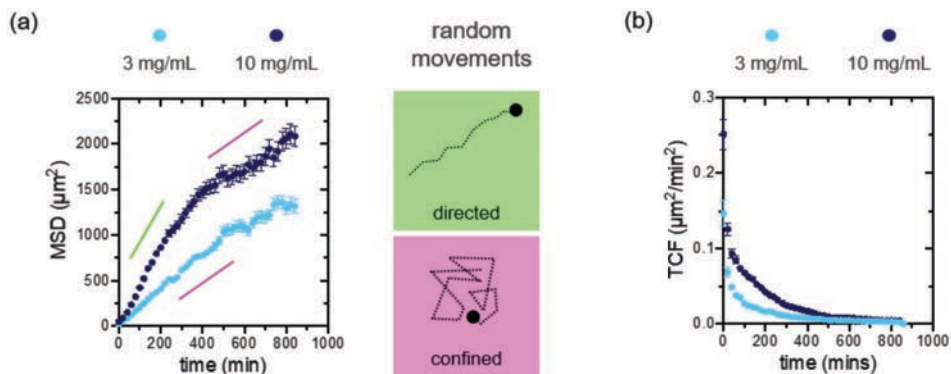


Figure 4.1.9. (a) GFP⁺ cell mean-square displacements (MSD) for organoid-derived single cells grown on Matrigel at 3 and 10 mg mL⁻¹ concentrations as a function of the culture time. The values are plotted as mean \pm SEM. N = 1 experiments, n = 3 different zones with > 250 stem cell trajectories analyzed per zone. Schemes illustrating the regions of the curves corresponding to directed cell movement (in green) and partially confined random movement (in pink). (b) Temporal correlation function (TCF) for the experiments described in (a). Mean \pm SEM. N = 1 experiments, n = 3 different zones with > 250 stem cell trajectories analyzed per zone.

4.1.6 Epithelial cell lines form transient 3D cell aggregates but not tubular networks on Matrigel thin films

We have reported that intestinal organoid-derived single cells self-organize in 3D-tubular networks that transit to 2D monolayers on Matrigel thin films at high Matrigel concentrations (> 4 mg mL⁻¹). Next, we were wondering whether the formation of such transient 3D structures is an intrinsic property of primary organoid-derived cells or if it is a feature shared with other epithelial cell types when cultured on the same type of substrates. To answer this question, we selected an intestinal epithelial cell line, Caco-2 cells, which form monolayers of mature enterocytes, and a kidney cell line, MDCK cells, which in 3D environments are able to self-organize forming 3D structures with inner lumens and tubular-like structures reminiscent of kidney tubules^{38,149–151}.

Both cell lines were seeded on top of Matrigel-coated substrates with high concentration (10 mg mL⁻¹) and cultured for 96 hours. Time-lapse microscopy experiments allowed to follow their growth over this time period. We found that, already at 24 hours of culture, both cell lines self-organized to form 3D cell aggregates that did not appear to significantly wet the substrate (Figure 4.1.10 (a)). Then, at 48 hours, these structures were visibly larger, started to flatten in some regions and cells started to sprout, partially wetting the surface and initiating the growth of epithelial monolayers (Figure 4.1.10 (a)). As time went by, the 3D cell aggregates were still distinguishable but flattened and surrounded by spreading cells forming growing monolayers wetting the substrate. When evaluating the final status of the epithelial monolayers by the surface coverage (projected surface area

of the structures) we found that this parameter increased significantly with time, reaching $\sim 70\%$ after 96 hours of culture (Figure 4.1.10 (b)). Noteworthy, at the same culture time, the surface coverage for the monolayers formed by the organoid-derived single cells was $\sim 100\%$. Thus, from these experiments, we could conclude that both the epithelial cell lines tested self-organized into transient 3D aggregates at highly concentrated Matrigel films (10 mg mL^{-1}) before progressing to epithelial monolayers. Interestingly, we could also identify in these cultures a partial to total wetting transition over the culture time, but not the formation of tubular networks, which appears to be an intrinsic property of primary organoid-derived single cells.

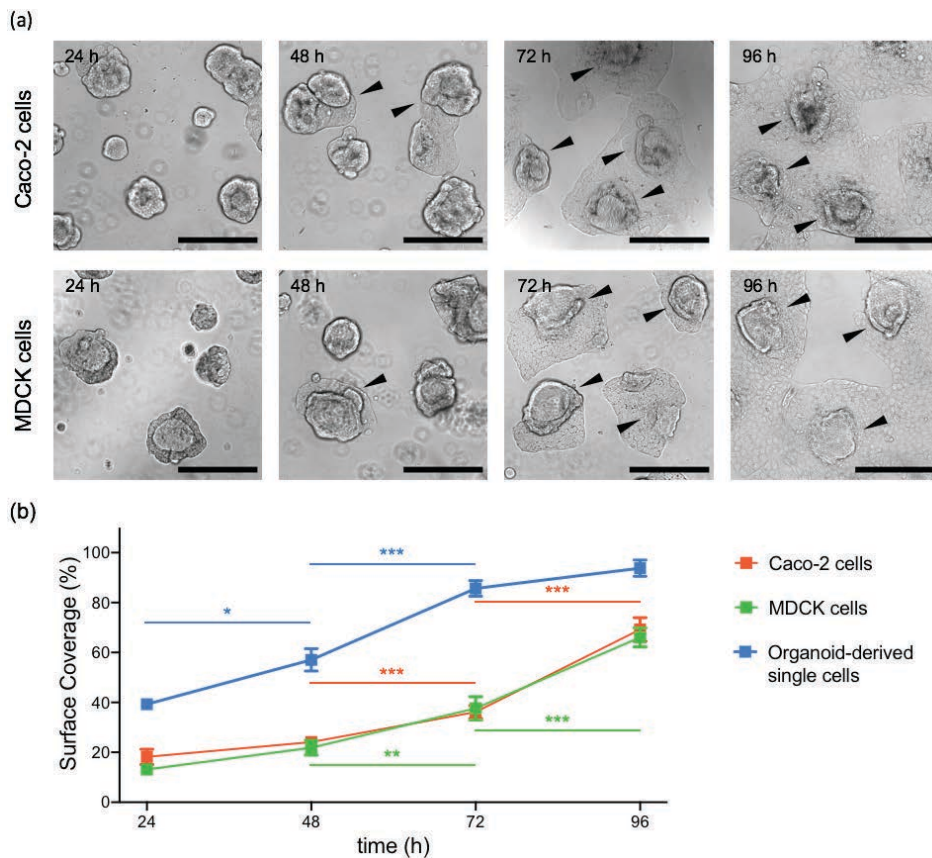


Figure 4.1.10. (a) Bright field snapshots of time-lapse microscopy experiments performed over 96 hours of culture after seeding Caco-2 and MDCK cells on Matrigel thin films at a concentration of 10 mg mL^{-1} . Black arrowheads indicate cells sprouting out from cellular aggregates. Scale bars: $200 \mu\text{m}$. (b) Percentage of surface coverage (with respect to the total surface area) as a function of the culture time for Caco-2, MDCK and organoid-derived single cells. Values are plotted as mean \pm SEM. (*) $p < 0.05$, (**) $p < 0.01$, (***) $p < 0.001$, t-test. $N \geq 3$ experiments.

4.1.7 Wetting phase transition in epithelial cell lines also depends on Matrigel concentration

Matrigel concentration induced a wetting phase transition in the organization of primary intestinal epithelial cells when cultured on Matrigel-coated surfaces. We also saw that epithelial cell lines could also form transient 3D structures when cultured on Matrigel at high concentration (10 mg mL^{-1}). Then, we investigated whether the formation of such transient structures in cell lines also depends on Matrigel concentration or if it is an intrinsic property of organoid-derived single cells growth.

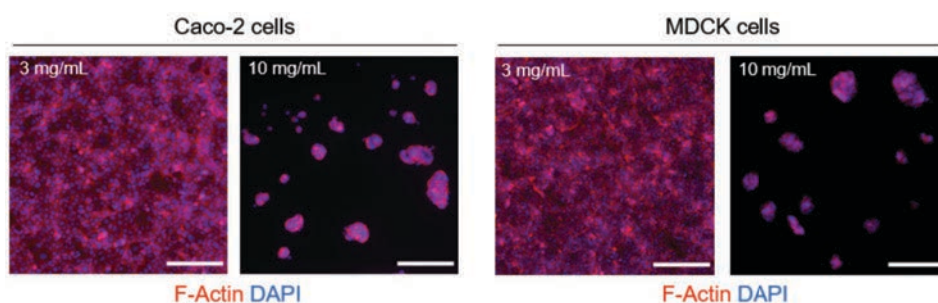


Figure 4.1.11. Representative sum intensity projection images obtained for F-Actin and cell nuclei (DAPI) after 24 hours of culture for Caco-2 cells (right panels) and MDCK cells (left panels). The corresponding Matrigel concentration for each image is shown in each panel. Scale bar: $200 \mu\text{m}$.

To investigate this, Caco-2 and MDCK cell lines were cultured on Matrigel thin films at different concentrations ranging from 1 to 10 mg mL^{-1} for 24 hours. Fluorescence microscopy images of F-actin and nuclei immunostaining showed that both cell lines at that time of culture self-organized in fully-grown monolayers when cultured onto Matrigel thin films at low concentrations (Figure 4.1.11, representative pictures at 3 mg mL^{-1}). However, these very same cells self-organized in 3D cellular aggregates when cultured on Matrigel thin films at high concentrations (Figure 4.1.11, representative pictures at 10 mg mL^{-1}). Therefore, analogously to what we had observed for the organoid-derived single cell cultures, cells organized as monolayers or 3D aggregates depending on Matrigel concentration. Then, to get a quantitative figure accounting for this effect, we evaluated the surface coverage as the projected surface area occupied by the cells according to the F-actin images (Figure 4.1.12 (a)). When plotting this parameter versus Matrigel concentration, we could clearly observe for both cell lines a sigmoidal dependence and identify two regions with an abrupt transition (Figure 4.1.12 (b)). Monolayers with surface coverage $> 80\%$ were observed below a threshold of Matrigel concentration ($\leq 3 \text{ mg mL}^{-1}$) while cell aggregates with surface coverage $< 20\%$ were observed above a threshold of Matrigel concentration ($> 4 \text{ mg mL}^{-1}$). For the intermediate Matrigel concentration 4 mg mL^{-1} , Caco-2 cells sometimes organized in monolayers and

sometimes in aggregates, but we did not observe both organizations coexisting at the same time, as it happened with organoid-derived single cells. Overall, although the morphology of the 3D transient structures formed differ, our results point out the existence of two phases in the epithelial organization at 24 hours of culture time regardless of the epithelial cell type employed here. Both phases could be interpreted as complete to partial wetting phases and their transition appears to be triggered by a common threshold of Matrigel concentration (3 mg mL^{-1}).

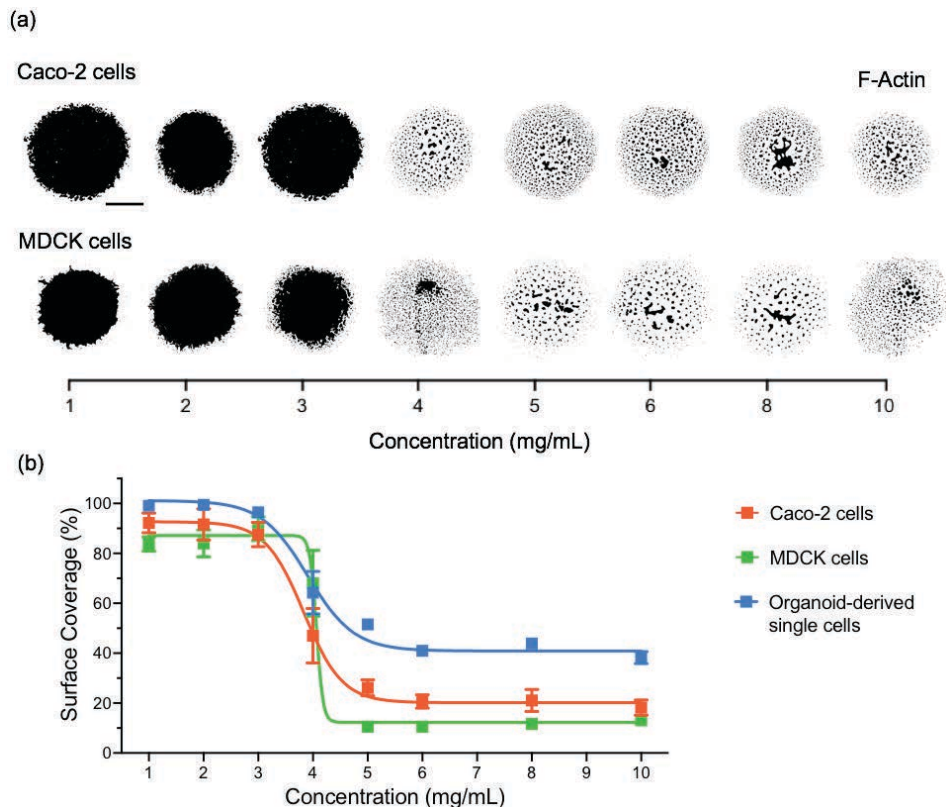


Figure 4.1.12. (a) Representative binary images from thresholded fluorescence microscopy pictures of F-Actin for Caco-2 cells (upper panel) and MDCK cells (lower panel) cultured on substrates coated with Matrigel at different concentrations after 24 hours of culture. Scale bar: 2 mm. (b) Surface coverage percentage of the cultures (with respect to the total seeded surface area) as a function of Matrigel concentration for the different cell types. The symbols correspond to the experimental measurements. The lines represent the fitting performed using a sigmoidal function. Values are plotted as the mean \pm SEM. (*) $p < 0.05$, (**) $p < 0.01$, (***) $p < 0.001$, t-test. $N \geq 3$ experiments (except for MDCK cells at 5 and 6 mg mL^{-1} Matrigel concentrations with $N=2$).

4.1.8 Epithelial monolayers formed at low Matrigel concentrations present an apico-basal polarity regardless of the cell type

We saw in previous experiments that cell polarization of organoid-derived single cells depends on their organization either as monolayers or as tubular networks. Then, we were interested in exploring if, for each of these transient organizations, cell polarization was present, and if it was dependent on the epithelial type tested. To answer this question, we cultured the three different cell types on Matrigel-coated substrates at low concentration (3 mg mL^{-1}) for 24 hours to achieve epithelial monolayers. Then, cell polarity was analyzed by checking the actin cytoskeleton organization at different planes along the vertical matrix-cell axis (cell height) through confocal images^{152,153}. Specifically, we imaged F-actin organization at the basal cell side (in contact with the Matrigel coating), at half-cell height and at the apical cell side (in contact with the cell culture medium).

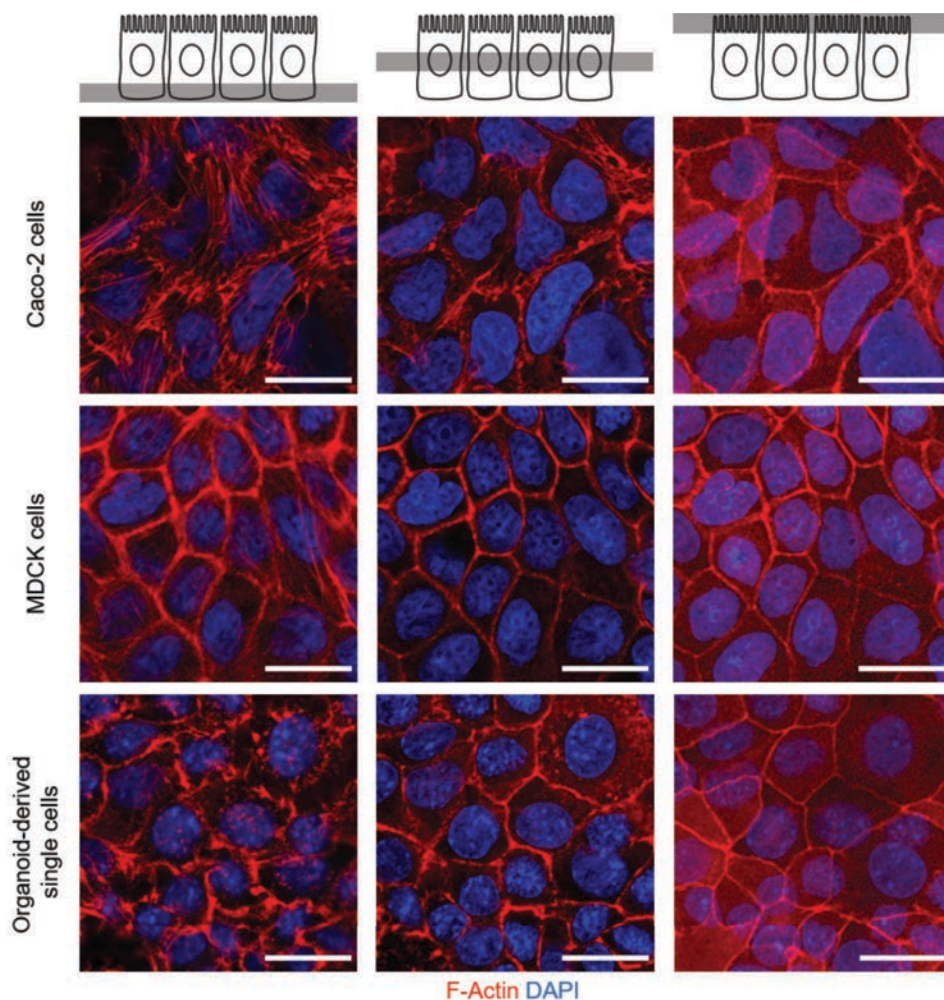


Figure 4.1.13. Representative images of maximum intensity Z projections for the three regions defined across monolayer cross-sections: basal cell side, close to the substrate (left panels), half-cell height (middle panels) and apical cell side, close to the cell culture medium (right panels), for Caco-2 cells, MDCK cells and organoid-derived single cells after 24 hours of culture. Scale bars: 20 μ m.

At their basal sides, Caco-2 and MDCK cell lines organized their actin filaments into contractile bundles known as stress fibers (Figure 4.1.13, left panels). These stress fibers have a nematic order, mostly aligned throughout the cells. Many epithelial cell types throughout the kidney *in vivo* make basal actin stress fibers²⁰⁻²². The main physiological role of stress fibers in epithelial cells *in vivo* is to provide contractility to regulate intraluminal pressure. Thus, Caco-2 and MDCK cells presented stress fibers that are used not to power cell motility, but to provide a static, asymmetric contraction to cells that are exposed to mechanical stress. In addition, stress fibers may also be involved in cell-substrate adhesion. In contrast, organoid-derived single cells showed small actin-rich basal aggregates and no stress fibers. Similar actin aggregates at their basal planes have been recently reported in migrating enterocytes (fully differentiated cells) *in vivo*²⁵. These actin aggregates are protrusions at the basal level orientated in the direction of cell movement. Thus, we suggested that cell migration in our *in vitro* system might be similar to cell migration *in vivo*.

At half-cell height, actin appeared to be distributed contouring the cell borders, which corresponds to cell-cell junctions (Figure 4.1.13, middle panels). Cell-cell junctions couple the actomyosin cortex of neighboring epithelial cells together, where the balance between cell-cell adhesion tension and cortical contraction dictates tissue organization¹⁷. In our case, the typical polygonal shape organization found naturally in epithelia¹⁸ was observed.

At the apical cell side, all the cell kinds tested presented a uniform dotted actin staining that corresponds to actin located at the core of the microvilli, which form the so-called brush-like borders (Figure 4.1.13, right panels). Microvilli are microscopic cellular membrane protrusions typical of epithelial cells that possess several functions such as absorption, secretion or assisting the cell in response to its extracellular environment¹⁵.

Overall, these experiments demonstrated that the three epithelial cell types tested organized in highly packed monolayers with apico-basal polarity when grown onto low concentrated Matrigel-coated substrates.

4.1.9 3D epithelial transient structures formed at high Matrigel concentrations present cell-dependent apico-basal polarization

We next examined the apico-basal polarity of the 3D transient structures formed by the different epithelial cells when cultured on high concentrations of Matrigel (10 mg mL^{-1}). To do this, Caco-2, MDCK and organoid-derived single cells were cultured for 24 hours, stained for F-actin and imaged through confocal microscopy. Representative pictures of F-actin and nuclei distribution for the cell aggregates and the tubular networks at their half-height are shown in Figure 4.1.14. The intensity profiles of F-actin fluorescence signal across the structures are also plotted as a function of their horizontal position across the images.

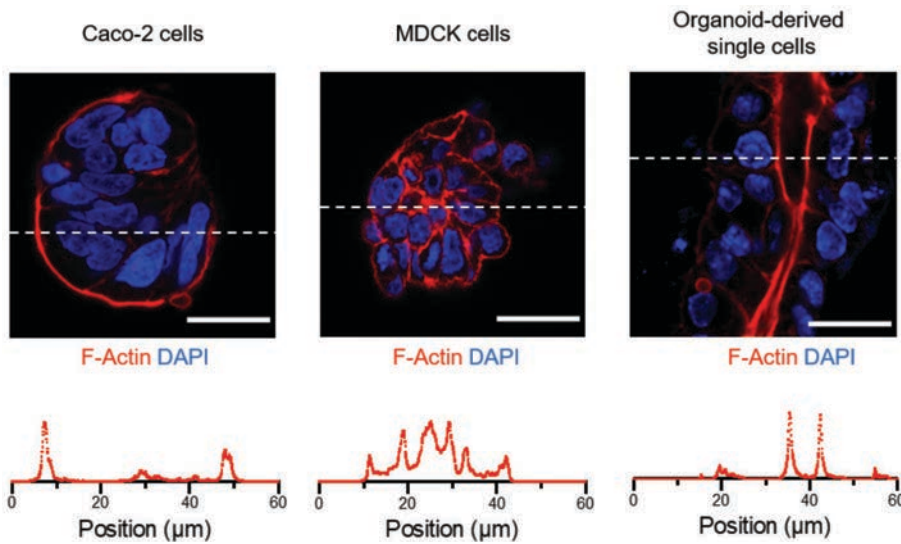


Figure 4.1.14. Representative z-stacks of 3D cellular structures at their half-heights (upper panels). Plots of the fluorescence F-Actin intensity (arbitrary units) along the white dashed lines of the x-y planes shown (lower panels). Scale bars: $20 \mu\text{m}$.

We observed that Caco-2 cells in the aggregates exhibited an apical-out polarity, which implies that there is an accumulation of F-actin at the external membrane area that surrounds the aggregates and is in contact with the liquid medium (Figure 4.1.14, left panels). No inner lumens were identified in these structures. In contrast, MDCK cell aggregates had a basal-out polarity, with accumulation of F-actin at the cell membrane although without inner lumens, as in the case of Caco-2 cells (Figure 4.1.14, middle panels). Preliminary studies have reported that MDCK aggregates had apical-out polarization cultured in suspension or soft agar, whereas these very same aggregates in collagen had basal-out polarity^{38,150,151}. The epithelial organization avoided the contact of the apical surface with the surrounding ECM. These studies point to the importance of cell-cell and cell-ECM interactions in the epithelial

organization. In the tubular structures formed by organoid-derived single cells, we found out the formation of inner lumens. These cells, as MDCK ones, also presented a basal-out polarity, with F-actin accumulated at the internal luminal surfaces of the tubes (Figure 4.1.14, right panels).

Therefore, from these experiments, we could conclude that the polarity of the cells forming the 3D transient structures onto Matrigel-coated surfaces with high protein concentration depends on the epithelial cell type cultured. Noteworthy, after the transient period, all these epithelial cell types formed epithelial monolayers with apico-basal polarization along the luminal-matrix axis. This implies that MDCK cells and organoid-derived single cells must revert their polarization status. If we assume that cell-cell contacts have the potential of being similar for the cultures performed at low and high Matrigel concentrations, we then hypothesize that in these transient structures, cell-matrix interactions might be highly relevant when dictating cell polarity.

4.1.10 Epithelial cells redistribute the ECM of the coated substrates to form 3D transient structures

The organization of epithelial cells depends on cell interaction with both the extracellular matrix (ECM) and adjacent cells⁵⁷. While for Caco-2 cells, cell polarity was maintained both when cells were in monolayers and 3D structures, for MDCK and organoid-derived single cells, cell polarity was reverted when cultured onto low or high concentrations of Matrigel. Therefore, we wanted to assess if cell-ECM interactions were behind these different epithelial cell organizations. As laminin is one of the major components of Matrigel¹³³, we decided to analyze the localization of laminin as a function of cell organization. For this purpose, the three different cell types were cultured onto substrates coated with low (3 mg mL⁻¹) and high (10 mg mL⁻¹) Matrigel concentrations for 24 hours to achieve monolayers and 3D structures, respectively. To visualize the relative distribution of the ECM and the epithelial cells, we performed immunostainings of F-actin and laminin and we imaged the structures using confocal microscopy.

We observed that when cells formed monolayers, despite some protein aggregates being observed, mostly laminin protein was homogeneously distributed over the imaged areas for all cell types (Figure 4.1.15 (a)). This laminin organization coincides with the homogeneity observed when imaging the Matrigel-coated surfaces before cell culture (Figure 4.1.4), so, not obvious laminin redistribution was observed as a consequence of cell growth. In contrast, when cells were organized in 3D structures, either cell aggregates or tubular structures, laminin was found accumulated at their perimetries, surrounding the 3D cellular structures (Figure 4.1.15 (b)). In particular, laminin tracks were clearly visible on the substrate in some

images (Figure 4.1.15 (b), left panel), as if the cells pulled and dragged the matrix when partially de-wetting from the surface to form the 3D aggregates. Since, without cells, laminin was homogeneously distributed over the surface (Figure 4.1.4), these observations revealed that cells were able to redistribute the ECM of the substrate when they were organized in 3D structures. Noteworthy, bringing together this result with the polarization results of the previous section, we can conclude that while MDCK and organoid-derived single cells have the correct apico-basal polarization versus the matrix in the 3D structures, Caco-2 cells present an inverted polarization when forming these aggregates. This inverted polarity was reported for mutated Caco-2 cells to induce anoikis resistance when embedded in collagen-Matrigel mixture⁴¹ and colorectal carcinomas during their dissemination¹⁵⁴. It is worth noting that, this inverted polarity is in contrast with the correct apico-basal polarization of Caco-2 cells embedded in Matrigel⁴⁰, where they form cysts with the cell apical side facing the inner lumen. However, this was observed for cysts grown from single cells for several days, which differs from the aggregates of our experiments, which were formed by the aggregation of several cells in few hours. Altogether, our results suggest that organoid-derived single cells rearrange the ECM in the most efficient manner to balance cell-cell and cell-ECM interactions.

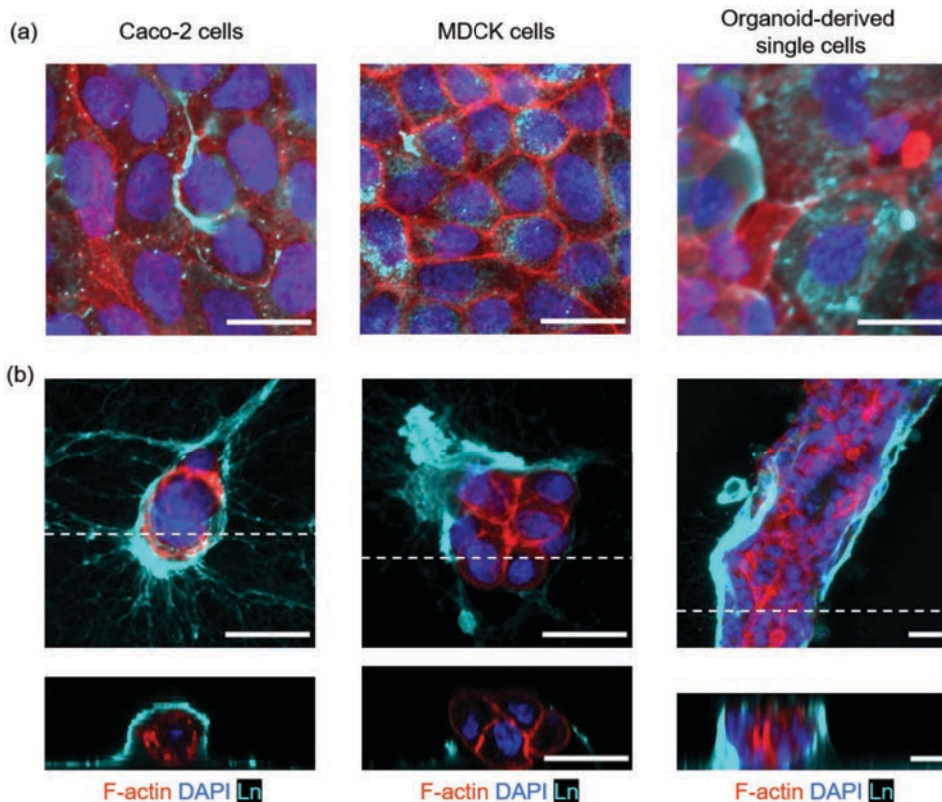


Figure 4.1.15. (a) Confocal representative sum intensity projection fluorescence images of F-actin, cell nuclei (DAPI) and laminin (Ln) for Caco-2 cells (left panel), MDCK cells (middle panel) and organoid-derived single cells (right panel). Scale bar: 20 μm . (b) Confocal representative sum intensity projection (upper panels) and cross sections along the white dashed line (lower panels) of F-actin, cell nuclei (DAPI) and laminin (Ln) for Caco-2 cells (left panel), MDCK cells (middle panel) and organoid-derived single cells (right panel). Scale bar: 20 μm .

4.1.11 Intestinal organoid-derived single cells redistribute the ECM as a function of the stem cell distribution

Focusing our efforts on the cellular structures produced by organoid-derived single cells, we could summarize our findings so far by stating that these cells, when coated on highly concentrated Matrigel, are able to redistribute the matrix proteins to form tubular structures with a lumen. In these structures, cells present the correct epithelial apico-basal polarization. Later on, we know that such tubular structures progress to form epithelial monolayers, which implies a change in cell organization that might presumably be accompanied by a reorganization of the ECM. We were then interested in investigating the dynamics of ECM distribution along this wetting transition over time. For this purpose, organoid-derived single cells were cultured on Matrigel-coated substrates at high concentration (10 mg mL^{-1}). Then, laminin distribution was analyzed over culture time (from 24 to 96 hours). For this purpose, immunostainings of laminin, cell nuclei, F-actin and GFP⁺ cells were performed.

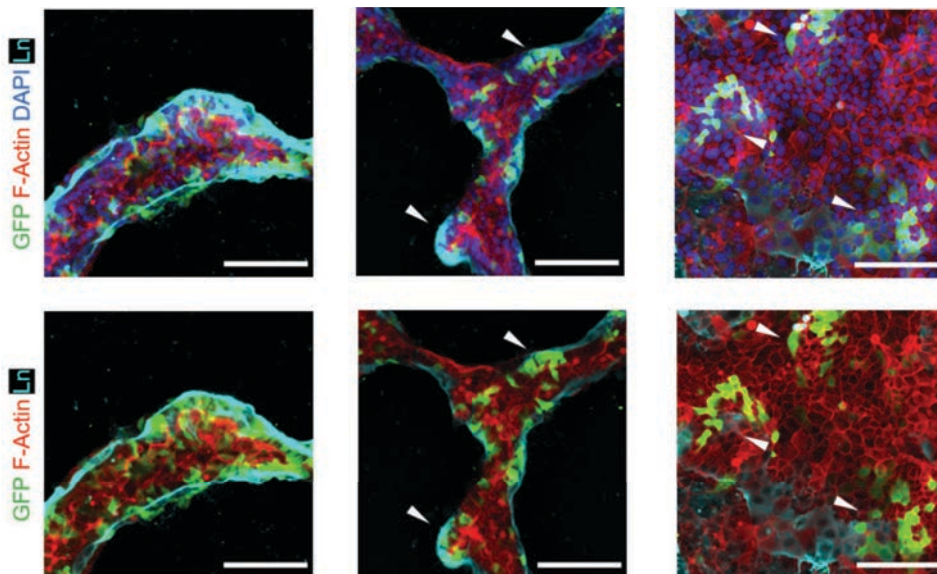


Figure 4.1.16. Representative sum intensity projections of fluorescence images corresponding to organoid-derived single cells cultured on Matrigel at 10 mg mL^{-1} concentration from 24 to 96 hours (from the formation of tubular networks till the formation of monolayers). Images are immunostained for GFP (GFP⁺ cells corresponding to Lgr5⁺ intestinal stem cells), F-Actin, cell nuclei (DAPI) and laminin (Ln). White arrowheads indicate domains of Lgr5-GFP⁺ cells. Scale bars: 100 μm .

Consistent with our previous experiments, single cells self-organized to form 3D-tubular networks after 24 hours of culture. On these structures, GFP⁺ intestinal stem cells (ISCs) (corresponding to Lgr5⁺ cells) were homogeneously distributed along the formed tubes and laminin was also homogeneously distributed surrounding the 3D structures (Figure 4.1.16, left panels). Then, as the culture progressed, we observed that laminin immunostaining was not uniform in intensity along the tubular structures, but it was accumulated in certain regions. These regions were protruding from the tubular shapes forming buds. Interestingly, Lgr5⁺ ISCs were not uniformly distributed either but cells had the tendency to accumulate at certain regions that overlapped with the enriched-laminin regions (Figure 4.1.16, middle panels). After 96 hours of culture, cells completely wetted the surface forming epithelial monolayers that covered the entire substrate. At that point, laminin staining was difficult to observe, but Lgr5⁺ ISCs clearly formed clusters (Figure 4.1.16, right panels). Such crypt-like structures that cluster stem cells can also be identified in the budding structures of intestinal organoids embedded in Matrigel drops. Therefore, we hypothesize that the budding structures enriched in stem cells and laminin that protrude from the tubular networks are crypt-like structures formed upon the self-organization of the stem cells within the tubular structures. In a recent publication, we demonstrated that both organoid-derived crypt pieces and organoid-derived single cells formed functional epithelial monolayers when cultured on Matrigel-coated substrates¹⁴⁹. In here we prove that cell-ECM interactions are key in this process: when ECM protein surface density is above a well-defined threshold, cells increase their mobility, redistribute the ECM, form 3D-tubular networks and then provide the stem cells with a favorable environment to cluster around laminin accumulations forming primitive crypt-like structures that later evolve in intestinal monolayers preserving the crypt-villus organization. Therefore, there is a strong relationship between stem cell distribution and ECM redistribution and, in particular, we hypothesize that laminin accumulations are crucial in this process.

4.1.12 3D-tubular networks can form onto Matrigel-coated substrates but not onto collagen I-coated substrates

Studies using MDCK aggregates^{38,150} or intestinal human organoids¹⁵⁵ previously demonstrated that epithelial organization can be regulated by manipulating the extracellular matrix (ECM) proteins. Specifically, MDCK aggregates and human organoids have been demonstrated to reverse their polarity upon varying the ECM composition. On the one hand, MDCK aggregates exhibit apical-out polarity in liquid suspension. In contrast, these aggregates embedded in collagen type I, thereby providing a strong ECM cue on the outside of these structures, exhibit a basal-out polarity. On the other hand, human organoids in a basement membrane extract

(BME), which is comprised of ECM proteins, have a basal-out polarity, but these organoids in suspension without BME exhibit apical-out polarity. Taking these observations into account and, as in our previous results we were able to determine the influence of laminin in the epithelial organization, we then wondered if other ECM proteins that are also able to form gels were eliciting the same cell organization. To test this, we decided to use collagen type I as ECM matrix and culture organoid-derived single cells on collagen-coated substrates at low (3 mg mL^{-1}) and high (8 mg mL^{-1}) concentrations for 24 hours. We used collagen type I because it was a major ECM component in the repairing epithelium⁸⁷ and it was employed in previous reports that question the ECM regulation of the epithelial organization^{38,150}. In addition, in a recent publication, researchers used collagen to culture intestinal organoid derived crypts due to its similar chemical makeup and stiffness relative to those of the basement membrane underlining the intestinal epithelium¹¹⁶. As controls, cells were also cultured on Matrigel-coated surfaces at the same concentrations.

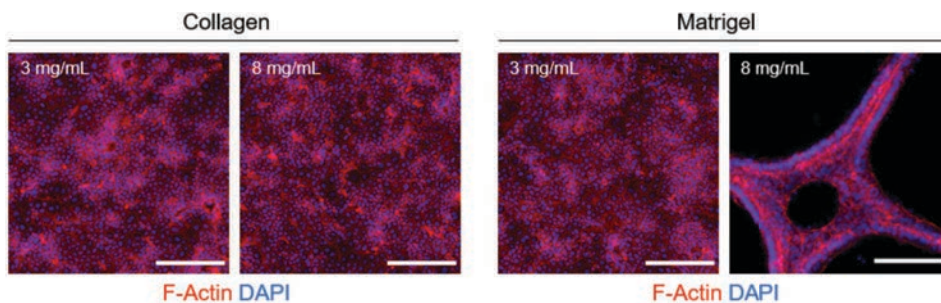


Figure 4.1.17. Representative sum intensity projections of fluorescence images corresponding to organoid-derived single cells seeded on collagen type I and on Matrigel. Images are immunostained for F-Actin and cell nuclei (DAPI). The corresponding matrix concentration for each image is shown in each panel. Scale bars: $100 \mu\text{m}$. $N=2$ experiments.

We found out that organoid-derived single cells were able to grow onto both collagen and Matrigel matrices. However, when cultured on collagen type I, they were not self-organized into the 3D structures that we observed on Matrigel for any of the concentrations assayed (Figure 4.1.17). Within the studied protein density range, cells seeded on collagen formed epithelial monolayers fully covering the substrate. So, our results demonstrated that the growth of epithelial monolayers was not impaired but transient 3D structures forming *de novo* crypt-like domains were not formed. These findings are in agreement with a recent publication which reported that collagen type I 3D matrices were not able to sustain the growth of intestinal organoid-derived cells without the addition of Matrigel or Wnt factors^{87,102}. Also, recent works link the maintenance of primary epithelial cells *in vitro* to culture environments able to sustain the activation of the Yes-associated protein 1 (YAP)^{104,105}. YAP activation is regulated by mechanical cues such as ECM rigidity, strain, shear stress, or adhesive area and has been shown to be involved in

cellular reprogramming during tissue repair^{87,106}. As intestinal tissue repair is influenced by the accumulation of collagen I fibers around the newly formed crypts, both the matrix composition (rich in collagen IV in the homeostatic tissue) and the mechanical properties are altered. In this scenario, it is not clear the influence of these stimuli in the YAP activation process. Taking into account the literature and our results, we then wondered if YAP activation is a key factor to consider in our system and if its potential activation is sensitive to the matrix composition and density.

We therefore decided to analyze YAP activation in our cell culture system. YAP has recently emerged as a primary sensor of the mechanical signals that cells receive from epithelial cell organization and extracellular matrix (ECM)¹⁵⁶. YAP activation leads to its enhanced translocation from the cytoplasm into the cell nucleus. YAP activation has been reported in response to increased mechanical tension (stiff environments)¹⁰⁴, during intestinal tissue regeneration^{87,157} and in the crypt formation in organoid cultures^{88,89}. To analyze YAP activation in our system, we cultured organoid-derived single cells on collagen I and Matrigel substrates for 24 hours and we analyzed YAP position with respect to the cell nuclei by immunostaining and confocal microscopy.

First, we compared YAP activation on the monolayers formed by organoid-derived single cells grown on collagen type I and Matrigel. We found that basically all the cells forming monolayers onto the collagen-coated substrates displayed YAP signal confined to their nuclei (Figure 4.1.18). In contrast, onto the Matrigel-coated surfaces, cell monolayers displayed a heterogeneous activation of YAP, as we can identify regions where the YAP signal is restricted to the cell nuclei and regions where is both cytoplasmatic and nuclear (Figure 4.1.18). Proliferative cells displayed YAP location both cytoplasmatic and nuclear (Figure 4.1.18), whereas non-proliferative cells presented fully nuclear YAP showing that these two domains were distinct both in proliferation and YAP localization. In contrast, proliferative cells onto collagen-coated surfaces were scattered over the surface and all presented YAP translocated into the nucleus. Therefore, in our system, YAP translocation depended on the matrix composition. It was translocated into the nucleus regardless of the proliferative state of the cells on collagen-coated surfaces, whereas onto Matrigel-coated substrates YAP was not fully translocated for the cells forming proliferative clusters or crypt-like domains.

Next, we compared YAP activation in the two types of 3D structures formed by organoid-derived single cells, either when cultured onto Matrigel-coated surfaces at high protein concentration forming tubular networks or when embedded within 3D Matrigel drops forming organoids after 24 h of culture. We observed that cells forming organoids displayed YAP signal mainly at the cytoplasm (Figure 4.1.18). However, cells forming tubular networks showed both cytoplasmatic and nuclear YAP localization. Note that cells forming these structures are mostly proliferative (Ki67⁺

cells). In addition, the proliferative cells do not show any clustering but are scattered over the structures (Figure 4.1.18). Therefore, the compartmentalization in YAP signaling observed in monolayers cultured onto Matrigel thin films was not retrieved.

Thus, from these results, we could conclude that in our monolayers at 24 hours of culture, YAP is activated in a different manner depending on the matrix composition and on the cellular environment, as it is not fully translocated at proliferative foci that we identified as crypt-like domains. On the other hand, in 3D structures, at this early time point proliferative foci were not formed and differential YAP translocation was not observed. At this point, and considering that YAP translocation depends on the mechanical properties of the cell environment, we were wondering if the different YAP translocation patterns found in cells cultured on Matrigel-coated surfaces when forming either monolayers or 3D-structures indicated that the cellular wetting transition observed by changing the protein surface density could also be affected by the substrate stiffness.

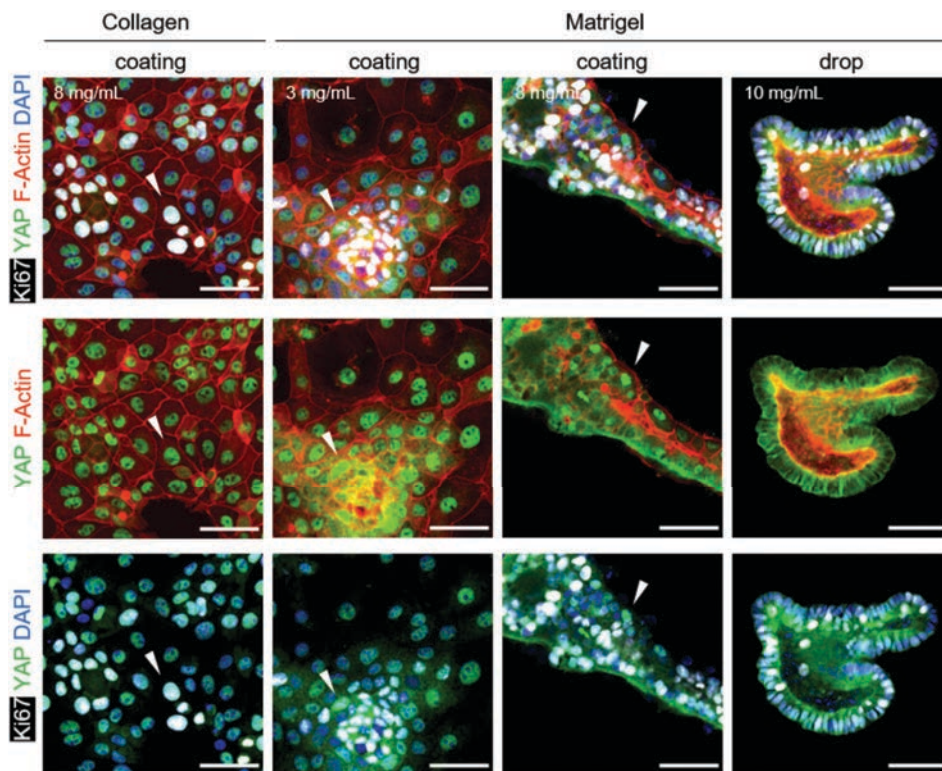


Figure 4.1.18. Representative confocal microscopy images of fluorescently labelled organoid-derived single cells seeded on collagen at 8 mg mL^{-1} (sum intensity projection), on Matrigel at 3 mg mL^{-1} (sum intensity projection), on Matrigel at 10 mg mL^{-1} (middle z-stack), and embedded in Matrigel at 10 mg mL^{-1} (middle z-stack). Cell cultures were immunostained for Ki67 (proliferative cells), YAP, F-Actin and cell nuclei (DAPI). A median filter with a radius of 2 pixels was applied to Ki67 in order to remove background noise. White arrowheads indicate proliferative cells (Ki67⁺) with nuclear YAP activation. Scale bars: 50 μm . N=2 experiments.

4.1.13 *Intestinal epithelial monolayers present a wetting phase transition depending on the substrate stiffness*

It is known that epithelial cell organization is not only sensitive to the biochemical properties of the substrate, but it also depends on its mechanical properties^{56,59,60,63}. For example, when cell aggregates were placed on top of relatively stiff substrates, they usually spread and formed an extended cell monolayer. In contrast, on soft substrates, cell aggregates retained spheroidal shapes. For example, murine sarcoma (S-180) spheroidal aggregates deposited on stiff (~1.8 MPa) fibronectin-coated PDMS spread forming a cellular monolayer expanding from the aggregate⁵⁹. In contrast, these very same aggregates no longer spread on soft (< 8 kPa) fibronectin-coated polyacrylamide (PA) hydrogels. In view of the differential YAP activation observed for the cells cultured onto Matrigel-coated surfaces of different concentrations, we hypothesized that maybe the wetting transition observed in this system was sensitive to the mechanical cues of the substrate. To investigate this, we fabricated PA hydrogels of three different stiffnesses (3, 37 and 145 kPa) that were functionalized with representative low and high Matrigel concentrations (3 and 10 mg mL⁻¹) and we seeded organoid-derived single cells on them for 24 hours. We performed time-lapse experiments and recorded bright-field videos of the epithelial structures obtained. As controls, samples coated on Matrigel-coated polymer substrates (stiffness of ~3 GPa) were also analyzed.

After 24 hours of culture, we observed that on low Matrigel concentration (3 mg mL⁻¹), organoid-derived single cells formed epithelial monolayers fully covering the substrates regardless of the substrate stiffness tested (Figure 4.1.19 (a), upper row). On the other hand, on high Matrigel concentration (10 mg mL⁻¹), these very same cells formed tubular networks on the stiffest substrates (37 and 145 kPa and 3 GPa) and monolayers on the softest substrate (3 kPa) (Figure 4.1.19 (a), lower row). Quantitative values of the surface coverage obtained for these samples revealed that, while the two wetting phases were clearly observed depending on the Matrigel concentration for the stiffest substrates, such phase transition was interrupted for the softest substrate (Figure 4.1.19 (b)). On this softest substrate (3 kPa), monolayers with surface coverage values close to 100% were formed irrespectively on the Matrigel concentration employed (Figure 4.1.19 (c)). Therefore, in terms of the wetting/de-wetting analogy, it appears that a phase diagram in which the wetting phase transition depends on the substrate stiffness can also be established. Altogether, it seems that, as YAP activation tests were pointing out, our system is sensitive to the mechanical cues and, in particular, lowering substrate stiffness can prevent the wetting phase transition triggered by Matrigel concentration.

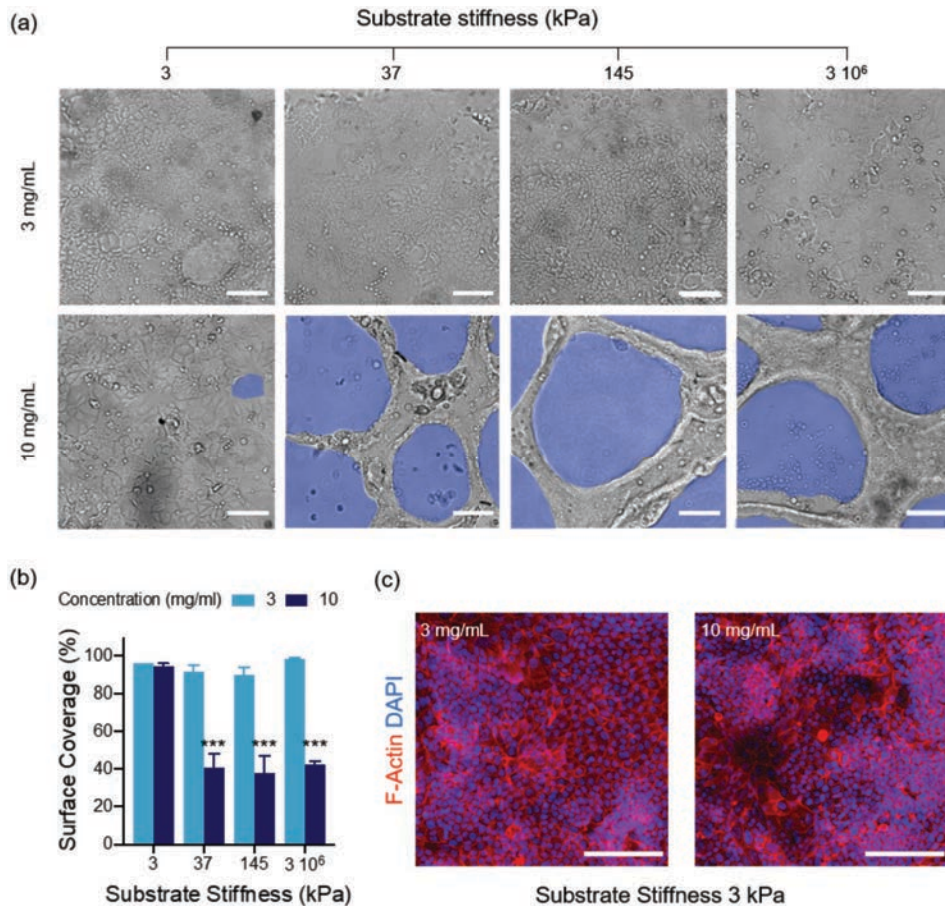


Figure 4.1.19. (a) Bright field images corresponding to snapshots of time-lapse experiments obtained 24 hours after seeding organoid-derived single cells on Matrigel-coated substrates at different concentrations (10 or 3 mg mL⁻¹) and on substrates with different stiffness (3, 37, 145, 3·10⁶ kPa). To improve visualization, zones without cells were marked in dark blue. Scale bars: 100 μm. (b) Surface coverage percentage (with respect to the total surface area) as a function of substrate stiffness for Matrigel concentrations of 3 mg mL⁻¹ (light blue) and 10 mg mL⁻¹ (dark blue). Mean ± SEM. (***) $p < 0.001$, t-test. $N \geq 1$ experiments. (c) Representative sum intensity projections of fluorescence images of F-Actin and cell nuclei (DAPI) for single cells from organoids forming monolayers on 3 kPa substrates with Matrigel concentrations of 3 mg mL⁻¹ (left panel) and 10 mg mL⁻¹ (right panel). Scale bars: 100 μm.

From these results, we could conclude that both Matrigel concentration and substrate stiffness are key parameters in determining the intestinal epithelial cell organization. In agreement with literature, organoid-derived epithelial cells seem to be successfully cultured on substrates possessing a wide range of stiffnesses^{119,121,126}. However, in contrast with the wetting behavior often described for other epithelial cells, the migration of organoid-derived single cells is not impaired on the softest substrates. Remarkably, when cells are cultured onto substrates with stiffness values higher than those attributed to the basement membrane of the intestinal epithelium (~20 kPa)¹⁵⁸, the formation of 3D-tubular

networks promotes stem cells self-organization and enables the creation of crypt-like structures.

4.1.14 Intrinsic self-organization properties of the intestinal organoid-derived epithelial cells depend on the stem cell ratio

From the previous experiments, we could determine that matrix composition, density and stiffness are key parameters in driving the growth of epithelial cells and their transition to epithelial monolayers. Additionally, we determined that, for Matrigel-coated substrates at high concentrations and substrate stiffness values > 37 kPa, intestinal organoid-derived single cells formed 3D-tubular networks that later gave rise to crypt-like buds. Such structures were not found in other epithelial cells tested, neither when organoid-derived single cells were cultured at lower Matrigel concentrations or softer substrates. Therefore, as it seems that these properties are related to the nature of the primary epithelial cells employed, we decided to investigate further the cell types found in the monolayers and the tubular networks. Specifically, we focused our attention on the number of proliferative cells and Lgr5⁺ stem cells found on both cultures. To do this, monolayers and tubular networks obtained after 24 hours of culture were immunostained for Ki67 and GFP and imaged through confocal microscopy (Figure 4.1.20 (a)).

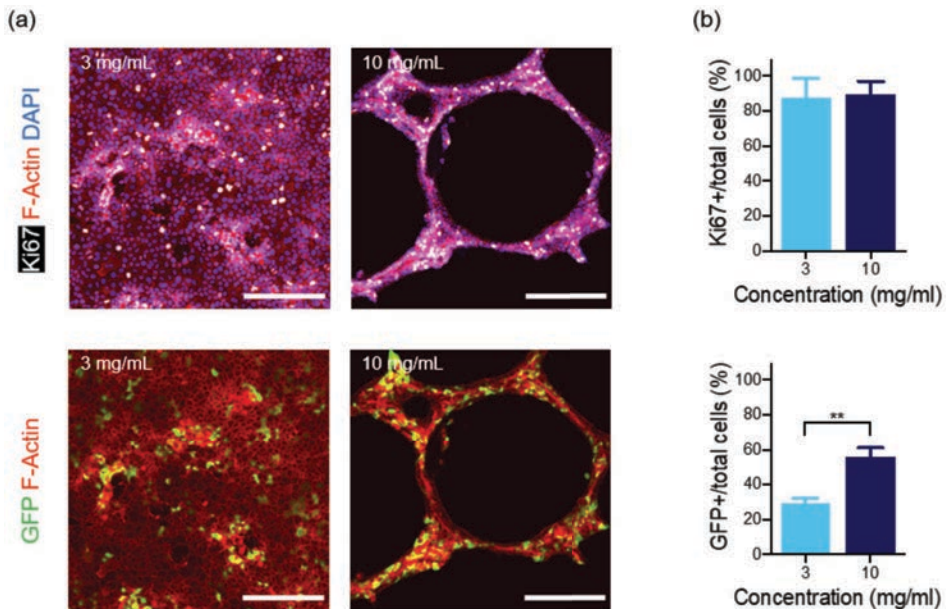


Figure 4.1.20. (a) Representative sum intensity projections of fluorescence images of proliferative cells (Ki67⁺ cells), F-Actin and cell nuclei (DAPI) (upper panels) and of Lgr5⁺ ISCs (GFP⁺ cells) and F-Actin (lower panel) for organoid-derived single cells on Matrigel-coated substrates after 24 hours of culture. The corresponding Matrigel concentration for each image is shown in each panel. Scale bars: 200 μ m. (b) Graph plotting the percentage of positive cells from the total cell number counted for proliferative cells

(Ki67⁺ cells) (upper panel) and Lgr5⁺ ISCs (GFP⁺ cells) (lower panel). Mean \pm SEM. (**) $p < 0.01$, t-test. N = 3 experiments.

The results showed that a similar proportion of cells are expressing the proliferative marker Ki67 for both monolayers and tubular networks (Figure 4.1.20 (b), upper graph). However, the percentage of stem cells is statistically significantly lower for the cells forming monolayers than for the cells on the tubular networks (Figure 4.1.20 (b)). As the cells are cultured using the same culture medium, it appears that cell-matrix interactions and improved migration cell capabilities enhanced the stemness potential of the culture and allowed the formation of 3D-tubular structures. We then hypothesize that the formation of such 3D structures can be modulated by regulating the ratio of the stem cells present in the cultures.

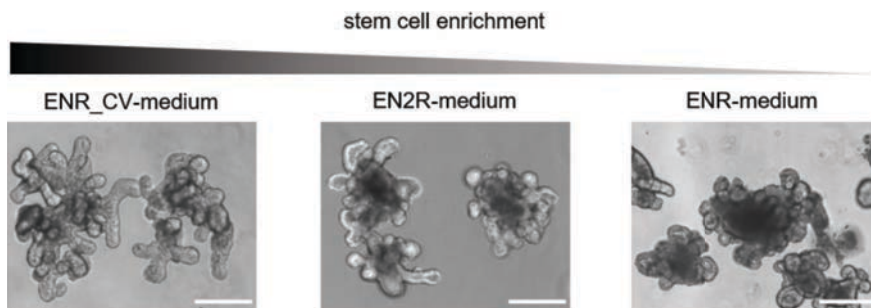


Figure 4.1.21. Brightfield microscopy images of representative morphologies of organoids at day 4 of culture with different cell culture media: ENR_CV-medium (left panel), EN2R-medium (middle panel) and ENR-medium (right panel). These three culture conditions yielded organoids with crypt-villus architectures, but the crypt-length increases as a result of the stem cell enrichment due to the culture media. Scale bars: 200 μ m.

To test our hypothesis, we cultured organoid-derived single cells with different percentages of stem cells on Matrigel-coated substrates for 24 hours. As representative values for low and high Matrigel concentrations, we used 3 and 10 mg mL^{-1} , respectively. To vary the proportion of stem cells within the cultures, intestinal organoids cultured within Matrigel drops were treated with three different culture media, named ENR_CV-, EN2R- and ENR-medium. The ENR_CV medium contains two small molecules, CHIR99021 and valproic acid, that are known to boost the stem cell population of the organoids. Then, the EN2R-medium doubles the normal concentration of R-spondin factor with respect to the basic medium (ENR-medium), also enhancing its stemness capacity. We compared the morphology of the obtained organoids by brightfield microscopy (Figure 4.1.21). The three conditions yielded organoids with crypt-villus structures. Consistent with the results of previous reports¹⁰⁸, we found that organoids cultured under ENR_CV-medium yielded increased length and size of the crypt-like domain buds compared with those of organoids cultured under ENR-medium. Interestingly, we found that

EN2R-medium promoted an intermediate length of the crypt-like domain buds formed in the organoids. As budding structures are correlated with the presence of stem cells, we assumed that their number was enriched, gradually diminishing from ENR_CV-medium to ENR-medium.

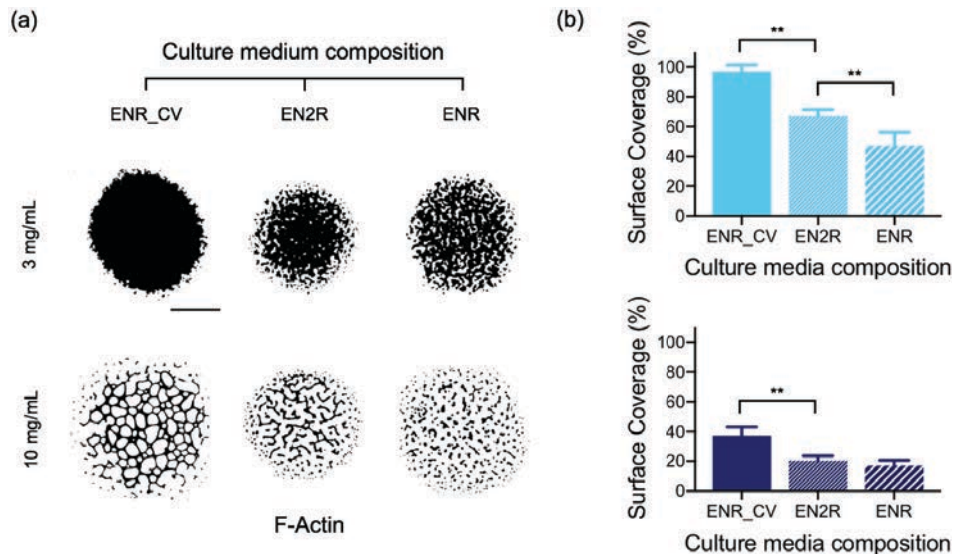


Figure 4.1.22. (a) Representative binary images from thresholded fluorescence images of F-Actin for organoid-derived single cells on Matrigel-coated substrates with concentrations of 3 mg mL⁻¹ (upper panel) and 10 mg mL⁻¹ (lower panel) 24 hours after culture. Scale bar: 2 mm. (b) Surface coverage percentage (with respect to the total surface area) as a function of the culture media composition for the cells cultured at r 3 mg mL⁻¹ (upper panel) and 10 mg mL⁻¹ (lower panel). Mean \pm SEM. (**) $p < 0.01$, t-test. $N \geq 1$ experiments with $n = 3$ replicas each.

We then cultured onto Matrigel-coated substrates single cells obtained from organoids grown with the different cell culture media. After 24 hours of culture, cells were fixed and stained with F-actin and DAPI. F-actin fluorescence pictures of the whole seeded area were converted into binary images, which are shown in Figure 4.1.22 (a). We can visually perceive that single cells cultured on Matrigel at 3 mg mL⁻¹ form monolayers with a gradual reduction in their confluency (Figure 4.1.22 (a), upper panels). The confluency of the monolayers, quantified by surface coverage (Figure 4.1.22 (b), upper graph), diminished significantly with the cell culture composition, going from values $\sim 100\%$ for ENR_CV-medium to values $\sim 50\%$ for ENR-medium. On the other hand, single cells cultured on Matrigel at high concentration (10 mg mL⁻¹) formed complete tubular networks using organoids cultured with ENR_CV-medium, uncomplete tubular networks using organoids cultured with EN2R-medium and cell aggregates using organoids cultured with ENR-medium (Figure 4.1.22 (a), lower panels). Complete networks showed the highest values for surface coverage. However, there were no significant differences

in surface coverage between uncomplete networks and aggregates (Figure 4.1.22 (b), lower graph). Therefore, cell density is not the parameter determining the formation of any of these last structures.

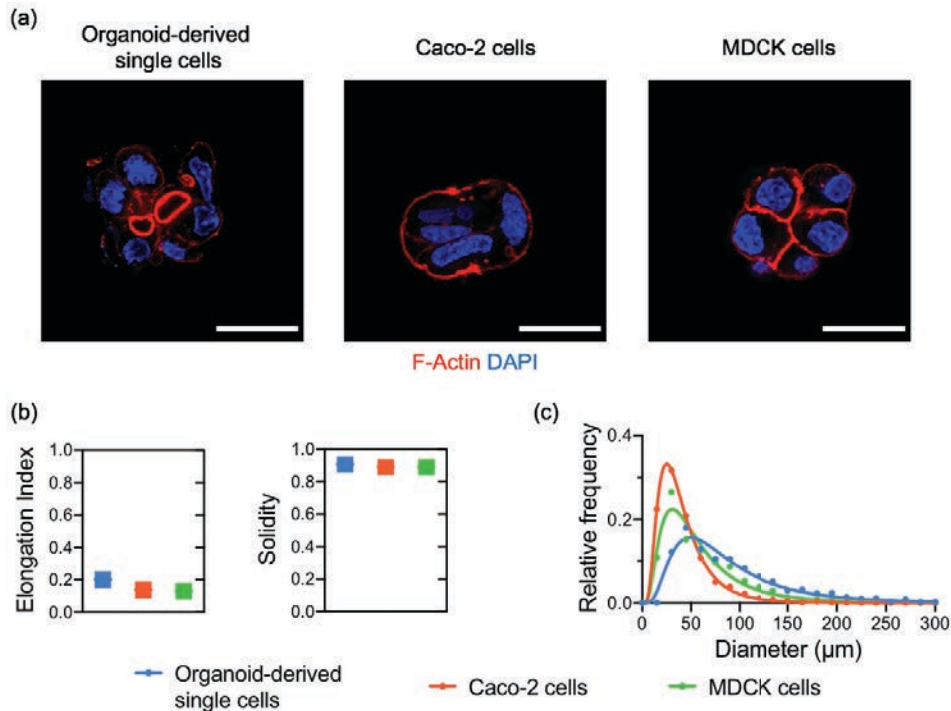


Figure 4.1.23. (a) Representative middle z-stack of fluorescence confocal images of F-Actin and cell nuclei (DAPI). Scale bars: 20 μm . (b) Solidity and elongation index for the aggregates formed by organoid-derived single cells, Caco-2 cells and MDCK cells. Mean value \pm SEM. $N \geq 3$ experiments and $n > 1400$ aggregates. (c) Relative frequency for the diameter of cell aggregates formed by organoid-derived single cells, Caco-2 and MDCK cells. The symbols correspond to histograms of the experimental measurements. The lines are the diameter distributions fitted using Lognormal functions. $N \geq 3$ experiments and $n > 1400$ aggregates.

As this was the first time that we obtained cell aggregates when culturing organoid-derived single cells, we decided to investigate these structures in more depth. Such aggregates reminded us of the structures formed by the two epithelial cell lines tested, Caco-2 and MDCK cells (Figure 4.1.23 (a)). Two shape descriptors were analyzed for all the aggregates: the elongation index and the solidity. For all of them, the elongation index is ~ 0 and the solidity is ~ 1 (Figure 4.1.23 (b)). This indicates that aggregates tend to have a spherical shape with minimal irregularities. Because of this, we could compute their diameters (Figure 4.1.23 (c)). The cell lines employed have narrower diameter distributions than organoid-derived single cells. The mean diameter values obtained were: $(94.8 \pm 1.6) \mu\text{m}$ for organoid-derived single cells, $(43.3 \pm 0.6) \mu\text{m}$ for Caco-2 cells, and $(62.0 \pm 1.2) \mu\text{m}$ for MDCK cells. Compared to

the typical size of organoids (~ 300 μm) the cell aggregates obtained were considerably smaller.

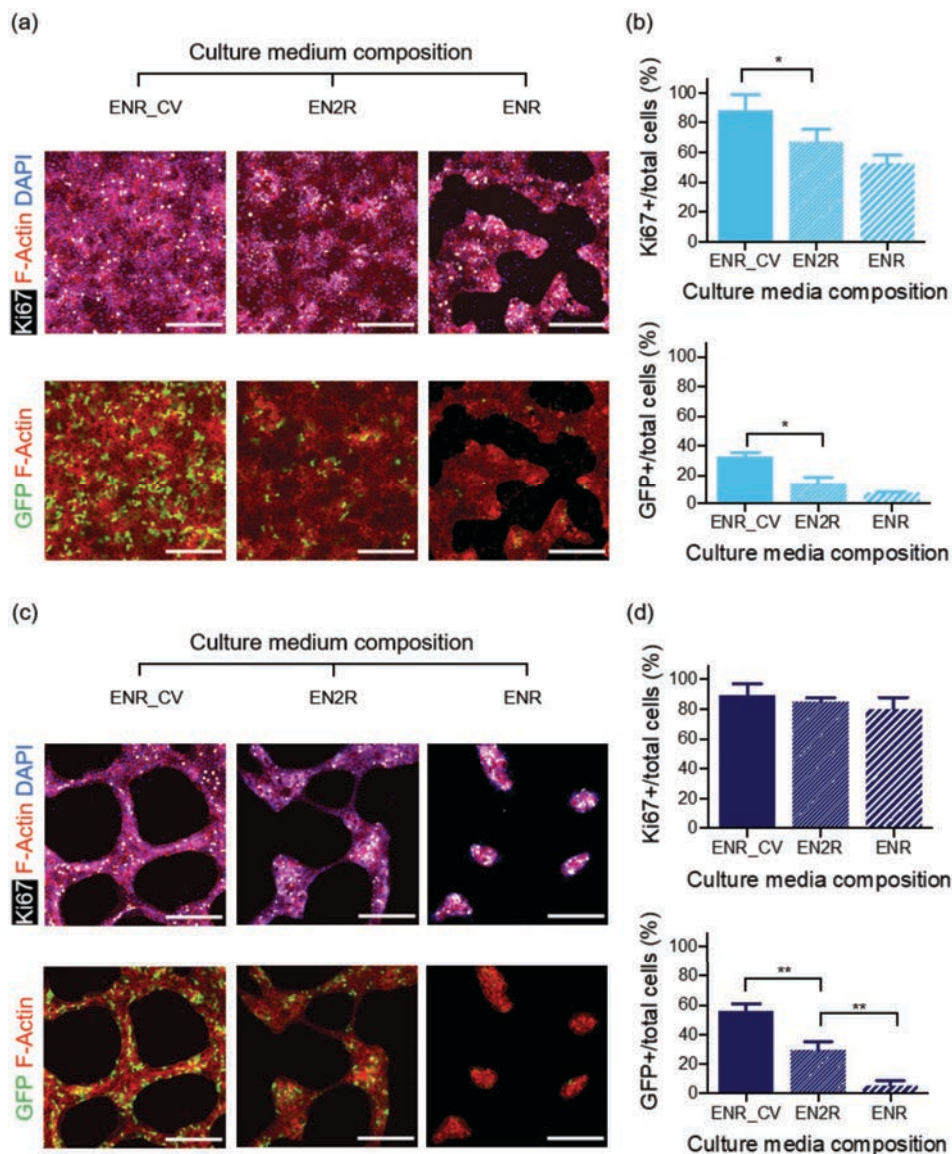


Figure 4.1.24. (a) Representative confocal fluorescence images of proliferative cells (Ki67⁺ cells), F-Actin and cell nuclei (DAPI) (upper panels) and of F-Actin and Lgr5⁺ ISCs (GFP⁺ cells) (lower panel) for organoid-derived single cells after 24 hours of culture. Scale bars: 200 μm . (b) Graphs plotting the percentage of positive cells from the total cell number counted for proliferative cells (Ki67⁺ cells) (upper panel) and Lgr5⁺ ISCs (GFP⁺ cells) (lower panel). Mean \pm SEM. (*) $p < 0.01$, t-test. $N \geq 1$ experiments with $n = 2$ replicas each. (c) Representative confocal fluorescence images of proliferative cells (Ki67⁺ cells), F-Actin and cell nuclei (DAPI) (upper panels) and of F-Actin and Lgr5⁺ ISCs (GFP⁺ cells) (lower panel) for organoid-derived single cells after 24 hours of culture. Scale bars: 200 μm . (d) Graph plotting the percentage of positive cells from the total cell number counted for proliferative cells (Ki67⁺ cells) (upper panel) and Lgr5⁺ ISCs (GFP⁺ cells) (lower panel). Mean \pm SEM. (**) $p < 0.01$, t-test. $N \geq 1$ experiments.

We next characterized the cell types obtained from the different cell culture conditions and substrates, focusing our attention on the proliferative cells (Ki67⁺) and the stem cells (GFP⁺). On the one hand, monolayers obtained on Matrigel at low concentration (3 mg mL⁻¹) showed higher percentages of both proliferative and stem cell positive cells for cells derived from organoids cultured with ENR_CV-medium than for those cultured with EN2R- and ENR-media (Figure 4.1.24 (a-b)). Between EN2R- and ENR-media we did not see any statistically significant difference but there was a decreasing trend. Therefore, the differences in the stemness potential of the cells that were seen in the organoids were also translated to the monolayer cultures and were probably the reason of gradual decrease in surface coverage reported in Figure 4.1.22. On the other hand, 3D structures obtained on Matrigel at 10 mg mL⁻¹ displayed similar percentages of proliferative cells, but a remarkable enhancement of stem cells in the complete networks compared to the uncomplete networks and, specially, to the cellular aggregates (Figure 4.1.24 (c-d)). These results clearly indicate that the formation of the tubular network structures is an intrinsic property of organoid-derived cells linked to the presence of stem cells. Combined with the other results obtained, it appears that the presence of such stem cells in high enough numbers drives the formation of tubular structures by triggering the proper redistribution of the laminin-rich matrix and, in a later stage, also drives stem cell clustering in laminin-enriched areas forming buds that are reminiscent of the crypts found in the tissue *in vivo*.

4.2 Effects of cell-cell and cell-secreted biomolecular signals on the self-organization of organoid-derived intestinal monolayers

In vivo, the organization of the epithelium of the small intestine is regulated by cell-cell and cell-substrate interactions. The effects of cell-substrate interaction have been investigated in deep in the first part of this thesis. Cell-dependent signaling molecules impacting on the organization of the epithelium will be addressed next. These cell-dependent signaling molecules may be secreted by epithelial or stromal cells and diffuse over a short distance to influence cells nearby (paracrine signaling) or may be expressed as membrane proteins to produce interactions at the cell-cell level (juxtacrine signaling). For example, at the cell membrane, Eph/ephrin repulsive interactions control cell positioning along the crypt-villus axis mediating the communication signaling between cells⁸⁴. Proliferative crypt cells express EphB receptors in a decreasing gradient fashion from the bottom to the top of the crypts, whereas ephrinB ligands form a complementary gradient with the highest concentration present at the villi tips (Figure 4.2.1 (a))^{84,85}. On the other hand, biochemical factors such as Wnt, Notch and bone morphogenetic protein (BMP) among others⁹¹ are secreted by epithelial and non-epithelial (stromal) cells into the extracellular space. In particular, Wnt plays a crucial role in regulating the proliferation and organization of epithelial cells⁹²⁻⁹⁴. It arises from multiple sources in the intestinal tissue such as the Paneth cells and the intestinal sub-epithelial myofibroblasts⁹⁴⁻⁹⁶. Wnt exerts a supporting role for the intestinal stem cells (ISCs), it is present at the crypts bottoms and its expression decreases toward the top of the crypts (Figure 4.2.1 (a))⁸¹. Given the different sources of signaling, it is unclear what role each source plays in regulating the epithelium. Recently, organoid-derived monolayers with *in vivo*-like domains were exposed to the perturbation of some of these molecular signals by supplementing or inhibiting Wnt and BMP¹²⁰. These experiments revealed the importance of these signals in controlling the proliferation and the compartmentalization of the intestinal epithelia. However, the effects of the *in vivo* spatial distribution of these factors could not be challenged in this work.

Here, taking advantage of our knowledge to form 2D epithelial monolayers, we systematically studied the role of localized signals in the self-organization of organoid-derived intestinal epithelial monolayers into crypt- and villus-like domains. Particularly, we examined the role of ephrinB1, a juxtacrine signal, and Wnt3a, the major paracrine signal secreted specifically by Paneth cells⁹⁵. To reach this goal, we employed a bioengineering approach that allowed us to precisely tune both the molecular signaling and their localization. For the sake of simplification, the *in vivo* gradients were simplified using an on/off signal (Figure 4.2.1 (b)). Thus, we explored if localized external signal molecules could provide positional cues that target the spatial localization of crypt-like domains on epithelial monolayers

constitutes the second objective of this thesis. The experiments performed and results found toward this aim are reported in this section.

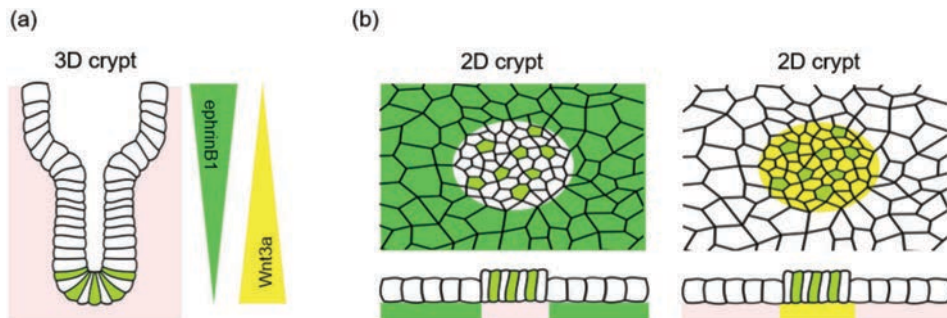


Figure 4.2.1. (a) Schematic representation of the crypt in the small intestine. EphrinB1 ligands form a gradient of which the highest concentration is present at the villus tips, while Wnt3a is present at the crypt bottoms and its expression decreases in a gradient fashion toward the top of the crypts. Thus, ephrinB1 and Wnt3a are expressed in a complementary pattern. (b) Scheme depicting the system with both ephrinB1 and Wnt3a patterns, where the *in vivo* gradient signaling is simplified using an on/off signal and the intestinal epithelial monolayer cultured on top. Top view (upper panels) and cross section (lower panels). The stem cells are marked in light green.

4.2.1 Micropatterns of ephrinB1 retain the biological activity of the ligand

In previous works, we had established a protocol to anchor ephrinB1 ligands to glass surfaces coated with Poly-L-lysine through micro-contact printing technique and we had verified that the printed ligands were effective in stimulating the clustering and activation of EphB2 receptors in human epithelial kidney cells (HEK293T)^{144,159}. On the basis of this previous experience, and considering the fact that ephrinB1 ligand is spatio-gradually expressed by intestinal epithelial cells (reaching the lowest concentration at the crypts), we decided to study the effects of ephrinB1 on our primary intestinal cultures by employing the micro-contact printing technique. However, as organoid-derived cells could not be successfully cultured onto Poly-L-lysine surfaces, we first determined whether ephrinB1 micropatterns could be produced on top of laminin-coated surfaces through micro-contact printing and if these ligands retained their biological activity after the printing procedure.

Figure 4.2.2 (a) outlines the sequential steps for the micro-contact printing technique of ephrinB1 ligands onto laminin-coated surfaces. The procedure involves the use of a PDMS stamp where the ephrinB1 molecules are adsorbed before being transferred to the substrate upon the conformal contact of both surfaces while manually applying pressure. EphrinB1 ligands need to be dimerized to activate their membrane EphB2 receptors. Actually, effective receptor activation requires the ephrinB1 ligands to be presented in clusters, and the activation level is highly sensitive to ligand cluster size^{143,144}. To produce such clusters, ephrinB1 ligands are

commercialized as dimers fused to Fc groups and linked through disulfide bridges, named as ephrinB1/Fc ligands. These Fc groups are used to link dimers together by incubating them in a solution containing anti-Fc antibodies (Figure 4.2.2 (b)). We had previously determined that upon 30 min of incubation with anti-Fc antibodies, mostly tetramers (dimers of ephrinB1/Fc dimers) of hydrodynamic diameters of ~ 70 nm are obtained¹⁴⁴. These clusters are the species that we employed to “ink” the PDMS stamps and are transferred to the surfaces. In this thesis we will refer to ephrinB1 as ligands in this clustered fashion. On the other hand, as controls, only Fc molecules clusterized through anti-Fc antibodies are used. Those will be referred in what it comes as Fc molecules.

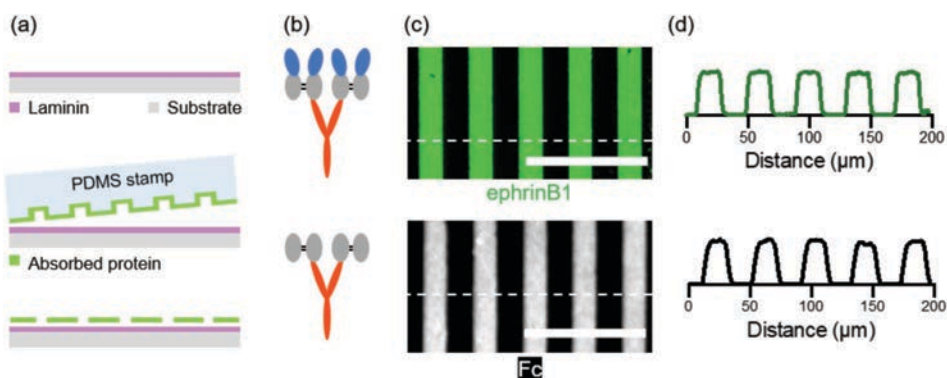


Figure 4.2.2. (a) Scheme depicting the micro-contact printing procedure followed to transfer ephrinB1 and Fc species onto laminin-coated substrates. First, the substrate was incubated with a laminin solution. Then, the micro-contact printing procedure was performed onto the surface. (b) Schematic diagram showing the strategy to form clusters of ephrinB1 and Fc dimers (in blue and grey, respectively) through conjugation via anti-Fc antibodies (in red). (c) Representative fluorescence microscopy images of micropatterns fabricated by micro-contact printing. For visualization, ephrinB1 and Fc were immunostained. Scale bars: 100 μm . (d) Fluorescence intensity profiles corresponding to the dash lines depicted in (c), showing the uniformity of the micropatterns for ephrinB1 (upper panel) and Fc (lower panel).

Micropatterns of ephrinB1 and Fc in the shape of 20 μm wide lines with a pitch of also 20 μm were then performed on top of the laminin-coated surfaces. To check for the success of the micro-contact printing process, the micropatterns produced were visualized by immunofluorescence. It could be then assessed that the printed lines had very good uniformity, high contrast and nice edge definition (Figure 4.2.2 (c)). The coverage of ephrinB1 and Fc species was investigated by plotting the fluorescence intensity of the images along the axis perpendicular to the lines (Figure 4.2.2 (d)). For both micropatterns, there were abrupt changes in the fluorescence intensity that matched in their dimensions with the theoretical width and separation of the lines. Therefore, we could conclude that the micro-contact printing technique employed was successful in creating micropatterns of ephrinB1 and Fc onto laminin-coated substrates.

Once the patterns were produced, we wanted to check if the printed ligands retained their biological function and, in particular, if they were able to be recognized by EphB2 cell receptors. Upon ligand recognition, activated Eph receptors are known to act as positional cues in tissue patterning by regulating cell adhesion and repulsion^{160,161}. It has been reported that cells expressing Eph receptors show strong morphological responses when exposed to linear micropatterns of ephrin ligands¹⁶². In here, we decided to present our ephrinB1 micropatterns to embryonic-derived fibroblasts (NIH/3T3), which express EphB2 receptors endogenously¹²⁴. NIH/3T3 fibroblasts were cultured onto these micropatterns for 24 hours. After this time, cells were fixed, immunostained for F-actin, cell nuclei (DAPI) and ephrinB1 (to localize the micropatterns) and imaged through fluorescence microscopy. Cell response was evaluated screening for several cell seeding densities (10^5 , $3 \cdot 10^5$ or $5 \cdot 10^5$ cells cm^{-2}) and two line widths (10 and 20 μm), and measured by the orientation and position of cell nuclei with respect to the micropatterned lines.

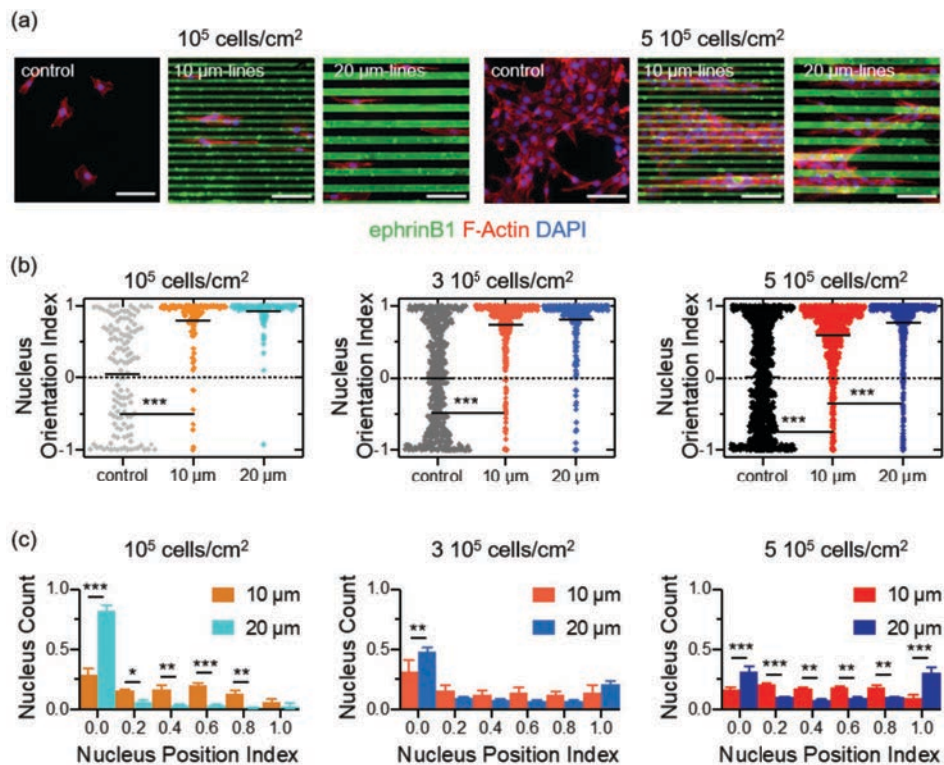


Figure 4.2.3. (a) Representative fluorescence images of NIH/3T3 fibroblasts cultured onto ephrinB1 micropatterns produced on laminin-coated substrates. Images were obtained upon immunostaining of ephrinB1, F-actin and cell nuclei (DAPI). Experiments of two different cell densities and two pattern sizes are shown. As control, laminin substrates were employed. Scale bars: 100 μm . (b) Nucleus orientation index for three different cell densities. (***) $p < 0.001$, t-test. Median. $N = 3$ experiments. (c) Normalized histograms of the cell nuclei number as a function of the nucleus position index for three different cell densities. (*) $p < 0.01$, (**) $p < 0.005$, (***) $p < 0.001$, t-test. Mean \pm SEM. $N = 3$ experiments.

Representative images showed that indeed NIH/3T3 fibroblasts morphology, orientation and position were strongly influenced by the presence of the ephrinB1 micropatterns with respect to the controls (Figure 4.2.3 (a)). In general, for all the cell seeding densities tested, cell nuclei were aligned with the micropattern axis (nucleus orientation index > 0.5) for both line sizes tested (Figure 4.2.3 (b)). However, the highest degree of alignment was obtained for cells seeded at the lowest density of 10^5 cell cm^{-2} on the lines of 20 μm in width (orientation index ~ 1). Then, the analysis of the nucleus position with respect to the pattern (nuclei on top of the ephrinB1 lines, in between lines or without a preferred position) revealed that NIH/3T3 fibroblasts positioning strongly depended on the pattern size and the cell seeding density (Figure 4.2.3 (c)). For lines of 10 μm in width, cell nuclei did not position preferentially with respect to the micropatterns (position index values were homogeneously distributed), probably because the line width was not large enough. On the other hand, at high cell seeding densities, cell nuclei were also not showing any preferential position with respect to the patterns, probably because cells established cell-cell contacts that were indeed dictating their location. For the lowest cell seeding density of 10^5 cells cm^{-2} and micropatterns of 20 μm width, almost all nuclei were fully positioned in between the ephrinB1 lines. Therefore, for the ephrinB1 concentration tested, the ephrinB1 micropatterns seemed to induce cell repulsive effects for NIH/3T3 fibroblasts.

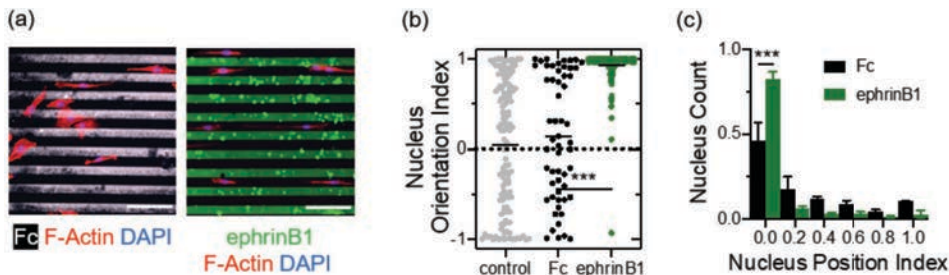


Figure 4.2.4. (a) Representative fluorescence images of NIH/3T3 cells cultured at a cell seeding density of 10^5 cells cm^{-2} on micropatterns of Fc and ephrinB1 species (lines of 20 μm in size) produced on laminin-coated substrates. Images are immunostained for ephrinB1, Fc, F-actin and cell nuclei (DAPI). Scale bars: 100 μm . (c) Nucleus orientation index. Median. (***) $p < 0.001$, t-test. $N \geq 2$ experiments. (b) Normalized histograms of the cell nuclei number as a function of the nucleus position index. Mean \pm SEM. (***) $p < 0.001$, t-test. $N \geq 2$ experiments.

At this point, we were wondering if these strong cell repulsive effects observed were really due to EphB2-ephrinB1 interactions or were due to an increased affinity of the cells to adhere onto the laminin regions in between the ephrinB1 lines. To tackle this question, a set of experiments were performed seeding cells at a cell density of 10^5 cells cm^{-2} on micropatterns of 20 μm in size printed with ephrinB1 or with Fc species (Figure 4.2.4 (a)). As controls, laminin-coated substrates were used. As shown in Figure 4.2.4 (b-c), ephrinB1 strongly influenced cell nuclei orientation

(orientation index ~ 1), while Fc micropatterns and control substrates showed no preferred orientation (orientation index ~ 0). Also, despite the presence of laminin lines per se produced some confinement of the cell nuclei, this effect was significantly enhanced when ephrinB1 was present in the system (Figure 4.2.4 (d)). These results confirmed that ephrinB1 micropatterns trigger a cell repulsive effect and therefore, the ligand retains its biological activity after the printing procedure.

4.2.2 *EphrinB1 signaling strength can be effectively controlled through micropatterns*

In vivo, cells of the small intestine crypts are subjected to complementary gradients of ephrin/Eph ligand-receptor signals, which indicates that ephrin signaling depends on the ligand concentration^{84,85}. Indeed, it has also been reported in experiments *in vitro* that ephrin might allow cell adhesion or trigger cell repulsion depending on the ligand concentration^{160,161}. Therefore, once we knew that ephrinB1 micropatterns were biologically active, we investigated whether the biological activity of the ligand could be regulated by this technique. To explore this issue, we fabricated a set of ephrinB1 micropatterns of lines of 20 μm in size on laminin-coated substrates where we varied the ephrinB1 concentration of the solutions used to “ink” the PDMS stamps. A broad range of ephrinB1 concentrations ranging from 1 to 10^{-4} dilutions from the stock concentration ($69.0 \mu\text{g mL}^{-1}$ ephrinB1/Fc + 0.559 mg mL^{-1} anti-Fc antibodies) were tested. On the micropatterns produced, NIH/3T3 fibroblasts were seeded at a density of $10^5 \text{ cells cm}^{-2}$ and cultured for 24 hours. After this time, samples were fixed, immunostained for F-actin, cell nuclei (DAPI) and ephrinB1, and imaged with a fluorescence microscope. Then, we quantified cell nuclei orientation with respect to the line direction, and cell nuclei position with respect to the patterns for the different ephrinB1 dilutions tested.

We observed that the dilution of the ephrinB1 ligand produced micropatterns with gradient ephrinB1 fluorescence intensities (Figure 4.2.5 (a)). We could also visually assess that, when decreasing ephrinB1 concentration, its effects on directing cell orientation and position in between lines were progressively lost. This was quantitatively assessed for the cell nuclei orientation, where we found a transition triggered by the ephrinB1 dilution (Figure 4.2.5 (b)). For the highest ephrin concentrations, cells showed strongly elongated morphologies and were almost fully aligned parallel to the lines (orientation index ~ 1). In addition, they were strongly confined in between the ephrinB1 lines (position index distribution centered at ~ 0) (Figure 4.2.5 (c)). When reducing the ephrin concentration, cells showed an increasingly spread morphology, a random orientation (orientation index ~ 0), and a random distribution over all the cell culture area (position index homogeneously distributed). In particular, for the lowest dilution, ephrinB1 cell

repulsive effects completely disappeared. Taken these results together, we can conclude that ephrinB1 ligands presented as micropatterns elicit a cellular response that can be modulated by changing the ligand concentration printed.

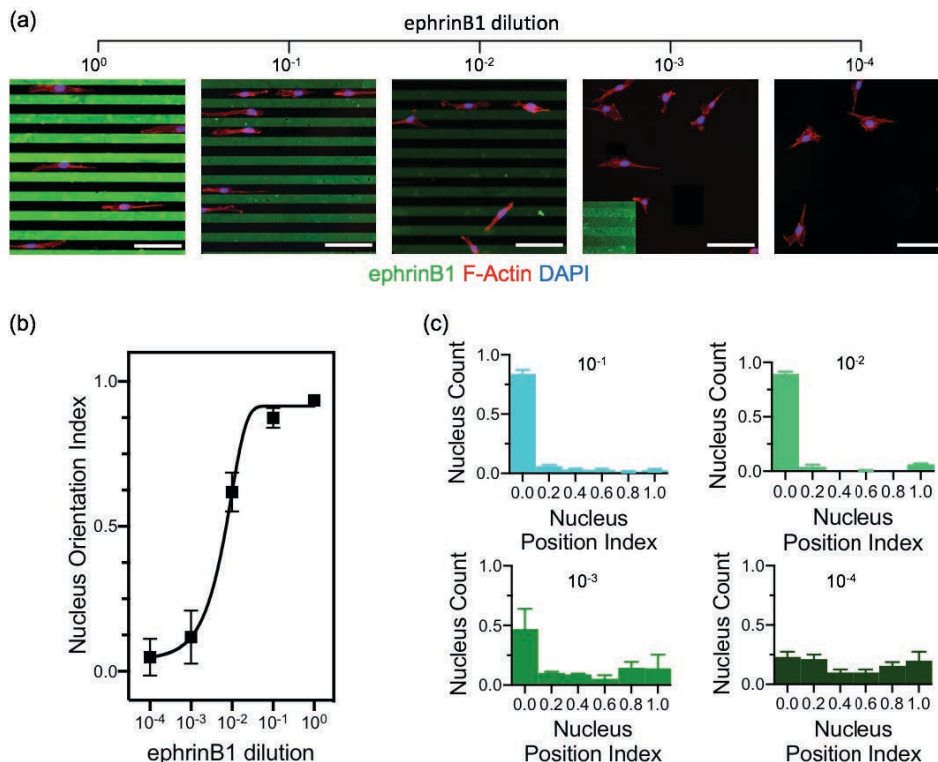


Figure 4.2.5. (a) Representative fluorescence images for NIH/3T3 cells cultured on ephrinB1 micropatterns of lines of 20 μm in size printed on laminin-coated substrates. The micropatterns have been produced using ephrinB1 solutions at several dilutions. Images were generated upon immunostaining of ephrinB1, F-actin and cell nuclei (DAPI). Scale bars: 100 μm . (b) Nucleus orientation index as a function of the ephrinB1 concentration. The symbols correspond to the experimental measurements, and the solid line is a fitting of the data using an allosteric modulator (logEC50). Data are plotted as mean \pm SEM. N = 3 experiments. (c) Normalized histograms of the cell nuclei number as a function of the nucleus position index for different ephrinB1 concentrations. Mean \pm SEM. N = 3 experiments.

4.2.3 Biochemical micropatterns can be successfully transferred on Matrigel-coated surfaces

While through the previous experiments we proved that we could successfully transfer biomolecular patterns on top of laminin-coated surfaces, we failed in growing our intestinal organoid-derived single cells on top of these substrates. Therefore, on the basis of the results presented in section 3.1, we decided to use as cell culture substrates Matrigel-coated surfaces. However, micro-contact printing is not a well-suited technique to be employed with soft, sticky materials. Thus, we

decided to pursue a strategy developed in our lab a few years ago based on performing the micro-contact printing procedure on Matrigel-coated substrates previously subjected to a freeze-drying process¹²⁵. Through this process, the soft hydrogel becomes mechanically resistant enough to sustain the PDMS stamp pressure (Figure 4.2.6 (a)). After printing, the Matrigel substrates were reconstituted by adding PBS at room temperature. As this procedure might modify the Matrigel and organoid-derived single cells have proven to be very sensitive to the matrix employed, freeze-dried Matrigel coatings prepared this way were first characterized in terms of protein distribution (focusing on laminin distribution) and thickness. As controls, fresh Matrigel (non-freeze-dried) samples were used. Freeze-dried and fresh Matrigel coatings were produced employing diluted Matrigel solutions (0.25 mg mL^{-1}), were visualized by immunofluorescence using laminin antibodies and imaged using confocal microscopy.

Images in Figure 4.2.6 (b) are representative of the laminin distribution in the treated and fresh Matrigel samples. The positive staining for laminin demonstrated a stable adhesion of Matrigel coatings after freeze-drying, reconstitution, and immunostaining processes. As shown here, both samples presented a punctate protein distribution with non-significant differences in terms of the average intensities measured (Figure 4.2.6 (c)). On the other hand, non-significant differences in thickness between the freeze-dried and the fresh samples were measured (Figure 4.2.6 (d)). In light of these results, we considered that the freeze-dried and reconstitution process did not modify significantly the Matrigel.

Next, we proceeded to use the micro-contact printing process to create ephrinB1 patterns on the freeze-dried Matrigel-coated substrates. PDMS stamps with features of different shapes (lines, squares, circles, and more complex structures) with sizes covering three orders of magnitude (from $1 \text{ }\mu\text{m}$ to 0.1 mm) were successfully printed onto the freeze-dried Matrigel surfaces (Figure 4.2.6 (e)). The ephrinB1 ligands were clearly shown upon immunostaining, as well as the laminin of the underlying Matrigel. The micropatterns showed an excellent homogeneity across the printed surface areas, and faithfully reproduced the features of the PDMS stamps employed. Noteworthy, not only positive stamps (those with protruding features) were successfully printed but also negative stamps (with holes, as the circular example in Figure 4.2.6 (e)) could be reproduced. We also assessed that this technique was not only successful with ephrinB1 ligands, but that it could transfer other relevant biomolecules for the organization of the small intestinal epithelium such as the EphB2 receptor (Figure 4.2.6 (f)) or Wnt3a ligands (not shown in this section).

Overall, these results demonstrated that we successfully designed a simple method to produce biochemical micropatterns on top of Matrigel-coated substrates in a highly reproducible manner.

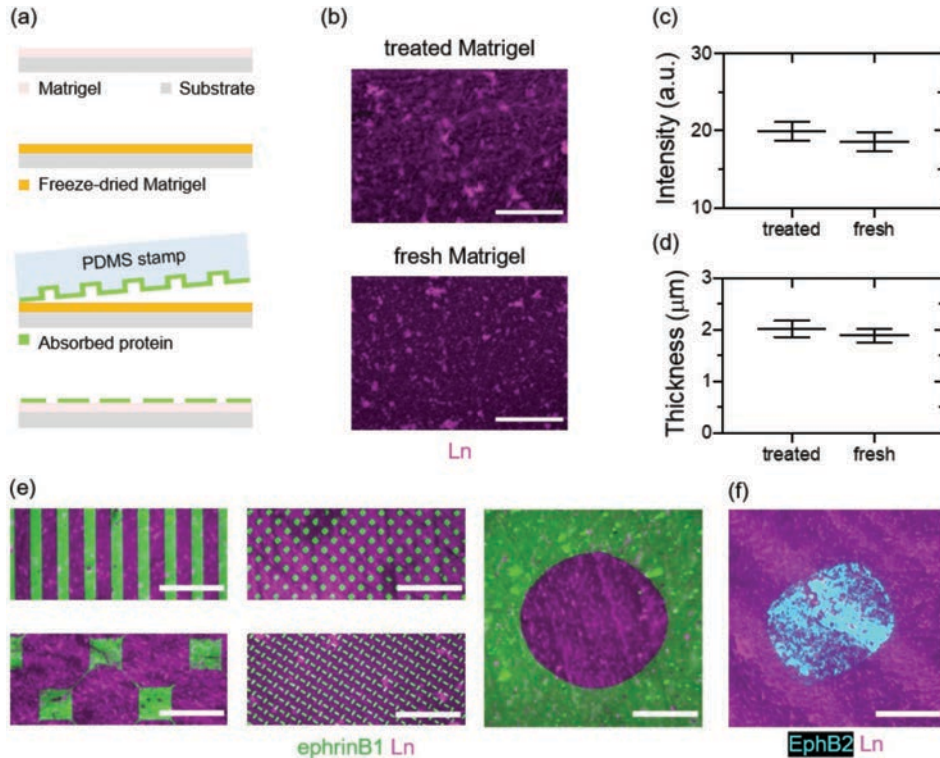


Figure 4.2.6. (a) Scheme depicting the micro-contact printing procedure to transfer biomolecules onto Matrigel-coated substrates. First, Matrigel-coated substrates were freeze-dried (Matrigel was diluted at 0.25 mg mL^{-1}). Then, the micro-contact printing procedure was performed onto the dried surfaces and afterwards, samples were reconstituted with PBS. (b) Representative fluorescence images of treated (freeze-dried and reconstituted) Matrigel-coated substrates and fresh Matrigel. Samples were immunostained for laminin. Scale bars: $20 \mu\text{m}$. (c) Graph plotting the average fluorescence intensity of immunostained laminin measured from treated and fresh Matrigel-coated substrates. Mean \pm SEM. N = 3 experiments. (d) Graph plotting the thickness of the treated and fresh Matrigel coatings. Mean \pm SEM. N = 3 experiments. (e) Representative fluorescence images of micropatterns of ephrinB1 ligands printed on treated Matrigel-coated substrates. Images were immunostained for ephrinB1 and laminin. Scale bars: $50 \mu\text{m}$. (f) Representative fluorescence images of micropattern of EphB2 receptors printed on treated Matrigel-coated substrates. Images were immunostained for EphB2 and for laminin. Scale bar: $50 \mu\text{m}$.

4.2.4 Matrigel-coated substrates support the growth of intestinal organoid-derived single cells after being freeze-dried and reconstituted

Once we knew that we could successfully produce biomolecular patterns on Matrigel-coated substrates, we proceeded to check whether organoid-derived single cells could grow on these treated (freeze-dried and reconstituted) Matrigel surfaces. For that purpose, intestinal organoid-derived single cells (see section 3.2) were seeded on top of treated and fresh Matrigel-coated substrates and cultured for 5 days.

Figure 4.2.7 (a) demonstrates that organoid-derived single cells were able to form growing monolayers that over the culture time increased in size, doubling the

surface area covered by the cells from day 1 (24 h) till day 5 (120 h) (Figure 4.2.7 (b)). As we were using Matrigel-coated substrates at very low concentrations (0.25 mg mL^{-1}), these results agree with those reported in the first part of this thesis. Over time, monolayers showed a morphology that also agrees with our previously published data¹¹⁹, as we observed the appearance of zones densely packed with cells surrounded by less compact regions.

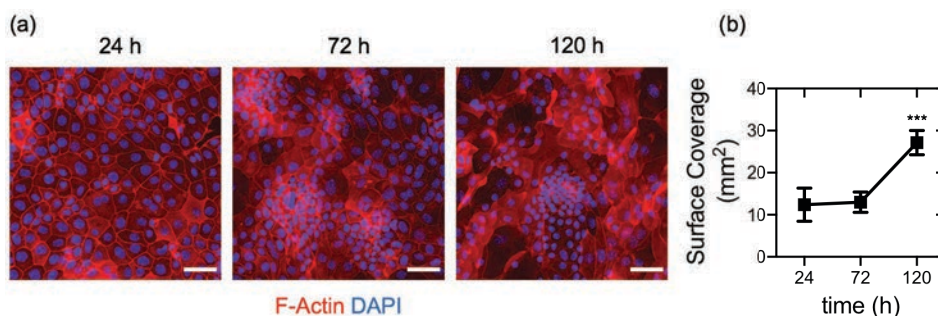


Figure 4.2.7. (a) Confocal representative fluorescence images of F-Actin and cell nuclei (DAPI) for organoid-derived single cells seeded on diluted Matrigel treated (freeze-dried and reconstituted) at 24, 72 and 120 hours of culture. Scale bars: $50 \mu\text{m}$. (b) Graph plotting the surface coverage at 24, 72 and 120 hours of culture. Mean \pm SEM. (***) $p < 0.001$, t-test. $N \geq 3$ experiments.

We then compared cell performance on these substrates versus the very same cells grown onto fresh Matrigel-coated substrates at the same low Matrigel concentration (0.25 mg mL^{-1}). To do that, we quantified the area projections of the F-actin images obtained from the cultures at days 1, 3 and 5 (Figure 4.2.8 (a), black and green boxes). The fold change in these surface areas, which we called surface coverage, was plotted as a function of the culture time in Figure 4.2.8 (b), upper graph. This graph showed non-significant differences for the first 3 days of culture, and that by a slightly better performance of the treated samples by day 5. On the other hand, if we compared the performance of the treated Matrigel in diluted (0.25 mg mL^{-1}) and non-diluted (10 mg mL^{-1}) concentrations (Figure 4.2.8 (a), black and yellow boxes) we did not observe any significant differences in surface coverage (Figure 4.2.8 (b), middle graph). We also observed that, in these conditions, we partially recovered the tubular network structures reported in previous sections of this thesis, now modulated by the treatment of the Matrigel. Finally, we also checked if our monolayers grown in these conditions were also sensitive to the cell culture medium employed, as we previously reported for fresh Matrigel. To do that, cells seeded on treated Matrigel-coated substrates were cultured with ENR_CV-medium and with ENR-medium (Figure 4.2.8 (a), black and pink boxes). The surface coverage measurements revealed significant differences in the surface coverage after 5 days of culture, so the use of ENR_CV-medium is essential to maintain the integrity of the

monolayers over time also for the monolayers grown onto the treated Matrigel (Figure 4.2.8 (b), lower graph).

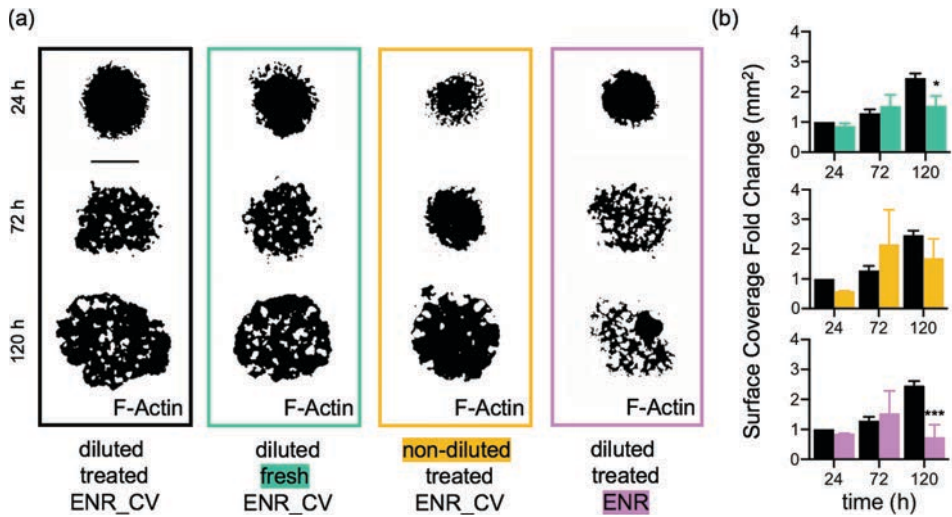


Figure 4.2.8. (a) Representative binary images from thresholded fluorescence images of F-Actin for organoid-derived single cells seeded on Matrigel-coated substrates. Color code: black box: Matrigel-coated substrates diluted at 0.25 mg mL^{-1} and treated by freeze-drying and reconstitution with PBS; green box: fresh Matrigel-coated substrates non-diluted (concentration at 10 mg mL^{-1}); yellow box: Matrigel-coated substrates non-diluted (concentration at 10 mg mL^{-1}) and treated; pink box: Matrigel-coated substrates diluted at 0.25 mg mL^{-1} and treated, where cells cultured with ENR-medium (for the other three conditions was ENR_CV medium). Scale bar: 3 mm. (b) Surface coverage fold change (with respect to the surface coverage of the Matrigel-coated substrate diluted at 0.25 mg mL^{-1} , treated and cell cultured with ENR_CV-medium at 24 h. The color code is the same as in (a). Mean \pm SEM. (*) $p < 0.01$, (***) $p < 0.001$, t-test. $N \geq 2$ experiments.

Taken together, with these experiments we demonstrated that freeze-dried and reconstituted Matrigel-coated substrates allow the formation of intestinal epithelial monolayers and their maintenance over time.

4.2.5 Epithelial monolayers maintain *in vivo*-like cell type composition and spatial organization on freeze-dried and reconstituted Matrigel

Next, we assessed the potential effects of using treated Matrigel (freeze-dried and reconstituted) on the cell composition and spatial organization of the grown monolayers. To that aim, we cultured organoid-derived single cells on treated Matrigel for 5 days and we investigated the presence and spatial arrangement of two cell populations, proliferative and differentiated cells, at different time points. This was performed upon immunostaining of F-actin, nuclei (DAPI), Ki67 (positive for proliferative cells) and Ck20 (positive for differentiated cells).

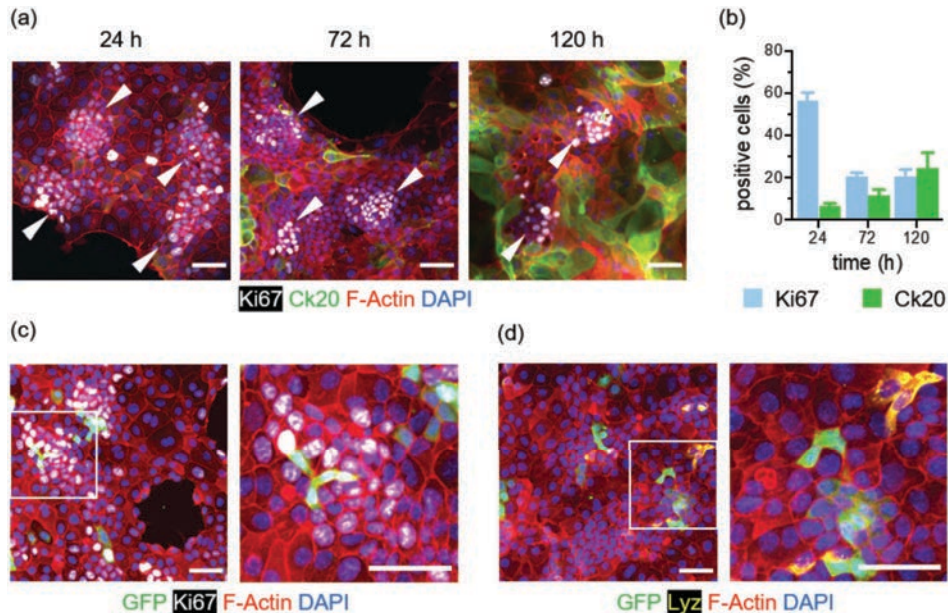


Figure 4.2.9. (a) Representative confocal fluorescence images of organoid-derived single cells seeded on freeze-dried and reconstituted Matrigel at 24, 72 and 120 hours of culture. The images are immunostained for the Ki67 (proliferative cells), Ck20 (differentiated cells), F-Actin and cell nuclei (DAPI). White arrowheads indicate the proliferative cell domains. Scale bars: 50 μ m. (b) Graph plotting the percentage of positive cells (from the total cell number counted) for Ki67 and Ck20 at 24, 72 and 120 hours of culture. Mean \pm SEM. $N \geq 2$ experiments. (c) Representative confocal fluorescence images of organoid-derived single cells seeded on diluted and treated Matrigel at 24 hours of culture. Images were immunostained for GFP⁺ cells (corresponding to Lgr5⁺ stem cells), Ki67⁺ cells, F-Actin and cell nuclei (DAPI). A median filter with a radius of 0.5 μ m was applied to Ki67 fluorescence images and a mean filter with a radius of 0.5 μ m was applied to GFP fluorescence images in order to remove background noise. Scale bars: 50 μ m. (d) Representative confocal fluorescence images of cells as in (c) immunostained for GFP, F-Actin, cell nuclei (DAPI) and Lysozyme (Lyz) (a marker for Paneth cells). Scale bars: 50 μ m.

We found that for all the time points tested, intestinal epithelial monolayers displayed clusters of proliferative (Ki67⁺) cells self-organized into densely packed zones (Figure 4.2.9 (a)). On the other hand, at 24 hours few non-proliferative cells showed positive staining for Ck20, but this proportion greatly increased over time. By day 5 of culture, populations of proliferative and differentiated cells were distributed in a clear spatially segregated fashion. Quantification of the Ki67⁺ and Ck20⁺ cell populations as a function of the culture time was performed based on these immunostainings and it is plotted in Figure 4.2.9 (b). We found that at 24 h of culture, the percentage of proliferative Ki67⁺ cells in the monolayer was very high (~55%) and decreased abruptly to ~20% by day 3. Noteworthy, this decrease correlated with an evident increase in the percentage in the differentiated Ck20⁺ cells, suggesting that when growing, the epithelial monolayers are evolving to a homeostatic stage. These results agree with our previous observations of monolayers growing onto fresh Matrigel-coated substrates¹¹⁹. Additional immunostainings demonstrated that the proliferative clusters were formed by a

pool of cells that stained double-positive for GFP, a marker of Lgr5⁺ intestinal stem cells (ISCs), and Ki67 (Figure 4.2.9 (c)). The stem cells formed a compartment that was surrounded by a ring of Ki67⁺ proliferative cells. Furthermore, Lgr5⁺ ISCs and Paneth cells (Lysozyme, Lyz⁺ cells) were found to be located adjacent one to each other (Figure 4.2.9 (d)), indicating that Paneth cells are forming part of the stem cell niches. Thus, these proliferative clusters resemble in their cell composition to the intestinal crypts found in the tissue *in vivo* and hereafter we will refer to them as crypt-like domains.

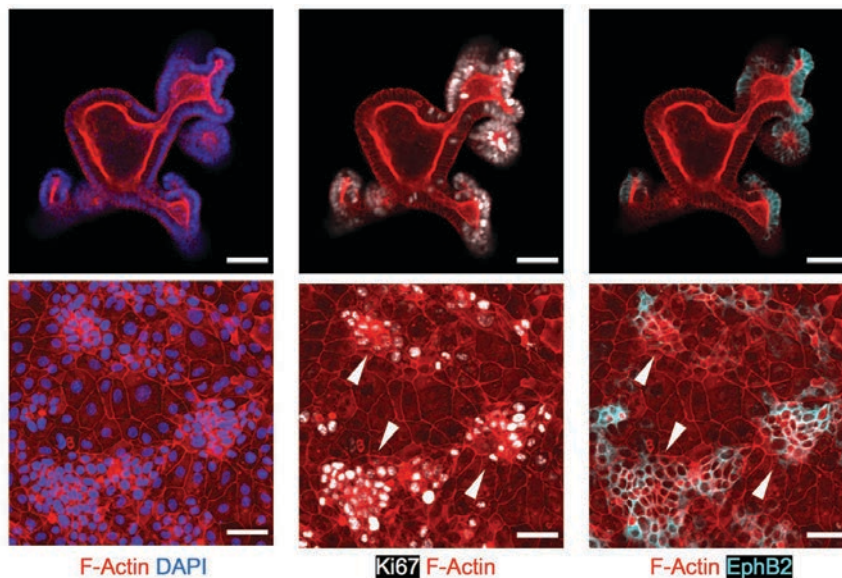


Figure 4.2.10. Representative confocal images of organoids cultured within Matrigel drops (middle z-stack) (upper panels) and monolayers of organoid-derived single cells seeded on diluted and treated Matrigel (max intensity projection) (lower panels). Fluorescence images correspond to the immunostaining of F-Actin, cell nuclei (DAPI), Ki67, and EphB2 receptor. Scale bars: 50 μ m.

To gain insight into the actual resemblance of these crypt-like domains to the *in vivo* crypt compartments, we also checked if cells were able to express EphB2 receptors in a gradient fashion. In the small intestinal tissue, it has been reported that crypt compartmentalization is associated to the ephrin-Eph ligand-receptor interactions, with ephrinB1 concentrations setting the boundaries of the compartment by triggering cell repulsion upon EphB2 receptor activation^{84,163}. Then, we performed immunostainings for EphB2 receptor for both organoids cultured on Matrigel drops and organoid-derived single cell monolayers (Figure 4.2.10). These experiments showed clearly distinguishable proliferative domains (Ki67⁺ cells) for both intestinal organoids and monolayers. Such regions were overlapping those expressing the EphB2 receptor at its highest levels, gradually fading away of the contours limited by the proliferative domains. For the non-proliferative cells, no

expression of EphB2 was observed neither for the intestinal organoids nor for the monolayers. Remarkably, this localization and gradual silence of EphB2 coincides with the one observed *in vivo*^{84,12}.

Overall, we could observe that the intestinal epithelial monolayers grown from organoid-derived single cells cultured on freeze-dried and reconstituted Matrigel preserved the ability to self-organize in proliferative crypt-like domains and non-proliferative regions. Moreover, the proliferative crypt-like domains contained the cells populations characteristic from the intestinal stem cell niche, as Lgr5⁺ intestinal stem cells and Paneth cells could be identified. Last, we also found out that the expression of the EphB2 cell membrane receptor is confined to the crypt-like domains and fades when there are non-proliferative cells. Therefore, in the light of these results and taking into account our ability to produce ephrinB1 ligands presented as micropatterns that trigger cellular positioning on substrates suitable for the culture of organoid-derived cells, we were wondering if these cells would also respond to micropatterns of these or other relevant ligands that might affect the intrinsic morphology and distribution of crypts-like domains in organoid-derived epithelial monolayers.

Previous studies have shown that intestinal epithelial monolayers possess an intrinsic organization where crypt-villus domains are self-regulated by molecular pathways with Wnt and Bone Morphogenetic Proteins (BMP) as key regulators¹²⁰. Those are intrinsic signals that are derived from the different cell types composing the intestinal epithelium and the stroma. Thus, the epithelial organization is orchestrated by molecules of both epithelial and non-epithelial origin. This became evident through a study where the Paneth cells were depleted. *In vivo*, removing the Wnt signal coming from the Paneth cells did not alter the normal intestine homeostasis, while *in vitro*, intestinal organoids development was dependent on Paneth cells as a source of Wnt signaling⁹⁷⁻⁹⁹. Thus, establishing a system able to expose the intestinal epithelium to epithelial and non-epithelial factors in a simple manner could be a way to disentangle these complex molecular pathways. As we proved that we could generate biomolecular patterns onto substrates amenable for the culture of organoid-derived single cells, our next step involved the study of the effect of such micropatterns to act on the epithelial composition and organization. We decided to focus on ephrinB1-EphB2 ligand-receptor interactions because of their cell-repulsive action triggers an easy read-out, but we also explored Wnt3a ligand.

However, before moving on to study the behavior of the monolayers on the micropatterned surfaces, we decided to better characterize the morphology and distribution of the crypt-like domains without such patterns. To do that, we cultured organoid-derived single cells on diluted and treated Matrigel-coated substrates to form epithelial monolayers (which we called control samples). After 48 hours of

culture, we fixed the samples, performed immunostainings of Ki67, F-actin and DAPI and imaged them with fluorescence microscopy. Fluorescence images obtained were analyzed through custom-made image-processing algorithms to identify the crypt-like domains of the monolayers (Figure 3.16). Once identified we computed the crypt-like domains areas, their elongation index, the distance to their first neighbors and the angle between one crypt and their two first neighbors, which we called the orientation index (Figure 4.2.11). Crypt-like domains presented areas with mean values of $(4.3 \pm 0.4) \times 10^3 \mu\text{m}^2$ (mean \pm SEM). The domains are quite circular (elongation index ~ 0.3). Thus, we calculated the crypt-like domain diameter as $74 \pm 11 \mu\text{m}$ ($2\sqrt{(\text{area}/\pi)} \pm \Delta\text{area}/\sqrt{(\text{area}/\pi)}$, where Δarea is the SEM error of the area). The mean interdomain distance a is $160 \pm 10 \mu\text{m}$ (mean \pm SEM) and they are randomly distributed across the surface of the sample (orientation index ~ 0). These values were consistent along the experiments performed, so we decided to take these dimensions into account to design micropatterns of biomolecular signals. As the order of the distribution was zero, we decided to use this parameter as an easy read-out of any effect of the micropatterns on the monolayer cell organization. Therefore, we designed and fabricated biomolecular micropatterns with regular geometries to check for any ordering effect.

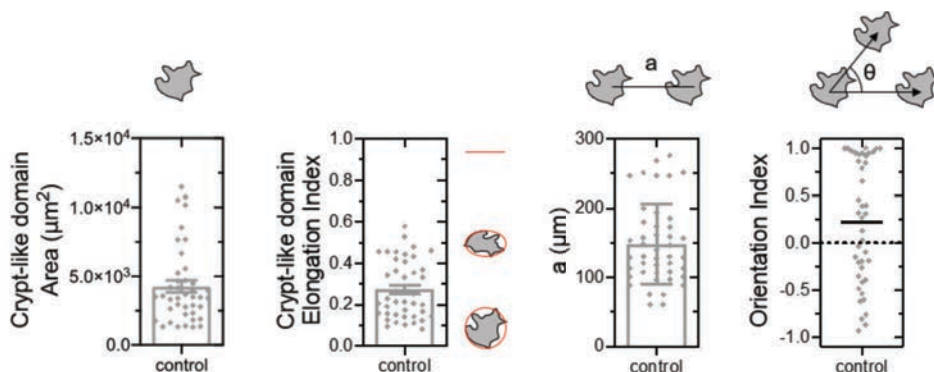


Figure 4.2.11. Analysis of the morphology and distribution of crypt-like domains in organoid-derived epithelial monolayers. The parameters plotted are; the crypt-like domain areas (mean \pm SEM); the crypt-like domain elongation indexes (mean \pm SEM); the distance between the first neighbours (mean \pm SD) and the angle between the first neighbours or orientation index (median). N = 5 experiments.

4.2.6 Design and fabrication of micropatterns with regular geometry and crypt-like domains morphology and dimensions

On the basis of the previous section, we designed and fabricated a set of photomasks, silicon-based molds and, finally, PDMS stamps that had circular features (such as the crypt-like domains) of diameters ranging of 100 and 200 μm and spaced (center-to-center) distances ranging from 150 to 400 μm . The features were disposed forming square arrays. We fabricated both holes and posts because, while some ligands such

as ephrinB1 have their highest expression outside of the crypts, other ligands such as Wnt3a have their highest expression within the crypts.

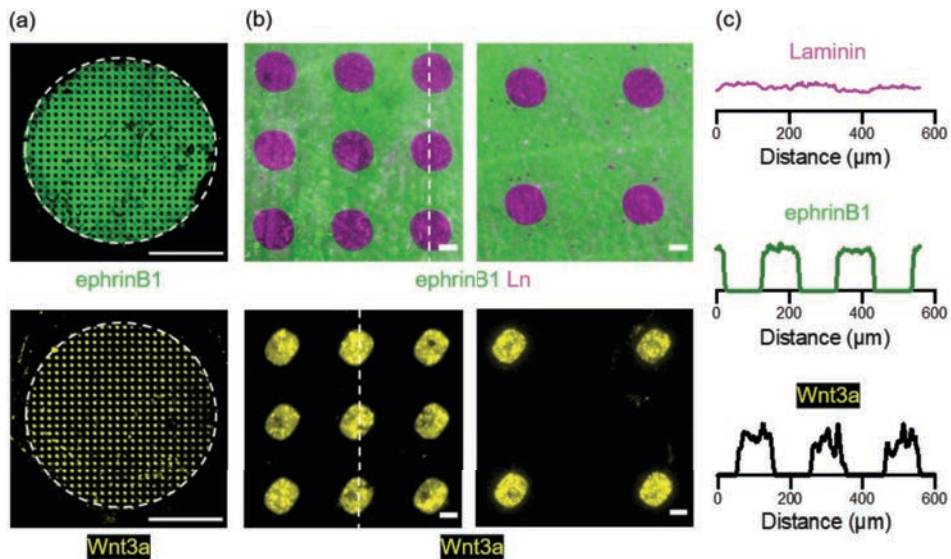


Figure 4.2.12. (a) Representative fluorescence images for ephrinB1 and Wnt3a micropatterns produced by micro-contact printing on freeze-dried Matrigel-coated substrates. Images have been obtained after reconstitution with PBS and immunostaining. PDMS stamps bearing holes were used to produce the ephrinB1 micropatterns while PDMS stamps with posts were used to produce the Wnt3a micropatterns. Scale bars: 2 mm. (b) High-magnification images of ephrinB1 and Wnt3a micropatterns. For ephrinB1, micropatterns of holes of 100 μm in diameter with a spacing (center-to-center) of 200 μm (right panel) or 400 μm (left panel) were produced (laminin was also immunostained). For Wnt3a, posts of equivalent dimensions were produced. Scale bars: 50 μm . (c) Fluorescence intensity profiles corresponding to the dash lines in (b), showing the uniformity of the Matrigel layer (upper graph) and the good contrast and proper dimensions of the ephrinB1 and Wnt3a micropatterns (middle and lower graphs).

Micropatterns of ephrinB1 and Wnt3a ligands were then produced by micro-contact printing on top of freeze-dried Matrigel substrates. After reconstitution with PBS, the micropatterns were visualized by immunofluorescence upon staining ephrinB1, laminin and Wnt3a. As shown in (Figure 4.2.12 (a)), we were able to produce highly uniform patterns in a reproducible manner over large areas ($\sim 20 \text{ mm}^2$) of both holes and posts designs. The distance between holes and posts could also be successfully varied (Figure 4.2.12 (b)). Moreover, the positive laminin staining (Figure 4.2.12 (b), upper panel) showed that the Matrigel coatings were preserved after the micropatterning and reconstitution process. Actually, laminin intensity was found to be uniformly distributed across the micropatterned areas (Figure 4.2.12 (c), upper graph), indicating that Matrigel integrity had not been substantially compromised. In addition, the fluorescence intensity of the ephrinB1 and Wnt3a micropatterns showed that their dimensions were consistent with those of the PDMS stamps and were not altered by the reconstitution procedure (Figure 4.2.12 (c), middle and lower graphs). Both graphs evidenced abrupt changes in the

fluorescence intensities of patterned and non-patterned regions, therefore suggesting a successful biomolecular transfer.

4.2.7 *Micropatterns of ephrinB1 and Wnt3a ligands are able to guide the distribution of crypt-like domains in organoid-derived epithelial monolayers*

Intestinal epithelial cells are self-organized in crypt- and villus-like domains *in vivo* but also *in vitro* in organoids and monolayers format. This process is driven by complex and interdependent biochemical signals, so it is difficult to disentangle the effects of individual factors. Thus, we examined whether our technological approach could be suitable to study the effects of such individual factors in a controlled environment. As stated above, ephrinB1 and Wnt3a ligands are shown to control the cellular compartmentalization found in the intestinal crypts both *in vivo* and in organoids^{84,85,92-94}. Therefore, we decided to test if micropatterns of ephrinB1 and Wnt3a ligands could guide the organization of organoid-derived intestinal epithelial monolayers. In particular, as a read-out parameters, we tested the size, morphology and distribution of the crypt-like domains and we compared them with the monolayers grown onto non-patterned surfaces (see section 3.5). For this purpose, we produced micropatterns of ephrinB1 ligands all over the surface except on circular holes of 100 μm in diameter and spaced (center-to-center) 200 μm ; and micropatterns of Wnt3a ligands forming circles of the same dimensions and spacing onto freeze-dried Matrigel-coated surfaces. Then, we reconstituted Matrigel with PBS, we seeded organoid-derived single cells on top of the micropatterned surfaces and we cultured them for 48 hours. As controls, organoid-derived single cells cultured on freeze-dried but non-patterned Matrigel-coated surfaces were employed. After the 48 h of culture, cells were fixed, immunostained for F-actin, cell nuclei (DAPI), Ki67, ephrinB1 and Wnt3a and imaged through a confocal fluorescent microscope.

First, the effect of the micropatterns was qualitatively assessed by processing the fluorescence microscopy images obtained (Figure 4.2.13 (a), left panels). From these pictures, individual cells were segmented, and cell area contour maps were produced as explained in section 3.7.3 (Figure 4.2.13 (a), middle and right panels). As we had previously identified in organoid-derived monolayers, cell proliferative domains that include Ki67 cells and stem cells are characterized by an increased cell density compared to non-proliferative domains, thus implying considerably smaller cell areas (Figure 4.2.9). These regions of smaller cells are clearly identified in the cell area contour maps (in yellow) and their corresponding histograms (Figure 3.17). From such histograms, we defined cell area threshold values to identify cell proliferative clusters that we attribute to crypt-like domains. To account for cell clusters and not only individual proliferative cells, a minimum area for the crypt-like domains was also introduced, as detailed in section 3.7.3. By doing this image processing, we could observe that those crypt-like domains identified in the color-

coded cell area contour maps were clearly different for the micropatterned samples and the control monolayers. In particular, while crypt-like domains appeared visually randomly distributed in the control samples, they were quite ordered on the ephrinB1 micropatterned samples and almost perfectly matching the Wnt3a micropatterned regions.

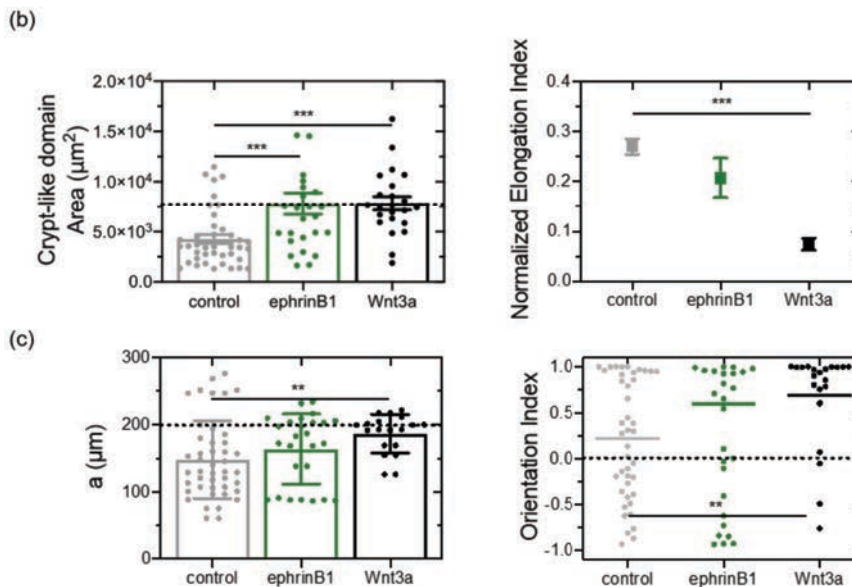
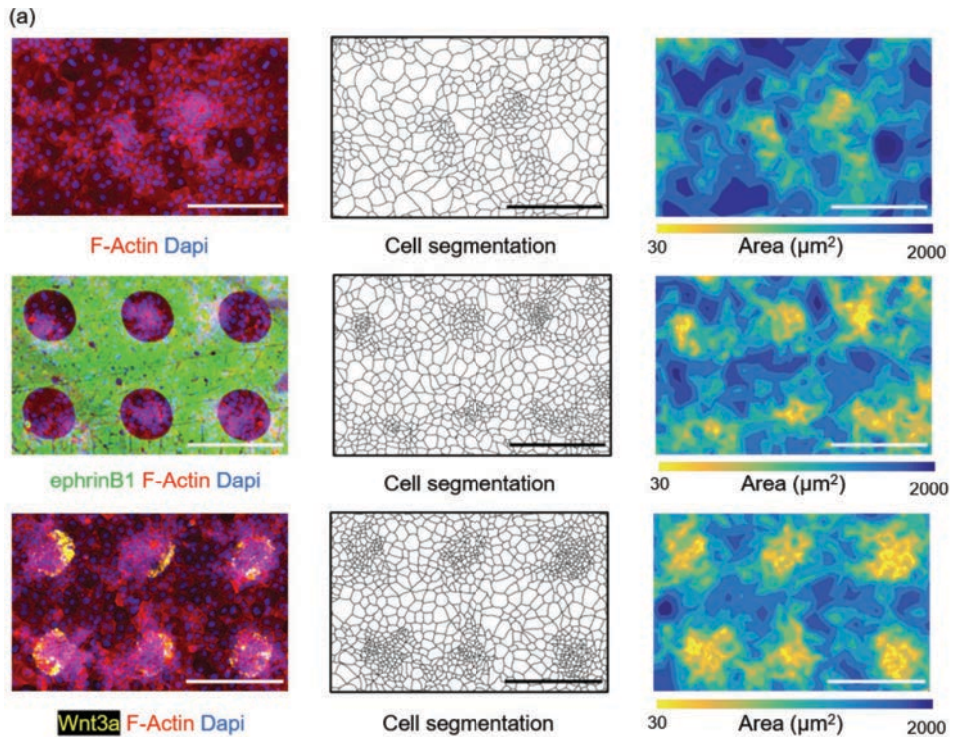


Figure 4.2.13. (a) Organoid-derived single cells seeded on diluted and treated Matrigel without pattern (upper panel), with the ephrinB1 micropatterns (middle panel) and with the Wnt3a micropattern (lower panels) at 48 hours of culture. Representative fluorescence images of F-Actin and cell nuclei (DAPI), ephrinB1 oligomers (just middle panel) and Wnt3a (just lower panel) (left panels). Representative cell area segmentation (middle panels). Representative cell area contour map (right panels). Scale bars: 200 μm . (b) Crypt-like domain area. Mean \pm SEM. Crypt-like domain normalized elongation index. Mean \pm SEM. (c) Distance between crypts (a). Mean \pm SD. Orientation index. Median. (*) $p < 0.05$, (**) $p < 0.01$, (***) $p < 0.001$, t-test. N = 3 experiments.

To quantitatively evaluate the effects of the micropatterns on the crypt-like domains, we further analyzed their morphology by computing their areas and their shape through their elongation indexes (Figure 4.2.13 (b)). On the one hand, crypt-like domain areas significantly increased with respect to the control for both ephrinB1 and Wnt3a micropatterns. In addition, the area values obtained nicely matched those imposed by the micropatterns, which surpass the areas found in the non-patterned monolayers. Therefore, by submitting the cells to ephrinB1 or Wnt3a ligands, the size of the proliferative domains could be tuned. On the other hand, we computed the circularity of the crypt-villus domains formed on the micropatterned and control samples. Since the micropatterns were not perfectly circular when produced, due to slight pressure variations during the stamping process, we introduced this effect by calculating the normalized elongation index. This parameter was obtained upon subtracting the elongation index of the micropatterns to the elongation index of the crypt-like domains. What we found was that, compared to the control, the ephrinB1 micropatterns did not significantly alter the elongation of the crypt-like domains.

Last, we quantitatively evaluated the crypt-like domain distribution found in the micropatterned surfaces and we compared it with the random distribution found for the control samples (Figure 4.2.11). As parameters, we computed the distance between first neighbors a and the angle formed between the two first neighbors and a given crypt-like domains (orientation index). The results obtained showed that crypt-like domains are further apart in the micropattern samples than in the control samples (Figure 4.2.13 (c), left graph). Thus, this parameter illustrates that the organization of crypt-like domains is altered by the micropatterns. Intestinal epithelial monolayers cultured on ephrinB1 micropatterns showed an increment in the interdomain distance with respect to the control but without any statistically significant differences. The average value of this interdomain distance is slightly smaller than the dimensions imposed by the micropattern features. However, for some domains this parameter is significantly smaller, thus indicating that the cell repulsive effects of ephrinB1 ligands on proliferative cell clusters do not impose sharp boundaries, but gradual signaling. Conversely, for Wnt3a micropatterns, the interdomain distance did not show a high dispersion and its average value matched that imposed by the micropattern features, therefore accounting for the good regularity of the crypt-like domains observed in Figure 4.2.13 (a), left panels. In

agreement with the graphs of Figure 4.2.13 (b), it seems that Wnt3a ligands presented on surfaces are very effective in confining the position and extension of crypt-like domains. When checking the orientation index, we could see that both micropatterns have a much more regular distribution of the crypt-like domains than the control samples, which was basically random. However, ephrinB1 micropatterns do not show statistically significant values with respect to the control samples. In contrast, crypt-like domains formed on the Wnt3a micropatterns showed an obvious order (orientation index ~ 1 for most of the domains), with statistically significant differences with respect to the control (Figure 4.2.13 (c), right graph).

An interesting observation in this respect that might require further attention is the molecular mechanism behind the strong action of Wnt3a ligands. Despite being out of the scope of this thesis, fluorescence microscopy pictures of the printed Wnt3a before and after cell growth clearly show what appears as a clustering effect of the cells on these substrate-presented ligands (Figure 4.2.14). We recently demonstrated that clustering ephrinB1 ligands through nanopatterned surfaces results in faster and more efficient signaling by speeding up the clustering of EphB2 receptors^{144,159}.

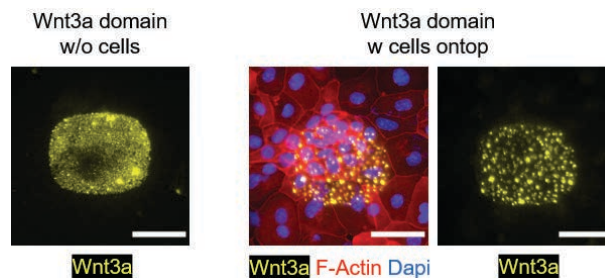


Figure 4.2.14. Representative fluorescence images of Wnt3a micropatterns before and after cell seeding and growth. The images show the clustering of the Wnt3a ligands upon the action of the cells. Scale bars: 50 μm .

Overall, these results suggest that the morphology and distribution of crypt-like domains formed in organoid-derived intestinal epithelial monolayers can respond to the presentation of surface-bound ligands in a micropatterned fashion. EphrinB1 micropatterns significantly altered their size and spatial distribution in response to the presence of the ligands, but the cell repulsive effects was not very efficient in confining the shape of the crypt-like domains to that imposed by the circular holes in the micropattern. In contrast, Wnt3a micropatterns significantly determined the size, shape and spatial distribution of the crypt-like domains in response to the surface-bound ligands. Thus, this ligand was very efficient in confining the size and the shape of the proliferative domains to the size imposed by the pattern features.

The different responses of the monolayers to these ligands might stem from their different expression patterns *in vivo*. While ephrinB1 ligands are expressed in a gradient manner along the crypt-villus axis^{84,85}, the Wnt3a signal is mainly restricted to the bottom of the crypts where the stem cells reside, as their main source in the absence of non-epithelial tissue compartments, is the Paneth cells^{94,95}. Thus, the strong confinement evidenced here by the Wnt3a ligand versus the not so strong confinement produced by the ephrinB1 ligands suggests that our system, despite its simplicity, is able to reproduce the signaling patterns found in the tissue *in vivo*. Through these experiments, though, we can conclude that we have designed and produced a tool to systematically investigate the effects of individual ligands on the self-organization of organoid-derived intestinal epithelial cells. One might then speculate that such a system could be employed in gathering some information that could be useful as an input to predict the behavior of more complex systems such as organoids or tissues *in vivo*.

4.2.8 The characteristic dimensions of ephrinB1 and Wnt3a micropatterns might be counterbalanced by the intrinsic self-organization properties of the organoid-derived intestinal epithelial monolayers.

To further examine the potential of our technological tool in testing the effects of individual ligands on the cellular self-organization abilities of organoid-derived cell monolayers, we varied the design of the micropatterns. In a first set of experiments, we maintained the size of the holes or posts in 100 μm of diameter, but we increased the interdomain spacing (center-to-center) to 400 μm . We then produced micropatterns of ephrinB1 and Wnt3a ligands onto freeze-dried Matrigel-coated surfaces by micro-contact printing. Equivalent freeze-dried Matrigel surfaces without patterns were used as controls. After Matrigel reconstitution, we seeded organoid-derived single cells and we cultured them for 48 hours. After this time, we fixed the cells, immunostained the monolayers for F-actin, cell nuclei (DAPI), Ki67, ephrinB1 and Wnt3a, and we imaged the samples in the confocal fluorescence microscope.

As hereinbefore, we first qualitatively evaluated the effects of the micropatterned ligands by processing the fluorescence images (Figure 4.2.15 (a), left panels). Upon individual cell area segmentation, cell area contour maps were produced (Figure 4.2.15 (a), middle and right panels). Contrary to what was seen in the previous section, no obvious order could be visually identified upon performing the thresholds imposed for the cell area and minimum size of the crypt-like domains. We then decided to quantitatively evaluate the effects of the micropatterns on the size and the shape of the crypt-like domains formed in these monolayers. We observed that for none of the tested ligands the crypt-like domains showed sizes significantly different than those measured on the control samples (Figure 4.2.15

(b), left graph). Moreover, on these samples, the proliferative domains were smaller than the theoretical dimensions imposed by the micropatterned features. There were, however, significant effects on the elongation indexes, which were found to be more circular on the micropatterns than on the control samples (Figure 4.2.15 (b), right graph). On the other hand, regarding the organization parameters, intestinal epithelial monolayers cultured on ephrinB1 or Wnt3a micropatterns did not show interdomain distances close to those imposed by the micropattern features. On the contrary, these distances were indistinguishable from the ones found in the non-patterned control samples (Figure 4.2.15 (c), left graph). A similar trend was observed for the orientation index, which was in all the cases not showing any evident order, as it was seen for the controls (Figure 4.2.15 (c), right graph). Taken together, these experiments indicate that intestinal organoid-derived monolayers not change their intrinsic self-organization properties when they are exposed to micropatterns of ephrinB1 and Wnt3a ligands if the interdomain distance between features is increased by 2.5-fold with respect to their natural value ($400 \mu\text{m}$ vs. $160 \pm 10 \mu\text{m}$).

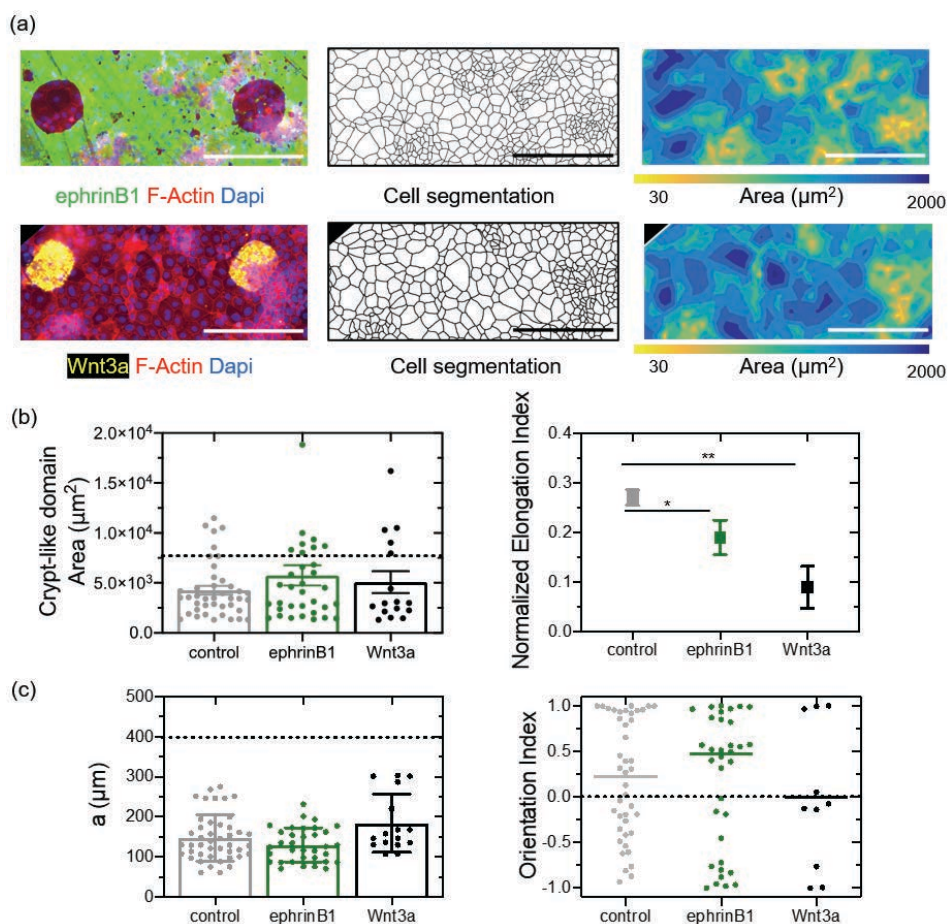


Figure 4.2.15. (a) Organoid-derived single cells seeded on diluted and treated Matrigel with the ephrinB1 micropatterns (upper panel) and with the Wnt3a micropattern (lower panels) at 48 hours of culture. Representative fluorescence images of F-Actin, cell nuclei (DAPI), ephrinB1 oligomers (just upper panel) and Wnt3a (just lower panel) (left panels). Representative cell area segmentation (middle panels). Representative cell area contour map (right panels). Scale bars: 200 μm . (d) Crypt-like domain area. Mean \pm SEM. Crypt-like domain normalized elongation index. Mean \pm SEM. Distance between crypts (a). Mean \pm SD. Orientation index. Median. (*) $p < 0.05$, (**) $p < 0.01$, t-test. N = 3 experiments.

Then, in a second set of experiments, we designed micropatterns maintaining the dimensions of the holes and posts features to 100 μm in diameter and decreasing their interdomain spacing to 150 μm , which is a slightly smaller value than the natural one measured on monolayers grown onto non-patterned substrates. In this case, and due to the not so sharp confinement effects observed for the ephrinB1 ligands, we decided to first perform these experiments with Wnt3a ligands. After printing, we proceeded as before in terms of cell culture, immunostaining, and image processing.

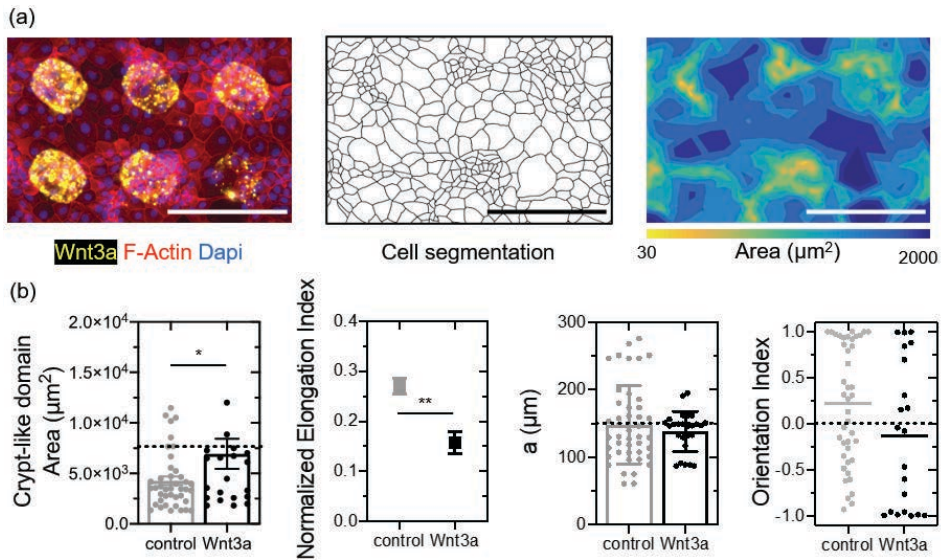


Figure 4.2.16. (a) Organoid-derived single cells seeded on diluted and treated Matrigel with the Wnt3a micropattern at 48 hours of culture. Representative fluorescence images of F-Actin, cell nuclei (DAPI) and Wnt3a (left panel). Representative cell area segmentation (middle panel). Representative cell area contour map (right panel). Scale bars: 200 μm . (d) Crypt-like domain area. Mean \pm SEM. Crypt-like domain normalized elongation index. Mean \pm SEM. Distance between crypts (a). Mean \pm SD. Orientation index. Median. (*) $p < 0.05$, (**) $p < 0.01$, t-test. N = 3 experiments.

The fluorescence pictures and cell area contour maps allowed us to identify the regions attributed to the crypt-like domains (Figure 4.2.16 (a)), where not a very clear order could be seen. The quantification of the morphological parameters revealed that the crypt-like domains showed an increase in their area with respect to the control (Figure 4.2.16 (b), left graph). In addition, the mean value of crypt-like

domain areas obtained matched with the area stipulated by the micropatterns. Furthermore, the Wnt3a micropattern triggered more circular crypt-like domains with respect to the control (Figure 4.2.16 (b), right graph). Regarding the interdomain spacing, it matched the distance imposed by the micropattern and coincided with the interdomain distance showed by the controls although the crypt-like domains were randomly oriented (orientation index ~ 0). Taken together, approaching the distance between the centers of Wnt3a micropatterns increases the cell confinement within the dimensions of the micropatterns, maintains the crypt-like domains apart the distance imposed by the pattern design and increases the circularity of crypt-like domains. On the other hand, the crypt-like domains were found to be randomly oriented.

4.2.9 Micropatterns of different biomolecules modulate the crypt-like domain morphology and distribution in epithelial monolayers according to their biological role

Finally, we systematically performed the experiments presented in the previous section for ephrinB1 and Wnt3a micropatterns of circles of 100 μm in diameter and varying spacings between 150 and 400 μm . We then quantified the same parameters as before and we compiled the results as a function of the micropattern spacing (crypt-like domain spacing) in the graphs shown in Figure 4.2.17. On the one hand, crypt-like domain area showed the same tendency for both ephrinB1 and Wnt3a micropatterns: they were close to the area imposed by the micropatterns for spacings between 150 and 200 μm (Figure 4.2.17 (a)). These interspacing values were close to the one found for spontaneously assembled crypt domains ($\sim 160 \mu\text{m}$). For values higher than 200 μm , the areas of the crypt-like domains decreased and no longer matched those imposed by the patterns for any of the ligands. In addition, for the largest distances of 400 μm , the cells seeded on the micropatterned surfaces self-assembled in crypt-like domains of areas approaching the intrinsic size of the cultures, as if the intrinsic signaling that regulates the crypt-like domains¹²⁰ was overcoming the signaling imposed by the micropatterns (Figure 4.2.17 (b)). Thus, for relatively large distances between exogenous signals, the epithelium stops responding to the exogenous signals and recover their intrinsic compartmentalization.

The evaluation of the crypt-like domains elongation for the ephrinB1 micropatterns showed close-to-circular domains such as those generated on non-patterned substrates (Figure 4.2.17 (c)). Moreover, there were not showing significant differences with the distances between the micropatterns, probably because this was close to the intrinsic values displayed by the self-assembled system. On the other hand, the Wnt3a micropatterns imposed a more circular morphology for the crypt-like domains, following the shape template provided by the micropatterns. In

addition, micropatterns that were $\sim 200 \mu\text{m}$ apart showed an almost perfect circular shape. This correlates well with the previous observations on the strong confinement effect produced by the Wnt3 factors *in vivo*⁸¹.

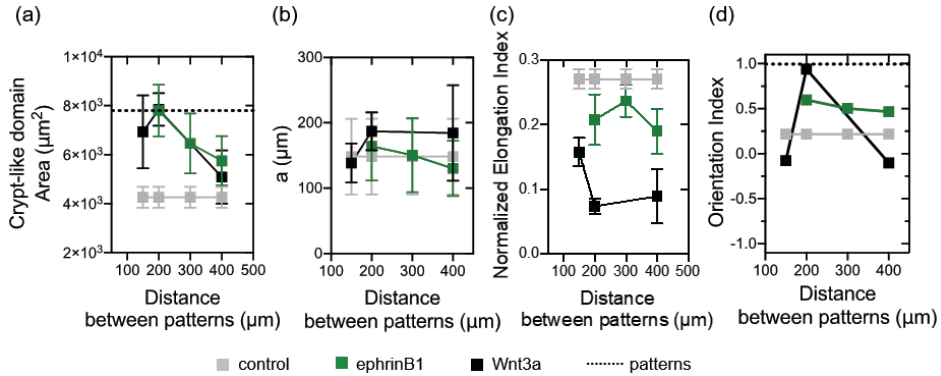


Figure 4.2.17. Summary of the morphological and order parameters related to the organization of crypt-like domains of organoid-derived intestinal monolayers cultured onto micropatterns with different pitch distances. The control refers to the same cells cultured onto non-patterned surfaces. (a) Crypt-like domain areas. Mean \pm SEM. (b) Distance between crypt-like domains. Mean \pm SEM. (c) Crypt-like domain elongation index. Mean \pm SD. (d) Orientation index. Median. N = 3 experiments.

Finally, the distribution of the crypt-like domains across the surface was a parameter quite sensitive to the presence of the micropatterns. Despite no statistically significant differences could be accounted for, the orientation index of the crypt-like domains on ephrinB1 micropatterns tended to be higher than that measured for the control samples, indicating a certain order in the system attributed to the spatial disposition of the micropatterns. This degree of order did not depend on the distance between the micropatterns (Figure 4.2.17 (d)). On the contrary, Wnt3a micropatterns strongly ordered the crypt-like domains when they were 200 μm apart. For interdomain distances smaller (150 μm) or larger than this one (400 μm), the crypt-like domains were randomly oriented. Thus, patterns of Wnt3a ligands, mainly expressed by Paneth cells located within the crypts in the *in vivo* tissue, also demonstrated their ability to highly confine the crypt-like domains *in vitro*.

Overall, the response landscape of organoid-derived intestinal cells to ephrinB1 and Wnt3a ligands suggests a specific balance for the pitch distance of the features of the micropatterns and the organization of the crypt-like domains. Noteworthy, our results also reveal that the response to ephrinB1 and Wnt3a signals is differential. While in general ephrinB1 does produce more shallow confinement effects, the confinement effects of Wnt3a are very strong. This might be related to the differential expression of these ligands in the tissue *in vivo*. The Wnt3a is a factor mostly compartmentalized at the bottom of the crypts, while ephrinB1 forms gradients along the whole crypt-villus axis.

4.2.10 Crypt-like domain areas depend on the size of the micropatterned features

To gain insights into how individual signals regulate the size of the proliferative cell clusters in our organoid-derived intestinal monolayers, we did perform experiments analogous to those reported in the previous section but changing the area of Wnt3a micropatterns while keeping the ratio between their diameter and the interdomain spacing. Therefore, we cultured the cells onto micropatterns of circles of 200 μm in diameter with a spacing (center-to-center) of 400 μm and micropatterns of circles of 100 μm in diameter with a spacing (center-to-center) of 200 μm . Through this design, we could decouple the strong effect caused by the interdomain distance observed before.

We first qualitatively evaluated the effects of the micropatterns on the crypt-like regions by fluorescence microscopy images and their corresponding cell area contour maps (Figure 4.2.18 (a)). Quantitative measurements on these samples showed that the crypt-like domain areas were increasing according to the increasing size of the Wnt3a micropattern features. (Figure 4.2.18 (b)). Through these experiments, we could then demonstrate that by adding Wnt3a ligands in an exogenous manner, the size of the crypt-like domain areas could be tuned, and, in consequence, this suggests that the proliferative capacity of the monolayer could be altered.

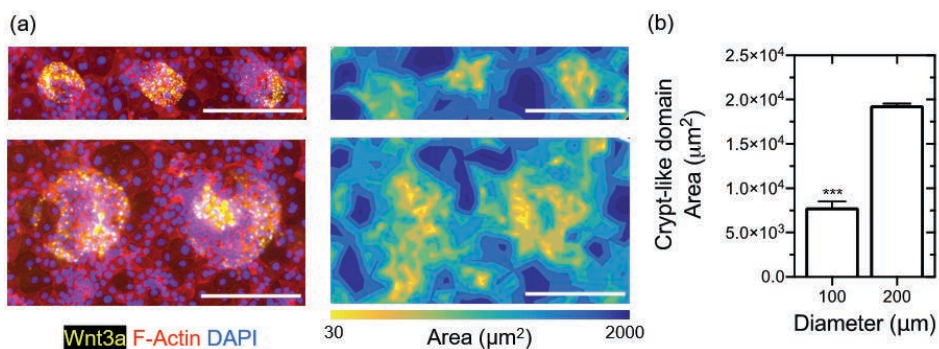


Figure 4.2.18. (a) Organoid-derived single cells seeded on diluted and treated Matrigel with Wnt3a micropatterns after 48 hours of culture. Representative fluorescence images of F-Actin, cell nuclei (DAPI) and Wnt3a (left panels). Representative cell area contour maps (right panels). The diameters of the Wnt3a micropatterns are: 100 μm (upper panel) and 200 μm (lower panel). Scale bars: 200 μm . (d) Crypt-like domain areas. Mean \pm SEM. (***) $p < 0.001$, t-test. $N \geq 1$ experiments.

Overall, the experiments presented in this section demonstrate the success of our bioengineering approach based on micropatterning to study the effects of cell-cell and cell-secreted biochemical factors on the self-organization of organoid-derived intestinal epithelial monolayers.

5 Discussion

The culture of intestinal organoids has opened unprecedented opportunities for studying epithelial tissue organization by providing systems that recapitulate *in vitro* the *in vivo* physiology of the tissues⁶⁶. By employing organoids, much has been discovered about the biology of complex 3D epithelial tissues, and it is now widely recognized the key role of the interplay between substrate-derived cues and cell-dependent signaling molecules for tissue development, homeostasis, and regeneration. However, disentangling the role of individual components cannot be efficiently studied *in vitro* even when employing organoids. Limitations arise from the fact that organoids are normally embedded in 3D cell-derived protein mixtures where the spatial distribution of ECM proteins and cell-derived signaling molecules that orchestrate the tissue organization *in vivo* cannot be easily retrieved. Recent studies report that organoid-derived cells are able to self-organize into 2D intestinal epithelial monolayers that also recapitulate the *in vivo*-like cell type composition and organization when seeded on thin layers of the same cell-derived protein mixture^{119,120}. The formation of these intestinal monolayers provides a cell culture system easier to probe and analyze to gain a better understanding of the tissue organization and its properties. The experiments and results presented in this thesis aim to make use of this biological *in vitro* model and bioengineering tools to investigate the impact of substrate-derived cues in the self-organization process of organoid-derived intestinal epithelial cells.

The first part of this thesis deals with the role of ECM cues in guiding intestinal epithelial self-organization. We focused our attention on the role that ECM density and composition has in the formation of self-organized 2D intestinal monolayers and, in particular, in the transition from scattered organoid-derived single cells to the growth of compartmentalized intestinal monolayers fully covering the culture surface. Our main finding is that although self-organized epithelial monolayers are always achieved, the dynamics of this process are not unique, but they depend on the protein surface density and the proportion of stem cells in the cultures. These two factors regulate the direct formation of monolayers or the formation of transient 3D structures, namely 3D-tubular networks or 3D-aggregates (Figure 5.1), that eventually evolve into monolayers. Noteworthy, these factors and the observed cellular outcomes define a phase diagram in which the different phases are clearly distinguishable and phase boundaries are quite sharply defined. While protein surface density dictates the formation of monolayers or transient 3D structures, the stemness of the culture dictates the shape of the 3D structures.

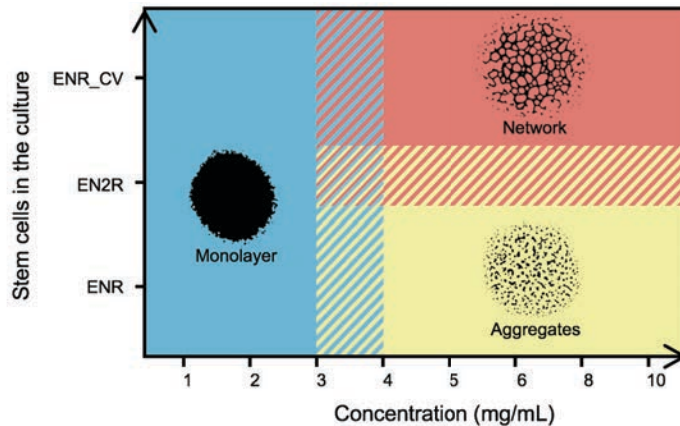


Figure 5.1. Phase diagram of the intestinal epithelial organization as a function of Matrigel concentration and stem cells in the culture. The three top images are representative binary images from thresholded fluorescence images of F-Actin for organoid-derived single cells on Matrigel thin films with different concentrations after 24h.

Prior research on epithelial tissues employing *in vitro* models has explored the impact of cell-ECM interactions on the tissue organization by two different approaches. In one of them, epithelial cells such as MDCK, Caco-2 or breast cells are embedded within 3D matrices, mainly Matrigel or collagen with protein concentrations $> 1 \text{ mg mL}^{-1}$, in a range similar to the one found in tissues^{37-41,43,44}. Through this strategy, cells proliferate and self-organize into 3D structures that retain some of the features of their tissues of origin such as the presence of a lumen and cell polarization. In the other approach, epithelial cells are cultured onto 2D substrates coated with protein surface densities in the range of $1 - 80 \text{ } \mu\text{g mL}^{-1}$,⁴⁸ concentrations or protein surface densities of $0.01-1 \text{ } \mu\text{g cm}^{-2}$.⁴⁷ These are typically several orders of magnitude below those found in the 3D matrices. On substrates coated with protein surface densities within this range, cells such as MDCK⁴⁸ or primary hepatocytes⁴⁷ organize in monolayers for the highest concentrations and on 3D aggregates for the lowest concentrations (very far away from the physiological values of tissue matrices). By employing a hybrid strategy that used protein concentrations typical from 3D matrices but distributed on 2D surfaces we were able to retrieve the formation of 3D epithelial structures such as tubular networks or cell aggregates on top of 2D substrates. In addition, the 3D-tubular networks formed when employing organoid-derived intestinal epithelial cells had basal-out polarity like intestinal organoids embedded in 3D matrices with this very same protein concentrations. Therefore, although we fixed the substrate 2D dimensionality, the ECM density could trigger cell organizations typical of 3D environments, suggesting that protein concentration (or density if we deal with surfaces) drives culture dimensionality in the epithelial cells tested. Even though the relevance of the protein density for cell adhesion in 2D cultures is widely

recognized, our results point out that it is also a key parameter in guiding the architecture of the cultures obtained.

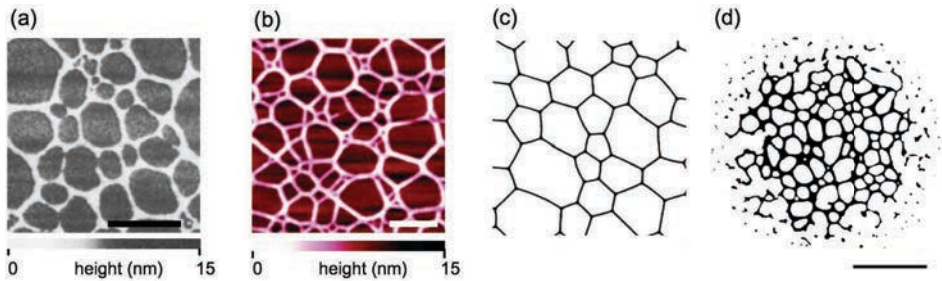


Figure 5.2. (a) Scanning Tunneling Microscopy images of polystyrene network on a silicon surface. Scale bar: 1 μ m. Reproduced with modifications by permission of Stange et al. 1992. (b) Scanning Force Microscopy micrographs of collagen network on a mica surface. Scale bar: 1 μ m. Reproduced with modifications by permission of Mertig et al. 1997. (c) Representative detail photograph of 2D soap foams. Reproduced with modifications by permission of Glazier et al. 1987. (d) Representative binary image from thresholded fluorescence microscopy picture of F-Actin for organoid-derived single cells cultured on substrates coated with Matrigel at 10 mg/mL after 24 hours of culture. Scale bar: 2 mm.

Although the formation of tubular structures *in vitro* is commonly reported for vascular cells, to our best knowledge, the transient 3D tubular networks shown in this thesis for intestinal epithelial cells have not been previously reported. These 3D-tubular networks are similar to soap foams^{49,50,138}, de-wetted collagen networks^{52,138}, or de-wetted polystyrene networks^{51,138} (Figure 5.2). In spite of their different nature, all these systems are distributed according to a polygonal Voronoi tessellation. The well-defined topological and metrical properties of these networks indicate that they have a homogeneous order in space. If we consider the second moment of the distribution of the edge number of the polygons as a measure of disorder^{52,138}, we find out that the order of our intestinal epithelial networks is close to the order shown by protein collagen networks, and both systems are more disordered than polystyrene networks or soap foams. In these two last cases, their order is achieved during their temporal evolution¹³⁸. For instance, the rupture of the thinnest rims between holes of very different sizes in the polystyrene networks leads to the coalescence of holes. Similarly, the diffusion of gas through the cell walls due to pressure differences of holes with different sizes leads to coalescence in soap foams. We hypothesize that neither coalescence nor diffusion takes place during the evolution of our networks, because as reported to happen in collagen networks¹³⁸, we did not observe a temporal evolution of the polygon sizes. In systems such as collagen networks, it has been reported that the formation of Voronoi tessellation-like structures is related to processes that occur almost simultaneously across large areas⁵¹. In this case, network emergence is driven by the evaporation rate of the solvent, which drags the collagen molecules in a passive manner in what is called a de-wetting process. It is therefore appealing to think that the organization evolution

observed in our cultures due to the ECM protein surface density might be interpreted as a transition into different wetting states. Actually, we attributed the two phases found in tissue organization to a complete-to-partial wetting transition from 2D-monolayers to 3D-structures induced by Matrigel concentration.

Previous studies have shown that cells and cellular monolayers placed on non-adhesive substrates (e.g. agarose gels, PEG-PLL) form 3D aggregates by a de-wetting process^{62,164}. These studies did not observe, however, networks distributed according to a Voronoi tessellation. As we previously hypothesized that the cellular organization of intestinal epithelial organoid-derived cells in networks might similarly occur as in collagen networks, we did proceed to study their process of formation. As opposed to collagen monolayers, where the molecules are passively dragged by the liquid evaporation, our system is composed of cells able to actively migrate. Indeed, our experiments demonstrated that in our system, the intestinal stem cells (ISCs) motility depends on the ECM concentration. On the one hand, the increased motility could have arisen from their reduced adhesion to the ECM, as cell motility and cell-ECM adhesion are in general related by a bi-phasic curve¹⁶⁵. Usually, cell adhesion is linked to the protein amount present in the matrix. However, the data gathered in our experiments pointed out that ISCs have increased motility on the substrates with the highest protein concentration. Although the mechanism of this enhancement of the active ISCs migration has not been explained yet, our results agree with a recent paper that studied the formation of large-scale structures of HeLa cancer cells in Matrigel with different thickness¹⁶⁶.

Moving further in investigating the formation of the tubular networks, we found out that these were not formed when we changed the Matrigel matrices to collagen type I matrices. On these substrates, 2D epithelial monolayers were formed regardless of the protein concentration employed. Therefore, we speculated that the two phases of tissue organization observed could be attributed to cues provided by Matrigel composition. At this point and given the accumulated evidence of the impact of ECM protein concentration and composition on the intestinal epithelial self-organization, we used Yes-associated protein 1 (YAP) to investigate how these two different matrix compositions, i.e. Matrigel and collagen type I, influence cell mechano-responses. We showed that YAP is activated in a different manner depending on the matrix composition, the cellular environment and the substrate dimensionality⁸⁸. Therefore, the activation of YAP could provide critical information about the mechanical signals needed for more physiological maintenance of intestinal organoid-derived cells. Our results indeed indicate that substrate stiffness is a key parameter in determining the self-organization properties of intestinal epithelial cells. When cells are cultured onto substrates with stiffness values higher than those attributed to the basement membrane of the intestinal epithelium (~ 20 kPa)¹⁵⁸, 3D-tubular networks are formed. On the softest substrates, however, organoid-derived

single cells form 2D monolayers in a fast and efficient manner regardless of the ECM concentration. The successful formation of these monolayers is in contrast with the wetting behavior often described in the literature for other epithelial cells cultured on soft substrates, where cell migration is impaired at relatively low stiffness values^{56,59,60,63}.

Cell-ECM interaction is reciprocal: while cells interface with their ECM through focal adhesions, ECM directs their organization¹⁶⁷. Besides this, the optimal substrate for organoid formation is mechanically dynamic and constantly remodeled by cell-ECM interactions¹⁰⁴. Our experiments indicate that when Matrigel concentration is above a well-defined threshold, organoid-derived intestinal epithelial cells can redistribute the ECM to form 3D-tubular networks. The identification of this ECM redistribution provides a basis on which to further explore the mechanism that controls epithelial organization.

Finally, not only cell-ECM interactions seem to be key for the formation of the 3D tubular networks observed. On the contrary, such tubular structures are not observed when culturing other epithelial cell types such as Caco-2 or MDCK cells. Therefore, taking into consideration the multicellular character of the organoid-derived intestinal epithelial cells, we hypothesized that cell-derived signals were also needed for the tubular networks to form. When analyzing the cell population in detail, we did observe that there was a similar percentage of proliferative cells in both monolayers and tubular networks. However, the percentage of stem cells was statistically significantly lower in the monolayers than in the networks. Since all the cells used for biological replicates were coming from the same organoid pool and were cultured using the same culture medium, we attributed the differences in the stem cell population to an increased stemness potential fueled by the presence of the 3D tubular structures. Due to ISCs proliferative capacity, we speculate that cell-ECM interactions and cell migration enhancement promoted the formation of ISCs clusters formed around laminin accumulations. These regions might provide ISCs with a favorable environment for their symmetric division and formation of crypt-like structures enriched in stem cells. To test this hypothesis, we reduced the proportion of intestinal stem cells (ISCs) in the culture. Our findings reveal that there is a strong correlation between the stem cell proportion and the formation of the tubular structures. Indeed, this is impaired when the ISCs population decreases below a certain threshold. In such conditions, organoid-derived intestinal epithelial cells will behave similarly than cell lines and will form 3D cellular aggregates. In this regard, one has to consider that *in vivo* intestinal crypts are formed by a certain number of stem cells to guarantee cell renewal and tissue homeostasis¹⁶⁸. This intrinsic property of the tissue is, till some extent, mimicked by our *in vitro* model.

Actually, *in vivo* intestinal crypts not only allocate a certain number of ISCs, but also have pre-defined dimensions. Interestingly, in the 3D-tubular networks found here,

the mean edge length of the polygons ($\sim 200 \mu\text{m}$) is comparable with the *in vivo* dimensions of intestinal crypts¹⁴⁷. While in de-wetted collagen networks, the length of the collagen monomers is comparable to the characteristic diameter of the pores¹⁴⁸, analogously in here we can speculate that the emerging tubular structures might be the equivalent to collagen monomers. These emergent structures appear via cell-cell crosstalk facilitated by cell-ECM interactions and triggered by characteristic lengths of the *in vivo* tissue and depend on the ISC number. Thus, primary intestinal epithelial cells have the capability to form structures with physiological dimensions independently on the dimensionality of the culture or external signaling gradients, at least temporarily.

Indeed, while passive building elements like collagen molecules may generate very stable networks^{52,138}, our results demonstrate that intestinal epithelial networks are transient structures. On the other hand, polystyrene networks or soap foams, which are built from elements that are much smaller than the polygon edges of the network formed, decay into droplets via Rayleigh instability⁵². We have to consider that this is also the case in our networks, as the building elements, which are the organoid-derived single cells, are also much smaller than the polygons forming the network structures. In addition, as intestinal epithelial cells proliferate and therefore consume energy, the intestinal epithelial network is out of equilibrium. Overall, these factors might explain the partial-to-complete wetting transition happening when the network undergoes the transition and becomes a monolayer.

In the second part of this thesis, we explored the effects of cell-derived signals on the self-organization of organoid-derived intestinal epithelial monolayers. Epithelial or stromal cell-derived signals might exert their effects through cell-cell contacts (juxtacrine signals) or through paracrine action via cell-secreted molecules that diffuse through the ECM of the tissue. *In vivo*, these signals regulate tissue development, maintain homeostasis, and induce regeneration upon damage by a set of complex inter-dependent mechanisms. Regulation might involve the establishment of gradients along the crypt-villus axis such as the case of ephrinB1/EphB2 ligand/receptor pair^{84,85} or feedback loops such as the regulation of proliferation and differentiation via Wnt and BMP pathways¹²⁰, respectively. Usually, these complex signaling pathways are studied by genetic approaches, blocking with antibodies or by tuning the composition of the cell culture medium. In our studies, as an alternative we decided to propose the use of surface-bound ligands spatially located through micropatterning techniques.

We first determined that micro-contact printing technique can be successfully adapted to transfer both cell-membrane and soluble molecules onto soft, sticky substrates such as Matrigel. Not only the transfer was successfully achieved with features such as lines but also more challenging structures such as circles of hundreds of microns in diameters could be patterned with high fidelity when

employing PDMS stamps with the proper aspect ratio between the feature size and height (close to 10:1). The molecules transferred were active and the strength of their activity could be controlled by tuning their concentration when “inking” the stamp. Altogether, the system designed demonstrated a high versatility and was amenable for the culture of organoid-derived intestinal epithelial cells.

We then used the above-mentioned system to mimic the *in vivo* spatial distribution of ephrinB1, a juxtacrine signal involved in the compartmentalization of the intestinal epithelial cells, and Wnt3a, the major paracrine signal involved in this process. They were transferred to specific sites and at physiologically relevant densities. Although the *in vivo* gradients were simplified in here using an on/off signal, one might think on using a similar approach by employing other micropatterning technologies such as inkjet printing or microfluidics, previously used at the laboratory^{169,170} or photopatterning (PRIMO)¹⁷¹. The use of inkjet printing using piezoelectric pipettes able to dispense nanoliter volumes of solutions, enables the creation of arrays of biochemical molecules by non-contact protein deposition directly on top of the surface¹⁶⁹. The microfluidic device allows the formation of biochemical molecular gradients with customizable length and slope at the micrometer scale¹⁷⁰. The PRIMO is an optical setup that enables protein photopatterning by UV-light through the objective of a conventional inverted microscope¹⁷¹. These methodologies are useful because they allow us to precisely control and manipulate these gradients. However, their compatibility with soft and sticky Matrigel layers is not straightforward. On the contrary, our technique allows the easy transfer of relevant biomolecules for the organization of the small intestinal epithelium such as ephrinB1 ligands and their EphB2 receptor or Wnt3a to specific sites on thin Matrigel coatings.

First, we investigated the crypt-like domain distribution spontaneously generated on our non-patterned substrates by defining customized algorithms based on cell area. Through this analysis, we found that the non-patterned substrates had crypt-like domains with mean diameters $\sim 70 \mu\text{m}$, while the interdomain distance was $\sim 160 \mu\text{m}$. Then, using our micropatterning platform we evaluated the effects on this intrinsic crypt-like domain distribution induced by either ephrinB1 or Wnt3a ligands. To do that, we challenged the response of the system to several micropattern sizes and interdomain spacing. Overall, we found that when using micropatterning dimensions close to the ones displayed by the self-organized monolayers, both ephrinB1 and Wnt3a ligands redistributed the crypt-like domains following the signals imposed by the micropatterned template. This means that, through the exogenous signals, we imposed the endogenous dimensions of the crypt- and villus-like domains. However, Wnt3a micropatterns were much more efficient in confining the distribution on the crypt-like domains than ephrinB1 ligands. We suggest that this might be related to the differential expression of these

ligands in the tissue *in vivo*. Wnt3a of epithelial origin is produced by Paneth cells, which sit within the crypts between the stem cells. Therefore, their signaling is mostly confined at the bottom of the crypts. Meanwhile, ephrinB1 forms gradients along all over the length of the crypt-villus axis. Crypt-like domains are composed of ISCs, Paneth cells and transit-amplifying (TA) cells, particularly stem cells form a compartment that is surrounded by a ring of TA cells. Thus, differences in size between the micropatterned features and the proliferative crypt-like domains observed may arise from the fact that while Wnt3a signals for the location of a specific and steady subset of cells (stem cells), ephrinB1 defines the boundaries of a more heterogeneous and dynamic group of cells (TA cells), which could be more sensitive to fluctuations and therefore translate into less order.

An additional effect derived from imposing certain dimensions to the crypt-like domains is that, as the micropattern size is slightly larger (100 μm in diameter) than the natural size of the crypt-like domains formed spontaneously on the monolayers, the area of the crypt-like domains is also increased. This is even more evident when increasing the area of the exogenous signals and maintaining the area in between, thereby tuning the proliferative domains. If by increasing the crypt-like domain area the proliferative capacity of these monolayers may have been enhanced is a question yet to be solved. The tuning of the proliferative capacity could be studied either by verifying the proportion of Ki67⁺ cells per crypt-like domain or by verifying if there are changes in the number and positioning of ISCs or Paneth cells in the crypt-like domains, since the monolayer may regulate their proliferation through downregulation of the Paneth cell population under high Wnt condition¹²⁰. If indeed the increase in crypt-like domains area translated into an increase in the proliferative capacity, this would confirm the role of Wnt3a in the regulation of the intestinal proliferation, but would also suggest a role for ephrinB1 in this process. This effect might be used in practice to mimic the over-growth observed in intestinal tissues of colorectal cancer mutations such as *Adenomatous polyposis coli* (*Apc*) mutations¹⁷². Inactivation of *Apc* in the intestinal stem cells stops their migration and differentiation, and efficiently drives intestinal cancer formation. In contrast, inactivation of *Apc* in differentiated cells does not induce sustained tumors¹⁷².

Interestingly, through these micropatterning experiments we also discovered that by increasing the interdomain distance, meaning decreasing the exogenous signaling associated to crypt-like domains in favor of differentiated villus-like domains, the epithelium stopped responding to the exogenous signals imposed. For both ephrinB1 and Wnt3a signals, the monolayers recovered their intrinsic compartmentalization properties (crypt-like domain size, first neighbor distance and orientation). It has been previously reported that these monolayers have an intrinsic feedback loop¹²⁰ that sets the formation of the crypt-like domains. We have shown in this thesis that their size and order may be tuned by spatially localizing

one of the signals involved in this feedback loop (Wnt3a). However, the distance between crypt-like domains (i.e. the villus-like domains) is insensitive to these patterns. Whether this is due to biochemical signaling, mechanical forces that ensure the monolayer integrity or other causes, we can not foresee and should be addressed in future projects.

Finally, we could unveil the clustering of Wnt3a proteins during the process of crypt-like domain formation. To the best of our knowledge, this is the first time that such type of Wnt3a clustering is reported. Earlier work highlighted ephrinB1 oligomerization as a requirement to activate EphB receptor. Recently, we reported that clusters of ephrinB1 are critical determinants of targeting response^{144,159}. We speculate that Wnt3a aggregates could be functionally comparable with the ephrin ones. However, future experiments should clarify if oligomerization of Wnt3a transmembrane receptors¹⁷³ is also involved in the signal transduction process.

Altogether, we believe that these experiments suggest that we have designed and set up a tool to effectively address such type of questions: investigate the self-organization of organoid-derived intestinal epithelial cells and systematically study the effects and mechanisms of individual ligands on this process. On the long run, one might then speculate that such a system could be employed in gathering relevant information that could be useful as an input to predict the behavior of more complex systems such as organoids or tissues *in vivo*.

6 Conclusions

- On the epithelial cellular systems studied in this work, which include both primary organoid-derived cells and cell lines, the density of the extracellular matrix was able to trigger a sharp transition between two binary cell organizations: monolayers and 3D structures (tubular networks and cellular aggregates). Despite the role of surface protein density in cell adhesion has been extensively described, our results identify a key role for this parameter in guiding cellular self-organization. Above a threshold protein density value, 3D structures with epithelial tissue-like features were able to form on 2D substrates. By using the wetting analogy, these binary cellular organizations might be interpreted as a complete-to-partial wetting transition induced by the substrate protein concentration. These two phases could be attributed to cues provided by a specific matrix composition, in which laminin content appears as relevant. Additionally, this wetting phase transition is prevented when cells are cultured on substrates of stiffness values lower than their ECM *in vivo* (~20 kPa). In this case, the low substrate stiffness prevents the formation of 3D tissue-like structures.
- When referring to organoid-derived intestinal epithelial monolayers formed upon the culture of single cells, the dynamics of the formation process of monolayers or transient tubular networks revealed that the intestinal stem cells present in the culture have a motility that depends on the protein substrate concentration. The highest protein concentrations, which usually promote higher adhesion to matrices, increase cell motility. Likewise, we also found that above a well-defined protein concentration threshold, epithelial cells can redistribute the extracellular matrix to form 3D structures. The identification of this protein redistribution process sets the basis to further investigate the mechanistic insights of cell-extracellular matrix signals that control epithelial organization.
- Despite the transition between monolayers and 3D structures was observed for all the cells tested here, only the organoid-derived intestinal cells displayed the formation of tubular networks, suggesting that this is an intrinsic property of these cultures. We found that the tubular networks displayed a higher percentage of stem cells than monolayers, so we attributed the ability of organoid-derived intestinal cells to self-assemble in tubular structures to the presence of intestinal stem cells. We then demonstrated that by reducing the proportion of stem cells in the culture the formation of such tubular networks was impaired and cells self-assembled in 3D aggregates similar to the ones formed by the cell lines. Actually, we suggest that the tubular networks of our cultures were the precursors of primitive crypt-like structures, as they have dimensions comparable with the *in vivo* intestinal crypts, and display clusters of stem cells surrounded by laminin. As *in vivo* crypts are formed by a specific number of stem cells, our results suggest that the stemness of the culture is a relevant parameter in the self-organization process of the intestinal epithelial monolayers and that the dimensions of the crypt-like domains formed do

not depend on the dimensionality of the culture or external signaling gradients, at least for a period of time.

- A variation of the micro-contact printing technique was successfully applied to transfer epithelial or stromal cell-derived signals relevant for the organization of the small intestinal epithelium onto Matrigel-coated substrates. The transfer of large (ephrinB1 clusters) and small (Wnt3a) molecules could be performed in a precise way over large printing areas for structures of a large variety of dimensions (from 2 to 200 μm). Moreover, the strength of the signals can be easily tuned by changing the concentration of the solutions used to print the substrates. We proved that the micropatterned technique designed is versatile and suitable for the culture of organoid-derived intestinal epithelial cells, which were able to form monolayers with compartmentalized crypt- and villus-like domains on these micropatterned surfaces.
- The micropatterning technique described above was successfully employed to study the effects of cell-derived cues upon their binding to specific locations on a substrate. By mimicking the *in vivo* spatial distribution of ephrinB1 and Wnt3a ligands, we evaluated their effects on the intrinsic crypt-like domain distribution found in monolayers grown on non-patterned substrates. When the dimensions imposed by the micropattern template were similar to the ones intrinsically displayed by the self-organized monolayers, both ephrinB1 and Wnt3a ligands redistributed the crypt-like domains according to the micropatterns. Therefore, in this scenario, the effects of exogenous signals on the dimensions of the crypt- and villus-like domains were visible. By slightly increasing the diameter of the patterns, the proliferative capacity of these monolayers might be tuned and by slightly increasing in their interdomain distance, the size of the differentiated domains might also be tuned. However, we also discovered that when the dimensions of the micropatterns and, in particular, their center-to-center distances were far away from the intrinsic values of the monolayers, cells stopped responding to the exogenous signals imposed. For both ephrinB1 and Wnt3a signals, the monolayers recovered their intrinsic proliferation and compartmentalization status. Additionally, we found that Wnt3a micropatterns were much more efficient in confining the distribution on the crypt-like domains than ephrinB1 ligands. We suggest that this might be explained by the different confinement effect that these molecules have in the tissue *in vivo*. Altogether, we conclude that these results validate our tool to systematically investigate the effects of cell-derived individual signals on the self-organization of organoid-derived intestinal epithelial cells.
- Together, this thesis analyzes the impact of substrate-derived cues on the self-organization of organoid-derived intestinal epithelial cells. Therefore, it can have a wide range of applications reaching from basic research about cell-cell and cell-ECM interactions, to the improvement of studies of tissue development, homeostasis and regeneration.

7 References

1. Lowe, J. S. & Anderson, P. G. *Human Histology*. (2014).
2. Vrana, N. E. *et al.* Engineering functional epithelium for regenerative medicine and *in vitro* organ models: A review. *Tissue Eng. - Part B Rev.* **19**, 529–543 (2013).
3. Beyer, I., van Rensburg, R. & Lieber, A. Overcoming physical barriers in cancer therapy. *Tissue Barriers* **1**, e23647 (2013).
4. Hoffmann, W. Stem Cells, Self-Renewal and Cancer of the Gastric Epithelium. *Curr. Med. Chem.* **19**, 5975–5983 (2015).
5. Mullin, J. M. Epithelial Barriers, Compartmentation, and Cancer. *Sci. Signal.* **216**, (2004).
6. Laurie, G. W., Leblond, C. P. & Martin, G. R. Localization of type IV collagen, laminin, heparan sulfate proteoglycan, and fibronectin to the basal lamina of basement membranes. *J. Cell Biol.* **95**, 340–344 (1982).
7. Simon-Assmann, P. *et al.* The Laminins: Role in Intestinal Morphogenesis and Differentiation. *Ann. New York Acad. Sci.* (1998).
8. Roulis, M. & Flavell, R. A. Fibroblasts and myofibroblasts of the intestinal lamina propria in physiology and disease. *Differentiation* **92**, 116–131 (2016).
9. Timpl, R. Macromolecular organization of basement membranes. *Curr. Opin. Cell Biol.* **8**, 618–624 (1996).
10. Paulson, M. Basement membrane proteins: Structure, assembly, and cellular interactions. *Crit. Rev. Biochem. Mol. Biol.* **27**, 93–127 (1992).
11. Braga, V. M. Cell-cell adhesion and signalling. *Curr. Opin. Cell Biol.* **14**, 546–556 (2002).
12. Drubin, D. G. & Nelson, W. J. Origins of cell polarity. *Cell* **84**, 335–344 (1996).
13. Fath, K. R., Mamajiwalla, S. N. & Burgess, D. R. The cytoskeleton in development of epithelial cell polarity. *J. Cell Sci.* **106**, 65–73 (1993).
14. Shashikanth, N. *et al.* Epithelial organization: The gut and beyond. *Compr. Physiol.* **7**, 1497–1518 (2017).
15. Raman, R., Pinto, C. S. & Sonawane, M. Polarized Organization of the Cytoskeleton: Regulation by Cell Polarity Proteins. *J. Mol. Biol.* **430**, 3565–3584 (2018).
16. Braga, V. Spatial integration of E-cadherin adhesion, signalling and the epithelial cytoskeleton. *Curr. Opin. Cell Biol.* **42**, 138–145 (2016).
17. Wu, S. K. *et al.* Cortical F-actin stabilization generates apical-lateral patterns of junctional contractility that integrate cells into epithelia. *Nat. Cell Biol.* **16**, 167–178 (2014).
18. Li, Y., Naveed, H., Kachalo, S., Xu, L. X. & Liang, J. Mechanisms of regulating cell topology in proliferating epithelia: Impact of division plane, mechanical forces, and cell memory. *PLoS One* **7**, (2012).

19. Stricker, J., Falzone, T. & Gardel, M. L. Mechanics of the F-actin cytoskeleton. *J. Biomech.* **43**, 9–14 (2010).
20. Goto, K. & Ishikawa, H. Differential distribution of actin and cytokeratin in isolated full-length rabbit renal tubules. *Cell Struct. Funct.* **23**, 73–84 (1998).
21. Mulholland, D. J., Wilson, J., Vogl, W. & Webber, W. Distribution of actin bundles in Bowman's capsule of rat kidney. *Tissue Cell* **31**, 610–616 (1999).
22. Murakami, T. & Ishikawa, H. Stress Fibers in situ in Proximal Tubules of the Rat Kidney. *Cell Struct. Funct.* **16**, 231–240 (1991).
23. Trepap, X. *et al.* Physical forces during collective cell migration. *Nat. Phys.* **5**, 426–430 (2009).
24. Farooqui, R. & Fenteany, G. Multiple rows of cells behind an epithelial wound edge extend cryptic lamellipodia to collectively drive cell-sheet movement. *J. Cell Sci.* **118**, 51–63 (2005).
25. Krndija, D. *et al.* Active cell migration is critical for steady-state epithelial turnover in the Gut. *Science (80-.)*. **365**, 705–710 (2019).
26. Hartsock, A. & Nelson, W. J. Adherens and tight junctions: Structure, function and connections to the actin cytoskeleton. *Biochim. Biophys. Acta - Biomembr.* **1778**, 660–669 (2008).
27. Stevenson, B. R., Siliciano, J. D., Mooseker, M. S. & Goodenough, D. A. Identification of ZO-1: A high molecular weight polypeptide associated with the tight junction (Zonula Occludens) in a variety of epithelia. *J. Cell Biol.* **103**, 755–766 (1986).
28. Fanning, A. S., Jameson, B. J., Jesaitis, L. A. & Anderson, J. M. The tight junction protein ZO-1 establishes a link between the transmembrane protein occludin and the actin cytoskeleton. *J. Biol. Chem.* **273**, 29745–29753 (1998).
29. Gumbiner, B. M. Regulation of cadherin-mediated adhesion in morphogenesis. *Nat. Rev. Mol. Cell Biol.* **6**, 622–634 (2005).
30. Van Roy, F. & Berx, G. The cell-cell adhesion molecule E-cadherin. *Cell. Mol. Life Sci.* **65**, 3756–3788 (2008).
31. Gumbiner, B., Stevenson, B. & Grimaldi, A. The role of the cell adhesion molecule uvomorulin in the formation and maintenance of the epithelial junctional complex. *J. Cell Biol.* **107**, 1575–1587 (1988).
32. Mays, R. W. *et al.* Hierarchy of mechanisms involved in generating Na/K-ATPase polarity in MDCK epithelial cells. *J. Cell Biol.* **130**, 1105–1115 (1995).
33. Nieto, M. A., Huang, R. Y. Y. J., Jackson, R. A. A. & Thiery, J. P. P. Emt: 2016. *Cell* **166**, 21–45 (2016).
34. Garrod, D. & Chidgey, M. Desmosome structure, composition and function. *Biochim. Biophys. Acta - Biomembr.* **1778**, 572–587 (2008).
35. Amagai, M. Adhesion molecules. I: Keratinocyte-Keratinocyte interactions; cadherins and pemphigus. *J. Invest. Dermatol.* **104**, 146–152 (1995).

36. Hagios, C., Lochter, A. & Bissell, M. J. Tissue architecture: The ultimate regulator of breast epithelial function. *Phil. Trans. R. Soc. Lond. B* **353**, 857–870 (1998).
37. Hall, H. G., Farson, A., Chin, S. & Bissell, M. J. Lumen formation by epithelial cell lines in culture. *In Vitro* **18**, 4672–4676 (1982).
38. Wang, A. Z., Ojakian, G. K. & Nelson, W. J. Steps in the morphogenesis of a polarized epithelium: II. Disassembly and assembly of plasma membrane domains during reversal of epithelial cell polarity in multicellular epithelial (MDCK) cysts. *J. Cell Sci.* **95**, 153–165 (1990).
39. Ivanov, A. I. *et al.* Myosin II regulates the shape of three-dimensional intestinal epithelial cysts. *J. Cell Sci.* **121**, 1803–1814 (2008).
40. Jaffe, A. B., Kaji, N., Durgan, J. & Hall, A. Cdc42 controls spindle orientation to position the apical surface during epithelial morphogenesis. *J. Cell Biol.* **183**, 625–633 (2008).
41. Patankar, M., Eskelinen, S., Tuomisto, A., Mäkinen, M. J. & Karttunen, T. J. KRAS and BRAF mutations induce anoikis resistance and characteristic 3D phenotypes in Caco-2 cells. *Mol. Med. Rep.* **20**, 4634–4644 (2019).
42. Petersen, O. W., Ronnov-Jessen, L., Howlett, A. R. & Bissell, M. J. Interaction with basement membrane serves to rapidly distinguish growth and differentiation pattern of normal and malignant human breast epithelial cells. *Proc. Natl. Acad. Sci. U. S. A.* **89**, 9064–9068 (1992).
43. Weaver, V. M., Howlett, A. R., Langton-Webster, B., Petersen, O. W. & Bissell, M. J. The development of a functionally relevant cell culture model of progressive human breast cancer. *Semin. Cancer Biol.* **6**, 175–184 (1995).
44. Wang, F. *et al.* Reciprocal interactions between β 1-integrin and epidermal growth factor receptor in three-dimensional basement membrane breast cultures: A different perspective in epithelial biology. *Proc. Natl. Acad. Sci. U. S. A.* **95**, 14821–14826 (1998).
45. O’Brien, L. E. *et al.* Rac1 orientates epithelial apical polarity through effects on basolateral laminin assembly. *Nat. Cell Biol.* **3**, 831–838 (2001).
46. Martín-Belmonte, F. *et al.* Cell-Polarity Dynamics Controls the Mechanism of Lumen Formation in Epithelial Morphogenesis. *Curr. Biol.* **18**, 507–513 (2008).
47. Powers, M. J., Rodriguez, R. E. & Griffith, L. G. Cell-substratum adhesion strength as a determinant of hepatocyte aggregate morphology. *Biotechnol. Bioeng.* **53**, 415–426 (1997).
48. Ravasio, A. *et al.* Regulation of epithelial cell organization by tuning cell-substrate adhesion. *Integr. Biol.* (2015).
49. Glazier, J. A., Gross, S. P. & Stavans, J. Dynamics of two-dimensional soap froths. *Phys. Rev. A* **36**, 306–312 (1987).
50. Glazier, J. A., Anderson, M. P. & Grest, G. S. Coarsening in the two-dimensional soap froth and the large- Q potts model: A detailed comparison. *Philos. Mag. B Phys. Condens. Matter; Stat. Mech. Electron. Opt. Magn. Prop.* **62**, 615–647 (1990).

51. Stange, T. G., Mathew, R., Evans, D. F. & Hendrickson, W. A. Scanning Tunneling Microscopy and Atomic Force Microscopy Characterization of Polystyrene Spin-Coated onto Silicon Surfaces. *Langmuir* **8**, 920–926 (1992).
52. Mertig, M. *et al.* Scanning Force Microscopy and Geometric Analysis of Two-Dimensional Collagen Network Formation. *Surf. Interface Anal.* **25**, 514–521 (1997).
53. Thiele, U., Mertig, M. & Pompe, W. Dewetting of an evaporating thin liquid film: Heterogeneous nucleation and surface instability. *Phys. Rev. Lett.* **80**, 2869–2872 (1998).
54. Mertig, M., Thiele, U., Bradt, J., Klemm, D. & Pompe, W. Dewetting of thin collagenous precursor films. *Appl. Phys. A Mater. Sci. Process.* **66**, 565–568 (1998).
55. Scianna, M., Bell, C. G. & Preziosi, L. A review of mathematical models for the formation of vascular networks. *J. Theor. Biol.* **333**, 174–209 (2013).
56. Gonzalez-Rodriguez, D., Guevorkian, K., Douezan, S. & Brochard-Wyart, F. Soft Matter Models of Developing Tissues and Tumors. *Science (80-)*. **82**, 910–917 (2012).
57. Ryan, P. L., Foty, R. A., Kohn, J. & Steinberg, M. S. Tissue spreading on implantable substrates is a competitive outcome of cell-cell vs. cell-substratum adhesivity. *Proc. Natl. Acad. Sci.* **98**, 4323–4327 (2001).
58. Douezan, S. *et al.* Spreading dynamics and wetting transition of cellular aggregates. *Proc. Natl. Acad. Sci. U. S. A.* **108**, 7315–7320 (2011).
59. Douezan, S., Dumond, J. & Brochard-Wyart, F. Wetting transitions of cellular aggregates induced by substrate rigidity. *Soft Matter* **8**, 4578–4583 (2012).
60. Beaune, G. *et al.* How cells flow in the spreading of cellular aggregates. *Proc. Natl. Acad. Sci. U. S. A.* **111**, 8055–8060 (2014).
61. Beaune, G. *et al.* Reentrant wetting transition in the spreading of cellular aggregates. *Soft Matter, R. Soc. Chem.* **13**, 8474–8482 (2017).
62. Douezana, S. & Brochard-Wyart, F. Dewetting of cellular monolayers. *Eur. Phys. J. E* **35**, (2012).
63. Pérez-González, C. *et al.* Active wetting of epithelial tissues. *Nat. Phys.* **15**, 79–88 (2019).
64. Rossi, G., Manfrin, A. & Lutolf, M. P. Progress and potential in organoid research. *Nat. Rev. Genet.* **19**, 671–687 (2018).
65. Torras, N., García-Díaz, M., Fernández-Majada, V. & Martínez, E. Mimicking epithelial tissues in three-dimensional cell culture models. *Front. Bioeng. Biotechnol.* **6**, 1–7 (2018).
66. Sato, T. *et al.* Single Lgr5 stem cells build crypt-villus structures *in vitro* without a mesenchymal niche. *Nature* **459**, 262–5 (2009).
67. Foster, J. W. *et al.* Cornea organoids from human induced pluripotent stem cells. *Sci. Rep.* **7**, 1–8 (2017).

68. Lee, J. H. *et al.* Lung stem cell differentiation in mice directed by endothelial cells via a BMP4-NFATc1-thrombospondin-1 axis. *Cell* **156**, 440–455 (2014).
69. Boonekamp, K. E. *et al.* Long-term expansion and differentiation of adult murine epidermal stem cells in 3D organoid cultures. *Proc. Natl. Acad. Sci. U. S. A.* **116**, 14630–14638 (2019).
70. Huch, M. *et al.* In vitro expansion of single Lgr5 + liver stem cells induced by Wnt-driven regeneration. *Nature* **494**, 247–250 (2013).
71. Huch, M. *et al.* Unlimited in vitro expansion of adult bi-potent pancreas progenitors through the Lgr5/R-spondin axis. *EMBO J.* **32**, 2708–2721 (2013).
72. Huch, M. & Koo, B. K. Modeling mouse and human development using organoid cultures. *Dev.* **142**, 3113–3125 (2015).
73. Dekkers, J. F. *et al.* A functional CFTR assay using primary cystic fibrosis intestinal organoids. *Nat. Med.* **19**, 939–945 (2013).
74. Augustyniak, J. *et al.* Organoids are promising tools for species-specific in vitro toxicological studies. *J. Appl. Toxicol.* **39**, 1610–1622 (2019).
75. Forsythe, S. D. *et al.* Environmental toxin screening using human-derived 3D bioengineered liver and cardiac organoids. *Front. Public Heal.* **6**, (2018).
76. Bjerknes, M. & Cheng, H. Intestinal Epithelial Stem Cells and Progenitors. *Methods Enzymol.* **419**, 337–383 (2006).
77. Van Der Flier, L. G. & Clevers, H. Stem cells, self-renewal, and differentiation in the intestinal epithelium. *Annu. Rev. Physiol.* **71**, 241–260 (2009).
78. Barker, N. *et al.* Identification of stem cells in small intestine and colon by marker gene Lgr5. *Nature* **449**, 1003–7 (2007).
79. Ootani, A. *et al.* Sustained in vitro intestinal epithelial culture within a Wnt-dependent stem cell niche. *Nat. Med.* **15**, 701–706 (2009).
80. Takahashi, T. & Shiraishi, A. Stem cell signaling pathways in the small intestine. *Int. J. Mol. Sci.* **21**, 1–18 (2020).
81. Farin, H. F. *et al.* Visualization of a short-range Wnt gradient in the intestinal stem-cell niche. *Nature* **530**, 340–343 (2016).
82. Sato, T. & Clevers, H. Growing self-organizing mini-guts from a single intestinal stem cell: Mechanism and applications. *Science (80-.).* **340**, 1190–1194 (2013).
83. Qi, Z. *et al.* BMP restricts stemness of intestinal Lgr5⁺ stem cells by directly suppressing their signature genes. *Nat. Commun.* **8**, (2017).
84. Batlle, E. *et al.* B -Catenin and TCF Mediate Cell Positioning in the Intestinal Epithelium by Controlling the Expression of EphB / EphrinB. *Cell* **111**, 251–263 (2002).
85. Holmberg, J. *et al.* EphB Receptors Coordinate Migration and Proliferation in the Intestinal Stem Cell Niche. *Cell* **125**, 1151–1163 (2006).
86. Mahoney, Z. X., Stappenbeck, T. S. & Miner, J. H. Laminin α 5 influences the architecture of the mouse small intestine mucosa. *J. Cell Sci.* **121**, 2493–2502 (2008).

87. Yui, S. *et al.* YAP/TAZ-Dependent Reprogramming of Colonic Epithelium Links ECM Remodeling to Tissue Regeneration. *Cell Stem Cell* **22**, 35–49.e7 (2018).
88. Serra, D. *et al.* Self-organization and symmetry breaking in intestinal organoid development. *Nature* **569**, 66–72 (2019).
89. Gregorieff, A., Liu, Y., Inanlou, M. R., Khomchuk, Y. & Wrana, J. L. Yap-dependent reprogramming of Lgr5⁺ stem cells drives intestinal regeneration and cancer. *Nature* **526**, 715–718 (2015).
90. Imajo, M., Miyatake, K., Imura, A., Miyamoto, A. & Nishida, E. A molecular mechanism that links Hippo signalling to the inhibition of Wnt/ β -catenin signalling. *EMBO J.* **31**, 1109–1122 (2012).
91. Meran, L., Baulies, A. & Li, V. S. W. Intestinal Stem Cell Niche: The Extracellular Matrix and Cellular Components. *Stem Cells Int.* **2017**, (2017).
92. Pinto, D., Gregorieff, A., Begthel, H. & Clevers, H. Canonical Wnt signals are essential for homeostasis of the intestinal epithelium. *Genes Dev.* **17**, 1709–1713 (2003).
93. Fevr, T., Robine, S., Louvard, D. & Huelsken, J. Wnt/ β -Catenin Is Essential for Intestinal Homeostasis and Maintenance of Intestinal Stem Cells. *Mol. Cell. Biol.* **27**, 7551–7559 (2007).
94. Gregorieff, A. *et al.* Expression Pattern of Wnt Signaling Components in the Adult Intestine. *Gastroenterology* **129**, 626–638 (2005).
95. Sato, T. *et al.* Paneth cells constitute the niche for Lgr5 stem cells in intestinal crypts. *Nature* **469**, 415–418 (2011).
96. Crosnier, C., Stamatakis, D. & Lewis, J. Organizing cell renewal in the intestine: Stem cells, signals and combinatorial control. *Nat. Rev. Genet.* **7**, 349–359 (2006).
97. Sato, T. *et al.* Paneth cells constitute the niche for Lgr5 stem cells in intestinal crypts. *Nature* **469**, 415–418 (2011).
98. Garabedian, E. M., Roberts, L. J. J., McNevin, M. S. & Gordon, J. I. Examining the role of Paneth cells in the small intestine by lineage ablation in transgenic mice. *J. Biol. Chem.* **272**, 23729–23740 (1997).
99. Durand, A. *et al.* Functional intestinal stem cells after Paneth cell ablation induced by the loss of transcription factor Math1 (Atoh1). *Proc. Natl. Acad. Sci. U. S. A.* **109**, 8965–8970 (2012).
100. Jung, P. *et al.* Isolation and *in vitro* expansion of human colonic stem cells. *Nat. Med.* **17**, 1225–7 (2011).
101. Spence, J. R. *et al.* Directed differentiation of human pluripotent stem cells into intestinal tissue *in vitro*. *Nature* **470**, 105–9 (2011).
102. Jabaji, Z. *et al.* Type I Collagen as an Extracellular Matrix for the In Vitro Growth of Human Small Intestinal Epithelium. **9**, 1–10 (2014).
103. Pastuła, A. *et al.* Three-Dimensional Gastrointestinal Organoid Culture in Combination with Nerves or Fibroblasts: A Method to Characterize the Gastrointestinal Stem Cell Niche. *Stem Cells Int.* **2016**, (2016).

104. Gjorevski, N. *et al.* Designer matrices for intestinal stem cell and organoid culture. *Nature* **539**, 560–564 (2016).
105. Cai, J. *et al.* The Hippo signaling pathway restricts the oncogenic potential of an intestinal regeneration program. *Genes Dev.* **24**, 2383–2388 (2010).
106. Elosegui-Artola, A. *et al.* Force Triggers YAP Nuclear Entry by Regulating Transport across Nuclear Pores. *Cell* **171**, 1397-1410.e14 (2017).
107. Brusatin, G., Panciera, T., Gandin, A., Citron, A. & Piccolo, S. Biomaterials and engineered microenvironments to control YAP/TAZ-dependent cell behaviour. *Nat. Mater.* **17**, 1063–1075 (2018).
108. Yin, X. *et al.* Niche-independent high-purity cultures of Lgr5⁺ intestinal stem cells and their progeny. *Nat. Methods* **11**, 106–112 (2014).
109. Attayek, P. J. *et al.* *In Vitro* Polarization of Colonoids to Create an Intestinal Stem Cell Compartment. *PLoS One* **11**, 1–23 (2016).
110. Shyer, A. E., Huycke, T. R., Lee, C., Mahadevan, L. & Tabin, C. J. Bending Gradients: How the intestinal stem cell gets its home. *Cell* **161**, 569–580 (2015).
111. Moon, C., Vandussen, K. L., Miyoshi, H. & Stappenbeck, T. S. Development of a primary mouse intestinal epithelial cell monolayer culture system to evaluate factors that modulate IgA transcytosis. *Mucosal Immunol.* **7**, 818–828 (2014).
112. In, J. *et al.* Enterohemorrhagic Escherichia coli Reduces Mucus and Intermicrovillar Bridges in Human Stem Cell-Derived Colonoids. *Cmgh* **2**, 48-62.e3 (2016).
113. Ettayebi, K. *et al.* Replication of Human Noroviruses in Stem Cell-Derived Human Enteroids. *Science (80-.)*. **47**, 192–200 (2017).
114. Vandussen, K. L. *et al.* Development of an enhanced human gastrointestinal epithelial culture system to facilitate patient-based assays. *Gut* **64**, 911–920 (2015).
115. Kozuka, K. *et al.* Development and Characterization of a Human and Mouse Intestinal Epithelial Cell Monolayer Platform. *Stem Cell Reports* **9**, 1976–1990 (2017).
116. Wang, Y. *et al.* Self-renewing Monolayer of Primary Colonic or Rectal epithelial cells. *Cell. Mol. Gastroenterol. Hepatol.* **4**, 165-182.e7 (2017).
117. Scott, A. *et al.* Long-term renewable human intestinal epithelial stem cells as monolayers: A potential for clinical use. *J. Pediatr. Surg.* **51**, 995–1000 (2016).
118. Kim, R. *et al.* Formation of arrays of planar, murine, intestinal crypts possessing a stem/proliferative cell compartment and differentiated cell zone. *Lab Chip* **18**, 2202–2213 (2018).
119. Altay, G. *et al.* Self-organized intestinal epithelial monolayers in crypt and villus-like domains show effective barrier function. *Sci. Rep.* **9**, 1–14 (2019).
120. Thorne, C. A. *et al.* Enteroid Monolayers Reveal an Autonomous WNT and BMP Circuit Controlling Intestinal Epithelial Growth and Organization. *Dev. Cell* **44**, 624-633.e4 (2018).
121. Pérez-González, C. *et al.* Mechanical compartmentalization of the intestinal organoid

enables crypt folding and collective cell migration. *bioRxiv* (2020).

122. Sambuy, Y. *et al.* The Caco-2 cell line as a model of the intestinal barrier: Influence of cell and culture-related factors on Caco-2 cell functional characteristics. *Cell Biol. Toxicol.* **21**, 1–26 (2005).
123. Rindler, M. J., Chuman, L. M., Shaffer, L. & Saier, M. H. Retention of differentiated properties in an established dog kidney epithelial cell line (MDCK). *J. Cell Biol.* **81**, 635–648 (1979).
124. Zimmer, M., Palmer, A., Köhler, J. & Klein, R. EphB-ephrinB bi-directional endocytosis terminates adhesion allowing contact mediated repulsion. *Nat. Cell Biol.* **5**, 869–878 (2003).
125. Castaño, A. G., Hortigiela, V., Lagunas, A., Cortina, C. & Samitier, J. Protein patterning on hydrogels by direct microcontact printing: application to cardiac differentiation. *RSC Adv* **4**, 29120–3 (2014).
126. Comelles, J. *et al.* Microfabrication of poly(acrylamide) hydrogels with independently controlled topography and stiffness. *Biofabrication* **12**, (2020).
127. Barriga, F. M. *et al.* Mex3a Marks a Slowly Dividing Subpopulation of Lgr5⁺ Intestinal Stem Cells. *Cell Stem Cell* **20**, 801–816 (2017).
128. Fernández-Majada, V. *et al.* The tumour suppressor CYLD regulates the p53 DNA damage response. *Nat. Commun.* **7**, (2016).
129. Watanabe, K. *et al.* A ROCK inhibitor permits survival of dissociated human embryonic stem cells. *Nat. Biotechnol.* **25**, 681–6 (2007).
130. Fischer, R. S., Myers, K. A., Gardel, M. L. & Waterman, C. M. Stiffness-controlled three-dimensional extracellular matrices for high-resolution imaging of cell behavior. *Nat. Protoc.* **7**, 2056–2066 (2012).
131. Tse, J. R. & Engler, A. J. Preparation of hydrogel substrates with tunable mechanical properties. *Curr. Protoc. Cell Biol.* 1–16 (2010).
132. Corning Collagen I High Concentration (HC) Rat Tail; Certificate of Analysis (SPC-354249).
133. Hughes, C. S., Postovit, L. M. & Lajoie, G. A. Matrigel: a complex protein mixture required for optimal growth of cell culture. *Proteomics* **10**, 1886–90 (2010).
134. Lang, S., Von Philipsborn, A. C., Bernard, A., Bonhoeffer, F. & Bastmeyer, M. Growth cone response to ephrin gradients produced by microfluidic networks. *Anal. Bioanal. Chem.* **390**, 809–816 (2008).
135. Brismar, H., Patwardhan, A., Jaremko, G. & Nyengaard, J. Thickness estimation of fluorescent sections using a CSLM. *J. Microsc.* **184**, 106–116 (1996).
136. Alcaraz, J. *et al.* Microrheology of human lung epithelial cells measured by atomic force microscopy. *Biophys. J.* **84**, 2071–9 (2003).
137. Lindeberg, T. Feature Detection with Automatic Scale Selection. *Int. J. Comput. Vis.* **30**, 79–116 (1998).

138. Thiele, U., Mertig, M., Pompe, W. & Wendrock, H. Polygonal Networks Resulting from Dewetting. *Foam. Emuls.* 127–136 (1999).
139. Tinevez, J. Y. *et al.* TrackMate: An open and extensible platform for single-particle tracking. *Methods* **115**, 80–90 (2017).
140. Bhujbal, S. V. *et al.* Effect of design geometry, exposure energy, cytophilic molecules, cell type and load in fabrication of single-cell arrays using micro-contact printing. *Sci. Rep.* **10**, 1–13 (2020).
141. Kane, R. S., Takayama, S., Ostuni, E., Ingber, D. E. & Whitesides, G. M. Patterning proteins and cells using soft lithography. *Biomater. Silver Jubil. Compend.* **20**, 161–174 (1999).
142. Caballero, D. *et al.* Atomic Force Microscopy Characterization of a Microcontact Printed, Self-Assembled Thiol Monolayer for Use in Biosensors. *Anal. Lett.* **39**, 1721–34 (2006).
143. Stein, E. *et al.* Eph receptors discriminate specific ligand oligomers to determine alternative signaling complexes, attachment, and assembly responses. *Genes Dev.* **12**, 667–678 (1998).
144. Hortigüela, V. *et al.* Nanopatterns of Surface-Bound EphrinB1 Produce Multivalent Ligand-Receptor Interactions That Tune EphB2 Receptor Clustering. *Nano Lett.* **18**, 629–637 (2018).
145. Comelles, J. *et al.* Epithelial colonies *in vitro* elongate through collective effects. *BioRxiv* (2020).
146. Aigouy, B. *et al.* Cell Flow Reorients the Axis of Planar Polarity in the Wing Epithelium of *Drosophila*. *Cell* **142**, 773–786 (2010).
147. Wang, Y. *et al.* Capture and 3D culture of colonic crypts and colonoids in a microarray platform. *Lab Chip* **13**, 4625–4634 (2013).
148. Mertig, M., Kirsch, R. & Pompe, W. Biomolecular approach to nanotube fabrication. *Appl. Phys. A Mater. Sci. Process.* **66**, 723–727 (1998).
149. Affolter, M., Zeller, R. & Caussinus, E. Tissue remodelling through branching morphogenesis. *Nat. Rev. Mol. Cell Biol.* **10**, 831–842 (2009).
150. Wang, A. Z., Ojakian, G. K. & Nelson, W. J. Steps in the morphogenesis of a polarized epithelium: I. Uncoupling the roles of cell-cell and cell-substratum contact in establishing plasma membrane polarity in multicellular epithelial (MDCK) cysts. *J. Cell Sci.* **95**, 137–151 (1990).
151. McAteer, J. A., Evan, A. P. & Gardner, K. D. Morphogenetic clonal growth of kidney epithelial cell line MDCK. *Anat. Rec.* **217**, 229–239 (1987).
152. Gupta, M. *et al.* Adaptive rheology and ordering of cell cytoskeleton govern matrix rigidity sensing. *Nat. Commun.* **6**, (2015).
153. Doss, B. L. *et al.* Cell response to substrate rigidity is regulated by active and passive cytoskeletal stress. *Proc. Natl. Acad. Sci. U. S. A.* **117**, 12817–12825 (2020).
154. Zajac, O. *et al.* Tumour spheres with inverted polarity drive the formation of

- peritoneal metastases in patients with hypermethylated colorectal carcinomas. *Nat. Cell Biol.* **20**, 296–306 (2018).
155. Co, J. Y. *et al.* Controlling Epithelial Polarity: A Human Enteroid Model for Host-Pathogen Interactions. *Cell Rep.* **26**, 2509–2520.e4 (2019).
 156. Piccolo, S., Dupont, S. & Cordenonsi, M. The biology of YAP/TAZ: Hippo signaling and beyond. *Physiol. Rev.* **94**, 1287–1312 (2014).
 157. Imajo, M., Ebisuya, M. & Nishida, E. Dual role of YAP and TAZ in renewal of the intestinal epithelium. *Nat. Cell Biol.* **17**, 7–19 (2015).
 158. Liao, D. *et al.* The effect of epidermal growth factor on the incremental Young's moduli in the rat small intestine. *Med. Eng. Phys.* **25**, 413–418 (2003).
 159. Cutrale, F. *et al.* Using enhanced number and brightness to measure protein oligomerization dynamics in live cells. *Nat. Protoc.* **14**, 616–638 (2019).
 160. Kiessling, L. L., Gestwicki, J. E. & Strong, L. E. Synthetic multivalent ligands as probes of signal transduction. *Angew. Chemie - Int. Ed.* **45**, 2348–2368 (2006).
 161. Janes, P. W., Nievergall, E. & Lackmann, M. Concepts and consequences of Eph receptor clustering. *Semin. Cell Dev. Biol.* **23**, 43–50 (2012).
 162. Tuft, B. W. *et al.* Photopolymerized micropatterns with high feature frequencies overcome chemorepulsive borders to direct neurite growth. *J. Tissue Eng. Regen. Med.* **12**, e1392–e1403 (2018).
 163. Clevers, H. & Batlle, E. EphB/EphrinB receptors and Wnt signaling in colorectal cancer. *Cancer Res.* **66**, 2–5 (2006).
 164. Douezan, S. & Brochard-Wyart, F. Active diffusion-limited aggregation of cells. *Soft Matter* **8**, 784–788 (2012).
 165. Smith, J. T., Elkin, J. T. & Reichert, W. M. Directed cell migration on fibronectin gradients: Effect of gradient slope. *Exp. Cell Res.* **312**, 2424–2432 (2006).
 166. Nakano, T. *et al.* Roles of Remote and Contact Forces in Epithelial Cell Structure Formation. *Biophys. J.* **118**, 1466–1478 (2020).
 167. Kechagia, J. Z., Ivaska, J. & Roca-Cusachs, P. Integrins as biomechanical sensors of the microenvironment. *Nat. Rev. Mol. Cell Biol.* **20**, 457–473 (2019).
 168. Gehart, H. & Clevers, H. Tales from the crypt: new insights into intestinal stem cells. *Nat. Rev. Gastroenterol. Hepatol.* **16**, 19–34 (2019).
 169. Rodríguez Seguí, S. A. Development of cellular microarrays for stem cell culture and early stage differentiation evaluation. (Universitat de Barcelona, 2010).
 170. Comelles Pujadas, J. Biochemical gradients on Poly(methyl methacrylate) surfaces. (2012).
 171. Melero, C. *et al.* Light-induced molecular adsorption of proteins using the primo system for micro-patterning to study cell responses to extracellular matrix proteins. *J. Vis. Exp.* **2019**, 1–19 (2019).
 172. Barker, N. *et al.* Crypt stem cells as the cells-of-origin of intestinal cancer. *Nature*

- 457**, 608–611 (2009).
173. Bommer, G. T. & Fearon, E. R. Developmental Signaling Networks: WNT/ β -Catenin Signaling in the Gastrointestinal Tract. in *Physiology of the Gastrointestinal Tract* **1**, 279–302 (Elsevier Inc., 2012).

8 Resumen en castellano

Efectos de señalizaciones derivadas del sustrato sobre la auto-organización del epitelio intestinal derivado de organoides

El cultivo de organoides intestinales ha generado nuevas oportunidades para estudiar la organización del tejido epitelial, ya que proporciona sistemas que recapitulan *in vitro* la fisiología del tejido *in vivo*. El uso de organoides ha permitido grandes avances en la biología de los tejidos epiteliales tridimensionales (3D) complejos, reconociendo ampliamente el papel vital de la interacción entre las señales derivadas del sustrato y las moléculas de señalización dependientes de las células, para el desarrollo, la homeostasis y la regeneración de los tejidos. Sin embargo, el papel que ejercen cada uno de los componentes de manera individual no se puede estudiar de manera eficiente *in vitro*, incluso cuando se emplean organoides. Las limitaciones surgen del hecho de que los organoides están cultivados en matrices 3D (normalmente de Matrigel) que no permiten estudiar fácilmente la distribución espacial de proteínas de la matriz extracelular y las moléculas de señalización derivadas de células que orquestan la organización del tejido *in vivo*. Estudios recientes señalan que las células derivadas de organoides son capaces de auto-organizarse en monocapas epiteliales intestinales bidimensionales (2D) que también recapitulan la compartimentalización celular del tejido *in vivo* cuando se siembran en capas delgadas de Matrigel. La formación de estas monocapas intestinales proporciona un sistema de cultivo celular más fácil de explorar y analizar para comprender mejor la organización de los tejidos y sus propiedades. Los experimentos y resultados presentados en esta tesis tienen como objetivo usar este modelo biológico *in vitro* así como herramientas de bioingeniería, para investigar el impacto de las señales derivadas del sustrato en el proceso de auto-organización de las células epiteliales intestinales derivadas de organoides.

En esta tesis, se analiza la organización de células epiteliales en monocapas 2D o redes tubulares 3D en función de la adhesión célula-sustrato. De esta manera, se ilustra la organización en estructuras con tamaños y formas bien definidas independientemente de la dimensionalidad o señalizaciones externas. Además, la proporción de células madre regula la geometría de dichas estructuras. Por otro lado, en contraste con lo que se observa *in vivo*, los dominios de cripta de las monocapas están desordenados y su forma no es uniforme. Mediante una plataforma que localiza micropatrones de proteínas, controlamos el posicionamiento de los dominios de cripta-vellosidad. Para concluir, nuestro trabajo proporciona información sobre cómo influye la composición y la distribución de la ECM y las células madre en la morfología del tejido *in vivo*, como la dimensión de las criptas. Además, la plataforma desarrollada permite analizar el efecto de diferentes proteínas en la compartimentación de las células y en otros procesos epiteliales como proliferación, migración o diferenciación celular, tanto en homeostasis como en procesos patológicos.